University of Southampton

Faculty of Physical and Applied Sciences

School of Physics and Astronomy

Energy Transfer between Surface Plasmon Polariton modes with Hybrid Photorefractive Liquid Crystal Cells.

by

Stephen Barnes Abbott

Thesis for the degree of Doctor of Philosophy

January 2012

Abstract

In this thesis, a hybrid photorefractive liquid crystal cell structure with the addition of a thin 40nm Gold layer is proposed that demonstrates significant photorefractive control of Surface Plasmon Polaritons (SPP). The photorefractive effects are generated through optically controlling the conductivity of a ~100nm photoconducting poly-N-vinyl-carboxyl (PVK) layer. Therefore, when a potential is applied across the cell, the liquid crystal alignment and the SPP wavevector is able to be controlled with light. The aim for developing this device is for the eventual demonstration of SPP gain to offset the high optical losses and increase the characteristically short propagation length of SPP. The mechanism we intend to use to demonstrate gain is analogous to the asymmetric energy transfer in a wave mixing system for two laser beams used to typically characterise photorefractive materials.

We first characterise the electrical and optical behaviour of the novel photorefractive plasmonic structure proposed with uniform illumination. Our system demonstrates a good photorefractive wavevector shift of $0.207\mu m^{-1}$ for a 1.24eV SPP; this shift is in excess of the FWHM of the SPP resonance in the attenuated total reflection spectrum ($0.154\mu m^{-1}$). However, the electric behaviour of the system is found to be highly complex and cannot be fully characterised by an equivalent electrical circuit. In addition, due to electronic stability issues, we require a slow AC potential to demonstrate consistent photorefractive effects.

In a step towards realising SPP gain, we then consider the SPP interaction with a refractive index grating written into the liquid crystal layer with the interference pattern of crossed laser beams. We find that a SPP is diffracted into additional SPP modes. Our investigation then determines the ideal parameters that maximise the energy transfer by examining the diffraction efficiency dependence of each variable of the system. The maximum energy transfer observed is 25.3±2.3% for a 1.05eV SPP from a 4μm grating. With the assistance of a numerical simulation of our system we present a series of qualitative and semi-analytical descriptions to describe the mechanisms behind the observed trends. We discover that the diffraction efficiency is dependent of three important effects; the orientation of the grating, the penetration depth of the SPP into the liquid crystal and the magnitude of the periodic electric field in the liquid crystal. In addition, to fully describe the quantitative values observed we must also consider the presence of a thin 100nm region of the liquid crystal near the photoconductor interface that does not strongly respond to the applied electric field due to anchoring forces.

Declaration of Authorship

I, *Stephen Barnes Abbott*,

declare that the thesis entitled:

"Energy transfer between Surface Plasmon Polariton modes Hybrid Photorefractive Liquid Crystal cells"

and the work presented in the thesis are both my own and have been generated by me as the result of my own original research. I confirm that:

- This work was done wholly or mainly while in candidature for a research degree at this University;
- Where any part of this thesis has previously been submitted for a degree or any other qualification at this University or any other institution, this has been clearly stated;
- Where I have consulted the published work of others, this is always clearly attributed;
- Where I have quoted from the work of others, the source is always given. With the exception of such quotations, this thesis is entirely my own work;
- I have acknowledged all main sources of help;
- Where the thesis is based on work done by myself jointly with others, I have made clear exactly what was done by others and what I have contributed myself;
- Parts of this work have been published as: Conference proceedings and journal articles.

Signed: ……

Date: ……

List of Publications

The following journal publications and conference presentations have presented part of the work contained in this thesis. A copy of the relevant publications is presented at the end of the thesis after the references.

Publications:

- K. R. Daly, S.B. Abbott, G. D'Alessandro, D.C. Smith, and M. Kaczmarek, *Theory of hybrid photorefractive plasmonic liquid crystal cells*, Journal of the Optical Society of America B, 2011. **28**(8): p. 1874-1881.

- S.B. Abbott, K. R. Daly, G. D'Alessandro, M. Kaczmarek, and D.C. Smith, *Photorefractive Control of Surface Plasmon Polaritons in a Hybrid Liquid Crystal Cell*, Submitted to Optics letters January 2011.

Presentations:

- *Resonant Surface Plasmon Polariton Diffraction with Hybrid Photorefractive Liquid Crystal Cells*, MRS Fall meeting 2010, Boston, Massachusetts, Symposium L, L5.5, 30th November 2010.

- *Non-linear Control of Surface Plasmon Polaritons with Photorefractive Liquid Crystal Cells*, Nonlinear Optics (NLO) 2011, Kauai, Hawaii, NTuC5, 18th July 2011.

Acknowledgements

There are a number of individuals whom I wish to thank for their assistance during my PhD candidature. First, I would like to thank my supervisor Dr. David Smith for allowing me to undertake this research in his group, as well for his constant advice and encouragement. In addition, his instruction in the methods of experimental optics and the characterisation of nanostructures has proved invaluable. I would also like to thank Dr. Keith Daly and Dr. Giampaolo D'Alessandro for their contributions to this work in developing a theoretical model alongside the experimental work presented. I would also like to thank them for their assistance in attempting to understand this complex system.

I further acknowledge the expert advice provided by my advisor Prof. Malgosia Kaczmarek, as well as the contributions from members of her research group. In particular, Dr. Oleksandr Buchnev for his assistance in the fabrication of hybrid photorefractive liquid crystal cells and Dr. Mark Herrington for our discussions on the cells complicated electrical characterisation. In addition, I would like to extend my gratitude towards Mark Bampton and Gareth Savage from the School of Physics and Astronomy's mechanical and electrical workshops for their assistance in designing and building parts of the experimental apparatus utilised. My gratitude is also extended to Zondy Webber for his assistance in using the equipment in the universities rapid-prototyping clean room. I also wish to thank my colleagues in the office for making my time during my candidature entertaining.

Finally, I would like to thank my family for their support during my time as a PhD student at the University of Southampton.

Contents

Table of Figures

Figure *Page*

Figure *Page*

List of tables

List of Abbreviations

AC	Alternating Current
AFM	Atomic Force Microscopy
ATR	Attenuated Total-internal Reflection
CCD	Charge-Coupled Device
DC	Direct Current
FWHM	Full-Width Half-Maximum
IMI	Insulator-Metal-Insulator
LCD	Liquid Crystal Display
LRSPP	Long-Range Surface Plasmon Polariton
LSP	Localised Surface Plasmon
MIM	Metal-Insulator-Metal
NIR	Near Infra-Red
NLO	Non-Linear Optics
PVD	Physical Vapour Deposition
QCM	Quartz Crystal Microbalance
RC	Resistor-Capacitor (circuit)
SHG	Second Harmonic Generation
SP	Surface Plasmon
SPP	Surface Plasmon Polariton
TBG	Two-Beam Gain
TE	Transverse Electric (wave)
TIR	Total Internal Reflection
TM	Transverse Magnetic (wave)
UV	Ultra-Violet
UV-VIS	Ultra-Violet-Visible (spectroscopy)
VIS	Visible

Chemical Abbreviations

Ag	Silver
Al	Aluminium
Au	Gold
$BaTiO_3$	Barium Titanate
C_{60}	Buckminsterfullerene
CB	Chlorobenzene
Cr	Chromium
Fe	Iron
Ga	Gallium
GaAs	Gallium Arsenide
ITO	Indium Tin Oxide
KTP	Potassium Tantalate Niobate
$LiNbO_3$	Lithium Niobate
MEH-PPV	Poly-[2-methoxy, 5-(2'-ethyl-hexyloxy) -p-phenylene vinylene]
P3OT	Poly-3-octylthiophene
PI	Polyimide
PMMA	Poly-Methyl Methacrylate
PVA	Poly-vinyl alcohol
PVK	Poly-N-vinylcarbazole
R6G	Rhodamine 6G ($C_{28}H_{31}N_2O_3Cl$)
TNF	2,4,7-Trinitro-9-Fluorenone
SBN	Barium Sodium Niobate

Chapter 1

Introduction

A Surface Plasmon Polariton (SPP) is an electromagnetic wave confined at the interface between media with opposite sign permittivities. These waves occur at the interface between a metal and dielectric. For the simplest case of an isotropic semi-infinite metal, semi-infinite dielectric structure, SPP are transverse-magnetic polarised waves that propagate in the interface plane between the metal and dielectric, whilst exponentially decaying away from this interface into each medium [1]. The dispersion relation for SPP is determined by the optical properties of both confining materials and results in SPP having a wavevector that is always larger than light propagating in the dielectric [2]. Therefore, SPP are a unique form of confined electromagnetic wave and research into their applications forms the diverse field of Plasmonics.

There are many well established applications of SPP, foremost is their application in chemical and biological sensors as a means of molecule detection [3]. This is due to the large sensitivity of the dispersion of SPP to changes in the dielectric permittivity within a few hundred nanometres of the interface plane. Other notable linear applications of SPP include negative refraction [4], superlens [5] and broad-band linear polarisers [6]. In addition, several non-linear plasmonic effects have also been demonstrated such as surface enhanced Raman scattering [7] and white light continuum generation with a low peak power [8].

However, the most enticing potential application of SPP is their inclusion in all-optical or integrated electro-optical circuits. The SPP would then act as the information carrier between electrical or optical components in such a system. If a system designed to allow SPP to have an ultra-small modal volume were correctly developed, SPP could potentially be used in nanoscale interconnects that operate at optical frequencies [9], a technological possibility of which electronics or optical waveguides are not capable.

Unfortunately, SPP are limited by a very short propagation length that is typically of the order of 10μm or less for the most ideal high energy SPP modes (>2eV), due to the absorption of the metal. This propagation length is too short a distance for practical applications in integrated electro-optics [10]. In addition, further functionality is limited from the lack of active SPP components using light or other SPPs as a control signal. The

furthest currently in development are spatial-light modulators that use SPP as large tuneable absorption features [11].

A potential way of overcoming the limitations of a low propagation length and a shortage of active components is in the development of a photorefractive SPP system, where the refractive index of one of the confining materials is dependent on illumination. The illumination is normally from an external laser source, though photorefractive effects could also be achieved by the SPP modes as they are also electromagnetic waves. The simplest application of such a photorefractive SPP system would be in the development of an active SPP switch, as the changing refractive index of the photorefractive material changes the SPP dispersion. This concept has previously been explored with the ultrafast excitation of Aluminium [12] and the photo-modulation of the plasmonic resonance of Gold nanoparticles [13]. However, the non-linear wave-mixing effects observed in photorefractive materials are of greater interest as they could potentially lead to SPP gain, to offset the absorption losses from the metal. The two-beam gain of laser beams [14] is commonly used to characterise photorefractive systems and with an appropriate system, the same mechanism could be used to demonstrate SPP gain as the only difference is the form of the electromagnetic wave.

To investigate this concept we will use a hybrid photorefractive liquid crystal cell [15], that has been modified to allow SPP to interact with the liquid crystal layer. Liquid crystal cells with the addition of a photoconductive layer show the same non-linear optical behaviour as photorefractive crystals [16]. They operate by first applying a potential across the cell and as the photoconductor has a low conductivity in the dark, the potential drop across the liquid crystal layer is reduced and thus the molecular re-alignment to the applied potential is limited. Illuminating the photoconductor to increase its conductivity, then increases the potential drop across the liquid crystal layer thus causing a greater molecular re-alignment. Therefore, the dielectric properties of the cell, which depend on the molecular orientation, can be controlled with light. Hybrid photorefractive liquid crystal cells are the ideal structure for this research as this type of photorefractive system has the largest reported two-beam exponential gain [17], they are relatively inexpensive and are easy to manufacture.

Prior to demonstrating SPP gain with a hybrid photorefractive liquid crystal cell we must first determine the extent that a SPP can interact with the liquid crystal layer in such a system. It is this research that is the subject of this thesis. Initially, the operation of the novel structures we have developed needs to be characterised to determine the electrical and optical control of SPP that can be achieved. We then consider how the formation of the refractive index grating near the photoconducting layer influences the transfer of energy between SPP modes, by examining the diffraction efficiency of a single SPP interacting with the refractive index grating in the liquid crystal layer. This information will lead to the future development of a system that will demonstrate a measureable amount of gain for a SPP mode.

1.1 Structure of the Thesis

The remainder of this thesis is arranged as follows: In *Chapter 2*, the theory required to understand the material in this thesis is presented along with a literature review of systems related to this work. The chapter is split into five sections; the first three described the theory and uses of SPP, photorefractive wave mixing and photorefractive liquid crystal cells respectively. A description of the design of the novel hybrid plasmonic photorefractive liquid crystal cells developed in this thesis is then presented. Finally, a brief description of the numerical simulations developed by Dr. Keith Daly and Dr. Giampaolo D'Alessandro from the School of Mathematics at the University of Southampton, used to assist us in understanding the complicated non-linear system is included.

Chapter 3 is a discussion of the experimental techniques used to acquire the data presented in this thesis. Initially the optical apparatus used to excite and analyse SPP in a hybrid photorefractive liquid crystal system is described. This apparatus is used for both the photorefractive measurements with uniform and non-uniform illumination. Following this is a description on the multiple methods used to characterise the operation and structure of our samples. This chapter concludes with a detailed description on the fabrication methods of the samples and indicates how to fabricate a greater number of fully operational devices.

In *Chapter 4*, we present all the information obtained on the characterisation of the novel hybrid plasmonic liquid crystal cells developed in this thesis. We begin by describing the optical characterisation of the samples; this section presents the effects that each layer of the sample has on the SPP modes within the system at various stages of a cells construction. The electrical response of the liquid crystal layer is then described. The electrical response of our cells is first characterised by impedance spectroscopy. In addition, the electro-optical properties of the liquid crystal are examine with cross-polariser measurements and we also determine the how the change in the liquid crystals refractive index with an applied potential alters the wavevector of the SPP modes. The final section of this chapter is the characterisation of the samples photorefractive control of the dispersion of SPP.

The most significant work in this thesis is present in *Chapter 5*. This work is on the interaction of a SPP with a refractive index grating written into the liquid crystal layer. In this chapter we demonstrate that the energy of a SPP mode is diffracted by a refractive index grating into additional SPP modes propagating in different directions. The magnitude of this diffraction into other SPP modes is then examined by considering the diffraction efficiencies dependence on all known experimental parameters; the magnitude and frequency of the applied potential, the illumination intensity, the orientation of the grating, the orientation of the liquid crystal director relative to the SPP, the energy (frequency) of the SPP and the pitch of the refractive index grating. In each section, we present a description of the experimental observations and propose theories, where possible, on the

mechanisms determining this dependence. Also presented are the trends predicted by the numerical simulations. The results presented in this chapter are of vital importance in understanding the hybrid plasmonic photorefractive liquid crystal systems we intend to use to demonstrate all SPP gain in future work.

The thesis is concluded by first summarising the previously presented work. Then the information obtained throughout the thesis is used to describe an experimental system that should subsequently be able to demonstrate SPP gain. In addition, we present details of possible methods to optimise the samples, leading to an enhancement of the desired photorefractive energy transfer.

Chapter 2

Theory and Literature Review of SPP and Photorefractive Liquid Crystals

In this chapter, a description of the physics necessary to understand the work contained in this thesis is provided. Initially, the physical behaviour of SPP is described with information on the various methods used to excite SPP modes with light. Included in this section is a general literature review of the many varied applications of SPP. Then the general operation and uses of photorefractive materials is described in *section 2.2*, including a description of previous research into controlling SPP with photorefractive materials. Following this in *section 2.3*, information on photorefractive liquid crystal cells, the photorefractive material used in the experimental data in this thesis, is presented and contains a description of the fundamental physics of liquid crystals that will be subsequently required. A review of the various ways of generating photorefractive effects in liquid crystals and an SPP's interaction with a liquid crystal material is included in this section. *Section 2.4* then describes the design of the novel hybrid photorefractive plasmonic liquid crystal device developed and tested in this thesis. Finally, in *section 2.5*, a brief description is presented on the theoretical model of a SPP's interaction with a spatially modulated liquid crystal.

2.1 Surface Plasmon Polaritons

At the interface of a metal and dielectric, electromagnetic radiation can be coupled to the metals electron plasma [2]. The subsequent coupled oscillations are referred to as Surface Plasmon Polaritons (SPP) and are a form of electromagnetic mode that propagates within the interface plane between the two materials and has a field that decays away from the plane in both the metal and dielectric.

The discovery of SPP is linked to the prior prediction of Surface Plasmons (SP) by Ritchie [18] in 1957. In this paper, he predicted the existence of localised, non-propagating oscillations in the electron plasma whilst studying the loss mechanisms of fast electrons transmitted through thin metal films. This prediction was then later experimentally verified in the loss spectra of Aluminium [19] and Magnesium [20] films in 1959. SP were first excited by photons to form SPP in 1968 by both Kretschmann [21] and Otto [22]. The SPP modes excited were in fact an identical form of electromagnetic mode to the type of SP described in 1960 in a paper by Stern and Farrell [23] (where the term surface plasmon is first introduced).

In this paper, based on the earlier work of Ritchie, they considered the energy loss of non-normal incidence fast-electrons onto thin metal films. The loss mechanisms examined were the same as the SP previously predicted by Ritchie, with the exception that the energy of the incident radiation is transferred into a propagating mode. Hence, SPP are often thought of as propagating SP. Equivalently, SP may be considered a limiting case of SPP where the group velocity of the mode is infinitely large [2]. Both comparisons are commonly used in the literature to distinguish between SP and SPP.

2.1.1 A Mathematical Description of SPP

As later demonstrated, SPP in isotropic media must be a transverse-magnetic (TM) polarised wave. Therefore, the mathematical description of the SPP's plane propagating magnetic field, which decays away from the interface between a metal and dielectric is,

$$\underline{\mathrm{H}}_m = \begin{pmatrix} 0 \\ \mathrm{A}_m \\ 0 \end{pmatrix} e^{(ik_x x + (-1)^m k_{z\_m} z - i\omega t)}, \tag{2.1}$$

where m =1 defines the field in the dielectric and m = 2 defines the field in the metal. The interface between the metal and dielectric is defined as the x-y plane at z = 0. Hence, k_x is the propagating in-plane wavevector and k_{z_m} is the decay of the field into each material. The A_m terms describe the magnitude of the field in each medium and ω is the angular frequency of the wave. Using Maxwell's equations and assuming there are no free currents ($\underline{\mathrm{J}}$ = 0), the SPP's electric field is,

$$\underline{\mathrm{E}}_m = \frac{-\mathrm{A}_m}{i\omega\varepsilon_m} \begin{pmatrix} -(-1)^m k_{z\_m} \\ 0 \\ ik_x \end{pmatrix} e^{(ik_x x + (-1)^m k_{z\_m} z - i\omega t)}, \tag{2.2}$$

with ε_m as the dielectric constant of each material. We have also made the assumption that the waves propagate in uniform isotropic materials, so we can constrain the propagating wave to the x-direction without a loss in generality. However, subsequent analysis in this thesis will have to consider the effects of a non-uniform birefringent dielectric as well.

The form of the SPPs electric field described in *equation 2.2* is better understood by the field diagrams presented in *figure 2.1*. This demonstrates the form of the charge-density wave at the surface of the metal, indicating the elliptical polarisation of the electric field vector. In general, $|\mathrm{E}_z|$ is larger than $|\mathrm{E}_x|$ in the dielectric and $|\mathrm{E}_z| < |\mathrm{E}_x|$ in the metal[I]. Also presented is a representation of the attenuation of the field into each material. Due to the difference in sign of the dielectric constant between metals and dielectrics (metals have negative dielectric constants), the electric field of an SPP extends further from the interface into the dielectric layer with a typical penetration depth of the order of ~λ/2 for high energy SPP, where $\lambda = 2\pi c/\omega n$. Whereas the penetration depth into the metal is only a few tens of nanometres.

[I] Determined by *equations 2.3* and *2.6* whilst considering typical values of ε for a metal and dielectric.

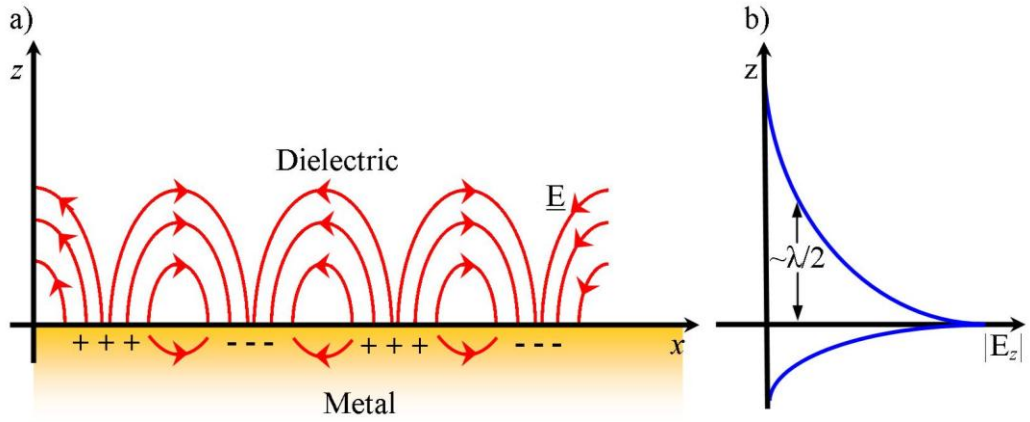

Figure 2.1: The electric fields of a Surface Plasmon Polariton. a) The charge-density wave propagation along the metal / dielectric interface. b) The attenuation of the electric field away from the interface.

As an SPP is a coupled oscillation of the electron plasma and an electromagnetic wave, SPP have a continuous series of eigenmodes described by a dispersion relation. The dispersion relation of an SPP is derived from solving Maxwell's equations at the boundary between the two materials. By substituting *equations 2.1* and *2.2* into the wave equation (*equation 2.4*) the decay of the fields away from the interface can be related to the optical wavevector,

$$k_{z\_m} = \sqrt{\left(k_x{}^2 - \varepsilon_m \left(\frac{\omega}{c}\right)^2\right)}. \tag{2.3}$$

$$\frac{\partial^2 \underline{\mathrm{E}}}{\partial t^2} = c^2 \nabla^2 \underline{\mathrm{E}}. \qquad \text{optical wave equation} \tag{2.4}$$

For the fields to decay infinitely far from the interface, k_{z_m} must be positive with a real component larger than the imaginary component. Using the standard optical boundary conditions, that the tangential electric and magnetic fields are equal in both media at the interface, the only non-trivial solution is,

$$\frac{k_{z\_2}}{k_{z\_1}} = -\frac{\varepsilon_2}{\varepsilon_1}. \tag{2.5}$$

For the wave to be confined to the interface, both k_{z_m} must be positive. Therefore, ε_1 and ε_2 must have opposite signs for the interface to support SPP modes.

Using *equations 2.3* and *2.5* the dispersion relation for the in-plane component of the SPP wavevector can be obtained,

$$k_x = \frac{\omega}{c}\sqrt{\frac{\varepsilon_1 \varepsilon_2}{\varepsilon_1 + \varepsilon_2}}, \tag{2.6}$$

where the term inside the square-root needs to be positive to describe a propagating SPP mode. Therefore, the real part of the negative dielectric constant material must be larger than the real component of the positive dielectric material.

In the near infrared (NIR) and visible (VIS) region of the electromagnetic spectrum typically used for the generation of SPP, metals such as Gold (Au), Silver (Ag), Aluminium and Copper are all examples of naturally occurring materials with a negative dielectric co-efficient [24]. In addition, for these metals the real part of the dielectric constant is larger than the dielectric constant for most common dielectrics such as air, glasses and polymers. Hence, SPP modes can be supported at the interface between these materials. It must be highlighted however, that for metals the dielectric co-efficient has a small imaginary component [24]. Therefore, in general, both k_{z_m} will then have a small imaginary component; however, the SPP is confined to the interface due to the larger real component of the wavevector. Consequently, k_x will also have an imaginary component leading to the SPP fields decaying during its propagation. This decay is one of the fundamental problems in developing applications for SPP modes as it severely limits their propagation length. Developing a method of increasing the SPP propagation length through replacing the lost energy is the long term goal of the work presented in this thesis.

If we were to instead consider a transverse-electric (TE) polarised wave for SPP at the metal-dielectric interface, then the electric and magnetic field are,

$$\underline{\mathrm{E}}_m = \begin{pmatrix} 0 \\ B_m \\ 0 \end{pmatrix} e^{(ik_x x + (-1)^m k_{z\_m} z - i\omega t)} \tag{2.7}$$

$$\underline{\mathrm{H}}_m = \frac{B_m}{i\omega} \begin{pmatrix} -(-1)^m k_{z\_m} \\ 0 \\ ik_x \end{pmatrix} e^{(ik_x x + (-1)^m k_{z\_m} z - i\omega t)}. \tag{2.8}$$

When the boundary condition of equality between the electric and magnetic fields at the interface of the two materials is applied, the only solution to Maxwell's equations is,

$$k_{z\_1} + k_{z\_2} = 0. \tag{2.9}$$

Hence, there are no solutions for TE waves where both k_{z_m} are positive to confine the mode to the interface. Therefore, SPP modes cannot be TE polarised waves.

There is also an additional sub-class of SPP known as Localised Surface Plasmons (LSP). LSP are also modes where light couples to the electron plasma of a metal; however, instead of a plane surface the metal surface is often curved, with a spherical object the typical example. The curved surface imposes additional boundary conditions of the electromagnetic wave, so that LSP are in fact localised standing SPP waves, hence they do not propagate [2]. LSP are

not generally considered in this thesis; however, many applications of SPP focus on exploiting LSP. In particular, applications that use nano-patterned structures such as nanoparticles [25] or bow-ties [26].

2.1.2 SPP Excitation with Light

The dispersion relation of SPP presented in *equation 2.6* is interpreted by comparing it to the dispersion of light, $\omega = kc/n$. The frequency dependent dielectric constant for the metal is often approximated by the Drude free electron model *equation 2.10*, with no dampening terms [2]. This approximation is valid in the NIR where losses in metals (from a complex component of the dielectric constant) are negligible but starts to break down in the visible spectrum when absorption becomes significant.

$$\varepsilon_2(\omega) = 1 - \frac{{\omega_p}^2}{\omega^2} \tag{2.10}$$

Where ω_p is the bulk plasma frequency for the metal; for example, in Gold ω_{pAu} = 1.30 x10^{16}Hz [27] and in Silver ω_{pAg} = 1.46 x10^{16}Hz [27].

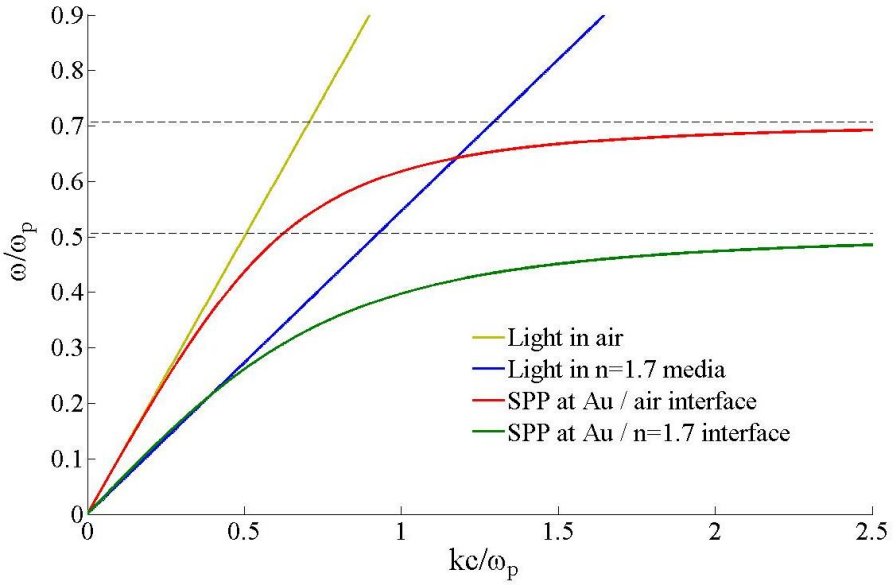

Figure 2.2: The dispersion relations for light in air, light in an *n*=1.7 dielectric, SPP at an Au/air interface and SPP at an Au/*n*=1.7 dielectric interface. The dashed lines mark the asymptotes of the SPP dispersions. Both ω and k are normalised by the plasma frequency for Au, 1.37 x10^{16}Hz.

The dispersion of SPP using the Drude model at an Au-dielectric interface and the dispersion of light in the dielectric are plotted in *figure 2.2*. The dielectric materials considered are air (*n* = 1) and an arbitrary dielectric with a refractive index *n* = 1.7 for all ω. The dispersion of light is linear with the slope determined by 1/*n*. The dispersion of SPP is approximately linear at low frequencies, the IR and longer wavelength region of the spectrum, and follows 1/*n*.

However, at higher frequencies the wavevector of an SPP is a curve with an increasingly larger wavevector compared to light, which eventually forms an asymptote with a value determined by,

$$\omega_{max} = \frac{\omega_p}{\sqrt{1+\varepsilon_1}}. \tag{2.11}$$

The important difference between the dispersion of SPP and light; is that an SPP at a metal-dielectric interface always has a larger wavevector than light propagating in the same dielectric material. Hence, SPP modes cannot be excited by directly incident light on a plane metal surface as there must be wavevector conservation. For SPP to be excited by light, the photon must gain an additional momentum component.

The simplest way to increase the wavevector of light is to pass it through a higher refractive index medium, which also increases the wavevector of SPP as demonstrated in *figure 2.2*. However, from *figure 2.2* we observe that the dispersion of light in an n = 1.7 dielectric overlaps the dispersion of SPP at a metal-air interface. Therefore, excitation of SPP with light is possible if we are able to couple light from a high dielectric material to SPP at a metal-lower dielectric material interface. This can be achieved by forcing the light to become an evanescent wave, with the evanescent wave overlapping the surface we wish SPP to be excited upon. This is the basis of SPP excitation using the method of Attenuated Total-internal Reflection (ATR).

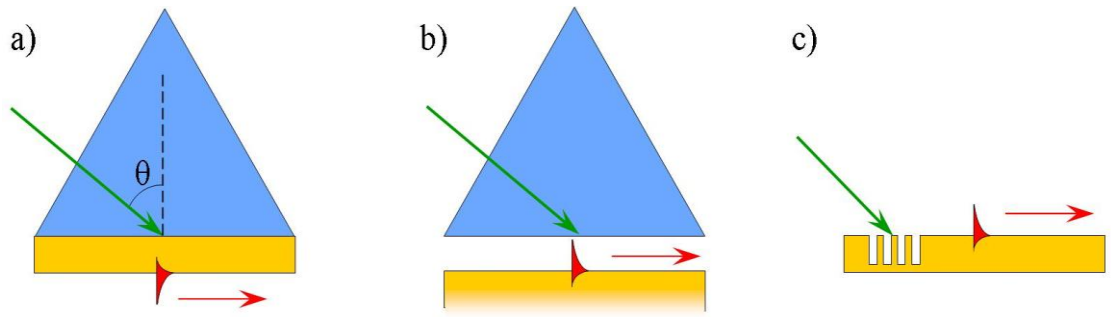

Figure 2.3: The three most common methods of coupling light into SPP modes. The Kretschmann (a) and Otto (b) prism configurations. Alternatively a grating coupler (c) can be used.

There are two distinct variations of an ATR apparatus used to excite SPP and both use the evanescent field of light undergoing total internal reflection (TIR) from a prism, the difference is in the relative position of the metal surface. The Kretschmann configuration [21, 28] demonstrated in *figure 2.3a*, has a thin metal film deposited directly onto the surface of the prism. Provided the metal layer is thin, <60nm for Au and <70nm for Ag (calculated from [24]), a sufficiently strong evanescent field penetrates through the layer and excites SPP on the opposing side of the metal film. The other variation is the Otto configuration [22] demonstrated in *figure 2.3b*, where the evanescent field is used to excite SPP modes on the surface of a metal by maintaining a small (<1μm for good excitation) gap between the prism

and the metal. This is a less common method of exciting SPP due to the difficulty of maintaining a small gap.

In both methods, light only couples into SPP modes when the wavevector component of the evanescent field parallel to the metal surface $\underline{k}_{||}$ and the wavevector of the SPP mode $\underline{k}_{SPP}$ with a frequency ω are equal. The angle of incidence of the light (also with a frequency ω) in the prism θ, determines $k_{||}$ by,

$$k_{||} = \frac{\omega}{c} n_{\text{prism}} \sin(\theta). \tag{2.12}$$

As we can control $k_{||}$ through θ, SPP can be excited with light by ATR for any ω below where the dispersion of light in the prism and dispersion of an SPP for a metal-dielectric interface cross. For example, using the dispersions presented in *figure 2.2*, light in a n = 1.7 prism can excite SPP at an Au-air interface for $\omega/\omega_p \leqslant 0.65$, as the dispersion of light presented represents $\theta = 90^o$, the maximum possibly $k_{||}$.

As the excitation of SPP by ATR is dependent on θ we can amass additional information on the SPP mode by acquiring the angular dependent reflection (often referred to as an ATR spectrum). A theoretical example of the ATR spectrum from a n=1.83 prism, 40nm Au layer in contact with air is presented in *figure 2.4*, where the annotations indicate measurements we can use to determine information about the SPP and the interface. When the angle of incidence is small ($<33^o$ in *figure 2.4*), the light is not totally internally reflected so the reflection is determined by the reflective properties of the metal layer, like a standard household mirror. When using a Kretschmann ATR apparatus, the difference between the measured reflection and complete reflection can be used as an estimation for the thickness of the metal layer [29]. However, this method of measuring the film thickness is not generally used, as other measurements during sample fabrication are more accurate. The reflection then increases at the angle θ_{TIR} as the light is totally internally reflected. This angle is determined by Snell's law using the refractive indices of the prism and the dielectric that forms the metal-dielectric interface (air in *figure 2.4*). The complex refractive index of the metal is not considered in determining this angle. Therefore, if either the refractive index of the prism or dielectric is known, the other can be calculated by this angle. The ATR spectrum then demonstrates a noticeable minima in the reflected intensity, when $k_{||} = k_{SPP}$, this is known as the SPP resonance. Therefore, k_{SPP} can be determined experimentally by θ_{SPP} and *equation 2.12*. This is often the measurement of interest when acquiring ATR spectrums, as there must be energy conservation in the excitation, $E_{light} = E_{SPP} = \hbar\omega$. Hence, if the ATR spectrum is acquired for several ω then the dispersion relation of SPP can be experimentally determined.

Finally it is possible to estimate the propagation length of the SPP δ_{SPP}, from the full-width, half-maximum (FWHM) of the attenuation peak in the ATR spectrum Δk. To do this we assume that the width of the attenuation peak is entirely due to the SPP's propagation losses, in this case $\delta_{SPP} = 2\pi / \Delta k$. In practice the SPP wavevector will be broadened due to small variations in k_{SPP} from SPP excited from different regions of the focused beams waist i.e.

inhomogeneous broadening. In this case the value of δ_{SPP} is a minimum. This method of estimating δ_{SPP} is analogous to determining the lifetime of an optical excitation from the linewidth of the emission spectrum [30]. An estimation of the propagation length is useful to know, to determine the maximum length scale of any surface patterning that you can use to control or manipulate SPP, such as the pitch of a grating.

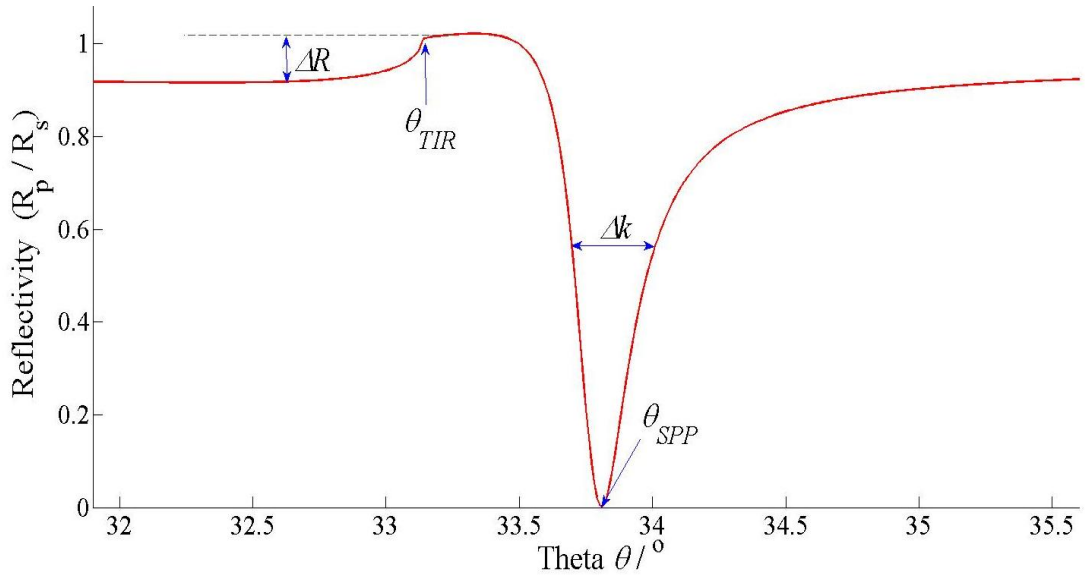

Figure 2.4: A Typical ATR spectrum from a Kretschmann apparatus (*n*=1.83 prism) for a SPP at a metal (Au)-air interface. An explanation of the annotations can be found in the text.

In addition to the ATR method of exciting SPP, there is a third type of excitation method that is related to this work, a grating (scattering) coupler [31] *figure 2.3c*. Grating couplers can take two forms. Metallic gratings are where corrugations in the metal surface form a grating. This type of grating is the basis of "Wood's anomalies" [32, 33] where the total reflected light from a rough metal surface was less than the total incident light. The reported discrepancies are now known to be due to the excitation of SPP. These gratings have been extensively studied in the literature [34-37] as devices for coupling light into and out of SPP. The other type of grating is a dielectric grating coupler [38-41] where either corrugations in the thickness of the dielectric material or a periodic variation in the refractive index can be used. However, applications of gratings are limited as they are often non-reconfigurable devices.

Of the two grating couplers, the dielectric gratings are of greater interest in this work as they are fundamentally similar to the gratings we will generate in the liquid crystal layer of our samples. The gratings we use are not to couple light into an SPP mode as this requires light to be directly incident on the grating, but are used instead to couple energy between SPP modes by positioning the grating so only the SPP interacts with it. It has been previously shown that SPP do interact with a refractive index grating through total internal diffraction [42]. The energy in the SPP is then re-radiated by the grating. The pitch of the grating determines the angle(s) at which this re-radiated light is seen. In our photorefractive system, described in

section 2.4, a grating will lead to the possibility of SPP-SPP or SPP-light scattering/coupling, a desirable non-linear effect. The devices will also be re-configurable unlike most dielectric gratings presented in the literature. Metallic gratings are not generally considered except as an additional radiative loss mechanism for SPP from a rough surface. In general, all the methods that can be used to excite SPP also slightly reduce the SPP propagation length (broader ATR minima) due to additional radiative losses[43] from energy in the SPP being transferred back out into light.

2.1.3 The length-scales of SPP

The interest in SPP modes often arises from their sub-wavelength length-scales, where the sub-wavelength refers to the wavelength of light in vacuum at the same ω. A comprehensive review of the length scales associated with SPP can be found in the article by Barnes [43]. However, a brief description of the important length scales relative to the work in this thesis is provided.

An important length scale is the penetration or skin depth of the SPP into the dielectric δ_d. This length scale provides a maximum size for a structure away from the interface that can be used to control or manipulate SPP and is determined by combining *equations 2.3* and *2.6*,

$$\delta_d = \frac{c}{\omega}\sqrt{\left|\frac{\Re(\varepsilon_2)+\varepsilon_1}{(\varepsilon_1)^2}\right|}, \tag{2.13}$$

where $\Re$ signifies the real component of a complex term. A similar length scale for the SPP decay length into the metal can also be obtained by replacing the $(\varepsilon_1)^2$ term with $\Re(\varepsilon_2)^2$, though this length-scale is not considered in this thesis. If we consider a SPP at a simple Au-*n*=1.5 dielectric interface then using *equation 2.13* a 1.77eV SPP (ω/c=700nm) has a penetration depth of ~175nm and a 1.24eV SPP (ω/c=1000nm) has $\delta_d \approx$ 400nm. Therefore, the typical SPP penetration depth for the range of E_{SPP} we examine is of the order of ~250nm depending on the dielectric material. Hence, any structure developed to manipulate SPP must have the 'active' component within this distance for significant control of SPP.

The other length-scale related to this work is the propagation length of the SPP δ_{SPP}. The propagation length is determined from the imaginary component of *equation 2.6* [43],

$$\delta_{SPP} = \lambda_0 \frac{(\Re(\varepsilon_2))^2}{2\pi\Im(\varepsilon_2)}\left(\frac{\Re(\varepsilon_2)+\varepsilon_1}{\Re(\varepsilon_2)\varepsilon_1}\right)^{\frac{3}{2}} \tag{2.14}$$

where $\Im$ signifies the imaginary component of a term and λ_0=ω/c (the wavelength of the light exciting the SPP). From *equation 2.14* it is clear that long propagation lengths are possible for SPP confined to the surface of a metal with large a $\Re(\varepsilon)$ and negligible $\Im(\varepsilon)$, i.e. a low loss material, as expected. However, metals do not have a negligible $\Im(\varepsilon)$, so the propagation

lengths are typically short. For example, the propagation length of SPP at a Ag-air interface is δ_{SPP} = 22μm for λ_0 = 514.5nm and δ_{SPP} = 500μm for λ_0 = 1060nm [1], these sub millimetre lengths are typical of SPP. The propagation lengths calculated by *equation 2.14* are for SPP at a plane homogenous interface and only correlate to the experimental measurements of the width of the SPP resonance Δk in the ATR spectrum of *figure 2.4* for SPP at the interface of two homogenous materials.

The propagation length imposes a maximum size to any structure that could manipulate SPP and typical δ_{SPP} represent an unpractical length scale for device applications. Hence, developing a method of increasing the propagation length is of significant importance for further progress into the use of SPP, in particular for the development of integrated electro-optic circuits.

2.1.4 Applications of SPP

Historically, the first application of SPP was in crafting coloured glasses by adding small quantities of precious metals, though the use of SPP by the craftsmen was unintentional. The most famous example is the Lycurgus Cup from the Byzantine Empire in the 4th century AD. This fascinating cup appears a green or jade colour when light is scattered from its surface, yet appears as a variety of reds and purples for transmitted light. The explanation for this effect is now known to be due to the excitation of LSP in the green region of the spectrum absorbing part of the transmitted light but not affecting the scattered light [44]. Other examples of this use of LSP can be observed in the much admired stain glass windows from the 10th to 12th centuries, where the colour is generated by SPP excitations on the metal nanoparticles used to dope the glass, as first experimentally documented by Garnett [45] in 1908.

Since the development of methods to intentionally excite SPP modes by Kretschmann and Otto, a variety of additional uses for SPP have been developed. The most widely used application is in SPP sensing equipment for chemical or biological systems [3]. SPP sensor systems work by measuring the angular position of the SPP resonance in the ATR spectrum acquired in the Kretschmann geometry, θ_{SPP} in *figure 2.4*. As θ_{SPP} is determined by the optical constants of the dielectric materials adjacent to the metal, θ_{SPP} will increase if additional material is deposited onto the metal. This is due to the effective refractive index of the dielectric layer increasing. Hence, SPP are often used to measure the concentration of compounds that bind to a metal or thin analyte coating, where chemicals binding to the surface slightly increase the effective refractive index thus changing required wavelength, or angle of the SPP resonance. This is an established method and has been used for the detection of small molecules with sensitivities of 10^{-1} pg mm^{-2} [46]. The reason for such a high sensitivity comes from SPP only probing a few hundred nanometres into the dielectric coating, which is of comparative size to complex molecules. Protein absorption [47], antibody–antigen binding [48] and DNA hybridization [49] have all been analysed using this

technique. For a more extensive review of SPP sensing the reader is directed to the following review articles: [50-53]. Later in this thesis we use SPP sensing to determine the thickness and optical constants of a dielectric material by measuring θ_{SPP} and comparing to Fresnel theory for a non-normal incidence reflection.

SPP also demonstrate an increased electric field strength compared to light, due to their smaller modal volume and resonance effects. Therefore, SPP can be used to enhance several non-linear effects, such as increasing frequency conversion in second harmonic generation (SHG) [54]. For example, the SHG signal from the reflection off Ag gratings showed an increase of up to 36 times more than a smooth film due to the excitation of SPP modes [55]. Enhanced third harmonic generation [56] and white light generation with Nano-antennas using a low peak power light source have also been demonstrated [8] by using SPP. In addition, the increased electric field of SPP has demonstrated the ability detect single molecules with surface enhanced Raman scattering [7, 57].

Since the development of nano-scale fabrication methods, SPP have been increasingly used in sub-wavelength optics. For example, SPP waveguides have been demonstrated in metal-insulator-metal (MIM) structures using visible light, where the SPP wavelength is only 55nm; the lateral dimensions of the waveguide are 150nm with a core of only 3nm [58]. Hence, SPP waveguides could be more densely packed onto an optical circuit board compared to standard light waveguides which have dimensions on the order of 1μm. Practical uses of SPP waveguides are limited by the poor propagation lengths of SPP. A more direct example of the sub-wavelength scale of SPP can be observed in surface plasmon enhanced photolithography, where lines less than 100nm wide have been patterned with light at a wavelength of 436nm using standard optical photo-resists [9].

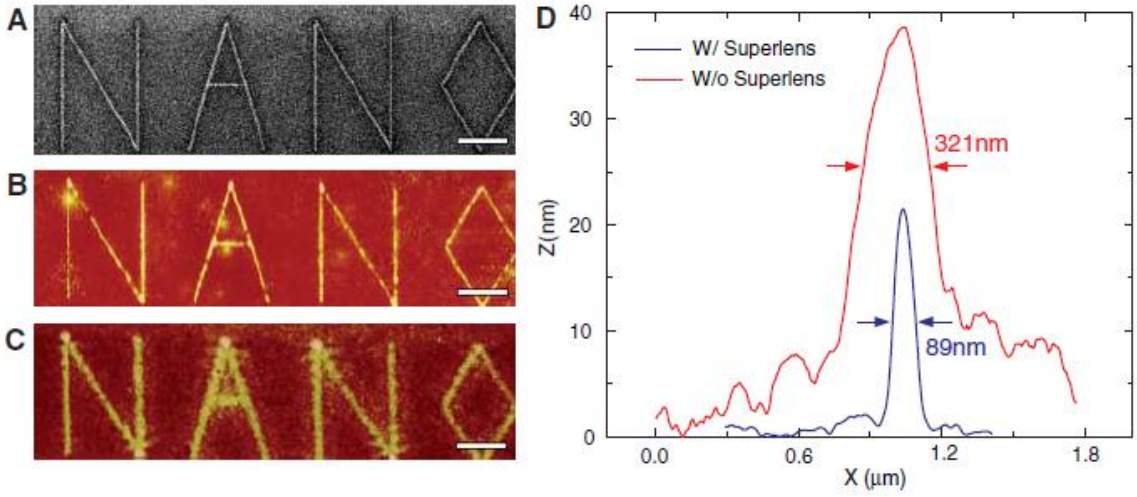

Figure 2.5: (A) A focused ion beam image of the 40nm lines, (B) optical image with superlens, (C) image without superlens. (D) The average cross-section of the letter A showing the enhance resolution. The bars on images A-C represent a 2μm scale. (Figure from [59])

As SPP exist at the boundaries of materials with opposite sign permittivities, in principle it is possible that one of the materials could have a negative refractive index, which could create a superlens, i.e. non-diffraction limited resolution [5]. In the visible spectral region it has been shown that only a negative dielectric constant is needed for this effect making noble metals ideal naturally occurring materials for a superlens [60]. This effect has been experimentally demonstrated using a 35nm silver film to increase the resolution of 40nm lines from 321nm to 89nm by exciting SPP to resonantly enhance the optical near field of the image [59], see *figure 2.5*. Fabricating truly negative-refractive index materials without a complex refractive index, unlike the noble metals, at visible frequencies for superlens applications is an active area of research with several interesting review articles [9, 61-63].

By far the most promising application of SPPs is in the creation of integrated electro-optic circuits (plasmonic circuits). Conventional optical circuits are restricted by diffraction, limiting the size of components to the order of the lights wavelength, whereas electronics are routinely fabricated below 100nm dimensions. However, the speed of information transfer is reduced in electronics as the components are scaled down. SPPs could provide a way to allow information to be transferred at optical frequencies along metallic interconnects on the nanoscale, a problem that limits tradition electric circuits [9]. However, for plasmonic circuits to become viable, technological solutions to controlling or redirecting the SPP and increasing the propagation length need to be developed.

Several technologies have demonstrated the ability to redirect SPP modes, such as using photonic crystals where near 100% SPP transmission is possible in 90^{o} bends [64]. Alternatively, the ability to pattern metallic films on the nanoscale has allowed a 2D equivalent of standard optical components, such as mirrors, lens and beamsplitters to be developed for SPP [2]. For mirrors the optical component is made by an ensemble of metal nanoparticles in parallel lines with the spacing and number of lines determining the reflectivity and wavelength response of the mirror. Combinations of plasmon equivalent Bragg mirrors and beamsplitters have then been shown to create a SPP interferometer [65], an example of a simple plasmonic circuit. In addition, V-shaped channels cut into the metal to guide the SPP have also demonstrated nearly 100% transmission through a 90^{o} bend, which was previously only possible with photonic crystals [66] . However, the quoted high transmission is only achieved with a sample with a ‘pillar’ defect at the intersection; without the pillar structure only a transmission of 86% is achieved due to noticeable back reflections within the structure. Currently, V-channels are the most promising SPP guiding structure as they have also demonstrated a slightly increased SPP propagation length [67], as the modes E-field is less confined to the metal.

Increasing the propagation length of SPP to a workable distance is technologically more challenging with no clear solution having been currently presented. The most successful methods involve the creation of smooth thin metal strips coated with dielectrics on all sides which can support long-range surface plasmon polaritons (LRSPP). The increased propagation length of LRSPP is achieved by optimising the thickness and width of the metal

so that two SPP on either side of the metal surface interfere to generate a new propagating LRSPP mode with a symmetric E-field distribution. Studies have been conducted to optimise the confining structure to increase the propagation lengths for LRSPP excited by light with a wavelength λ=633nm [68] and λ=1.55μm [69]. The optimum structures generate LRSPP with most of the electric field in the dielectric and not in the metal, thus reducing the magnitude of the loss for the mode. A homogeneous dielectric structure gives a more optimised system, but in general any two dielectrics can be used as a substrate and coating for the metal strips. This type of structure is referred to as an insulator-metal-insulator structure (IMI). Record propagation lengths of up to 1cm have currently been achieved using light with λ=1.55μm [70].

Other methods of increasing the propagation length have also been proposed, such as using chains of Ag nanoparticles to form a waveguide. In these nanoparticle waveguides a LSP's evanescent E-field away from the surface of the nanoparticle allows it to couple from one metal particle to the next in the chain, to create a propagating LSP mode [71, 72]. This method is effectively a way of diluting the metal content of the interconnect, therefore reducing the effective optical losses from the metal to increase the propagation length. The waveguides are often fabricated by electron-beam lithography and currently demonstrate propagation lengths of a few hundred nanometres for 90nmx30nmx30nm Ag particles separated 50nm apart [25]. This propagation length is significantly lower than δ_{SPP} for standard SPP on uniform plane metal surfaces. However, it is expected that with further development of a suitable bounding media and improved fabrication techniques an increase of an order of magnitude in the current reported propagation lengths can be achieved [73]. In their current state, nanoparticle chains may only find uses as terminating structures. Using metal nanospheres may also increase the propagation length of this type of waveguide as they are a more optimal shape [74], though nanosphere arrays are often created by self-assembly procedures which are poor at generating straight particle chains over a significant distance, which will lead to additional losses [75]. A significant benefit of nanoparticle chains is that they also have a calculated transmission of 100% through a 90^{o} bend [72] and are able to demonstrate a ~50% split in the signal at a Tee junction to fabricate a basic interferometric switch [76]. Alternatively, spherical voids in the metal which form nanoporous layers (the opposite of nanoparticle chains) can support SPP [77], these have also been theoretically predicted to be able to act as SPP waveguides [78].

Using V-channels and LRSPP to increase the propagation lengths of SPP all effectively reduce the plasmon content of the SPP, so that they are more akin to dielectric guided waves. Therefore, the wavelength and modal area of the SPP are increased, thus reducing their usefulness for the most-appealing sub-wavelength applications. In addition, nanoparticle chains require significant improvements in their capability if they are to become serious contenders for SPP waveguide applications. An alternative approach which could vastly increase the SPP propagation length is to use a dielectric capable of causing gain adjacent to the metal layer to increase the SPP signal to offset the losses of the metal [79]. This has been experimentally achieved by a doped polymer causing stimulated emission of the SPP.

Recently this was shown using the laser dye R6G in PMMA [80, 81], though semiconductor quantum dot lasing media are seen by many to be a better prospect [82]. SPP gain is the approach we take in developing a system to increase the propagation length. However, instead of using laser dye doped polymers[II] we intend to achieve gain through coherent photorefractive energy transfer between SPP.

A photorefractive system may also provide a device capable of significant non-linear SPP-SPP interactions of which there are currently few; additionally limiting the use of SPP. The furthest non-linear SPP-SPP interactions in development are spatial-light modulators based on using SPPs as large tuneable absorption features for a light addressable modulator [11]. More recently modulators that allow SPP-silicon electronics integration have been demonstrated [83]. However, active SPP devices need to be developed with an equivalent mechanism to the transistor, a 'plasmonster' [83, 84], if their full potential is to be realised.

2.2 Photorefractivity

Photorefractivity is a non-linear optical response of certain materials where the refractive index changes when illuminated. This non-linear effect was first discovered in 1966 and was initially believed to be the result of optical damage distorting the spatial integrity of the beams [85]. Photorefractive effects are generally attributed to certain crystals such as Barium Titanate ($BaTiO_3$) [86], Lithium Niobate ($LiNbO_3$) [87], Potassium Tantalate Niobate (KTP) [88], Barium Sodium Niobate (SBN) [89] and Gallium Arsenide (GaAs) [90]. The change in the refractive index with illumination in these crystals is generated by light exciting electrons into the conduction band where they are free to move throughout the crystal, leaving a hole. Due to diffusion the free electron charges will experience a net drift to locations within the crystal that have a lower illumination intensity where less free charges are generated. During their motion there is a probability that an electron will re-combine with a hole, where it remains trapped unless re-excited. This process re-distributes the charges within the crystal, thus establishing an internal space-charge field. The space-charge field then, via the linear electro-optic effect [91], alters the crystals refractive index. The key difference between photorefractive effects and thermal changes in the refractive index is that the change is not localised to the illumination.

Materials other than crystals have also demonstrated photorefractive effects. These include PLZT ceramics [92] and non-linear optical polymers [93]. Photorefractive effects have also been demonstrated through material structures such as waveguides [94], multiple quantum wells [95], organic crystals [96] and liquid crystal cells [97]. Photorefractive effects in liquid crystals are the photorefractive system used in this thesis and are discussed in detail, in *section 2.3*.

[II] An additional modification we can easily make to the photorefractive plasmonic liquid crystal system developed in this thesis.

The photorefractive effect is most often utilised in holography [98, 99]. Applications of photorefractivity are also found with phase-conjugate mirrors [100], optical spatial solitons [101] and wave-mixing [102, 103]. The non-linear wave-mixing process of Two-Beam Gain (TBG) where there is a net energy transfer between the two beams [97, 104-106], is the application of interest, as we intend to develop a similar process for gain of SPP with additional research following the work presented in this thesis. Initially, we develop a photorefractive system capable of controlling and transferring energy out of SPP modes; however, an understanding of the physical processes of TBG is necessary in this development process to achieve our long term goals.

2.2.1 Photorefractive Two-Beam Gain

To describe TBG we first consider two monochromatic electric fields with $\underline{k}_1$ and $\underline{k}_2$ respectively, crossed at a separation angle α in a photorefractive material. The total intensity I, at each position in the material is the summation of both fields multiplied by their complex conjugate, leading to a sinusoidal intensity modulation,

$$\underline{\mathrm{E}} = \underline{\mathrm{E}}_1 e^{i(\underline{k}_1.\underline{x}-\omega t+\varphi_1)} + \underline{\mathrm{E}}_2 e^{i(\underline{k}_2.\underline{x}-\omega t+\varphi_2)}, \tag{2.15}$$

$$\mathrm{I} = \underline{\mathrm{E}}^*.\underline{\mathrm{E}} \tag{2.16}$$

$$= \underline{\mathrm{E}}_1{}^*\underline{\mathrm{E}}_1 + \underline{\mathrm{E}}_2{}^*\underline{\mathrm{E}}_2 + \underline{\mathrm{E}}_1\underline{\mathrm{E}}_2{}^* e^{i\left((\underline{k}_1-\underline{k}_2).\underline{x}+(\varphi_1-\varphi_2)\right)} + \underline{\mathrm{E}}_1{}^*\underline{\mathrm{E}}_2 e^{-i\left((\underline{k}_1-\underline{k}_2).\underline{x}+(\varphi_1-\varphi_2)\right)},$$

$$\mathrm{I} = 2\left|\underline{\mathrm{E}}_1\right|^2 + 2\left|\underline{\mathrm{E}}_1\right|^2 \cos\left((\underline{k}_1 - \underline{k}_2).\underline{x} + (\varphi_1 - \varphi_2)\right). \tag{2.17}$$

Where we have made the assumption that $|\underline{\mathrm{E}}_1| = |\underline{\mathrm{E}}_2|$, each E-field also has an arbitrary phase of φ_1 and φ_2. Equality of the two E-fields is not essential; however, it is the simplest system to consider and describes the systems normally investigated. As the beams are monochromatic, $|\underline{k}_1| = |\underline{k}_2|$ and $|\underline{k}_1\text{-}\underline{k}_2| = 2|\underline{k}_1|\sin(\alpha/2)$.

In a photorefractive material this modulated intensity profile will lead to the formation of a refractive index grating. The physical processes behind the formation of the grating are described in *figure 2.6*. In general, the net direction of the drift and diffusion of the charge carriers in a photorefractive system is controlled by applying an external electric field [107, 108]. Some materials such as $BaTiO_3$ are also ferroelectric, hence do not require an external field; however, E-fields are often applied to these materials to enhance the photorefractive effects [109]. The net drift and diffusion of the charges leads to the refractive index grating having a phase shift of $\Delta\varphi$ relative to the incident intensity grating. The magnitude of $\Delta\varphi$ varies between materials and its sign (±) is dependent on the direction of the field.

The refractive index grating formed in the photorefractive material from the interference pattern is described by a spatial dependence in the materials permittivity:

$$\varepsilon_m = \varepsilon_i + a\cos\left(\left(\underline{k}_1 - \underline{k}_2\right).\underline{x} + (\varphi_1 - \varphi_2) + \Delta\varphi\right) \tag{2.18}$$

Where a is the strength of the modulation and is equal to the difference in the square of the refractive indices for the regions in the light and dark, i.e. $a = n_{\text{light}}^2 - n_{\text{dark}}^2$. The magnitude of a can be used to define how photorefractive a material is; larger a materials are better photorefractives. The constant ε_i term is equal to n_{dark}^2.

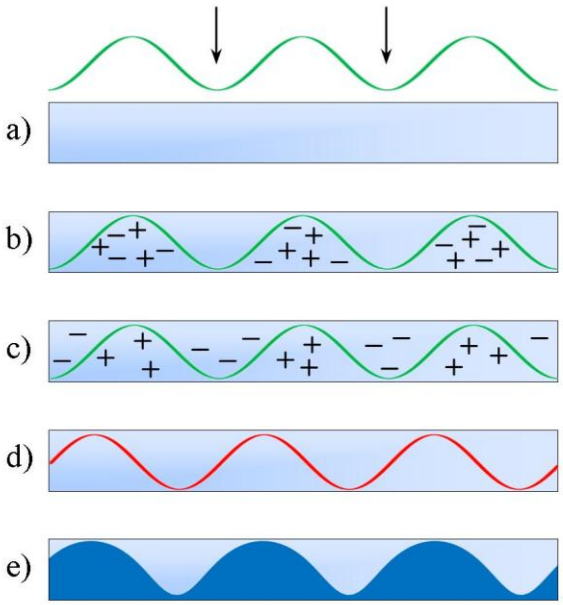

Figure 2.6: The formation of a refractive index grating in a photorefractive crystal. a) A optical interference pattern is incident onto the crystal, generated by crossed monochromatic beams. b) In the bright regions the crystal is photo-excited generating free charges. c) The negative charges diffuse to the dark regions where they become trapped. The positive charges do not move. d) The new charge distribution generates a modulated internal space charge field within the crystal. e) Therefore, due to the electro-optic effect the refractive index of the crystal becomes modulated with the same spatial variation as the incident interference pattern.

The incident waves forming the grating then subsequently interact with it. The total linear polarisation of the electrons in the photorefractive material $\underline{P}$, in response to the waves is,

$$\underline{P} = \varepsilon_0\varepsilon_m\left(\underline{E}_1 e^{i(\underline{k}_1.\underline{x}-\omega t+\varphi_1)} + \underline{E}_2 e^{i(\underline{k}_2.\underline{x}-\omega t+\varphi_2)}\right). \tag{2.19}$$

Equation 2.19 is interpreted by examining the polarisation response to each of the wave's $\underline{k}_1$ and $\underline{k}_2$ separately, i.e. $\underline{P} = \underline{P}_1 + \underline{P}_2$ and $\underline{P}_{1,2} = \varepsilon_0\varepsilon_m\underline{E}_{1,2}e^{i(\underline{k}_{1,2}.\underline{x}-\omega t+\varphi_{1,2})}$. Therefore, the materials partial polarisation due to the wave described by $\underline{k}_1$ is,

$$\underline{P}_1 = \varepsilon_i\varepsilon_0|\underline{E}|e^{i(\underline{k}_1.\underline{x}-\omega t+\varphi_1)}$$
$$+\frac{a}{2}|\underline{E}|\varepsilon_0 e^{i(\underline{k}_1.\underline{x}-\omega t+\varphi_1)}\left(e^{i\left((\underline{k}_1-\underline{k}_2).\underline{x}+(\varphi_1-\varphi_2)+\Delta\varphi\right)} + e^{-i\left((\underline{k}_1-\underline{k}_2).\underline{x}+(\varphi_1-\varphi_2)+\Delta\varphi\right)}\right). \tag{2.20}$$

Where the *cos* term of *equation 2.18* has instead been expressed as a complex exponential, by dropping the common $|\underline{E}|\varepsilon_0 e^{i\omega t}$ terms,

$$\underline{P_1} = \varepsilon_i e^{i(\underline{k}_1.\underline{x}+\varphi_1)} + \frac{a}{2} e^{i\left((2\underline{k}_1-\underline{k}_2).\underline{x}+(2\varphi_1-\varphi_2)+\Delta\varphi\right)} + \frac{a}{2} e^{i(\underline{k}_2.\underline{x}+\varphi_2-\Delta\varphi)}. \quad (2.21)$$

The linear polarisation of the material expressed in *equation 2.21*, demonstrates that when the electrons subsequently re-radiate the photons that initially polarised them, the energy propagates not only in the original direction of $\underline{k}_1$, but in the $\underline{k}_2$ direction and as an additional $2\underline{k}_1$-$\underline{k}_2$ wave as well. Therefore, the beam is effectively self-diffracted. Additional weaker intensity higher diffraction orders are also possible due to the subsequent polarisation response of the material to the diffracted waves; for example, a $3\underline{k}_1$-$2\underline{k}_2$ wave generated from the self-diffraction of the $2\underline{k}_1$-$\underline{k}_2$ wave.

From *equation 2.21* we highlight that the amount of energy re-directed into another wave is dependent on the value of *a*, i.e. the more photorefractive a material is the better it is at transferring energy. Therefore, *a* is an important parameter we will need to subsequently maximise in the development of photorefractive devices for the control of SPP.

As the waves are self diffracted the waves are automatically Bragg (wavevector) matched. Therefore, this process results in the coherent transfer of energy from one wave to another. The wave-mixing is generally in two distinct regimes, either the Bragg regime ($\Lambda \sim \lambda$) where there are only the two waves $\underline{k}_1$ and $\underline{k}_2$ or the Raman-Nath ($\Lambda >> L$ the effective grating thickness) regime where diffracted waves are also present. In addition, an intermediate regime between the Bragg and Raman-Nath has been reported to exist [110], where the wave-mixing has some properties of each regime. However, these regimes are not entirely appropriate for the photorefractive SPP gain system we intend to develop, so they are not discussed in detail. They are however, important for the general topic of TBG in photorefractive materials; hence, the reader is directed to the following articles for more information on the conditions for Bragg and Raman-Nath diffraction [111-113].

The additional terms in the polarisation that arise from the $\underline{k}_2$ wave are,

$$\underline{P_2} = \varepsilon_i e^{i(\underline{k}_2.\underline{x}+\varphi_2)} + \frac{a}{2} e^{i(\underline{k}_1.\underline{x}+\varphi_1+\Delta\varphi)} + \frac{a}{2} e^{i\left((2\underline{k}_2-\underline{k}_1).\underline{x}+(2\varphi_2-\varphi_1)-\Delta\varphi\right)}. \quad (2.22)$$

Hence, any energy transferred into $\underline{k}_2$ from the $\underline{k}_1$ wave, is offset by the energy transfer from $\underline{k}_2$ into the $\underline{k}_1$ wave. The important difference is that the phase of the transferred energy in one wave is delayed by $+\Delta\varphi$, whereas the other is by $-\Delta\varphi$. The total net energy transfer into a wave is therefore determined by a series of rate equations expressing the energy transfer into and any self-diffraction out of all the waves present in the system.

In a system where there is complete symmetry in the energy transfer between the beams, then both the initial wave's $\underline{k}_1$ and $\underline{k}_2$ are depleted, as there is only a net energy transfer into the

additional newly created (diffracted) waves. However, if an asymmetry is introduced into the system, for example by using beams with unequal intensities, then it is possible for one of the initial waves to experience a net gain at the expense of the energy in the other wave, in addition to the generation of self diffracted waves.

In the photorefractive system we describe, where the intensity of the beams is equal, a net gain of either $\underline{k}_1$ or $\underline{k}_2$ can still be observed. If we consider the gain of a wave for a Bragg regime system[III] then the gain G has then been shown to be a complex function [114],

$$\mathrm{G}_{1,2} = \int iAe^{(-1)^{1,2} i\Delta\varphi}\, dz, \tag{2.23}$$

where A is the magnitude of the gain and is proportional to a. Therefore, the gain of a wave is determined by both the phase shift of the refractive index grating relative to the intensity grating $\Delta\varphi$ and by the value of a. The phase dependence is due to the diffracted waves either constructively or destructively interfering with the original waves. This is a consequence of the additional phase shift term ($\Delta\varphi$) in the diffracted waves due the phase shift of the grating. As the sign of the phase shift differs for the waves diffracted into $\underline{k}_1$ and $\underline{k}_2$, one beam experiences gain and the other beam experiences a loss. The gain (real part of *equation 2.23*) is at a maximum when $\Delta\varphi = \pm\pi/2$. If $\Delta\varphi = 0$, then there is no gain for either wave. The phase shift of the grating is therefore a symmetry breaking mechanism so that the energy transfer is asymmetric.

In addition to using the phase shift of the grating or unequal initial intensities for asymmetric energy transfer, there is another mechanism that can demonstrate gain: an asymmetry in the amplitude of the gain A, for each wave. This later symmetry breaking mechanism is the important mechanism for gain in hybrid photorefractive liquid crystal cells (see *figure 3.9*).

In the literature the gain is more commonly described by the exponential gain per unit length Γ for waves with an equal initial intensity, instead of the absolute gain, therefore removing the sample's thickness dependence from the reported values, thus establishing an even comparison between various materials. The photorefractive gain values for inorganic crystals are typically Γ=10-100cm^{-1} [115], with the highest observation in $LiNbO_3$:Fe,Tb [116]. Photorefractive polymers have also demonstrated gain in the region of 10-200cm^{-1} [93, 117] depending on the doping level of charge-generators, NLO chromophores and plasticisers in the polymer matrix. The highest ever reported gain is 3700cm^{-1} from a hybrid photorefractive liquid crystal cell [17]. Hence, a liquid crystal system is the ideal material for the initial development of a device capable of photorefractive control and later gain of SPP.

[III] Where only two waves are present to considerably simplify the system described.

2.2.2 A Review of Previously Reported Photorefractive control of SPP

The possibility of controlling SPP with photorefractive effects has been previously recognised by the scientific community and initial results have been published. Most of this research is in the development of active SPP switches. Such a system has been demonstrated by changing the structural phase of Gallium (Ga) when illuminated with light [118, 119]. The structural phase of Ga is changed with illumination by a control wave from an initial α (dielectric) state to its *m* (metallic) state due to thermal heating effects. The *m*-Ga state does not allow the probe beam to couple into SPP modes; hence, it switches off the SPP. Once the control wave is removed, the probe beam can again couple to SPP as the Ga relaxes back into its α state. This relaxation determines the switching time and was reported to be ~50ns when the sample is at 17^{o}C [119].

Active SPP switches have also been demonstrated using photorefractive effects of other materials, for example: a high power ultrafast (<200fs) excitation of Al [12]. This produced a weak modulation of ~7.5% in the SPP excitation efficiency. The modulation is believed to be due to the control beam perturbing the electron plasma of Al, thus influencing the SPP modes of the system. The photo-modulation of the LSP resonance of Au nanodiscs has also been reported, by using the *cis-trans* deformation (a molecular shape change from a straight to bent molecule, induced by the light and is completely reversible) of an azobenzene based liquid crystal matrix [13]. In addition, ultra-compact nanoantenna switches have been demonstrated using the non-linear response of the free-carrier density of Indium Tin Oxide (ITO) to the injection of 'hot' electrons from the LSP excitation of the nanoantenna [120].

A photorefractive $LiNbO_3$: Fe crystal has also been used to demonstrate an alternative dielectric grating coupling method for SPP [121]. A holographic refractive index grating is generated in the crystal by two crossed writing beams. This holographic grating was then able to supply the additional wavevector component required for a probe beam to excite SPP on a plane silver film sputtered onto a facing of the crystal. The advantage of this device is that the photorefractive grating coupler is re-configurable.

These examples of active SPP control are achieved using an external light wave as the control signal. To develop a fully integrated active plasmonic system, SPP must be used as the control signal. All SPP-SPP modulation has been previously demonstrated using CdSe quantum dots [122]. However, the mechanism requires the generation of SPP at two different wavelengths. This requirement may prove a difficult obstacle to overcome in the subsequent development of SPP logic systems.

In addition, non-linear plasmonic photorefractive effects have been demonstrated such as a single-photon tunnelling device [123]. The device operates by using a photorefractive polydiacetylene layer to act as a photon blockade for the LSP transmission through a sub wavelength pinhole in a metal film. The blockade is formed from the LSP changing the polymers refractive index and therefore the resonant LSP mode in the pinhole structure.

Therefore, preventing further LSP excitation by additional photons until the LSP re-radiates and the polymer relaxes back to its original refractive index. This device demonstrates a similar staircase behaviour to the Coulomb blockade observed in single electron devices.

2.3 Photorefractive Liquid Crystals

Due to their high birefringence, relative cheap cost and ease of manufacture, liquid crystals are an attractive material for photorefractive applications. In order to describe the photorefractive properties of liquid crystals, a description is first presented on the fundamental physics of this state of matter including a description of the cell structures required to fully harness the properties of liquid crystals. The multiple ways of introducing photorefractive effects to liquid crystal cells is then briefly presented; however, *section 2.3.2* will focus on a detailed description of the surface-potential induced photorefractive effects in liquid crystals that we utilised in the samples described in this thesis. Finally, a review of previous SPP-liquid crystal interactions is presented.

2.3.1 Physics of Liquid Crystals

Certain materials demonstrate an additional intermediate state of matter between the solid crystal and liquid phases. This new state is defined as a liquid crystalline phase as the material has properties traditionally associated with either a crystal or liquid state. In general, molecules in a liquid crystal phase have a low positional ordering and can flow like a liquid as well as having a high degree of molecular orientation order, like crystals.

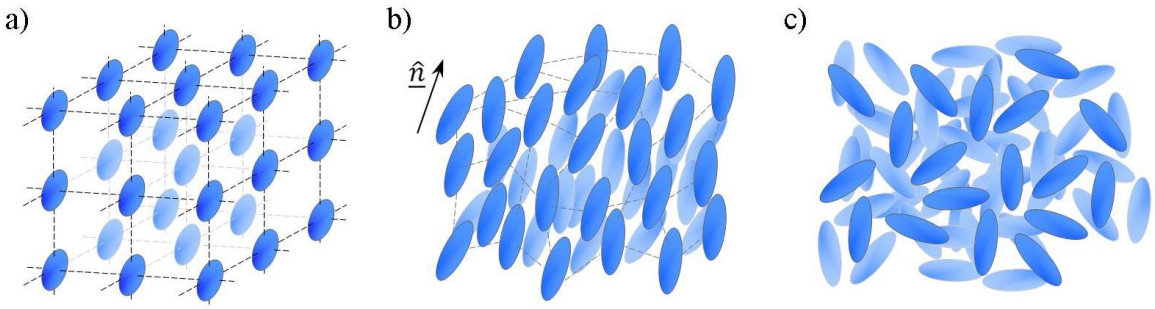

Figure 2.7: Phases of matter. a) Solid crystal, molecules have a fixed position and fixed orientation. b) Liquid crystal, the molecules have a weak spatial order and their orientation is defined statistically by the vector $\underline{\hat{n}}$. c) Liquid, the molecules have no positional and no orientation ordering.

The liquid crystalline state was first discovered in 1888 by Friedrich Reinitzer [124], when he observed that certain cholesterol compounds demonstrated two melting points. The liquid crystalline nature of the melted compounds was later determined through polarised microscopy measurements by Lehmann [125]. However, it was not until 1922 in a paper by Friedel [126] that liquid crystals were formally regarded as the fourth state of matter. In this paper the currently used terminology of mesophases, used to describe the various sub-classes

of liquid crystals, is first introduced. Using all known observations, Friedel identified three mesophases; Nematic, Smectic and Cholesteric. The molecules in a nematic liquid crystal are often described as having directional order while lacking or having zero positional order. Smectic liquid crystals also have directional order, however the molecules form layers as proven by x-ray diffraction [127]. Smectic liquid crystals are further categorised into sub-classes of which the Smectic A and Smectic C phases are the most common; these sub-classes are simply used to further categorise the degree of positional or directional order of the liquid crystal molecules. Finally, in a Cholesteric liquid crystal phase adjacent molecules are in a twisted orientation. This phase is in fact a chiral Nematic phase [126]. All these liquid crystals are further categorised into two additional groups; thermotropic, where the temperature determines the liquid crystal mesophase [128], this is the type of liquid crystal initially discovered by Reintzer; or lyotropic where the concentration determines the mesophase [129] and is often the liquid crystal class of interest in biochemistry. For the photorefractive device described in this thesis only thermotropic nematic liquid crystals are used. Hence, all other types of liquid crystal are not considered further.

The molecules of a liquid crystal are often described as rod-like or cylindrical in shape and are classed as Calamitic liquid crystals [130, 131]. Most liquid crystals are classed as Calamitics. Disc shaped (Discotic) liquid crystals also exist such as Phthalocyanine [132]; however, Discotic liquid crystal are of no interest in this work so will not be described. The rod like shape of a Calamitic liquid crystal is due to a rigid molecular ‘core’, often formed by linked Benzene rings, which are then attached at either end to a flexible hydrocarbon ‘tail’ [133]. For an example of a typical Calamitic liquid crystal molecular structure, see the inset of *figure 2.8* for the chemical formula of the liquid crystal 5CB. The cylindrical structure is a clear example of an anisotropic shape and it is this molecular shape anisotropy that generates the most important optical property of liquid crystals, its birefringence.

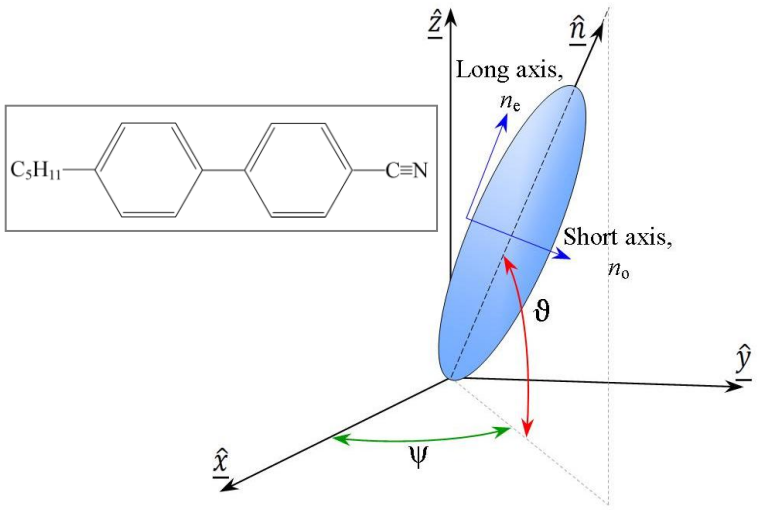

Figure 2.8: The orientation of the director $\hat{n}$ relative to the axis defined by the angles ϑ and ψ. The molecules long and short axis defines n_e and n_o respectively. Inset: The chemical structure of the liquid crystal 5CB (4-cyano-4’pentylbiphenyl), which demonstrates the rod-like shape of the molecule.

Liquid crystals are most often uniaxially birefringent and are characterised by an ordinary (n_o) and extraordinary (n_e) refractive index. The birefringence is thus $\Delta n = n_e - n_o$, where in a nematic liquid crystal mixture such as E7, $\Delta n = 0.219$ at $\lambda = 632$nm (calculated from data in [134]). The magnitude of the birefringence in liquid crystals is often comparable or larger than the significant birefringence of a uniaxial crystal like Calcite ($\Delta n = -0.172$ [135]); hence, they are attractive material's for optical applications that utilise birefringence. As the effective refractive index of a birefringent material is determined by the material's relative orientation to an incident optical wave, we describe the orientation of the cylindrical molecule with a unit vector $\underline{\hat{n}}$, known as the liquid crystals *director*. On a microscopic level the director corresponds to the long axis of the molecule and is used to define n_o (perpendicular to $\underline{\hat{n}}$) and n_e (parallel to $\underline{\hat{n}}$) as demonstrated in *figure 2.8*. The orientation of the director is characterised in a 3D system by two angles ϑ and ψ, relative to the generally used Cartesian co-ordinate axis. At this point we emphasise that for a liquid crystal there is an inversion symmetry; hence, an orientation of $+\underline{\hat{n}}$ is the same as an orientation of $-\underline{\hat{n}}$. In addition, for a wave propagating in the $\underline{\hat{z}}$-direction, the effective refractive index of a liquid crystal orientated at $+\vartheta$ is the same as a liquid crystal orientated at an angle $-\vartheta$. This symmetry has important consequences in a photorefractive system, as later described.

On a macroscopic level, the director concept is still used; however, it now describes the average molecular orientation of the liquid crystal molecules. In nematic liquid crystals the molecules are generally orientated parallel to the director, though due to thermal effects and the molecules positional freedom, slight fluctuations occur about this average position for individual molecules. Thus the average liquid crystal orientation is characterised not only by $\underline{\hat{n}}$ but by an order parameter S as well. The order parameter is expressed as the average deviation from the director and is often mathematically determined by the second Legendre polynomial [136],

$$S = \left\langle \frac{3}{2}\left(\underline{\hat{m}}\,.\,\underline{\hat{n}}\right)\left(\underline{\hat{m}}\,.\,\underline{\hat{n}}\right) - \frac{1}{2} \right\rangle = \left\langle \frac{3}{2}\cos^2\Theta - \frac{1}{2} \right\rangle, \tag{2.24}$$

where $\underline{\hat{n}}$ is the average director and $\underline{\hat{m}}$ is the director of each individual molecule. Therefore, Θ is the fluctuation angle. If $\Theta = 0$ for all molecules then there is no deviation and S =1, this is true for solid crystals. In a completely unordered (isotropic) system like a liquid then S =0. For nematic liquid crystals, the order parameter is typically in the range of S = 0.3-0.8 [128] and reduces with increasing temperature. The order parameter influences the magnitude of the anisotropy of a macroscopic liquid crystal system, with $\Delta n_{system} = S\Delta n_{S=1}$ [137]. However, it is more convenient to consider the physics of an S=1 system whilst using an experimentally determined value of Δn (as acquired in *section 5.2.2*), therefore indirectly factoring in the influence of a $S \neq 1$ order parameter into the described system.

The liquid crystal director does not have to be constant throughout the entirety of the medium like a crystal. Spatial variations in the director due to the elastic response of the material to an external force, in addition and separate to the thermal fluctuations parameterised by S, are

possible. The spatial variations are referred to as deformations and are described as being one of three different types; splay, twist and bend as presented in *figure 2.9*. A splay deformation is when the director of adjacent molecules perpendicular to the director is distorted. Twist deformations describe a rotation of the liquid crystal director between subsequent molecules forming a helix or chiral structure. Lastly, a bend deformation is where the adjacent molecules parallel to the director are distorted. These deformations can be caused by the boundary conditions of the liquid crystal, defects and with an applied electric or magnetic field. As a liquid crystal can flow these deformations do not result in large sheering stresses and translational displacement of molecules like in a solid [130].

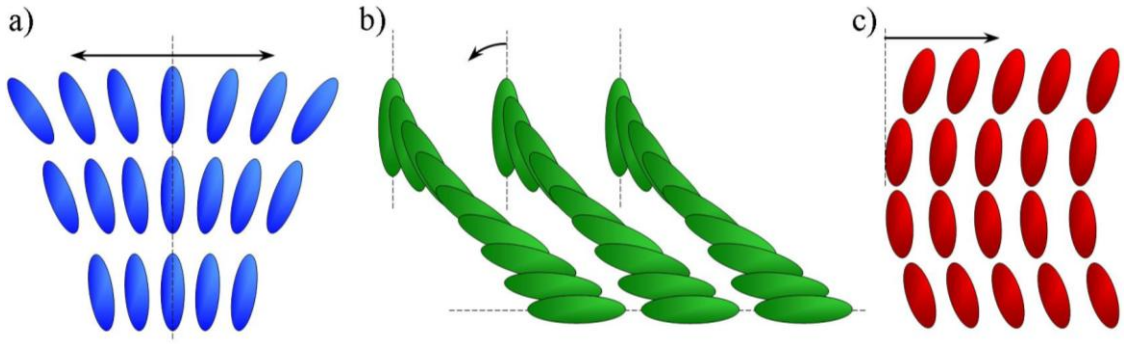

Figure 2.9: The splay (a), twist (b) and bend (c) deformations of a liquid crystal layer. The arrow indicates the deformation direction between adjacent molecules.

To describe these distortions we treat the macroscopic liquid crystal system as a continuous media, thus neglecting specific molecular details and use an elastic continuum theory. The use of a continuum theory is valid for liquid crystals as the deformations occur over a far larger length scale (typically ~1-10μm) than the size of the liquid crystal molecules (~10Å for the largest molecules) [130]. The free energy of the system due to the elastic deformations F_k is therefore expressed as [138, 139],

$$F_K = \frac{1}{2}K_1\left(\underline{\nabla}.\underline{\hat{n}}\right)^2 + \frac{1}{2}K_2\left(\underline{\hat{n}}.\underline{\nabla}\times\underline{\hat{n}}\right)^2 + \frac{1}{2}K_3\left(\underline{\hat{n}}\times\underline{\nabla}\times\underline{\hat{n}}\right)^2. \qquad (2.25)$$

Where K_1, K_2 and K_3 are the elastic constants for the splay, twist and bend deformations. In general, each deformation has a different value for the elastic constant. However, all the elastic constants are usually of the same order of magnitude with only a small variation between them. Hence, it is quite common for the liquid crystal to be described with a single elastic constant approximation [15, 140, 141]. The single elastic constant approximation is used in the theoretical modelling of our system, described in *section 2.5*.

Though the molecules within a liquid crystal have a high degree of orientational order; because the medium flows like a liquid there is no preferred orientation. Thus for applications of liquid crystals we need to use a cell structure to contain and impose a preferred orientation on the liquid crystal. This is commonly done by sandwiching the liquid crystal between two glass plates. The glass plates are often coated with ITO to form a transparent electrode to

allow an external electric field to be applied to the liquid crystal if desired. On top of the electrodes thin (<100nm) alignment layers, often polymers such as polyimide (PI), are added; the surface treatment of these layers then determines the liquid crystals director orientation at the interface. This alignment is due to the interaction between the alignment layer and liquid crystal generating a preferred director orientation where there is a minimum in the free energy. Alternatively, this effect can be considered as the alignment layer generating an intermolecular force that acts on the liquid crystal to impose a preferred orientation. This effect is described as the anchoring of the liquid crystal to a surface.

The anchoring force is generally much larger than any other forces within a liquid crystal system, even if external forces from electromagnetic fields are applied; hence, it is often considered to be of infinite strength [142]. Therefore, the liquid crystal molecules directly at the interface are fixed and no externally applied force can move them. This anchoring force is short ranged; hence, the liquid crystal only has a fixed alignment for a small region near the interface (typically <100nm [143]). We describe this region as a boundary layer where the liquid crystal cannot be influenced by external forces. The existence of the boundary layer is of noticeable importance in our later description and analysis of a SPP's interaction with a liquid crystal.

There are two general types of liquid crystal alignment; planar (parallel to the surface) and homeotropic (perpendicular to the surface). Within a cell structure there is no requirement for the alignment at each confining surface to be the same. Therefore, additional hybrid Pi and twisted cell structures are also possible. However, the only alignment structure we consider is of a planar alignment at both interfaces, with zero twist. The anchoring forces from the alignment layers impose boundary conditions onto the liquid crystal and provided the distance between each confining interface is thin (<100μm), when no external electric or magnetic fields are applied this alignment will be propagated throughout the entirety of the liquid crystal layer due to the weak intermolecular forces between liquid crystal molecules. In a planar cell, a constant planar director orientation throughout the entire liquid crystal layer has the lowest free energy of the system; hence, it will be this alignment that the system relaxes to when any external forces are removed.

Liquid crystals also have a low-frequency dielectric anisotropy $\Delta\epsilon = \epsilon_{\parallel}\text{-}\epsilon_{\perp}$, which in the presence of an electric field induces an electrical dipole moment. This additional electrical force on the molecules will perturb the system and in a macroscopic system is described by an additional term to the free energy [130],

$$F_E = -\frac{1}{2}\varepsilon_0 \Delta\epsilon \left(\underline{\hat{n}}.\underline{E}\right)^2. \tag{2.26}$$

The magnitude of this term is clearly dependent on the orientation of the director and for liquid crystals it can be very large. In general, the liquid crystal molecules are not held in place like the molecules in a crystal lattice; therefore, the liquid crystal director is free to

rotate to minimise the free energy requirement of the system. If $\epsilon_{\parallel}>\epsilon_{\perp}$ then the director aligns parallel to the field, if $\epsilon_{\parallel}<\epsilon_{\perp}$ then the director aligns orthogonal to the field. In a planar liquid crystal cell, only positive anisotropy ($\epsilon_{\parallel}>\epsilon_{\perp}$) liquid crystals are generally of use. On a microscopic level the resultant director alignment is determined by balancing all the torques (electrical, elastic and viscous) acting on the molecule.

In a liquid crystal cell, the director will not re-orientate with the application of an electric field until the additional electrical forces are in excess of the original elastic forces imposed from the alignment layers [144]. This generates a threshold effect for the re-orientation of the director known as the Freedericksz transition. The Freedericksz transition can occur with the application of electrical, magnetic or optical fields; however, we only consider the electrical Freedericksz transition, with a threshold given by [128],

$$\mathrm{E}_{th} = \frac{\pi}{\delta_{LC}}\sqrt{\frac{\mathrm{K}}{\varepsilon_0 \Delta\epsilon}}, \tag{2.27}$$

where K is the single elastic constant and δ_{LC} is the thickness of the liquid crystal layer. *Equation 2.27* can then be used to determine the threshold potential $V_{th} = E_{th}\delta_{LC}$. The threshold potential is therefore independent of the cells thickness. Physically this is a consequence of lower cell thickness having an increased electric field and an increased elastic energy as the liquid crystal must deform over a shorter distance.

For potentials above the Freedericksz transition, the molecules furthest from the interfaces begin to align first as the elastic alignment forces in this region are at their weakest. The realignment to the potential is then gradual (i.e. not bistable), with more of the liquid crystal layer beginning to realign, until a saturation potential; at which point, all but the molecules in the boundary region are fully aligned to field as demonstrated in *figure 2.10* for a planar cell.

The molecular reorientation from an applied field causes the effective refractive index and the birefringence of the liquid crystal layer, as seen by a wave passing through the cell, to change. For a positive anisotropy ($+\Delta n$) liquid crystal in an initially planar alignment the effective refractive index will increase, whilst the birefringence will decrease. Thus the optical properties of a liquid crystal cell are controlled through the magnitude of an applied potential, i.e. it is an electro-optic material. For a nematic liquid crystal such as E7, an applied potential (1 kHz) as low as 2.1V is needed to completely switch the liquid crystal from its ordinary to extraordinary refractive index [145], though the magnitude of the required switching potential is sample dependent. This is a considerably lower potential than the potential required for a refractive index change in an electro-optic crystal (kV potentials for a comparable effect [135]).

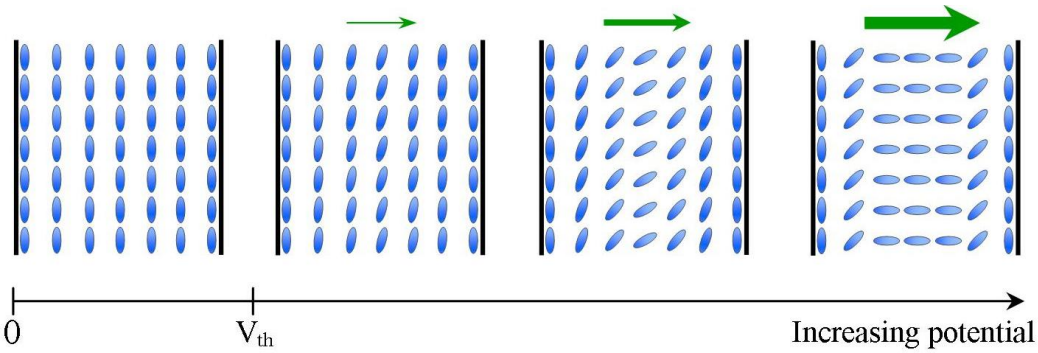

Figure 2.10: The re-orientation of the liquid crystals molecules as the applied potential across the cell increases. The green arrows represent the magnitude of the applied potential above the threshold potential V_{th}. The orientation of the liquid crystal molecules adjacent to the cell boundary is fixed even as the potential increases.

Controlling the birefringence of a liquid crystal layer is the principle mechanism behind their most wide spread use in liquid crystals displays (LCD's). The cell in an LCD is generally a twisted planar structure and when no potential is applied rotates the polarisation of light by $\pi/2$. When placed between crossed polarisers this allows incident light to be transmitted. Applying a potential forces the liquid crystal into an almost fully homeotropic alignment, which does not rotate the polarisation; hence, the light is not transmitted. This is a simplified description of the general operation of an LCD device, for a thorough description of the physics and operation of LCDs see [137].

The large change in the effective refractive index of the liquid crystal layer by applying a potential is also the mechanism we use to manipulate SPP modes. However, we will additionally spatially modulate the refractive index with photorefractive-like effects by spatially modulating the magnitude of the applied potential.

2.3.2 Photorefractivity in Liquid Crystals

Photorefractive effects were first discovered in liquid crystals in 1994 [15, 146], with a liquid crystal doped with the laser dyes D2, methyl red or R6G and using a cell with standard PVA alignment layers. The dyes act as a sensitizer to the incident light generating charges in the bulk liquid crystal medium, which were subsequently trapped to form a space-charge field. Such a liquid crystal system operates in a similar fashion to a photorefractive crystal. However, where the refractive index change is linear in a crystal (*equation 2.18*) and depends on the symmetry class of the crystal (sign of γ_{eff}), in a liquid crystal which is centrosymmetric ($+\underline{\hat{n}} \equiv -\underline{\hat{n}}$) the E-field induced change is quadratic (*equation 2.19*) [130];

$$\Delta n = \gamma_{eff}\, E \tag{2.28}$$

$$\Delta n = aE^2\,. \tag{2.29}$$

Hence, liquid crystals are potentially far better photorefractive materials. The TBG from this type of photorefractive system can be further increased by doping the liquid crystal with ferroelectric nano-particles [147] or C_{60} [97] to achieve a gain as high as 2890cm^{-1}.

The previous photorefractive liquid crystal systems described are examples of bulk photorefractivity; another class of liquid crystal photorefractive device is possible using surface (alignment) layers, where the layer's conductivity is modulated by illumination. This surface/interface based photorefractivity is of considerable interest for controlling SPP, which are also confined to the interface. Hence, the photorefractive systems we focus on in this thesis are based on this type of system. Photorefractive like effects are generated in such a system by using a photoconductive polymer for a cell's alignment layers, this method was first proposed by Ono [148]. Ono used a polymer with a low dark conductivity, Poly-N-vinylcarbazole (PVK) as the photoconductive alignment layer. This layer was capped with a PVA layer, as it was believed to be necessary to trap charges. The PVA layer was later found to not be a requirement in this type of cell and TBG values as high as 3700cm^{-1} have been reported from subsequent devices [17, 149]. Since the development of this liquid crystal structure, studies to find the optimum combination of dopants, liquid crystals and alignment layers have been presented [150]. However, no general consensus has been achieved on the optimum structure (layer thicknesses), as each paper in the literature uses a slightly different cell structure or material's; therefore making an accurate comparison of results difficult. As the liquid crystal is not directly photorefractive in this type of device they are referred to as *hybrid photorefractive liquid crystal cells*. In these cells the photoconductor is doped with a small amount of either 2,4,7-trinitro-9-fluorenone (TNF) or Fullerene (C_{60}) to sensitise it to visible light by a charge-transfer complex [151].

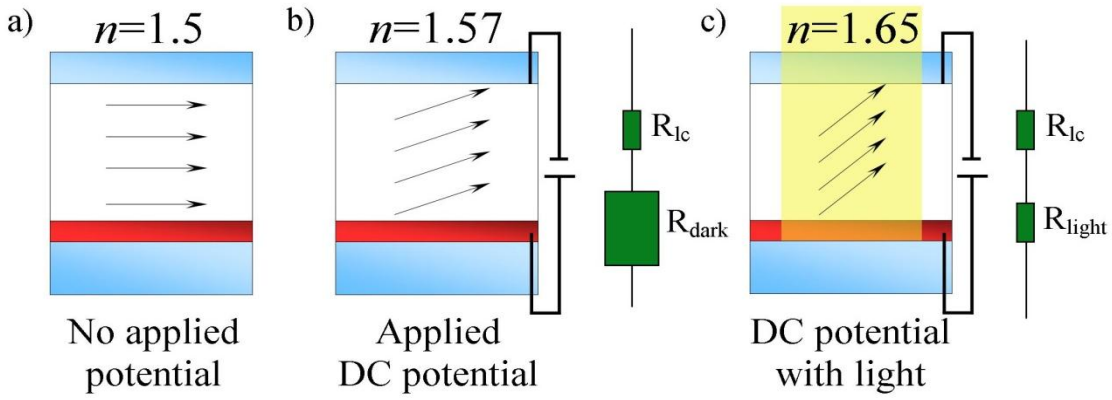

Figure 2.11: Characteristic operation of a hybrid photorefractive liquid crystal cell. a) In the dark, without an applied voltage, the liquid crystal director is determined by the boundary conditions from the cells alignment layers. b) Applying a potential in the dark results in a partial re-orientation of the liquid crystal director. The applied potential across the liquid crystal is limited due to the large resistance of the photoconducting layer. c) Illuminating the photoconducting layer reduces the layers resistance, allowing a larger potential drop across the liquid crystal. Further re-orientation is then possible from an increased applied potential. An approximation of the liquid crystals effective refractive index *n*, as observed by a SPP, is listed at the top of a-c. Hence the effective refractive index is controllable with light.

A hybrid photorefractive liquid crystal cell operates by controlling the resistance of a photoconductive layer, as presented in *figure 2.10*. When a DC or low-frequency potential is applied across the cell, the low conductivity of the PVK causes a significant fraction of the potential drop to occur across the photoconductor and not the liquid crystal [152]. The re-orientation of the director is therefore limited. When illuminated in the visible spectrum the conductivity of the PVK increases allowing a greater potential drop across the liquid crystal. This increased potential results in further re-alignment of the director and thus an increase in the refractive index in the illuminated region. Hence, a photorefractive like effect.

The photorefractivity of these hybrid photorefractive liquid crystal cells is also measured by TBG; however, the grating formation mechanism is slightly different. The sinusoidal intensity grating of light and dark regions caused by the interfering waves generates a sinusoidal variation of identical period and phase in the conductivity of the photoconducting layer. Applying a potential across the whole cell then results in a periodic potential across the liquid crystal due to the spatially varying conductivity. The electric field associated with this potential then generates a refractive index grating in the liquid crystal layer, *figure 2.12*. There is no grating formation through the generation of an internal space charge field within the liquid crystal. Hence, there are a few additional subtleties that need to be addressed when using surface mediated photorefractive liquid crystals for TBG.

The first is that because a modulated electric field is generated on the surface of the photoconductor, the field strength will decay through the liquid crystal. The modulated electric field penetrates a distance approximately equal to the grating pitch[IV]. Hence, the magnitude of the grating modulation is not the same throughout the entire layer, unlike a bulk photorefractive system. This can effectively reduce the 'active' thickness of the photorefractive medium, thus the TBG measured will likely under-predict the actual gain of the active region nearest to the photoconductor. This effect will also limit the fraction of the total incident power transferred between beams, as the active thickness of the devices is usually quite thin.

The inversion symmetry of the liquid crystal also influences the TBG mechanism of these devices. If the bisector of the two beams is at normal incidence to the cell then the fundamental grating formed has twice the wavevector of the interference pattern[V], as *figure 2.12* demonstrates. Hence, the system is not Bragg matched and little direct energy transfer between beams can occur. This effect can be removed by a molecular symmetry breaking mechanism such as a large initial non-parallel director alignment to the surface, a pre-tilt. Alternatively this can be experimentally achieved in a cell by applying a large uniform potential, i.e. not spatially modulated, across the entire liquid crystal cell to partially re-orientate the liquid crystals director. This is in fact the mechanism that generates the correct grating wavevector in our experiments presented in *Chapter 5*. However, even if a pre-tilt is

[IV] This is later proved in *section 5.8.4*.
[V] As the response of the liquid crystal is non-linear, a weaker strength grating of the correct wavevector and higher harmonics will also be generated.

used for the formation of the correct grating wavevector in the liquid crystal, TBG is still not observed as the measured phase shift of the grating is zero [152]. Physically, this is explained as the beams transferring an equal amount of energy into each other as there is no symmetry breaking mechanism to distinguish pump and probe, one beam observes a grating phase shift of $+\Delta\varphi$ and the other observes a phase shift of $-\Delta\varphi$; hence, there is no net gain [114].

Therefore, the symmetry of the system is broken by rotating the cell so that the bisector of the two interfering beams is not normal to the photoconductor surface [130, 152, 153]. This will also establish the correct grating wavevector. Breaking the system's symmetry with this method has further additional effects that influence the TBG mechanism, which need to be accounted for. As a SPP gain system cannot rotate the cell in this manner these effects are only briefly described. The most significant of these is that as the grating is only generated at the photoconductor surface, the grating will no longer be perfectly phase matched. There is a small mismatch term that will reduce the energy transfer [110]. In addition, the phase shift of the grating relative to the beams interference pattern becomes dependent on the distance into the cell; hence, beam coupling will favour different beams at different points with an almost zero net effect. Therefore, the phase shift of the grating does not influence the TBG. For a more detailed description of these two effects in a liquid crystal TBG system see [110, 114]. Gain is observed in a rotated cell system, as the cell orientation results in an unequal beam coupling strength between the two waves (unequal A from *equation 2.23*). The mechanism behind the asymmetric beam coupling co-efficient is described in *figure 3.9*.

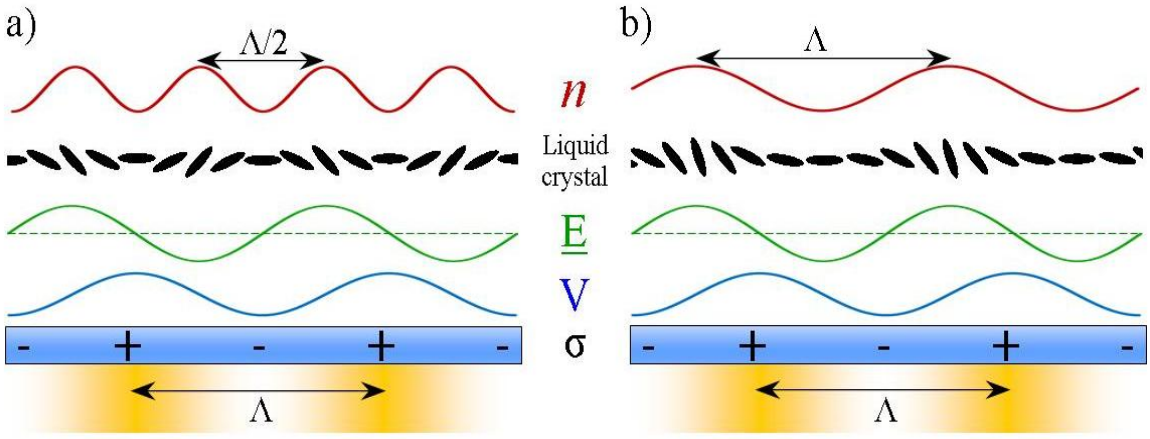

Figure 2.12: Grating periodicity matching for a hybrid photorefractive liquid crystal. The intensity profile (assumed to be $\sin^2 kx$) of the light with pitch Λ, modulates the conductivity (σ) and therefore the potential V. The E-field is the derivative of V and is responsible for the local liquid crystal alignment. a) Without a pre-tilt or cell tilt, the modulation of the refractive index n is $\Lambda/2$, as the refractive index of a $+\vartheta$ orientated molecule is the same as one orientated at $-\vartheta$. b) By rotating the cell relative to the bisector of the crossed beams, or with a molecular pre-tilt, the symmetry of the system is broken so the pitch equals Λ.

2.3.3 SPP Interactions with Liquid Crystals

Combined liquid crystal and SPP systems have been previously investigated. The first reported system was by Sprokel et al in 1981 [154] where they demonstrated that the wavevector of a SPP can indeed be controlled with the re-orientation of a planar aligned nematic liquid crystal to an applied potential. This experimental data was then used to determine the pre-tilt angle of the liquid crystal on a 20nm SiO_2 alignment layer surface [155].

Similar experiments later undertaken by Sambles et al also demonstrated this behaviour [156]; however, the results of Sambles indicate that when a potential is applied to the liquid crystal, guided modes can be supported in the liquid crystal layer. The presence of additional guided modes was explained by the formation of different refractive index regions in the liquid crystal layer due to the surface anchoring, and thus generating core and cladding regions of a waveguide that support the guided modes in the liquid crystal. At low voltages (6V) the guided modes overlapped the SPP resonance, whilst at higher potentials of 20V they did not. This is because the excitation angle for guided modes remains fairly static with an increasing potential as they are associated with the bulk liquid crystal alignment, which is fully aligned to the direction of the field for potentials above 6V. Whereas the excitation angle of an SPP is determined by the director at the surface which can still re-orientate with an increasing potential, thus allowing the SPP resonance to shift to excitation angles where there are no guided modes. Hence, for our system we should ideally apply high potentials so that guided modes do not interfere with the SPP resonance.

This data was also used to determine the orientation of the director near the surface [157] and demonstrated that the common assumption that the anchoring energy is infinite leads to a systematic error in the measured elastic constants of a liquid crystal. However, the infinite anchoring strength model is still correct as long as one accounts for actual finite anchoring strength by using a stiffer elastic constant associated with a thermotropic liquid crystal ~1.5^{o}C cooler. In addition, it was later shown that fitting both the SPP resonance and the guided modes leads to a significantly higher sensitivity to the director orientation near the aligning surface in hybrid cells [158].

SPP and liquid crystal systems have also been used to demonstrate optically non-linear systems such as optical bistability [159] due to the thermally induced phase transition of a liquid crystal near the metal interface where the SPP is excited [160]. However, liquid crystal systems are generally used as a method of controlling the dispersion of SPP with applications such as; electronically controlled optical transmission through hole arrays [161], voltage induced broad band reflectivity [162] and colour selective absorption [163], a microwave wavelength selector [164] and as a spatial light modulator [11].

2.4 The Design of our Hybrid Photorefractive Plasmonic Liquid Crystal Cell

The basis of the samples developed to control SPP with photorefractive effects in this thesis is a hybrid photorefractive liquid crystal cell. The liquid crystal layer structure is the same as in previously reported cells [152], *figure 2.13*. Only a single photoconductive layer is used, as using two photoconducting layers shows no benefit to the TBG [152] and in fact complicates the form of the liquid crystals modulation. This is due to the periodic conductivity profiles of two photoconducting layers either side of the liquid crystal rarely having maxima aligned with each other. Therefore, we use a standard polyimide (PI) layer as the opposing alignment surface as this material does not demonstrate photoconductive effects [153].

For the photoconductive polymer, we will utilise poly-N-vinyl-carboxyl (PVK) as this is the standard photoconductive material used in these types of cell. Other well known photoconductive polymers such as poly-[2-methoxy, 5-(2'-ethyl-hexyloxy)-p-phenylene vinylene] (MEH-PPV) [165] or poly-3-octylthiophene (P3OT) [166] could in principle also be used to generate photorefractive effects. However, PVK is a proven material in these systems and little work has been presented on using other photoconducting polymers.

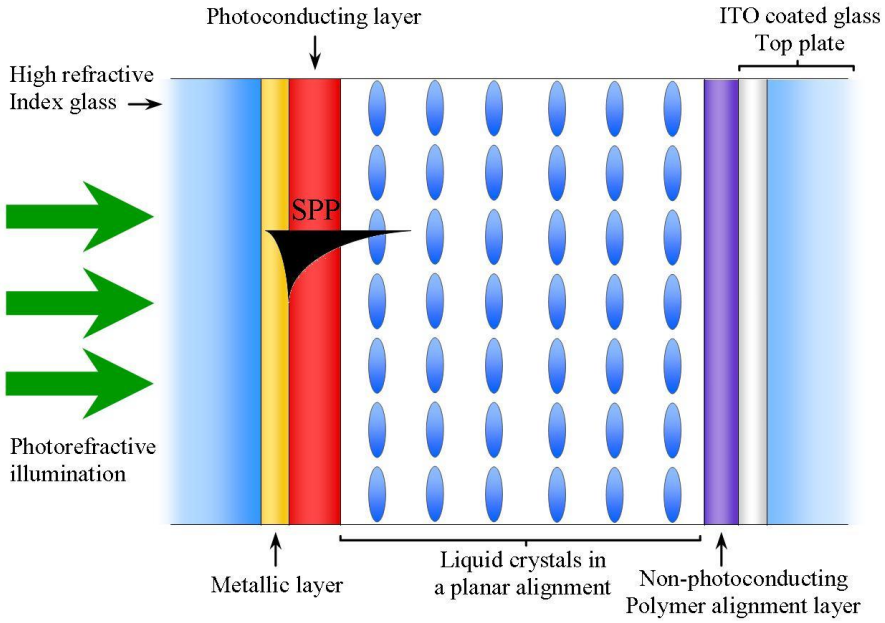

Figure 2.13: The general design of a hybrid photorefractive liquid crystal cell for controlling SPP. The SPP is excited at the metal/photoconductor interface. The electric field of the SPP should be able to probe the liquid crystal layer.

Various liquid crystal materials have been used in hybrid photorefractive liquid crystal cells such as 5CB [167], E7 [152] and TL205 [114]. The liquid crystal used for our samples is the Merck mixture E7, which is an ideal liquid crystal for our application due to its large

birefringence (n_o=1.519, n_e=1.737 at λ = 633nm [134]) and good thermal stability with a clearing temperature (isotropic transition) of 57^{o}C [168].

A few modifications are then made to the cells previously reported in order to allow SPP modes to be generated in the photorefractive system. The first is that the traditional ITO layer adjacent to the photoconductor is replaced with a thin metal layer. The metal will act as both an electrode, so a potential can be applied across the liquid crystal, and as the negative dielectric constant material required for SPP modes. The SPP modes will thus be generated at the metal-photoconductor interface. The glass substrate that the Au is deposited onto is also a high index glass and will act as part of the high dielectric constant prism required to excite SPP by the Kretschmann method (*section 3.1*). The refractive index of the glass must be higher than the highest refractive index of the dielectrics that the SPP interacts with; otherwise, the Kretschmann method cannot excite the SPP modes, therefore $n_{glass} > 1.71$.

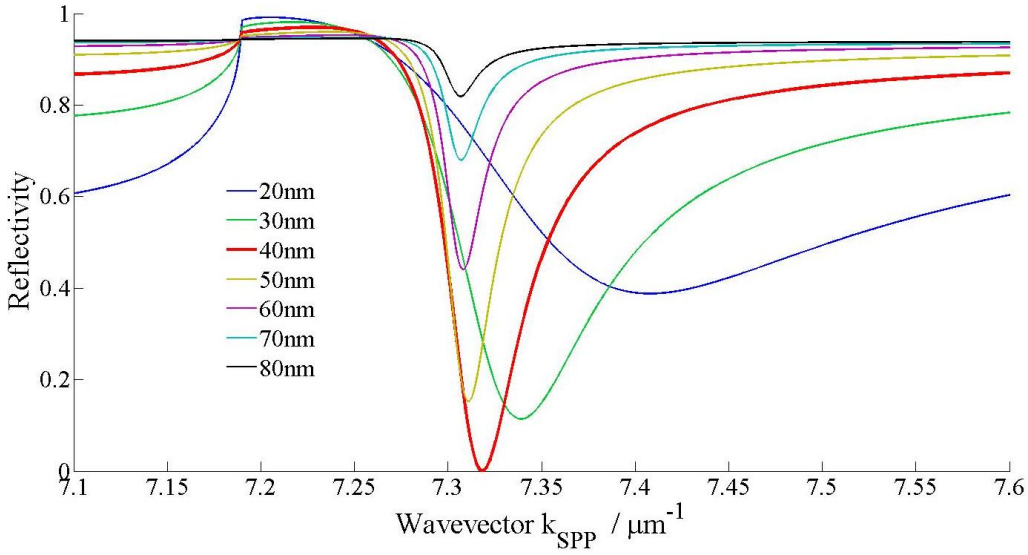

Figure 2.14: The theoretical SPP ATR spectrum for an Au/air interface with a variation in the thickness of the Au layer. A 40nm Au layer allows the best excitation of a SPP mode. The refractive index of the prism is 1.83.

We also consider the thickness of each of the layers in our samples. The first is the thickness of the metallic layer. To excite SPP the evanescent field of the light must pass through the metal; hence, the layer is typically thin (<100nm) due to the large attenuation of optical fields in metals. There is however, an ideal metal thickness. This is because if the layer is too thick, the optical field decays too much and less than 100% of the incident light can excite the SPP modes. If the layer is too thin, then there is insufficient metal to confine the SPP and the E-field in the metal extends back into the high index glass. Hence, the mode is loosely bound with noticeably reduced plasmonic properties. The metal thickness dependence on SPP excitation is demonstrated for Au in *figure 2.14*, where the theoretical ATR reflectivity from an Au(variable thickness)-air interface through a *n*=1.83 prism is simulated with a transfer matrix (T-matrix) optical algorithm. The figure clearly demonstrates that the optimum thickness of the Au for exciting SPP should be 40nm. An acceptable SPP excitation is also

possible with 30nm or 50nm layers; however, for fabrication purposes we set a tolerance of ±5nm of the ideal thickness. The 40nm ideal thickness is specific to Au, this will vary slightly with the metal used; for example, the ideal thickness for Ag is 50nm.

The thickness of the photoconductive layer is also an important parameter in the design of our samples. If we consider the theoretical SPP wavevector (T-matrix ATR prediction) of an isotropic approximation of our system, *figure 2.15*, when the liquid crystal has an effective refractive index of 1.5, 1.6 and 1.7 to represent the photorefractive change we expect this layer to undertake, we notice that the thinner the photoconducting layer the larger the change in the SPP wavevector, i.e. a larger photorefractive control. This is because the electric field of a SPP only penetrates a few hundred nanometres away from the interface into the dielectric layers, thus there is a greater SPP electric field overlap with the liquid crystal with a thinner photoconducting layer. Hence, the SPP wavevector is determined more by the variable refractive index of the liquid crystal. However, ultra-thin 10nm photoconducting layers are unlikely to generate a large resistance contrast between the illuminated and dark regions of the photoconductor that is necessary for a good photorefractive sample. For example, a 10nm layer may only have a sufficient resistance be able to generate an effective liquid crystal refractive index change of n=1.6 to n=1.605 with illumination. A large resistance contrast and therefore a large refractive index change with illumination would require a layer over 200nm thick. However, the SPP wavevector change for a layer this thick (*figure 2.15d*) is likely to be insufficient for our applications. As the thickness dependence on the photoconductor resistance is unknown, a photoconducting layer 50-100nm thick is likely a good compromise region between the theoretical changes in the SPP wavevector (*figures 2.15b-c*) and the necessary thickness required for generating a sufficient light-dark resistance contrast.

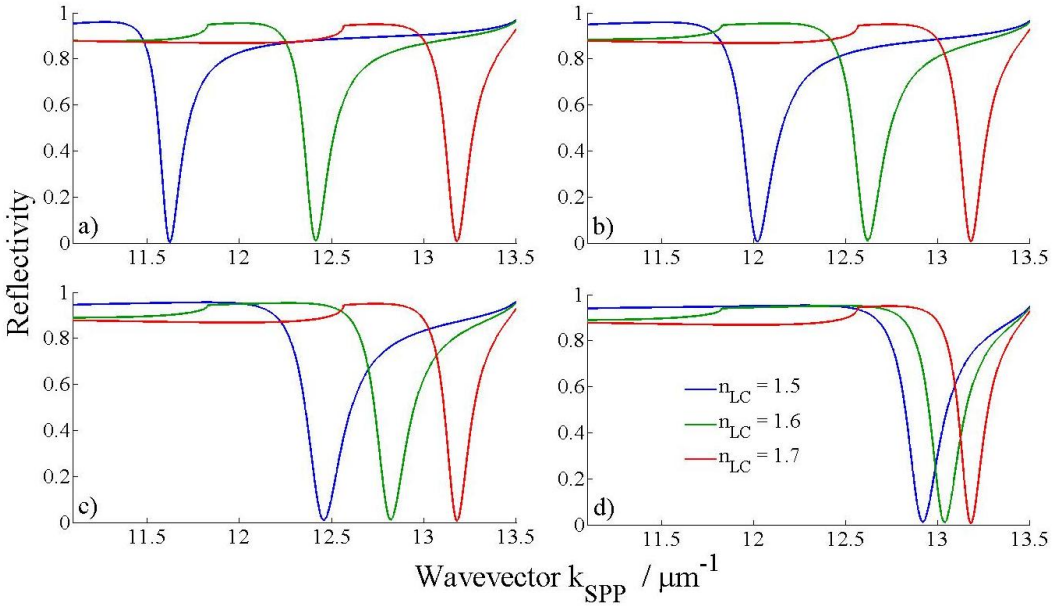

Figure 2.15: The theoretical SPP ATR spectrum for an Au/photoconductor/liquid crystal interface. The Au thickness is 40nm. The thickness of the photoconductor (n = 1.7) is 10nm (a), 50nm (b), 100nm (c) and 200nm (d). The figure considers how the refractive index of the liquid crystal affects the SPP wavevector. The refractive index of the prism is 1.83.

As the SPP only probe a small distance into the liquid crystal, the liquid crystal layer thickness is not considered a variable. A thickness of 12μm which is typical for these liquid crystal cells is more than sufficient [152]. Details on the fabrication methods of these devices are presented in *section 3.3*. These devices are not optimised; further investigations into materials used and the thickness of the photoconductor could lead to a significant improvement in their operation.

2.5 Theoretical Modelling of the Photorefractive Plasmonic Liquid Crystal Cells

During the characterisation of our cells in *Chapter 4*, we often require a theoretical fit to experimental data for the transmission of a sample in order to determine the thickness of a layer. In addition, determining the theoretical non-normal incidence reflection of a sample is useful to predict the ATR spectrum and wavevector of a SPP mode. As our structures are multilayered we use a transfer matrix (T-matrix) method [169] for these calculations. In a T-matrix, each layer is modelled as a homogenous media in the direction normal to the layers of the surface. We then consider the forward and backward electromagnetic fields that can propagate within the medium. By then setting boundary conditions that the tangential components of the electric and magnetic fields are continuous at the interface between two adjacent media, we generate a set of linear equations that are most easily solved using a matrix. In the case where only isotropic materials are used, i.e. samples without a liquid crystal layer, the TM and TE polarised waves can be separately considered. As SPP are TM waves, in general, we only have to consider the TM reflection and transmission of a sample. Examples of the T-matrix output in this thesis for an isotropic system can be found in *figures 2.14-15*, *4.1-4.3* and *4.5*.

A T-matrix simulation is not limited to isotropic materials and can be extended to anisotropic systems [170, 171] such as a liquid crystal, where both polarisations must be considered to account for the coupling between the polarisation modes [172]. However, when a significant potential is applied to a liquid crystal, the layer is no longer homogenous. To determine the non-homogenous director alignment of the liquid crystal when a potential is applied to the cell we use a code developed by our collaborators Dr. Keith Daly and Dr. Giampaolo D'Alessandro [173]. Their approach is to determine the alignment of the liquid crystal director in the presence of an electrical potential using an approximation to the Q-tensor method developed by de Gennes [139], which is suitable for liquid crystal devices free of defects. This model is noticeably quicker to calculate [173] than the full Q-tensor model of de Gennes. The subsequent spatial variation of the liquid crystal in the direction normal to the layers surface is then accounted for in the optical code by the method of Berreman [174]. This method involves slicing up the liquid crystal into a large number of layers so that each sliced layer can then be considered homogeneous. The typical number of Berreman layers used is 500; these layers are not evenly spaced and more layers are used near the interface, so that

large changes in the optical properties between adjacent Berreman layers do not occur, thus more accurately describing the optics of the liquid crystal system.

Because we need to model evanescent electric fields to excite SPP in our samples, using a large number of Berreman layers makes the optical code numerically unstable as the T-matrices then have terms both large (e^{+kx}) and small (e^{-kx}). Hence, for the simulations of samples with a liquid crystal layer we use a variation of the T-matrix, the Scattering matrix (S-matrix) [175-177]. An S-matrix relates all the inputs of a system to all the outputs, instead of relating the fields on the left hand side of the multilayer structure to the fields on the right hand side. This method is more complicated; however, the same mathematical approach required for the T-matrix is necessary for the S-matrix. The benefit of the more complicated S-matrix is that the terms in the S-matrices are then same order of magnitude, making the simulations stable for evanescent fields and a large number of layers.

The liquid crystal model developed by Daly and D'Alessandro is also appropriate for a system where there is a variation of the liquid crystal director in two directions, i.e. along the interface and perpendicular to the interface. Therefore, the code is ideal for simulating the refractive index grating we generate in the liquid crystal layer with a modulated surface potential due to a non-uniform illumination in the experiments presented in *Chapter 5*. In fact, the original motivation for developing this code was to model the TBG mechanisms of a hybrid photorefractive liquid crystal cell [114, 173] related to this work. The spatial variation in the director is calculated by determining the liquid crystals response to a spatially modulated surface potential V′ of the form of $V'=a+b^{*}\sin^{2}(k_{\Lambda}x)$; where a and b describe the magnitude of the uniform and modulated potentials respectively and k_{Λ} is the wavevector of the grating with a pitch Λ. The sinusoidal potential V′ is only generated on one side of the cell (physically corresponding to the PVK side of the cell), whereas the potential on the opposing side is uniformly zero (which is true for the non-photoconducting PI side). An example of the spatial variation of the potential throughout the cell for one grating period is presented in *figure 2.16a* and the subsequent variation in the director is presented in *figure 2.16b*, where the equipotentials show more clearly the modulation of the director.

A full numerical simulation of the SPP interaction with a refractive index grating in the liquid crystal layer is then developed by combining the periodic variation in the liquid crystals refractive index, determined by the liquid crystal code, with the S-matrix optical code. As the liquid crystal layers refractive index is harmonic, the rigorous diffraction theory developed by Moharam and Glytsis [178, 179] is used to determine the reflection of all the waves from our multilayer structures. Additional waves are generated by the refractive index grating diffracting the initial electromagnetic wave (these will all be SPPs). Physically, this represents the grating coupling energy from one SPP mode to another propagating in a different direction with the same frequency. In this thesis, we only consider a single initial SPP mode and examine the energy transfer by a grating into other SPP modes. However, in future work we intend to extend our system to consider two interfering SPP (that self-

generate the refractive index grating) so that the energy transfer by the grating is analogous to TBG.

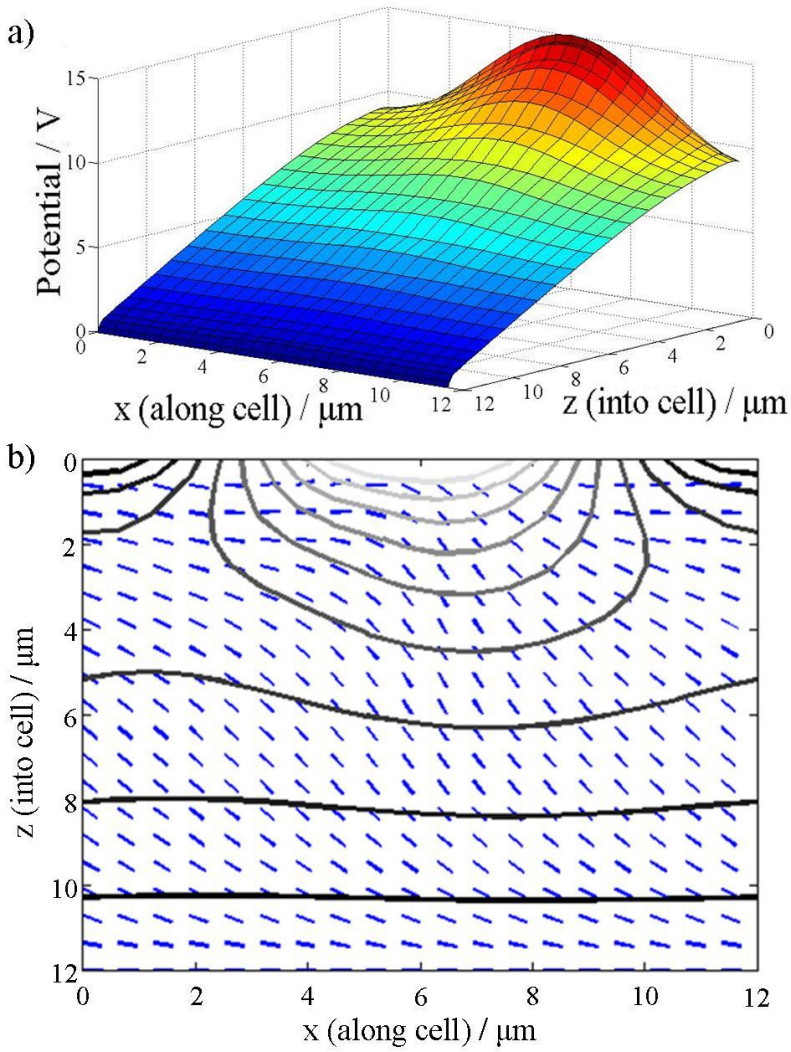

Figure 2.16: a) The spatial variations of the potential in the liquid crystal that we model. The parameters are Λ=12µm, *a*=9V and *b*=6V. b) The director orientation throughout the liquid crystal layer determined by the numerical simulations of K. Daly to a sinusoidal potential of the form of (a). The solid black lines are the equipotentials of the system..

In modelling our cells with the full numerical simulations we have made allowances for the huge variety of liquid crystal structures and optical geometries that we could in principle examine. Hence, we have numerous parameters that we can control within our simulations. A list of all the controllable parameters, their significance and typical values is presented in *table 2.1*. To achieve convergence with the full numerical simulations (where increasing the resolution does not change the output) the number of points used in the liquid crystal alignment model is 48; then with typical values for all the other parameters the code takes approximately 6 hours to compute, mostly due to the optical computations.

Variable	Symbol	Description	Typical values
Applied Voltage	$\|V\|$	Magnitude of the applied potential to the liquid crystal. Scaled by V' for spatial dependence.	10-15V
Grating Pitch	Λ	Pitch of the refractive index grating	1-10μm
Wavelength	λ	Wavelength of the incident light used to excite SPP	850nm
Polar angle	90^o-γ	Angle between grating and SPP propagation direction	84-87^o
Azimuthal angle	θ	Angle of incidence of the light onto the sample	60-75^o
Length LC	δ_{LC}	Thickness of the liquid crystal layer	12μm
Length Au	δ_{Au}	Thickness of the gold layer	40nm
Length PVK	δ_{PVK}	Thickness of the PVK layer	80-120nm
Elastic constant	K	Liquid crystal single elastic constant	15.9pN
theta PVK	ϑ_{PVK}	Liquid crystal pre-tilt at the PVK interface	0^o
psi PVK	ψ_{PVK}	Initial liquid crystal alignment at the PVK interface	90^o
theta PI	ϑ_{PI}	Liquid crystal pre-tilt at the PI interface	2^o
psi PI	ψ_{PI}	Initial liquid crystal alignment at the PI interface. Does not have to be the same as psi PVK; hence a twisted alignment geometry could be examined.	90^o
RI prism	n_{prism}	Refractive index of the Kretschmann prism	1.83
RI PVK	n_{PVK}	Refractive index of the photoconducting layer	1.67
RI LC parallel	n_e	Liquid crystal RI parallel to director	1.71*
RI LC perpendicular	n_o	Liquid crystal RI perpendicular to director	1.51*
epsilon parallel	$\epsilon_{\|}$	Low frequency dielectric constant parallel to the director	19.54
epsilon perpendicular	$\epsilon_{\perp}$	Low frequency dielectric constant perpendicular to the director	5.17
N		Resolution (number of points) of the liquid crystal alignment simulations in each dimension	24 or 48

Table 2.1: The variables we can control in the full numerical simulations. The symbols used to describe each parameter correspond, where possible, to the experimental parameters and terminology used in *Chapters 4* and *5*. *Alternatively a computed Cauchy relation for the refractive index can be used.

An example of the output of the full numerical code is presented in *figure 2.17*. The zeroth order is the theoretical ATR reflection spectrum for an SPP in a 100nm PVK sample. The additional orders describe the diffraction of energy in the SPP from interacting with the $\sin^2(k_\Lambda x)$ refractive index modulation in the liquid crystal layer. When interpreting the output we consider the maximum reflectivity (diffraction efficiency) for each order; for example, the +1 order has a diffraction efficiency of ~7%, we do not in general consider the angle at which this diffraction occurs as it does not directly correspond to the angle of reflection of the zeroth order. The guided modes are not used in our analysis.

The development of the full numerical model (all components) needs to be attributed to Dr. Keith Daly and Dr. Giampaolo D'Alessandro. My role was to rigorously test the code using my experimental observations.

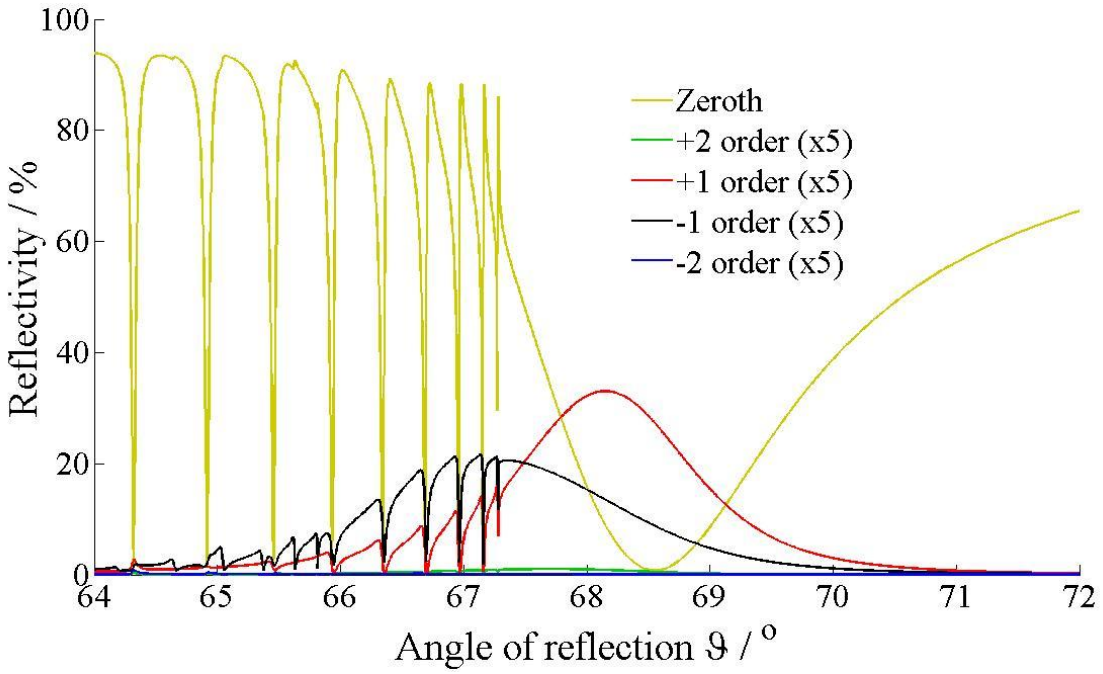

Figure 2.17: The reflection of 850nm light as a function of angle for a sample where the liquid crystal has a 5µm grating pitch with a 15V potential applied to the cell, $V'=12+3\sin^2(k_\Lambda x)$, the PVK layer is 100nm. The grating is slightly tilted (polar angle =87°) from being perpendicular to the initial liquid crystal alignment and SPP wavevector. The zeroth order shows an ATR reflection spectrum expected for a SPP in our samples and demonstrates the guided modes observed by Sambles [156]. The additional curves show the angular dependent diffraction efficiency of energy transferred from the zeroth order into higher diffraction orders (other SPP modes). In this example the slight tilt in the grating orientation causes an asymmetry in the diffraction efficiency for the positive and negative diffraction orders.

Chapter 3

Experimental Techniques

In this chapter, the reader is provided with background information on the experimental techniques used to analyse hybrid photorefractive plasmonic liquid crystal cells. The techniques can be categorised into one of three sections. The first presents details on the method used to excite SPP and how to extract data about their energy, wavevector and propagation length. The second section explains the various optical and electrical measurements undertaken to characterise the behaviour of a photorefractive liquid crystal cell as well as determining the properties of each layer in the cells structure. Finally, the fabrication techniques necessary to create the samples investigated in this work are described. A list of the specifications of the experimental equipment can be found in *Appendix A*.

3.1 Surface Plasmon Polariton Excitation and Analysis

To investigate the interaction of an SPP with a spatially modulated photorefractive liquid crystal, a method of exciting the SPP at the metal/photoconductor interface is required. As discussed in *section 2.1.2*, a SPP on a uniform metal film cannot be excited by directly illuminating the metal with light due to wavevector conservation. Thus, a system is used in our experiments where the evanescent field of light propagating in a high dielectric constant medium excites the SPP modes at the interface of a metal and a lower dielectric constant medium, an ATR apparatus.

Of the two distinct variations of the ATR apparatus, the Kretschmann (*figure 2.3a*) and Otto (*figure 2.3b*) configurations, we use the more widely used Kretschmann method as the basis of our experimental system. Though the Otto configuration is useful for generating SPP on bulk metal samples, it is not suitable for our application. This is because the SPP excitation efficiency would be low because of the gap between the prism and metal being at least 12μm due to the required thickness of the liquid crystal layer.

There are several variations of the Kretschmann configuration in the literature and the fundamental difference between them is the shape of the high refractive index prism. The original method of Kretschmann used an equilateral prism [21]. This is the most common type of prism for it is widely used in SPP biosensors [180]. An equilateral prism is also used in the related work of J. R. Sambles in investigating liquid crystals with SPP [156, 172, 181]

as well as research into SPP modes interacting with diffraction gratings [40]. Other variations use a hemi-cylindrical [182-184], or a hemi-spherical lens [185, 186] for the prism component, the advantage being that refraction effects do not need to be accounted for when determining the illumination angle [187].

For our experimental apparatus we use an almost hemi-spherical lens as the prism component, made from the high refractive index Schott N-LaSF9 glass, as displayed in *figure 3.1*. The hemisphere is modified so that a flat glass disc can be used as the sample substrate, by removing a small amount of material from the flat face. This allows an easier sample fabrication process, as well as the ability to change the sample without requiring a new prism, reducing the cost. The sample is attached to the prism by an n = 1.8900 index matching fluid (Cargille labs, n correct at 5893Å and 25^{o}C), with the metal layer of the sample passing through the focus of the hemisphere.

The experiments in *Chapter 5* require that a laser be used to form an intensity grating on the photoconductive layer. In general, lensing effects occur for a laser passing through a curved surface. This could lead to unwanted complications with the grating formation. Therefore, the prism is further modified by the addition of a flat located at the apex of the hemisphere that acts as a window for the photorefractive writing beams.

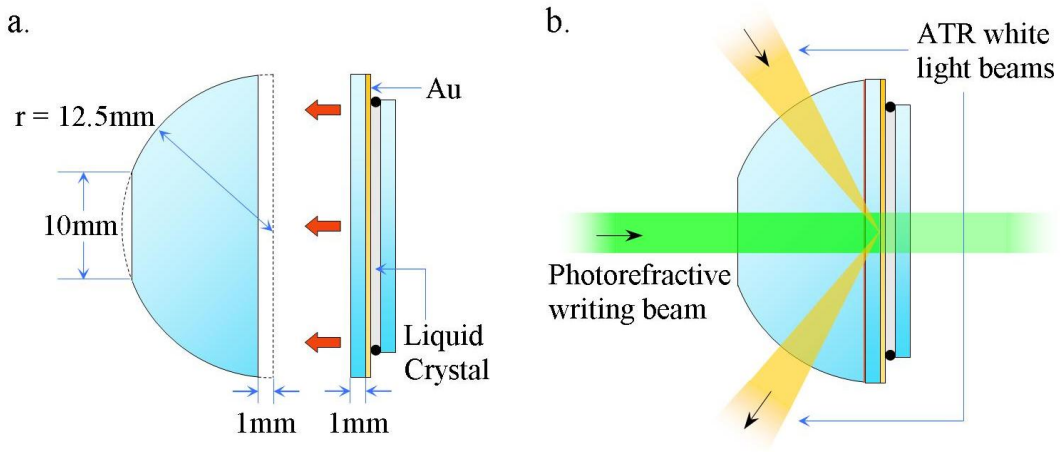

Figure 3.1: a) The design of the modified hemispherical prism used in our apparatus. An index matching fluid attaches the sample to the prism, to minimise internal reflections from the connection. b) Demonstration of the optics of the lens during operation. The ATR white light beams are able to focus onto the metal (yellow) layer of the sample without refraction. The photorefractive writing beams pass through the additional flat surface without lensing effects.

We generate SPP in our experimental system, shown in *figure 3.2*, using an incoherent Tungsten Halogen white light source that is collimated and then focused onto the sample, instead of using a laser. The use of a focused white light source allows light with a range of input wavevectors to excite SPP at various energies simultaneously. This approach is particularly useful in determining the dispersion relation of the SPP modes in our samples;

however, the use of an incoherent white light source limits the angular resolution of the ATR spectrum, as the detection fiber requires a core greater than 100μm to achieve sufficient signal.

The incoherent white light source is focussed through the curved surface of the hemispherical lens. No refraction or chromatic effects occur from the high dielectric material of the prism, as the wavefront of the focused white light is normal to the prisms surface at all points. Therefore, the angle of incidence and reflection in our experimental system are the same both inside and outside of the prism. This allows a method to quickly change the range of illumination onto the metal film without having to re-align the optics, and is achieved by mounting the optics onto a rail. The rail is attached at one end to a post and is allowed to rotate freely about a vertical axis passing through the focus position.

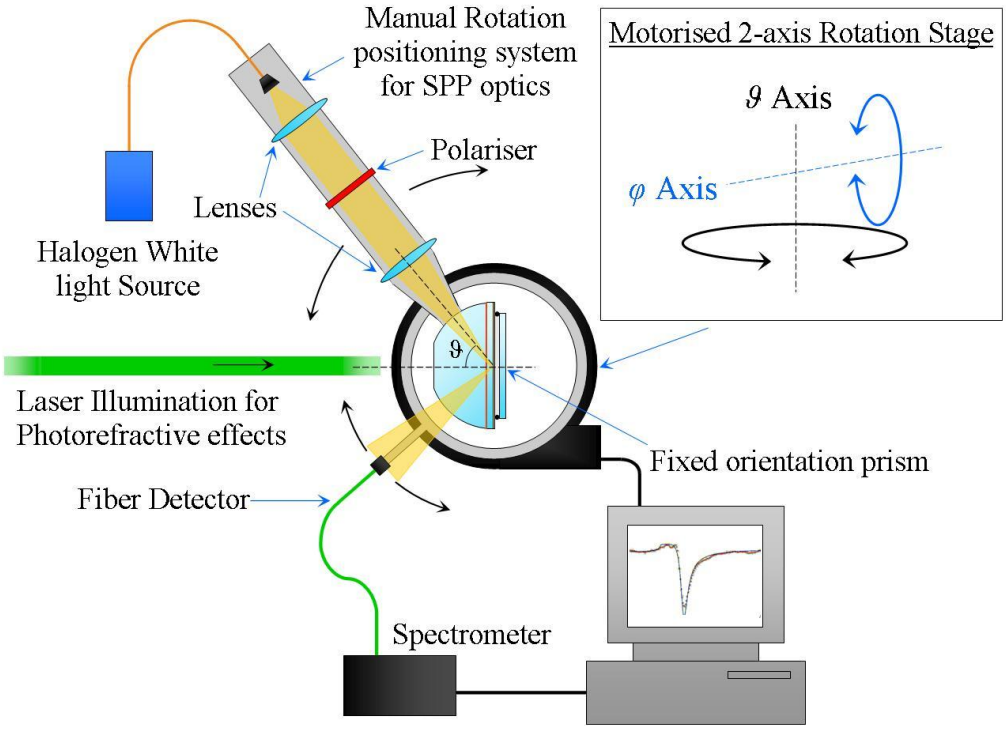

Figure 3.2: Diagram of the experimental system used to excite and analyse the SPP in our samples. The equipment allows manual positioning of the incident white light onto the sample over a 10^{o} range in the region of $\vartheta = 25^{o}$- 80^{o}. The fiber detector is mounted onto a 2-axis rotation rig. The φ axis rotation stage is connected to the ϑ stage, thus the detection can be at any point of a sphere around the sample. A 200μm core fiber is typically required for sufficient signal with an incoherent white light source, resulting in a system resolution of 0.1^{o}.

Excitation of SPP modes is only possible with TM polarised light. Hence, the most efficient SPP generation occurs when the light source is entirely TM polarised. Conversely, there is no SPP in the ATR signal for TE polarised light. Therefore, the TE polarisation reflection spectrum can be used for normalisation in this apparatus. The TE reflection spectrum is ideal for normalisation as the light source is initially unpolarised; hence, statistically the TE and

TM intensities are the same. In addition, the reflection from the sample for TE light is maximised as the incident angle is greater than the TIR angle. Fresnel reflections from the prism are polarisation independent as the incident light is normal to the surface, so normalisation by this method removes this effect on the data. The only source of error with the TE light normalisation method is the small change in the Fresnel reflection between the polarisations from the index fluid layer, which is not accounted for, due to its relative insignificance for the incident angles examined. To allow a quick change between the TM and TE polarisations a broadband polariser is placed into a rotation mount on the optical rail.

For the experiments in *Chapter 5*, the refractive index grating written in the liquid crystal layer is, to first approximation, orthogonal to the SPP propagation direction. Therefore, the signal we wish to detect is not confined to a single plane, with ϑ the only angle required to describe the magnitude of k_{SPP}. The signal needs to be described by a 2D *k*-space, which requires a two-angle measurement method. Thus, the detection fiber is mounted onto a 2-axis rotation stage. The detection fiber's position is therefore described by the angles ϑ and φ, and these are completely analogous to the longitudinal (ϑ) and latitude (φ) co-ordinate system. The *x* and *y* components of the *k*-space are therefore determined by the conversion equations,

$$k_x = k_0 \sin(\vartheta)\cos(\varphi), \tag{3.1}$$

$$k_y = k_0 \sin(\varphi), \tag{3.2}$$

with k_0 the wavevector of the light in vacuum. The normal to the metal film is 0^o on the ϑ axis. The φ axis has 0^o at the 'equatorial' point of this detection sphere; hence, when $\varphi = 0^o$, k_x is described only by ϑ. Mounting the fiber on this 2-axis stage results in the fiber always facing the focus at a constant distance and direction. The coupling efficiencies into the fiber are therefore relatively constant regardless of the detection angle. Any small change in the detection efficiency is removed by normalisation, as the detection is insensitive to polarisation with the fibers used.

Our apparatus determines the reflectivity of the sample at a single angle by acquiring a spectrum from a fiber optic USB spectrometer, providing chromatic information about the reflection. A custom LABVIEW program has been created that automates the data collection over the illuminated range by acquiring a spectrum at each point during the motion of the rotation stages. The raw data is then processed using MATLAB software.

To generate an ATR spectrum like the theoretical example in *figure 2.4*, which allows us to characterise the SPP modes in the sample, we acquire the reflection spectrums with a scan of ϑ and constant φ, generally this is at $\varphi = 0^o$. The annotations in *figure 2.4* and explanation in *section 2.1.2* provide details on how information about the SPP modes is obtained from the ATR spectrum. For the experiments investigating the SPP interacting with a refractive index grating, the white light exciting the SPP is limited to $k_y = 0$ by the use of a slit mounted onto

the optical rail. The two-axis rotation stage is then used to find the diffracted signal by rotating both the ϑ and φ axis.

The angular resolution of this apparatus is determined by the half-width of the core of the detection fiber and its distance from the ATR white light focus. The resolution for various fibers is provided in *Appendix A*.

3.2 Techniques to Characterise Photorefractive Liquid Crystal cells.

In this section all the characterisation methods that do not involve SPP are described.

3.2.1 Optical Transmission Spectroscopy

At various stages of their manufacture, the liquid crystal cell is characterised by its optical transmission with ultraviolet-visible (UV-VIS) spectroscopy. UV-VIS is a non-destructive technique of determining the optical transmission and absorption of a sample at normal incidence, from the near-UV to the NIR region of the electromagnetic spectrum (λ = 190-2500nm). The transmission of light through a multi-layer sample is determined by both the complex refractive index and the thickness of each layer and can be theoretically modelled using the T-matrix method.

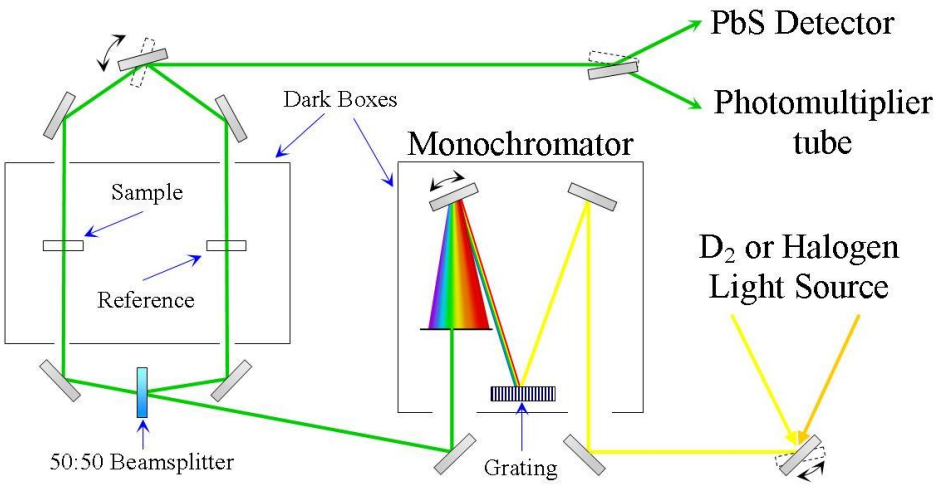

Figure 3.3: The optical layout of the computer controlled Jasco V570 UV-VIS spectrophotometer. Deuterium (D_2) and halogen lamps generate light over the 190-350nm and 330-2500nm ranges. The light from either source is monochromated before being split into sample and reference channels. Detection is by either a photomultiplier tube in the 190-850nm region or a PbS detector up to 2500nm. The signal from the sample channel is normalised by the reference channel signal.

Experimentally the equipment of *figure 3.3* determines the transmission spectrum of a sample compared to a reference. In general, the reference channel is left empty so that the signal represents the absolute and not a relative transmitted intensity. In the acquired transmission

spectrum two distinct types of feature are often present; absorption peaks and interference fringes.

The main use of UV-VIS spectroscopy is to determine the wavelength and magnitude of the absorption in a sample. This is particularly helpful in chemical analysis as it allows the concentration of a solution to be determined compared to a reference solution, using the Beer-Lambert law [188], though care must be taken to ensure the solution is not highly scattering, as scattered light reads falsely as absorption. For our samples, we use UV-VIS spectroscopy to keep the concentration of sensitizers added to the photoconductor during fabrication consistent between different batches. The method also identifies the wavelengths absorbed by the sensitizer, an important detail in designing the sample. In addition, this technique allows us to determine the thickness of the layers of the sample, with particular interest in the thin metal film. The magnitude of the transmission through the highly reflective metal film is inversely proportional to the thickness of the film. Therefore, by comparison to the theoretical transmission predicted by a T-matrix code, an estimate for the thickness of the metal can be acquired. The accuracy of this method is to within a few nanometres of the thickness determined by the more accurate method of ellipsometry.

Interference fringes in the transmission spectrum arise from interference between the Fresnel reflections at each interface of a multilayer structure with the initial beam. The magnitude of the fringes is dependent on the magnitude of the Fresnel reflection. However, provided the refractive index of the layers is known over the spectral range examined, the thickness of the layer generating the interference fringes can be calculated from the fringe spacing. Unfortunately, this technique can only determine the thickness of layers over 250nm thick; otherwise, there are insufficient fringes over the spectral range. Therefore, this is used almost exclusively to determine the thickness of the liquid crystal cell cavity during fabrication.

3.2.2 Liquid Crystal Orientation Response to an Electric Field

When light propagates through a birefringent medium, the polarisation components parallel and orthogonal to the optical axis propagate with different phase velocities. Therefore, the phase of one component is delayed by an amount $\Delta\varphi$, relative to the other. This changes the overall polarisation state of light that is transmitted through the medium. For a liquid crystal cell, this modification to the polarisation will change as the optical axis re-orientates to an applied electric field. Analysing the polarisation change will lead to information about the electrical response of the liquid crystal layer.

Experimentally the system of *figure 3.4* is used to determine the polarisation modification from the liquid crystal layer as the voltage is slowly increased from 0 to a value V_{max}. A half-wave plate and polariser are used to ensure the polarisation of the probe laser is at 45^{o} ($\pi/4$) to the optical axis of the liquid crystal when no potential is applied to the cell. This geometry is required so that the in-plane polarisation component $\hat{x}$, probes the ordinary refractive index

n_o, and the out-of-plane component $\hat{y}$, probes the effective refractive index n_{eff}, of the liquid crystal equally. Assuming the transmission of each polarisation is equal after propagating through the liquid crystal cell the electric field of light is described by

$$\underline{E} = \frac{E_0}{\sqrt{2}} \begin{pmatrix} \hat{x} \\ e^{i\Delta\varphi}\hat{y} \end{pmatrix} e^{i(\underline{k}.\underline{z}-\omega t)}, \tag{3.3}$$

with the out-of-plane component experiencing a phase delay. The analyser is then described by the Jones Matrix for a polariser at -45° (-π/4) and the resulting transmitted field is

$$\underline{E} = \frac{E_0}{2\sqrt{2}}\left(1 - e^{i\Delta\varphi}\right)\begin{pmatrix} \hat{x} \\ -\hat{y} \end{pmatrix} e^{i(\underline{k}.\underline{z}-\omega t)}. \tag{3.4}$$

The dot product between this electric field and its complex conjugate allows us to obtain an expression for the ratio of the transmitted intensity I, to the incident intensity I_0,

$$I/I_0 = \sin^2\left(\frac{\Delta\varphi}{2}\right). \tag{3.5}$$

Experimentally, I_0 is determined by the sum of the transmission through crossed and parallel polarisers. Hence, $I / I_0 = I_{crossed} / (I_{crossed}+I_{parallel})$. This is the only accurate method of determining I_0 in our cells due to the low sample dependent transmission through the Au layer. Inaccuracies in the experimental data that arise from drift in the light sources output are also reduced if both analyser orientations are measured before increasing the voltage.

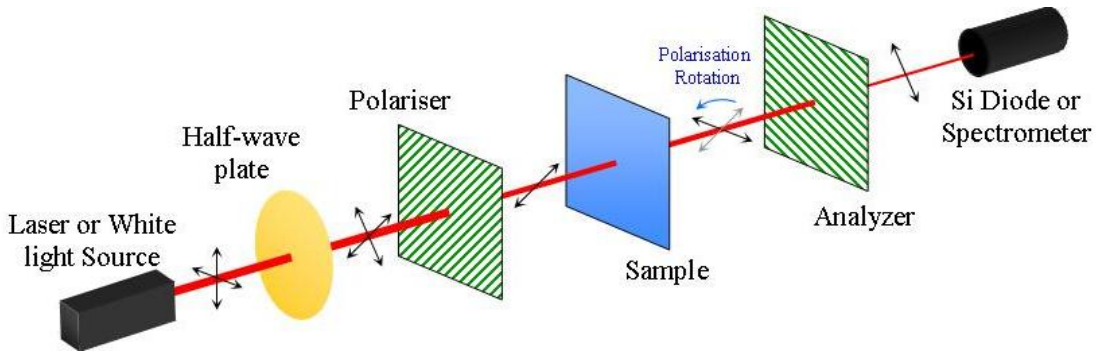

Figure 3.4: The apparatus for the crossed polariser intensity experiment. The polarisation of the light transmitted through the sample at normal incidence is determined by an analyser (a second polariser with a transmission axis orthogonal to the first) and a photo-detector. The measured signal is dependent on the additional phase shift of one of the polarisation components, resulting in an overall polarisation modification. A variation in the transmitted light intensity is seen when an electric potential (either DC or a 1 kHz AC) is applied to the cell, a result of the re-orientation of the liquid crystal molecules.

By using *equation 3.5*, the retardation of the liquid crystal layer can be determined. The calculated retardation is accurate assuming there are no interference effects from internal reflections within the cell. In practice, the liquid crystal cell cavity will produce interference fringes, though these have only a small effect, ~5%, and are removed by determining I_0 with the transmission through parallel and crossed polarisers.

The magnitude of the retardation is dependent on the orientation of the liquid crystals optical axis. In general, for a liquid crystal cell this results in the value of n_{eff} being dependent on the distance into the cell. However, for light propagating a small distance dz into the cell, the phase delay between polarisations is,

$$d\Delta\varphi = \frac{2\pi}{\lambda}\left(n_{eff} - n_o\right)dz. \tag{3.6}$$

The total phase delay is therefore the integral over the length of the cell. By using the theoretical model we have developed for the electrical response of the liquid crystal, this integral can be evaluated to predict the retardation of the layer. An algorithm developed by Dr. Keith Daly can fit the retardation to the 1kHz AC experimental results using the refractive index and elastic constants as the only fitting parameters; therefore, validating the liquid crystal model and allowing us to determine the refractive index of the liquid crystal and its alignment throughout the cell [189].

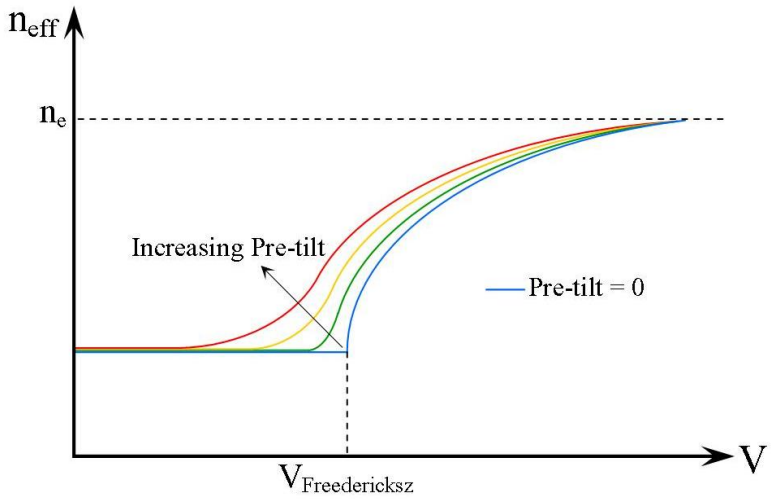

Figure 3.5: A demonstration of the sharp change in n_{eff} for a liquid crystal cell as a function of voltage. With zero pre-tilt this change is quite sharp, the Freedericksz transition for this cell. For an increasing pre-tilt of the liquid crystal the transition point becomes less obvious, however for small pre-tilts this is still often referred to as the Freedericksz transition even though this is not strictly true.

For a liquid crystal cell when no potential is applied, the alignment is determined by the surfaces adjacent to the liquid crystal. Applying a voltage to the cell only re-orientates the liquid crystal molecules when the electrostatic force is greater than the elastic alignment

forces. Until this point, the retardation of the layer is constant. If there is zero pre-tilt in the cell this transition point is a sharp change and represents the Freedericksz transition. However, if a small pre-tilt is present in the alignment this transition will not be as sharp, see *figure 3.5*. An increase in the magnitude of the potential above this threshold results in oscillations in the transmitted crossed polariser signal. The number of oscillations is dependent on the magnitude of the birefringence of the liquid crystal, the cell thickness and the wavelength of the probing light. Eventually, the transmitted signal will reach an asymptote at zero when all the molecules are aligned with the applied potential and $n_o = n_{eff}$.

3.2.3 Ellipsometry

The photorefractive properties and interaction of the SPP with the liquid crystal depend on the thickness of the photoconducting layer. Thus, accurately determining the polymer's thickness, which is designed to be less than 150nm, is vital in the characterisation of our samples. As the thin polymer film is smaller than the wavelength of visible light the most accurate non-contact method of ascertaining the layer's thickness is with spectroscopic reflective ellipsometry. This is an optical technique that determines the phase and intensity change of TM and TE polarised light upon reflection from a sample.

The configuration of the apparatus for the spectroscopic (multiple wavelength) rotating analyser ellipsometer utilized is detailed in *figure 3.6*. The non-normal incident light has a known input polarisation, as determined by the initial polariser, which is linear and contains both TM and TE components. After reflection from the sample the TM and TE polarisations experience different phase and amplitude changes according the respective *Fresnel* reflection co-efficients for each polarisation from the sample [30]. Therefore, the reflected beam's polarisation is, in general, elliptical. A continuously rotating polariser (referred to as the analyser) and the transmitted beam intensity acquired by the CCD detector then determines the exact polarisation of the reflected beam. This is then compared to the initial polarisation state to determine the polarisation change [190].

The measured value is known as the complex reflectance ratio ρ, and can be mathematically expressed as either the ratio of the TM and TE Fresnel reflection co-efficients, r_{TM} and r_{TE}, or by the variables Ψ and Δ

$$\rho = \frac{r_{TM}}{r_{TE}} = \tan(\Psi)e^{i\Delta} . \tag{3.7}$$

Thus, $\tan(\Psi)$ is the ratio of amplitudes and Δ is the phase shift between the polarisation states, which determine the form of the elliptical polarisation measured. As the measurement is a ratio and not an absolute, ellipsometry requires no reference beam or standard sample thus is reproducible and is only weakly affected, i.e. a small amount of noise, by fluctuations in the beam intensity [191].

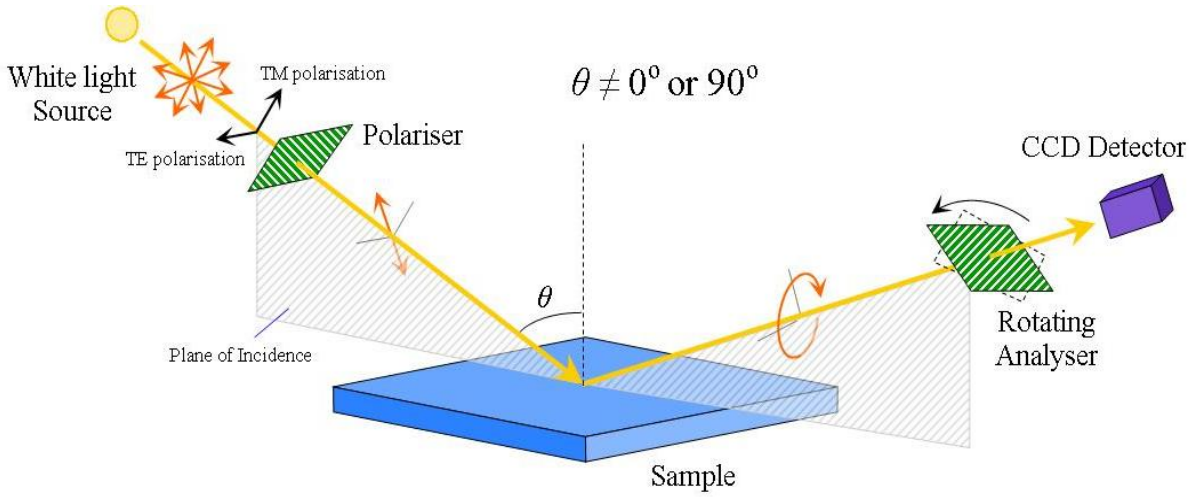

Figure 3.6: The experimental equipment for spectroscopic ellipsometry. Using a white light source improves the accuracy of the thickness measurement as it provides multiple fitting points, at the expense of improved accuracy in the polarisation change that is possible with a monochromatic laser. The incident angle θ should be larger than the TIR angle of the samples substrate to increase the reflected signal intensity.

Unfortunately, with a single measurement, the thickness and complex refractive index parameters of each layer of the sample are difficult to separately extract from Ψ and Δ. The ellipsometer used therefore takes measurements at multiple wavelengths and various angles of incidence, ϑ. However as a measurement of phase is cyclic, there exists the possibility of multiple incorrect values for the optical parameters. Hence, the optical characteristics of each layer are determined by the comparison of a model of the sample to the experimental data [190]. The model is a T-matrix representation of the multi-layer structure of the sample and is used to calculate the theoretical Fresnel reflection co-efficients. Any unknown values for the thickness and complex refractive index are left as fitting parameters. The software provided with the ellipsometer uses an iterative mean-square error method to generate a best fit for the unknown values using a user-defined model, initial values and constraints. Provided the number of unknown parameters is minimized, preferably 1 per data acquisition, and an appropriate model of the sample is used, i.e. good initial values for the properties of the other layers, this fitting method yields highly accurate results.

This technique was also used to extract the complex refractive index of the materials used in our samples in the UV to the NIR part of the spectrum. The methodology and results obtained by this are explained in *Appendix B*. For a more detailed explanation on the physics and applications of ellipsometry the reader is directed to two publications [190, 191] that provide an overview on all aspects of this technique.

3.2.4 Electrical Impedance Measurements

The alignment of a liquid crystal layer is determined by the electric field applied across it. However, our samples are multi-layered, so we need to characterise the electrical response of the cells structure and its composite materials to understand how a potential applied to the whole cell determines the liquid crystal alignment.

If characterisation is attempted using only a DC potential, it is hard to determine anything other than the overall resistance of the cell. Each layer of the sample is in series so their individual electronic properties cannot be isolated, a result of their only being a single data point and multiple variables. The same limitation applies to any capacitive behaviour from the thin layers. This problem is avoided with an AC potential, as the electrical response is complex and frequency dependent. The complex response of a material to an AC potential is known as the electrical impedance Z and is the total opposition of a material or device to an alternating current [192]. The impedance describes how both the magnitude and phase change, thus providing twice the information than that available with a DC potential. Furthermore, the frequency dependence of the impedance allows a large data set to be collected, with sufficient information to determine the response of individual layers of the sample.

There are many methods of measuring impedance such as the I-V method [193], the resonant method [194], the network analysis method [195] and the auto-bridge balancing method [193] to name a few. Each has their own advantages and disadvantage, the method chosen depends on the impedance measurement requirements. For our measurements, we use the auto-bridge balancing method with a Solartron 1260 Impedance/Gain - phase analyser. This method has the smallest measurement error and can determine the Impedance to an accuracy of 0.1%. However, it is limited to operating below 110MHz.

To measure our samples impedance the generator output is connected to the sample and voltage detection channel V_1. The opposing side of the cell is then connected to a voltage channel V_2 that determines the voltage required to maintain a zero potential across the cell through a known resistor, R (internal to analyser). The impedance is determined by the value of V_1R/V_2. It is necessary to connect the sample to a current pre-amplifier prior to the V_2 detection channel, as the real component of the impedance for our cells, is large ($>10M\Omega$ for $<100Hz$). The specifications for this impedance analyser are found in *Appendix A*.

When analysing the electrical impedance of a material or device it is useful to compare the response to that of ideal resistors, capacitors and inductors, the passive elements of basic electronics. The impedance of an ideal resistor is purely real where ideal capacitors and inductors have purely imaginary impedance. However, the impedance of a component is never entirely real or entirely imaginary. Capacitors will have finite resistance, resistors an inductance, inductors a capacitance, etc. This is known as parasitics, unwanted electrical properties in a component that are generally attributed to another type of component [193].

Thus, electrical impedance measurements are compared to equivalent circuits. The circuits are an arrangement of the basic electronic elements in series and parallel whose combined behaviour mimics that of the measured component or device.

Impedance measurements become truly useful when an equivalent circuit model is fitted to the acquired impedance data. A good model approximation allows us to dissect the electronic properties of the cell and attribute them to each layer, without difficult invasive measurements. In particular, it will allow us to determine the magnitude of the predicted resistive change of the photoconductor with varying levels of illumination.

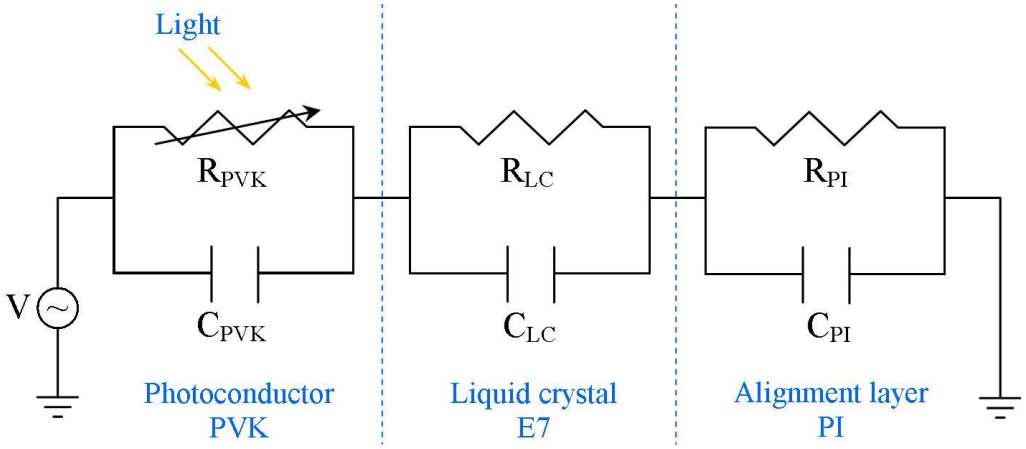

Figure 3.7: The equivalent circuit approximation for the photorefractive liquid crystal cells. The layers that determine the cells operation are modelled as a parallel resistor-capacitor circuit to explain the frequency behaviour. The resistance of the photoconductive layer is modelled to have a light dependent resistance.

The equivalent circuit model that is used to describe the general electrical behaviour of the cells is demonstrated in *figure 3.7*. In this model, the conductive Au and ITO layers are ignored as their resistance is significantly lower that the expected resistance for the polymers. The electrical behaviour is therefore determined by the PVK, PI and liquid crystal layers. These are each modelled as a parallel RC circuit in series with each other. The resistance of the PI and liquid crystal is assumed constant; however, the PVK's resistance is modelled as a variable resistor dependent on the light intensity. The capacitive effects arise from the physical dimensions of the layers and are significant due to the sub-micron thickness of the PVK and PI; these should not change with illumination of the cell.

With this model the impedance at DC and low frequencies is dominated by the resistive behaviour of the layers. Therefore, when the cell is illuminated the potential drop across the liquid crystal should change and photorefractive effects observed. At higher frequencies (>100Hz) the impedance is determined by the capacitive behaviour of the layers. By simply considering the designed thickness of each layer, a fast (≥0.5kHz) AC potential should be dropped almost entirely over the liquid crystal; hence, no photorefractive effects are expected to be observed. This frequency dependence on photorefractivity is consistent with the

behaviour observed in the literature [15, 148, 196]. A more detailed description of this model is presented in *Chapter 4* along with experimentally determined values for each component in a typical cell.

The frequency dependent impedance of our cells is determined over the range of 10^{-1} to 10^{3} Hz with an applied potential of $0.5V_{rms}$. The potential is limited to $0.5V_{rms}$, as the response of the liquid crystal layer is non-linear with voltage and frequency due to molecular re-orientation when the potential is above the Freedericksz transition. A $0.5V_{rms}$ potential is below the transition for all frequencies. Accurate impedance measurements require that the current response of a device scales linearly with the applied potential i.e. Ohmic. Therefore, the complete electrical behaviour of the cells under all conditions is not determined.

3.2.5 Two beam Gain Analysis of the Bulk Liquid Crystal Photorefractivity

The photorefractive properties from the bulk liquid crystal alignment of our cells are determined quantitatively by the energy transfer between two interfering coherent beams. The physics of this process are discussed in *sections 2.2.1* and *2.3*.2. Experimentally, a laser is split into two coherent beams that are crossed at an angle α. The crossed beams form an intensity grating due to interference. The pitch of this grating Λ, is determined by the relation

$$\Lambda = \frac{\lambda}{2\,sin(\alpha/2)}, \tag{3.8}$$

where λ is the wavelength of the laser, $\alpha/2$ also defines the bisector of the two crossed beams.

The crossing point of these beams is arranged so that it is located on the photoconductive layer of the sample. The optical arrangement that creates two equal intensity beams[VI] and allows easy changing of the angle α is demonstrated in *figure 3.8*.

The sample is also rotated to an angle β, so that the bisector of the beams is at non-normal incidence as a symmetry breaking mechanism [152]. Measurable photorefractive energy transfer between the beams requires symmetry breaking because without it there is no way to distinguish which beam is the probe or the pump. Physically, this can be understood as each beam transferring equal amounts of energy into the other, so that no net effect is observed. However, as *figure 3.9* displays, when the bisector is at non-normal incidence, an asymmetry appears in the magnitude of the refractive index modulation, $\Delta n_{grating} = n_{light} - n_{dark}$ seen by each beam. The magnitude of the energy transfer is dependent on the magnitude of $\Delta n_{grating}$ as *equations 2.21 and 2.23* detail. Therefore, more energy is transferred by one beam than by the other and a net gain is observed.

[VI] The value of the gain is distorted by *equation 3.9* if the beams are not of equal strength. Hence, it is conventional to have the beams of equal strength if a reliable comparison of the photorefractive strength is made.

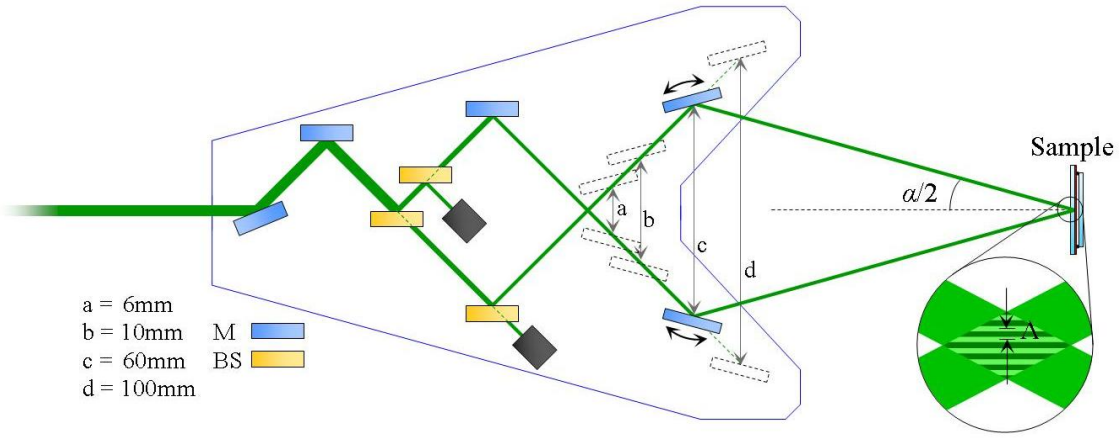

Figure 3.8: The optical apparatus to generate two coherent equal intensity beams. Multiple identical beam splitters are used so that both beams are reflected and transmitted, to ensure the final beam intensity is the same. The final pair of mirrors can rotate and be placed at varying separation distances (a, b, c or d) to allow quick, repeatable and accurate control of α and the grating pitch. These optics are mounted onto a single plate to be able to rotate about the bisector so that the grating can be orientated at any angle relative to the liquid crystal rubbing direction. M = Mirror, BS = Beam splitter. This arrangement can generate intensity gratings with a pitch of $\Lambda = 0.5\mu m$ to $60\mu m$.

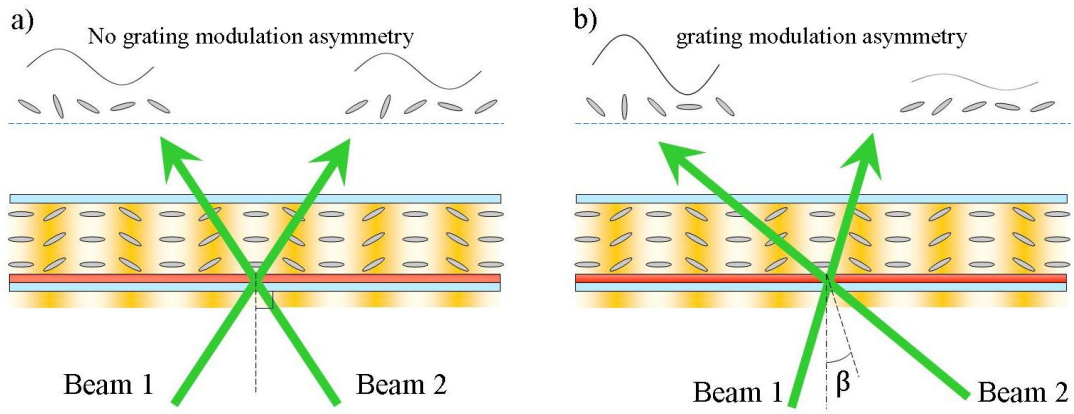

Figure 3.9: The liquid crystal alignment and refractive index modulation seen by each beam.
a) When the bisector is normal to the cell, each beam sees a refractive index grating with the same intensity modulation, as liquid crystal molecules orientated at an angle +ϑ have the same refractive index as those at -ϑ. b) Rotating the cell (non-zero β angle), results in an asymmetry in the refractive index modulation seen by each beam. As the energy transfer is dependent on the magnitude of the grating modulation this leads to unequal energy transfer and one beam experiencing gain.

This asymmetry becomes larger with increasing β, however there is a peak in the detected gain when $\beta \approx 25^{o}$ [152]. The limiting factor is the mismatch that arises between the wavevector of the grating written into the liquid crystal layer and the intensity grating of the crossed beams, when $\beta \neq 0$. Unlike other photorefractive materials, the grating wavevector in a hybrid liquid crystal cell is determined by the intensity grating projected onto the photoconductive layer, thus the resulting grating is parallel to the photoconductor's surface

and not orthogonal to the beam's bisector. A detailed explanation of this mismatch in wavevector and its effects on the two-beam energy transfer can be found here [110].

Diodes are then used to determine the intensity of each of the grating writing beams, *figure 3.10*. These beams are distinguished as probe and pump beams depending on which experiences a net energy gain and a net loss (The probe experiences a net gain in the presence of the pump). The exponential gain co-efficient Γ, is then determined with the equation,

$$\Gamma = \frac{1}{L} ln\left(\frac{gm}{m-g+1}\right) \tag{3.9}$$

where the beam coupling ratio $g = I_{probe\ +\ pump}/I_{probe}$, m is the initial beam intensity ratio ($m = I_{probe}/I_{pump} \approx 1$) and L is the optical path length through the liquid crystal layer of the cell [17]. Absorption within the liquid crystal is neglected. For gratings in the Raman-Nath regime, additional diffracted orders are also observed [16]. Diodes are also used to determine the energy transfer to these higher orders. Diffraction into higher orders does not require $\beta \neq 0$ and provides a quick method of determining if photorefractive effects and a grating are present within the sample.

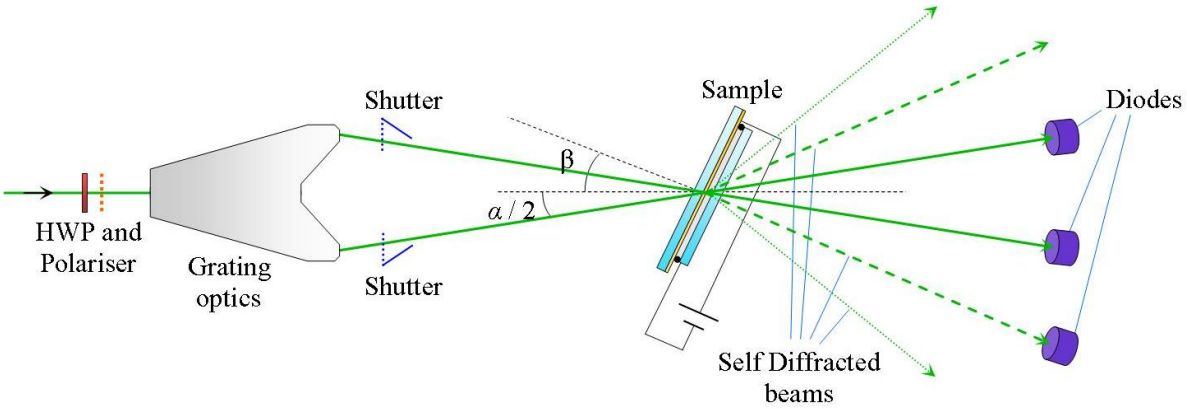

Figure 3.10: Apparatus to determine the photorefractive two-beam gain of a sample. A HWP and polariser are used as a power control device. Shutters in both beams allow singular measurements of the intensity of each beam without the others influence. The sample is rotated by an angle β, to break the symmetry of the system. The beam intensities measured by the diodes determine the gain of the sample.

3.3 Fabrication Methods.

In this sub-section details are presented on the fabrication techniques required to manufacture the samples used in this investigation. The processes to fabricate the sample structure displayed in *figure 3.11*, in order are

1. Evaporate a 1-2nm Cr layer and a 40nm Au layer onto the high refractive index glass substrate.
    - Measure Au thickness with UV-VIS.
2. Spin coat a PVK:C_{60} polymer layer onto the Au surface.
    - Measure PVK thickness with UV-VIS or Ellipsometry.
3. Spin coat a PI alignment layer onto an ITO coated glass plate.
4. Rub the PVK and PI surfaces of the substrate and top plate.
5. Glue the top plate to the substrate with 12µm spacers. Ensure the rubbing directions of the PVK and PI are orthogonal. Cure the glue with UV light.
    - Determine Cavity thickness with UV-VIS
6. Attach electrical contacts to the cell.
7. Fill the cavity with liquid crystals under vacuum.
8. Seal the edges of the cell with an epoxy.
    - Check crossed polariser operation of cell.

All the steps required were conducted on site at the University of Southampton in the either the Rapid Prototyping clean room facility or the fabrication lab of Prof. Kaczmarek. The following sections provide details on the techniques that result in an increased yield of operational devices.

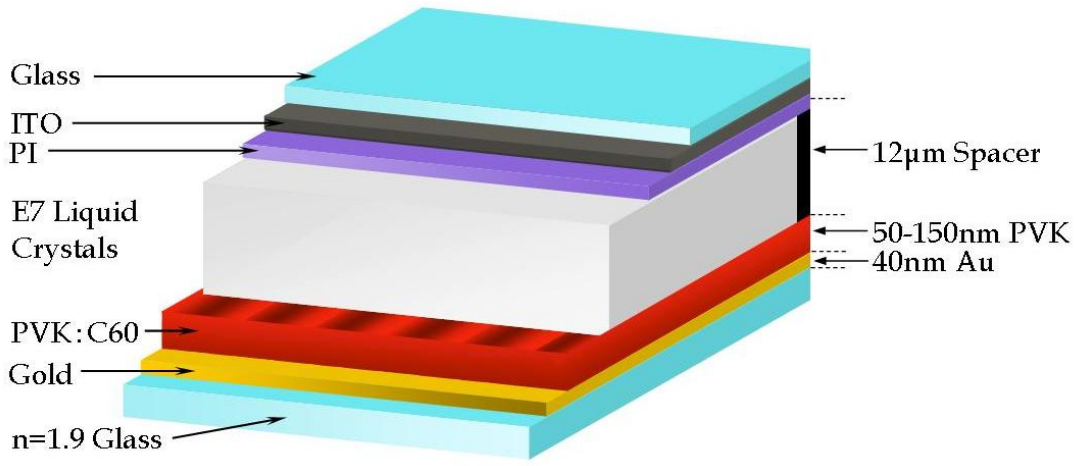

Figure 3.11: The multi-layer structure of the hybrid photorefractive liquid crystal cell for use of controlling SPP. The SPP modes propagate in the Au / PVK interface plane. The electric field of the SPP can probe the orientation of the liquid crystal molecules.

3.3.1 Thermal Deposition of a Thin Metal Film

The first layer (referring to *figure 3.11*) fabricated in our samples is the thin metal layer deposited onto the high refractive glass substrate as required for generating SPP modes by the Kretschmann method. This layer is fabricated by thermal evaporation, a physical vapour deposition (PVD) method that deposits metal layers onto a substrate by exposure to a jet of particles. Under vacuum conditions a bulk sample of the coating material is heated to several hundred or thousands of degrees by a high current power supply. The Ohmic heating of the bulk material results in the creation of a vapour cloud as the metal evaporates. These hot particles propagate away from the bulk sample in a straight trajectory and collide with the encapsulating environment [197].

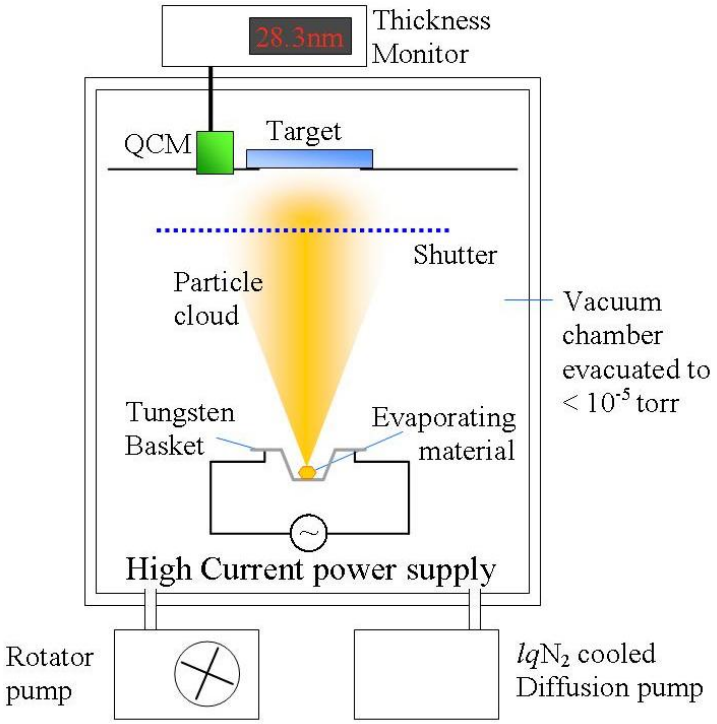

Figure 3.12: A Thermal evaporation chamber. The evaporating material is placed into a Tungsten basket, as the melting point is higher than the evaporating material. The particle cloud then coats the target with a thin solid layer. The thickness of this layer is determined by a QCM. An optional shutter can be used to control exposure of the target to the particle cloud. The two pumps generate the vacuum required for good deposition.

Deposition occurs when the collisions with a surface cools the particles sufficiently for them to sublimate into a solid coating. The vacuum is required not only to increase the diffusion length of the vapour particles, but also to maintain a sufficiently high chemical purity of the deposited layer. As hot metal particles are highly reactive with any oxygen present in the deposition chamber and the optical properties of a metal oxide are not adequate for our application. Typical pressures in the chamber are less than 10^{-5} Torr ($<1.3\times10^{-3}$Pa).

Silver (Ag) is the best metal to use for SPP in the visible and NIR spectrum; however, Ag is reactive with a room temperature oxygen environment, tarnishing the metal [198]. The oxidisation of the layer becomes total during subsequent fabrication steps, thus removing all metallic optical properties of the layer rendering the sample useless. Therefore, an almost inert Gold (Au) layer is used instead. The optical properties of Au are ideal for supporting SPP modes from the red to NIR part of the spectrum. However, adhesion of Au to a glass substrate is poor so an ultrathin (1-2nm) Chromium (Cr) layer is first deposited to allow Au to adhere to the substrate. The use of an ultrathin Cr layer does not significantly alter the optical reflection/transmission hence can be effectively ignored during sample characterisation. The thermal evaporator used allows multiple metals to be subsequently evaporated while under vacuum, removing any unwanted exposure of the Cr adhesion layer to O_2.

The rate of deposition is controlled by the magnitude of the heating current supplied to the bulk metal source. The deposition rate determines the morphology of the metal film and influences its surface roughness [199]. A deposition rate of 0.3-0.5nm per second is found to generate a good smooth film. Contaminants on the coated surface also reduce the film quality; therefore, prior to evaporation the substrate is sonicated with Acetone and Isopropyl-alcohol (IPA) to remove any dust and grease.

The in-situ thickness of the deposited layers is determined by a quartz crystal microbalance (QCM) that is also exposed to the evaporating metal. The frequency change of the crystal oscillator [200] when a mass is deposited onto it allows the thickness monitor to display the thickness of the deposited layer to an accuracy of 0.1nm. The optimum thickness for SPP modes is 40nm for an Au layer. A sample is rejected if the Au layer is <35nm or >45nm.

The coating of a metal film by thermal evaporation is directional; thus there is a geometrical factor in the coating thickness within the chamber. This limits the size of the target that can be coated while maintaining a reasonable average thickness. The variation over a 28mm diameter N-LaSF9 substrate (typical dimensions of our samples) is <2nm so the layer is considered to be uniform across the sample. For accurate in-situ thickness readings the QCM must be placed as close as possible to the target or a conversion tooling factor be introduced into the thickness calculations. The Au thickness of all samples is then determined after evaporation by UV-VIS transmission as a final check.

3.3.2 Spin Coating Deposition of Polymers

To generate photorefractive-like effects in our liquid crystal cells a thin photoconductive PVK layer is deposited onto the Au surface of the sample. This is most easily achieved by spin coating. First the polymer is dissolved into a solution or suspension. This is then applied to the entire surface to be coated before causing the sample to rotate (spin) normal to the surface at very high speeds. The centrifugal force causes the solution to coat the entire surface with a thin layer of the solution (*figure 3.13a-c*). Eventually the solvent the polymer is

dissolved in evaporates (*figure 3.13d*) leaving behind a thin polymer layer. The long molecular chains of polymers result in sufficient overlap and interaction between molecules for the layer to be a uniform amorphous material with minimal voids even when the solution concentration is low [201].

The thickness of the spin-coated layer is determined by several factors, most notably the spin speed, spin time, solution viscosity and solvent evaporation rate [202, 203]. The viscosity and volatility of the solution are inherent to the chemicals used and their concentrations, leaving the spin speed and time as variables. During fabrication tests we found that using a long spin time (~2min), gives the best repeatability of the coating thickness. As maximum flow and evaporation has occurred. Therefore, the thickness is controlled to within a few nm by the maximum spin speed alone. The thickness dependence on spin speed for the polymer solution used was determined prior to sample fabrication; the results are shown in *figure 3.13e*. The theoretical fit is proportional to $\omega^{-0.5}$, indicating the solvent evaporation rate is dependent on the spin speed for this polymer solution [204].

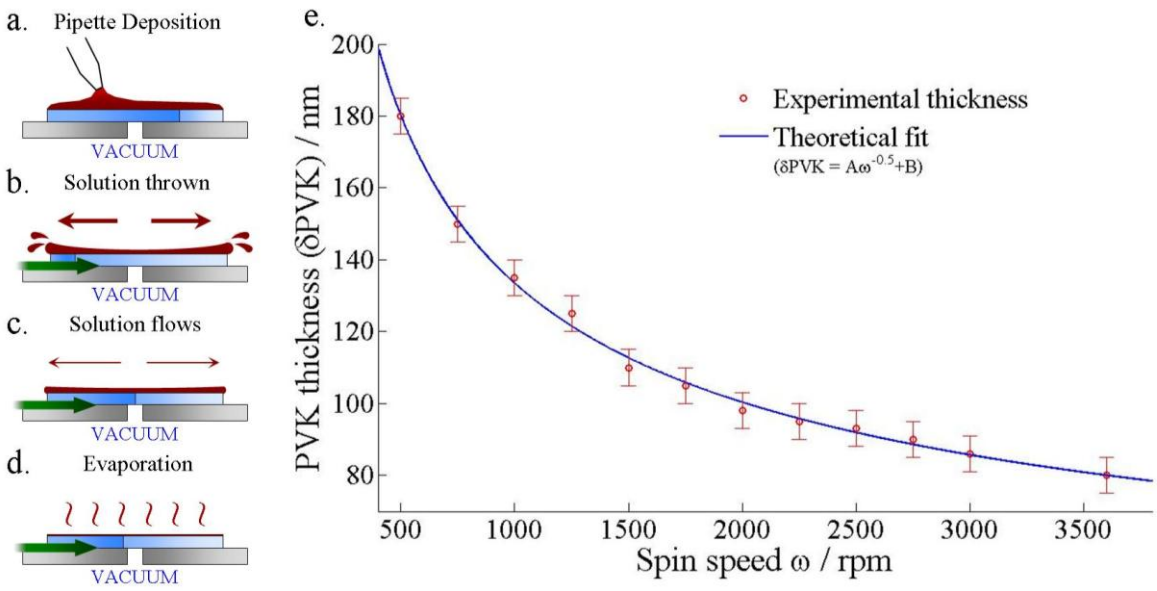

Figure 3.13: The process of spin casting. a) An abundance of the dissolved polymer solution is deposited by a pipette onto the substrate, affixed by a vacuum. b) The substrate is then made to rotate; this immediately throws off most of the solution. c) As the substrate continues to spin the solution flows outwards and the layer becomes shallower. d) The solvent then evaporates, leaving behind the thin polymer film. e) The thickness as determined by ellipsometry, of a 3:1 filtered PVK:C_{60} polymer layer dissolved in CB deposited by spin coating as a function of the spin speed. This chart allows a quick method of finding the appropriate spin speed to fabricate a PVK layer at the designed thickness. Theoretical fit A=3571, B=20.5.

Controlling the spin speed and time does not ensure that a uniform film will be created. It is vital that the substrate be clean and free of scratches, also the solution cannot contain any particles (>1-10μm). If this is not the case 'comet-like' structures are formed in the polymer coating from points where the solution flow is disrupted by an uneven surface. The film

behind the 'comets' is thin and uneven, potentially resulting in electrical shorts in the cell [201] and disrupting the local liquid crystal alignment. Other defects with less obvious causes are also possible such as swirls [205] that make the film a non-uniform thickness and appear as a spiral. This arises from an inappropriate ramp (acceleration) rate. Also possible are chuck marks [206], variations in the spatial thickness that form an image of the spin chuck in contact with the bottom of the substrate. The cause of the spatial thickness variations is the rate of evaporation of the solvent being influenced by thermal conduction through the spin chuck. These can be removed by ensuring good airflow over the sample, thus minimising the effect that substrate temperature has on the evaporation rate.

The actual solution spin coated onto the Au layer is not a pure PVK-solvent mixture. To sensitise the PVK's photoconductive properties to visible (instead of UV) light a C_{60} dopant mixture is added. The dissolved ratios are 20g/l PVK into a Chlorobenzene (CB) solvent, 7g/l C_{60} into CB, 3:1 mixing ratio between the PVK:CB and C_{60}:CB solutions. This final mixed solution is then passed through a 1µm filter to remove any undissolved particulates, of which there are few. UV-VIS spectroscopy shows no noticeable change to the solutions absorbance pre and post filtering. Hence, it is estimated that by weight our films are ~10% C_{60} assuming all the CB evaporates during the spin coating process. The spin recipe used for our samples is listed in *table 3.1*. After spin coating the polymer onto the sample, it is necessary to heat the sample to 240^{o}C for at least 1 hour. This heating anneals the PVK, thus transforming the deposited polymer into a more robust glassy layer, as well as evaporating off any residual CB.

At the same time as the PVK is deposited onto the Au layer, the top plate of the liquid crystal cell is also fabricated. This is achieved by spin coating a 10% weight polyimide (PI):CB solution onto an ITO coated glass plate (purchased from Sigma-Aldrich). This plate is also heated to 240^{o}C for 1 hour to anneal the PI.

	PVK:C60 Solution	PI Solution
Spin Speed lv.1	500rpm	1500rpm
Spin Time lv.1	5s	3s
Spin Speed lv.2	Various (1000-3500rpm)	4000rpm
Spin Time lv.2	120s	90s

Table 3.1: The spin coating recipes; listed as levels used to coat the samples. All ramp (acceleration) times are 1s.

3.3.3 Control of a Liquid Crystals Director through Surface Treatment

For our cells to operate as designed we require the liquid crystal molecules to be aligned parallel to the PVK and PI surfaces (planar alignment) when no potential is applied. The alignment must be uniform across the entire surface of the polymer. This is achieved by treating the surface of the alignment layer to impose an asymmetry in the macroscopic

topographical or microscopic molecular strength of the polymer [207]. There are several methods to do this; using lithographically micro-patterned polymers [208], nanopatterned surfaces using an atomic force microscope (AFM) [209], ion-beam etching [210] or simply mechanically rubbing the surface [211].

To enforce the desired alignment of the liquid crystals in our cells we mechanically rub the polymer surface with a velour cloth in a single straight direction. This method has been perfected by the LCD industry; however, we use a custom built machine that produces good liquid crystal alignment (*figure 3.14a*). The rubbing fibers of the cloth cause pulling forces that stretch the polymer chains inducing a macroscopic, statistically significant chemical bond asymmetry at the surface [212]. This bond asymmetry is significant enough to uniformly align the liquid crystal molecules to the rubbing direction of the polymer surface. For PI the in-plane alignment is parallel to the rubbing direction; however the in-plane liquid crystal alignment at the PVK surface is orthogonal to the rubbing.

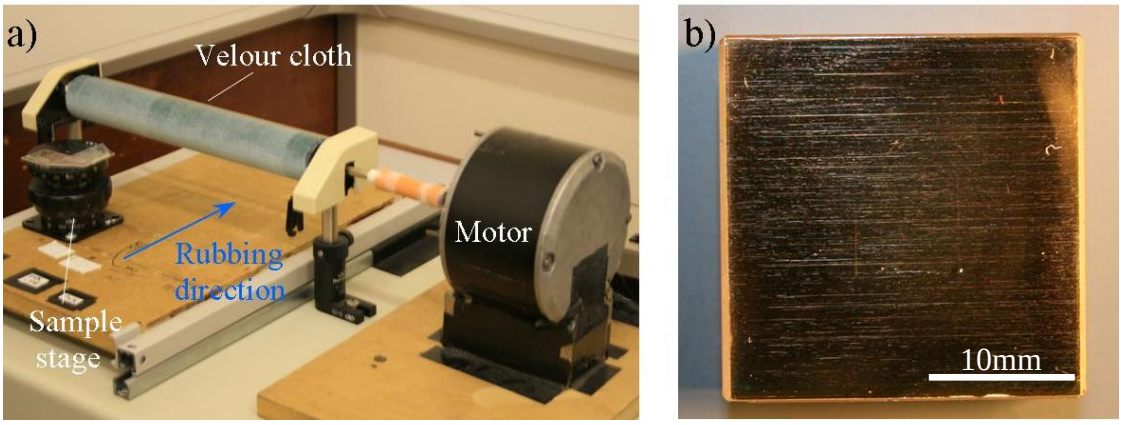

Figure 3.14: a) The design of the rubbing machine. The velour cloth attached to a spindle rotates at ~200rpm; the sample is pushed under the cloth to generate a uniform rubbing direction. The force of the rubbing is controlled by the height on the sample stage. To assist in later fabrication steps the direction of the rubbing is marked onto the uncoated side of the sample with an arrow. b) A visual example of an over-rubbed PVK polymer layer, clearly showing the scratches in the surface. This also highlights the unidirectional rubbing from this machine.

The force of the rubbing also needs to be considered and is controlled by the height of the sample rubbing stage. Too little a force risks an insufficient molecular asymmetry to align the liquid crystal across the entire polymer surface. This allows domains of other in-plane alignments to form, severely compromising the homogeneity of the cell (an example can be seen in *figure 3.17c*). An excessive force however removes portions of the polymer from the surface, as demonstrated by the atomic force microscope (AFM) image of the over-rubbed sample (*figure 3.15*). This surface will uniformly align the liquid crystal; however, the re-orientation response to an electric field is dependent on the PVK thickness. Therefore, an unwanted and significant spatial variation in the liquid crystal alignment will be present, compromising the operation of the cell.

An over-rubbed layer also generates a significantly rough surface. For SPP manipulation, it is desirable for the surface roughness to be minimised, as a rough surface is known to scatter the SPP into the coating medium (the liquid crystal in our case) [213]. Hence, the ideal rubbing force minimises the creation of any scratches to the polymer surface while still achieving good liquid crystal alignment. Unfortunately, this optimum rubbing force is found by trial and error, as it depends on the materials of the rubbed surface and their adhesion to the substrate. Therefore, a test substrate is used to ensure samples are not wasted while an ideal rubbing force is determined.

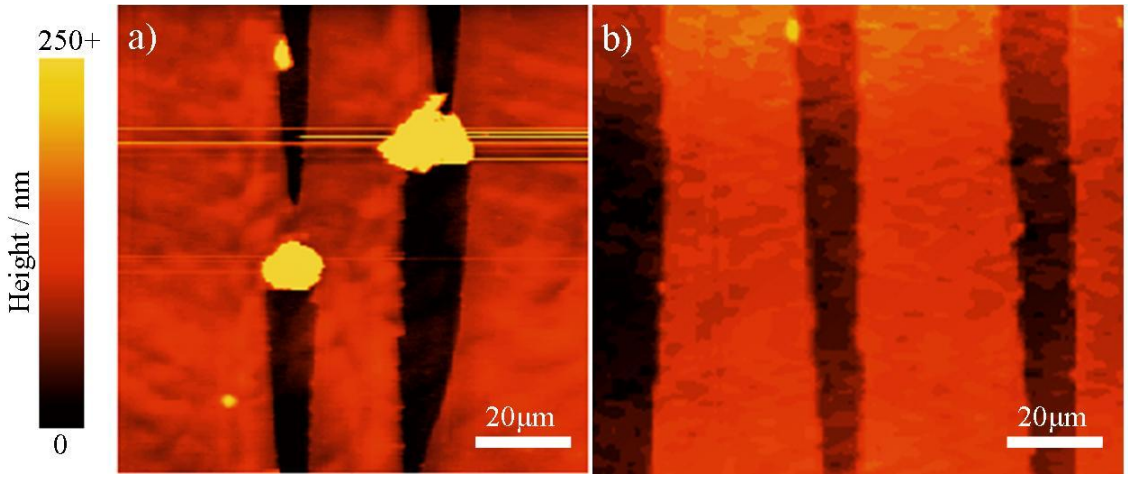

Figure 3.15: AFM topographical images of an over-rubbed PVK polymer surface. The rubbing removes strips of the polymer from the Au surface, as the adhesion of PVK to Au is low. The PVK layer thickness is ~90nm, so the 'trenches' represent a complete removal of the PVK and possibly some of the Au. The width of the removed strips is significant, ~10µm and would compromise the performance of the photorefractive liquid crystal cell. This removed material is deposited as lumps at the end of the scratches (a). The scratches are in fact random and not periodic, as (b) would suggest.

3.3.4 Liquid Crystal Cell Fabrication

To fabricate the liquid crystal layer of the sample, the thin confining cavity must first be created. This is simple to achieve by attaching the top plate (ITO/PI coated glass slide) to the substrate (PVK/Au coated high refractive index glass) and only applying the adhesive to points at the edge of the cell. The cavity is then the thin air gap between the two plates. The cavity thickness is controlled by the use of spacers of known thickness.

For our cells, we use 12µm Teflon beads as spacers; these are dissolved into a UV curing epoxy that is used as the adhesive. A very small amount is then placed onto the substrate at the corners of the cell. The top plate is positioned so that it does not completely overlap the substrate, to allow electrical contacts to later be attached to the cell, see *figure 3.16a*. The rubbing directions of the PVK and PI layers must be orthogonal to ensure the final liquid crystal alignment is planar with zero twist.

The top plate is then gently pressed down to ensure the spacers are controlling the cavity thickness. At this point, interference fringes from Fresnel reflections within the cavity are visible by eye, due to the significant reflections off the Au layer. By using a pencil (or another small area tip device, such as a pin) and gently pressing the top plate at the glued spots, the top plate can be aligned so it has a uniform cavity thickness across the entire surface of the cell, i.e. no interference fringes. The final thickness of the cavity is 12 ± 0.7μm. The UV glue is then quickly cured by exposing the cell to the emission of a Mercury vapour lamp for 5-10 minutes.

After the cavity is created, the electrical contacts are attached to the exposed PI/ITO and PVK/Au surfaces. The wire is attached by a thermally curing conductive epoxy, as standard electrical solder or indium have poor adhesion to the sample, in particular the Au surface. As a convention, red wire is attached to the Au side and black to the ITO side of the cell, so the direction of an applied potential is easily determined.

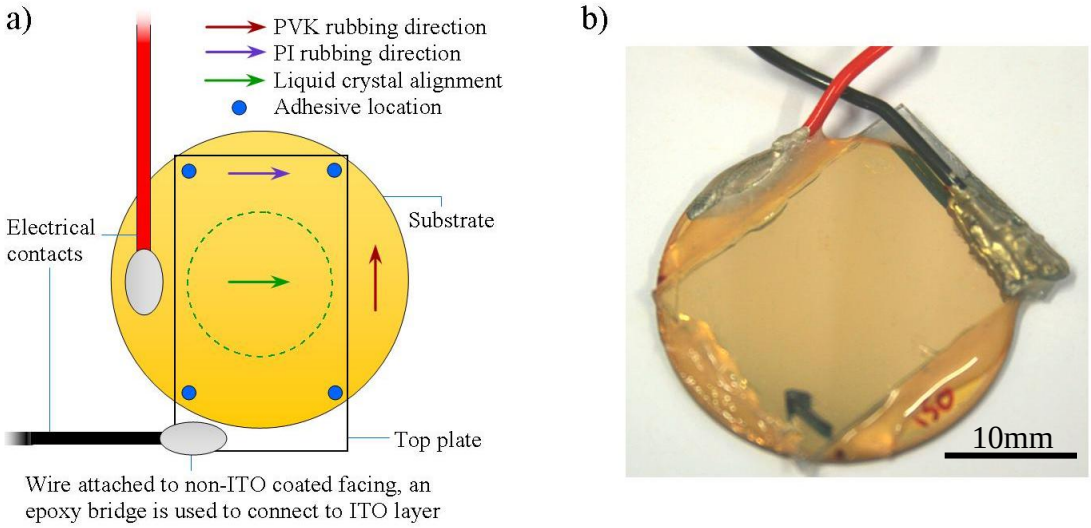

Figure 3.16: a) Schematic representation of the positioning of the cells substrate and top plate. The dashed green circle represents the area where the liquid crystal alignment should be homogenous and defect free. b) A completed cell, the arrow marks the PI rubbing direction and initial in-plane liquid crystal director.

The cavity is then filled with the E7 liquid crystals (Merck) by placing them at the cells edge. Capillary forces subsequently draw the liquid crystal into the cavity. This is often done in a small vacuum chamber (~1 Torr) to ensure that no air bubbles are present in the cell after filling. The liquid crystal molecules are automatically aligned throughout the cell, because of the rubbed polymer surfaces. Finally, the edges of the cell are sealed with epoxy to prevent contaminants entering the liquid crystal layer and thus modifying the cells behaviour.

3.3.5 Liquid Crystal Functionality Testing

The sample is now finished. However, checks are made to ensure that the liquid crystal alignment is homogeneous throughout the cell and that the electrical contacts are correctly attached. These tests are done by viewing the cells transmission through crossed polarisers; this is analogous to the experiment in *section 3.2.2*. However, the transmission is viewed by eye so a low intensity white light source is used instead of a laser. An example of good and bad alignment as well as the change with an applied voltage is demonstrated in *figure 3.17*.

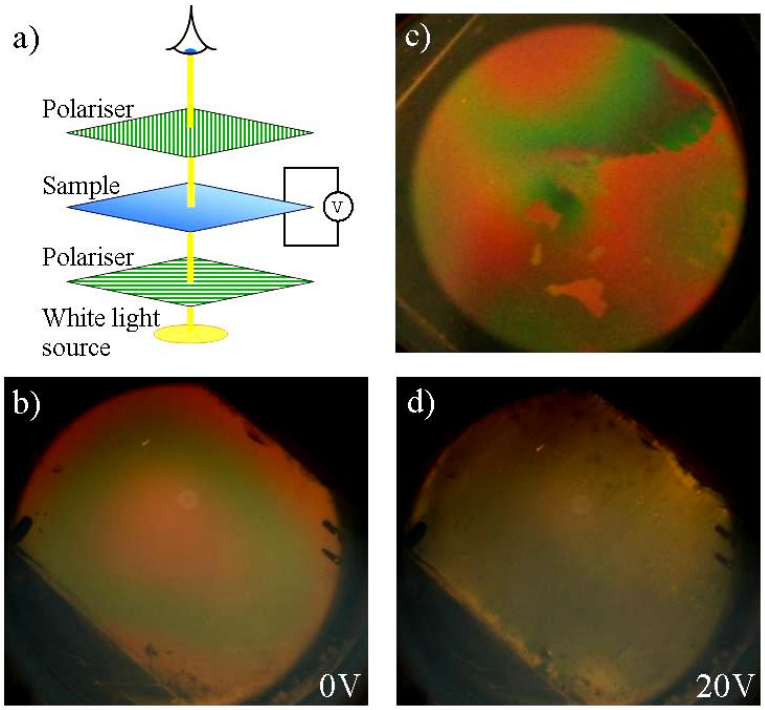

Figure 3.17: Image through the sample with crossed polarisers. a) Experimental set-up. b) With no voltage applied a uniform colour transmission is expected, the slight variation is from a small non-uniform cell thickness. c) In a sample with poor homogeneity any defects or different alignment domains would show up clearly as different colours. Therefore this type of sample is rejected. d) Applying a DC voltage to the cell should re-orientate the liquid crystal changing the observed colours (compare to b). Failure to see this behaviour indicates either a poor electrical contact or an electrical short.

Chapter 4

Characterisation of the Hybrid Plasmonic Photorefractive Liquid Crystal Cells

The wavevector of a SPP mode within our samples is determined by the dielectric properties and thicknesses of each layer. Therefore, the first section of this chapter is dedicated to the methods that acquire this information, as well as demonstrating how they influence the SPP modes. Most of this information is only required for quality control during fabrication. However, fitting of this data validates the optical component of our theoretical model.

The control we desire over SPP is accomplished by the re-orientation of the liquid crystal molecules. This can be achieved either with an electric potential, or for a hybrid cell that we have designed, light when a potential is also applied. Hence, we characterise the electrical response of the entire cell in *section 4.2* and demonstrate the magnitude of the change in the SPP wavevector that is possible with this type of device. Finally, information is presented on the photorefractive control of the wavevector of a SPP when uniformly illuminating the photoconductive layer.

4.1 Determination of the Physical Properties of the Multi-layer Structure

The wavevector of SPP modes is determined by the dielectric properties of the confining metal and dielectric coating layers. Therefore, accurate determination of these constants is vital for generating a good theoretical fit. The methodology of how the optical constants of the Au and PVK were acquired is explained in *Appendix B*, along with a list for these materials optical constants. However, the thickness of each layer also influences the SPP wavevector and determines the quality and functionality of the sample, so it is worthwhile to discuss how the layer thicknesses are determined and their effect on the SPP modes.

4.1.1 Optical Constants of the High Refractive Index Prism

The first material that needs to be considered is the glass that is used to create the prism and the substrates of our samples. The refractive index of the prism will determine the angle that couples light into a SPP mode in our ATR excitation apparatus (*section 3.1*). This dielectric property does not influence the wavevector of the confined SPP modes as the SPP will not

interact with it. However, is does determine the wavevector range accessible with our apparatus.

The optical constants of the glass are provided by the manufacture's (Schott) material catalogue [214] in the form of a Sellmeier formula. The co-efficients of this material are presented in *Appendix B*. This data is used to confirm the ATR apparatus used in the SPP experiments is aligned correctly by comparing the experimental and theoretical angle of total internal reflection. The results of this check are shown in *figure 4.1*. This figure demonstrates that the apparatus is appropriately aligned and that the measured reflection angles will determine the correct SPP wavevector. This also confirms the validity of the optical constants provided (i.e. the correct glass).

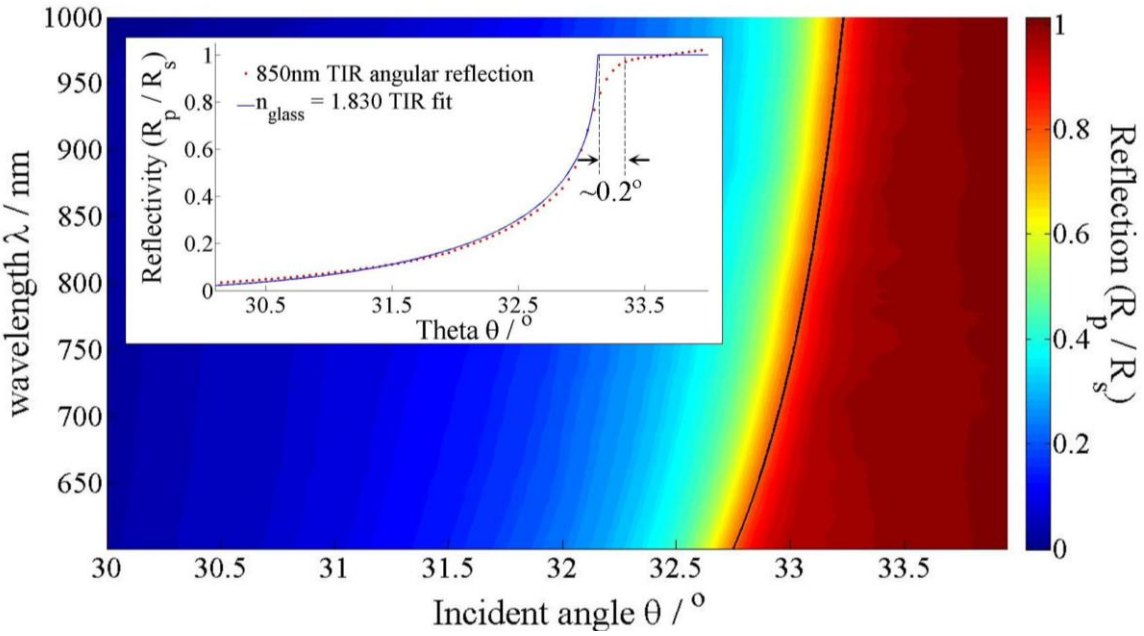

Figure 4.1: A colour contour plot of the TIR reflection from a N-LaSF9 substrate, air interface. The black line highlights the theoretical TIR angle based on the Sellmeier co-efficients provided by the manufacturer's catalogue. Inset: The theoretical fit to the TIR reflection for light with a wavelength of 850nm (in air).

The inset of *figure 4.1* also shows the effects of the apparatus resolution. The experimental data does not demonstrate a sharp square edge in the reflection intensity that is theoretically predicted at the TIR angle. This is a result of several factors;

1. The detector has a finite width; hence, each experimental data point is in fact the average over a small angular range.
2. The white light focus of the ATR apparatus will also have a finite spot size due to diffraction limitations (minimum spot size equal to the core of the fiber connected to the white light source, typical: 200µm). This is unavoidable with a focussed light ATR apparatus and decreases the resolution as a consequence.

3. The spectrometer has a moving average over a ±1.5nm range applied to the reflection spectrum to minimise noise in the detection signal.

The combined effect will make it harder to resolve sharp features (<0.2^{o}) in the reflection spectrum such as guided modes (see *section 4.2, 4.3*), however the SPP resonance in the ATR reflection spectrum is not a sharp feature so will be able to be resolved fully.

4.1.2 Au Layer Thickness Measurements

During fabrication the easiest way to reduce the quality of the SPP resonance in the samples is by depositing a non-optimal thickness of Au onto the substrate. The optimal thickness of Au as discussed in *section 2.4* is 40nm with a tolerance of ±5nm. The thickness of the deposited layer is monitored in-situ during thermal evaporation. However, the directionality and spatial variation of this deposition method results in a discrepancy between the displayed thickness and the actual deposited thickness. Therefore, it is a good practice to determine the thickness after deposition by UV-VIS transmission spectroscopy.

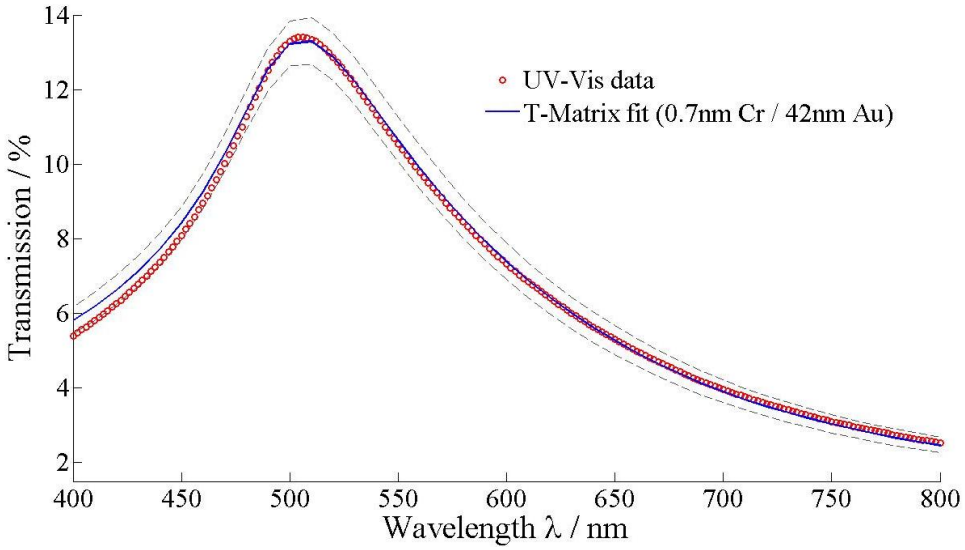

Figure 4.2: T-matrix fit for the transmission through the thin Au film acquired by UV-VIS spectroscopy. The dashed grey lines show the ±1nm tolerance to the Au thickness in this fit.

The transmission spectrum acquired from a 42nm Au layer with an ultra-thin Cr (<3nm) adhesion layer is displayed in *figure 4.2*. The transmission through the Au in our samples is less than 10% for most wavelengths. For the most common application of liquid crystals in displays, the visible light transmission through a liquid crystal cell is generally expected to be high. Obtaining a high transmission through the cell is not of concern to our application, though the magnitude of the transmission through the Au must be taken into consideration when illuminating the cell for photorefractive effects.

As a metal, the non-transmitted light through this layer will in general be reflected, though a small amount of energy will be absorbed by the film (the absorption is wavelength dependent) and lost as heat. The transmission through the Au layer has a maximum at 505nm. Therefore, the wavelength of the laser used to generate photorefractive effects should be as close to this as possible, to maximise the light intensity incident on the photoconductor. Other wavelengths could be used with a higher initial intensity, though this could heat the Au sufficiently to warm up the liquid crystal molecules in close proximity. An extreme case of the liquid crystal changing its phase state, from a nematic to an isotropic liquid, is unlikely, though a change in the thermotropic behaviour of the liquid crystal from a non-insignificant temperature increase is a possibility. The variation would follow the thermal gradient originating from the Au; adding a further unwanted complication to the description of the liquid crystal, as the SPP interacts with the region closest to the Au most strongly.

The fit to this data confirms that the optical constants of Au acquired in *Appendix B* are appropriate as the theoretical T-matrix transmission generates the same shape transmission curve. Fitting the Au transmission with a UV-VIS spectrum can easily determine the thickness of the layer to an accuracy of 1nm, as shown by the dashed grey tolerance lines in *figure 4.2*. Determining the thickness with a more accurate method such as ellipsometry or topographical AFM is not essential as the thickness of the Au has a minimal effect on a SPP wavevector in the 35-45nm accepted thickness region (*figure 2.14*) and is used only for quality control.

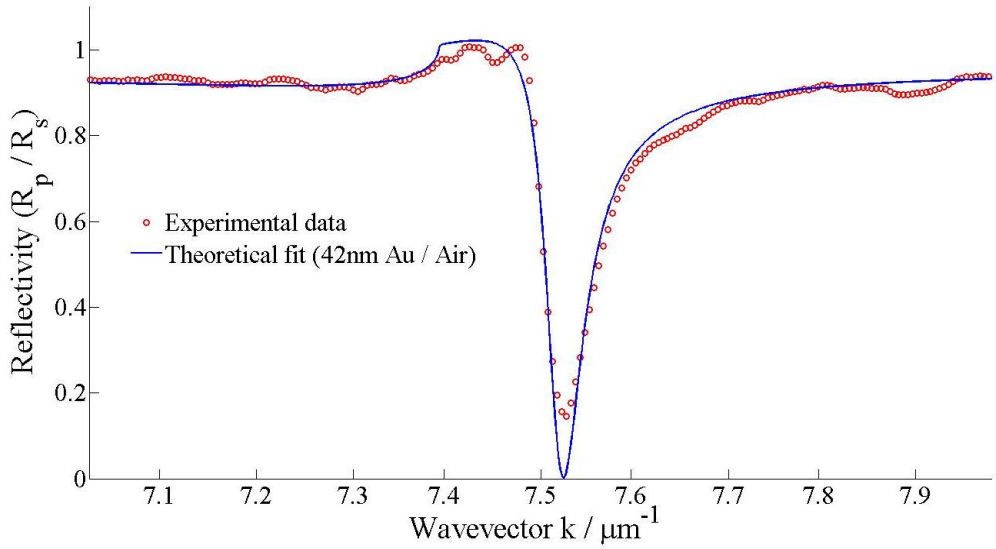

Figure 4.3: An ATR spectrum for a 42nm thick Au film. The sharp dip in the reflection when 1.462eV light has a wavevector component parallel to the surface of 7.53μm^{-1} is due to the excitation of an SPP mode.

In these fits, the thin Cr layer has no effect on the shape of the curve. The only effect of the Cr is a minor neutral density effect that lowers the transmission over all wavelengths by ~0.5-1%. Therefore, the Cr layer can be ignored in the modelling of the SPP modes ATR spectrum

(*figures 4.3-5, 4.8, 4.12)*. The small discrepancy in the transmission with wavelengths below 475nm arises from the failure to account for the absorption of the glass at higher energy wavelengths.

A typical ATR spectrum for an Au film deposited onto the high refractive index glass substrate is shown in *figure 4.3*. The spectrum shows all the expected features, such as the reflection step due to TIR followed by the almost complete dip in reflection that arises from light exciting an SPP mode. A small amount of noise is present from the random variations in the output intensity from the white light source that arise between acquiring the TM and TE reflection spectrums, though this does not appear to effect the SPP resonance dip. The resonance does not reach zero as a result of either a resolution issue or the surface roughness and layer morphology not allowing a complete excitation of SPP with the incident light. As the dip does not reach zero for the ATR spectrum when the cell is completed (*figure 4.11-12*), where the angular resolution of the apparatus is an issue, the layer roughness and morphology are the more likely cause. This is an inherent problem of how the samples are fabricated. This data has been fitted using a T-matrix model for a high refractive index glass, 42nm Au layer and semi-infinite air structure. The agreement between the theory and experimental data is good. Demonstrating the T-matrix model is correctly implemented.

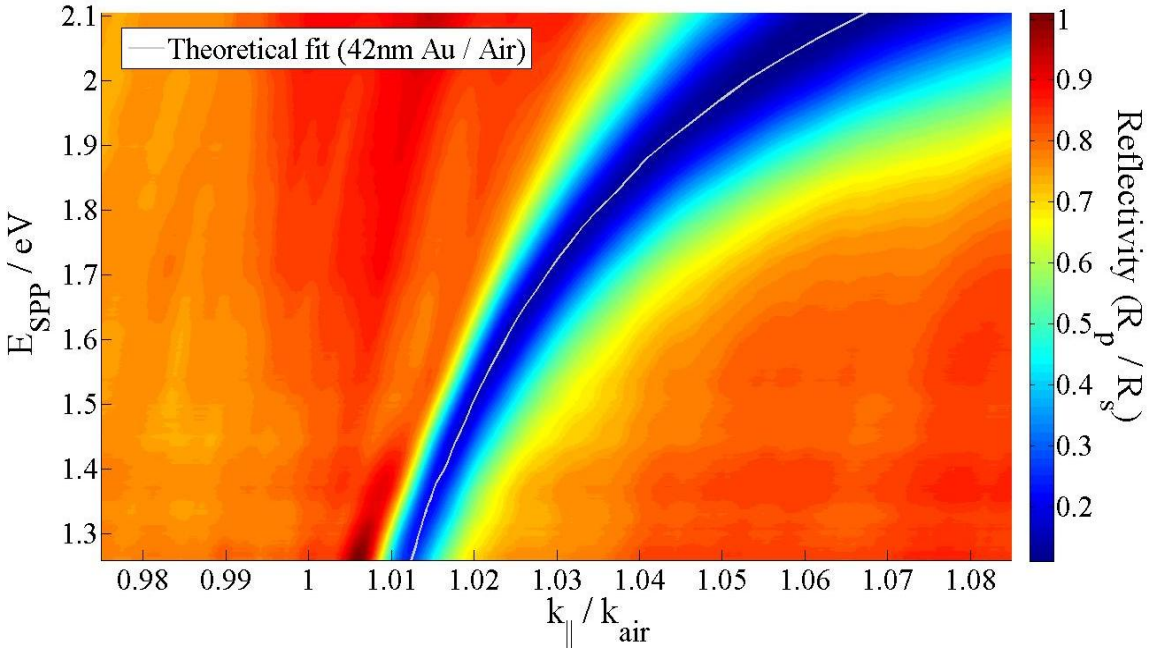

Figure 4.4: Colour contour plot of the ATR spectrum for a 42nm Au film exposed to air. The white line is the theoretical T-matrix fit using the refractive index of Au obtained in *Appendix B*. $k_{||}/k_{air}$ is a non-dimensional constant indicating the ratio of the experimentally measured wavevector parallel to the interface to the wavevector of light (with the same energy) propagating in air.

The use of a white light source and spectrometer in our apparatus acquires the multiple wavelength ATR data required in *figure 4.4* to determine the SPP dispersion simultaneously. The dip in reflection in the ATR spectrum (blue band in *figure 4.4*) from the SPP resonance is

the experimentally determined dispersion of the SPP modes in this structure. The dispersion is clearly non-linear, as predicted for SPP by the Drude free electron approximation (*section 2.1.1*). For comparison, the linear dispersion of light in air would be a vertical line with $k_{||}/k_{air} = 1$ for all energies.

The T-matrix optical model is also used to predict the dispersion of the SPP modes in the 1.25-2.1eV region. The good agreement between theory and experiment demonstrates that the measurements of the SPP wavevector with our apparatus are correct. The experimental data also allows us an estimation of the propagation length for various energy SPP as displayed in *table 4.1*. The measured propagation lengths confirm the characteristic problem of SPP of having a short (and often unworkable/unpractical) propagation length, particularly for higher energy SPP modes.

λ_{light} / nm	E_{SPP} / eV	k_{SPP} / μm^{-1}	d_{SPP} / µm
532	2.335	12.98	1.78
600	2.071	11.01	10.9
656	1.894	9.913	24.3
700	1.775	9.236	38.9
750	1.657	8.579	57.7
800	1.553	8.019	76.2
850	1.462	7.532	91.4
900	1.380	7.100	105.9
1000	1.242	6.377	137.0

Table 4.1: The experimentally determined wavevector k_{SPP}, and propagation length d_{SPP}, with various SPP energies confined to an Au, air interface. This estimation of the propagation length of SPP is consistent with the length scales reported by Kuttge [10].

4.1.3 The SPP Wavevector Dependence on the Thickness of the PVK Layer

The thickness of the photoconductive PVK layer is the most important measurement in characterising the samples structure. The thickness of this layer determines the sensitivity of the SPP to the re-alignment of the liquid crystal as well as the strength of the photorefractive effects.

Depositing a PVK layer shifts the wavevector of the SPP mode. An example of this is shown in *figure 4.5*, the resonant SPP wavevector for 1.462eV light is now $10.65\mu m^{-1}$ instead of $7.53\mu m^{-1}$ seen for an Au layer without a coating in *figure 5.3*, a shift of $3.22\mu m^{-1}$ by depositing only 114nm of the $n \approx 1.7$ polymer. Demonstrating the large wavevector sensitivity of SPP to the deposition of a small amount of material at the interface that supports the mode. This large wavevector shift is non-linear with the PVK thickness, as the SPP decays exponentially into the dielectric mediums. For example a semi-infinite PVK layer

(>1μm) would theoretically shift the SPP to 12.98μm^{-1}, whereas a 40nm PVK layer shifts the SPP to 8.099μm^{-1}. Ideally the PVK would be as thin as it could possibly be spin coated, ~20nm from *figure 3.13*, to maximise the SPP sensitivity to the liquid crystal layer. However, in practice the PVK must be thicker to prevent polymer lift-off and scratching during the rubbing stage of fabrication, as well as creating a sufficient light and dark resistance contrast for the polymer layer to generate good photorefractive effects in our cells.

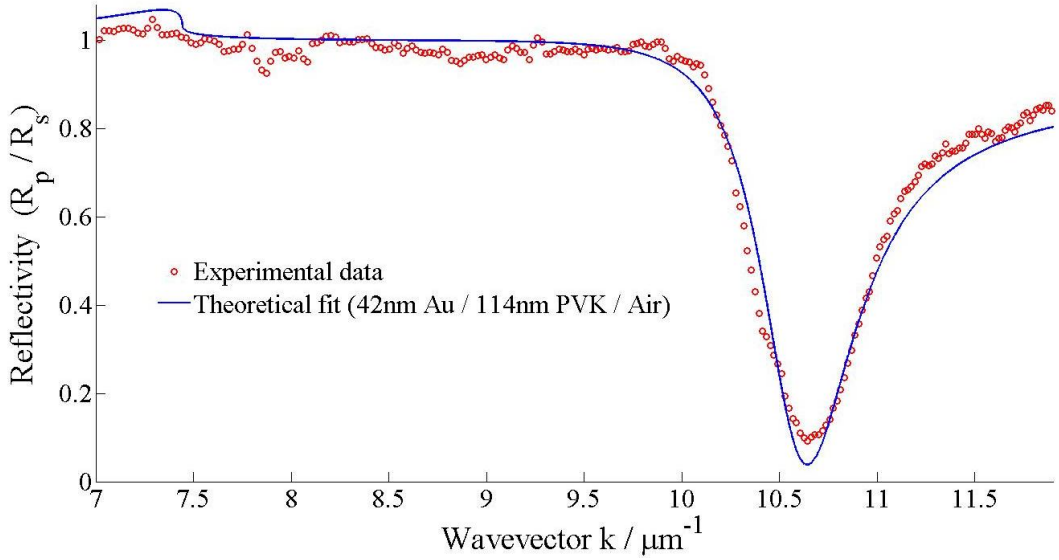

Figure 4.5: ATR spectrum for a 1.462eV light, for a PVK coated Au film. The SPP propagates at the Au/PVK interface. The theoretical fit also provides a method of determining the PVK thickness.

Several measurements are made of the PVK thickness to ensure the accuracy of the measurement. The first and most accurate of the measurements is with multiple angle spectroscopic ellipsometry. An example of the ellipsometry data at a single angle and the fit with a model of the sample is shown in *figure 4.6*; this also highlights the accuracy to which the thickness of each layer is determined.

The thickness and accuracy of the PVK layer fit is dependent on the values used for the refractive index. A mean-squared error (MSE) value is used to determine the appropriateness of the model, a MSE of ~10 signals a good fit. As only the thickness of the Au and PVK were used as fitting parameters, the MSE value of 12.386 in the data shown, demonstrates the optical constants extracted from a PVK layer in *Appendix B* are appropriate. If the optical constants for all layers (including the substrate, as its dispersion has not been accounted for in this fit) were left as fitting parameters, a MSE <2 can be acquired with minimal changes to the fitted thicknesses. Questions would, however, surround the validity of this fit as a large number of fitting parameters would have been used.

Another measurement of the PVK thickness is acquired with the UV-VIS transmission spectrum. A thickness measurement for polymer layers <250nm is usually not possible with UV-VIS as there are insufficient interference fringes in the examined spectral range.

However, when deposited onto Au the PVK layer modifies the transmission though the sample due to interference between internal Fresnel reflections. *Figure 4.7* shows an example of the transmission though a sample with a thin PVK layer. The form (spectral shape) of this transmission is noticeably different compared to a sample without a PVK layer, *figure 4.2*. Without the broad transmission peak at 505nm for Au, the PVK thickness measurement would not be possible with this technique. The magnitude of the change in the transmission through the sample is dependent on the PVK thickness for layers thicker than 30nm. The sharpest change with increasing layer thickness occurs in the λ = 520-670nm region. The T-matrix fit can acquire the PVK thickness to an accuracy of ±3nm. This value for the thickness of the layer agrees with the ellipsometry measurement to within 2-3nm.

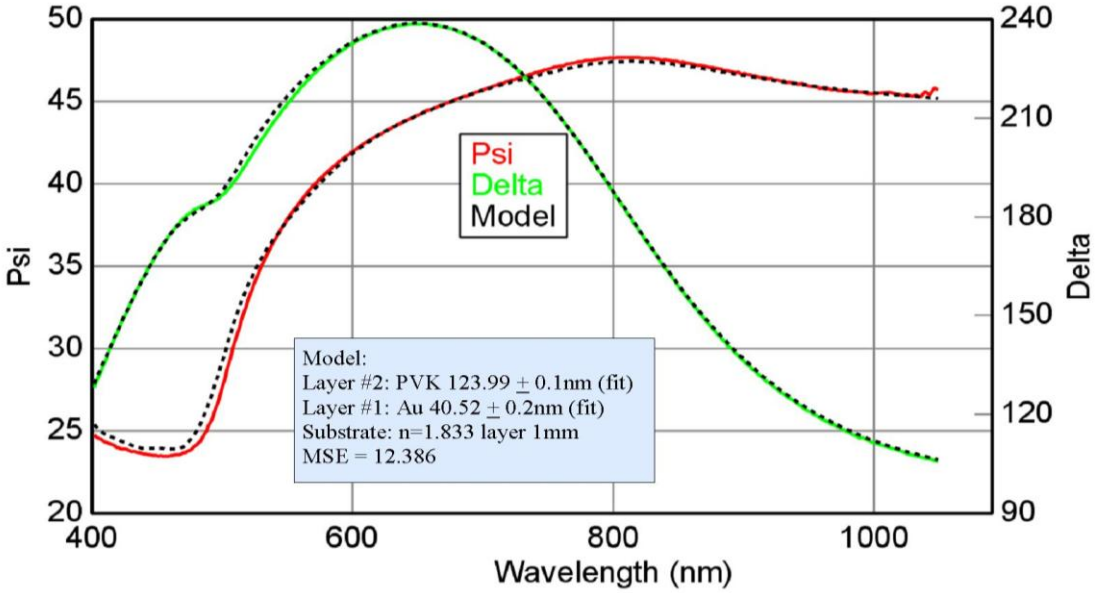

Figure 4.6: The theoretical fit from the *CompleteEASE* software package to the experimental data obtained by the ellipsometer for a 124nm thick PVK sample. This highlights the appropriateness of the fitting model (details in inset) and the accuracy to which the films thickness can be determined. The dispersion of the substrate has not been accounted for, though this will only reduce the quality of the fit by a small amount.

Because of this change in the transmission spectrum, the amount of light incident onto the photoconductor, instead of being reflected, increases. In the example of *figure 4.7*, approximately 16% of the λ = 532nm laser light, used to demonstrate photorefractive effects, is transmitted through the sample. The transmitted light is the illumination incident on the PVK layer. As the photorefractive effects are intensity dependent (*section 4.3 and 5.7*) the transmission at 532nm needs to be determined by UV-VIS for all samples to ensure the photorefractive effects are maximised. This is a requirement for accurate comparisons of the SPP interaction with a photorefractive liquid crystal cell between samples.

The last method for determining the PVK layer thickness is to compare the SPP dispersion from the sample to the theoretical value, *figure 4.8*. The predicted SPP dispersion is a good fit

for the PVK coated sample, like the T-matrix fit for the uncoated sample in *figure 4.4*. Again showing that the optical constants acquired for the PVK are appropriate and only the layer thickness is required as a fitting variable. The experimental data also provides an unexpected peak in the normalised reflection spectrum with values in excess of unity.

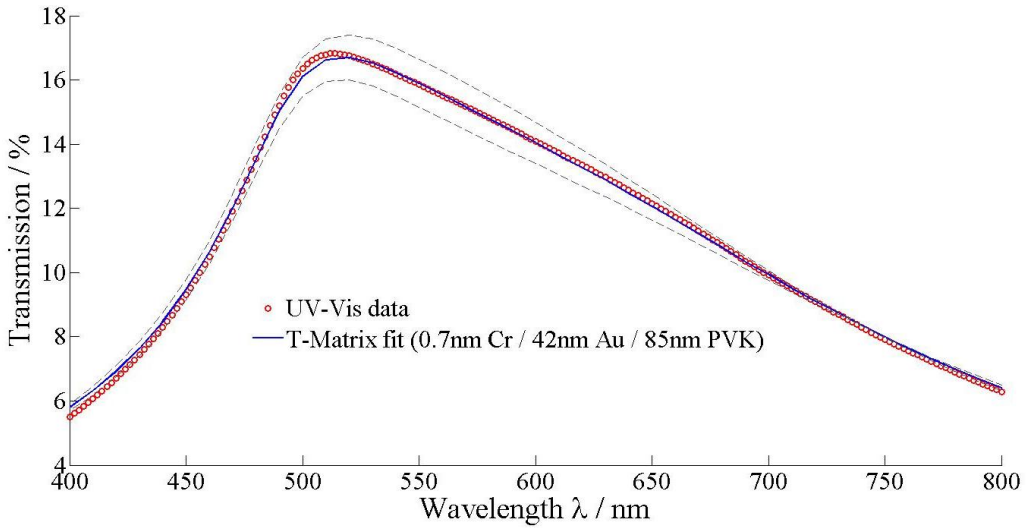

Figure 4.7: UV-VIS transmission through the 42nm Au film when a thin PVK layer has been deposited onto its surface. The dashed grey lines show the ±3nm tolerance to the PVK thickness for this fit. Sample differs to Ellipsometry measurement shown.

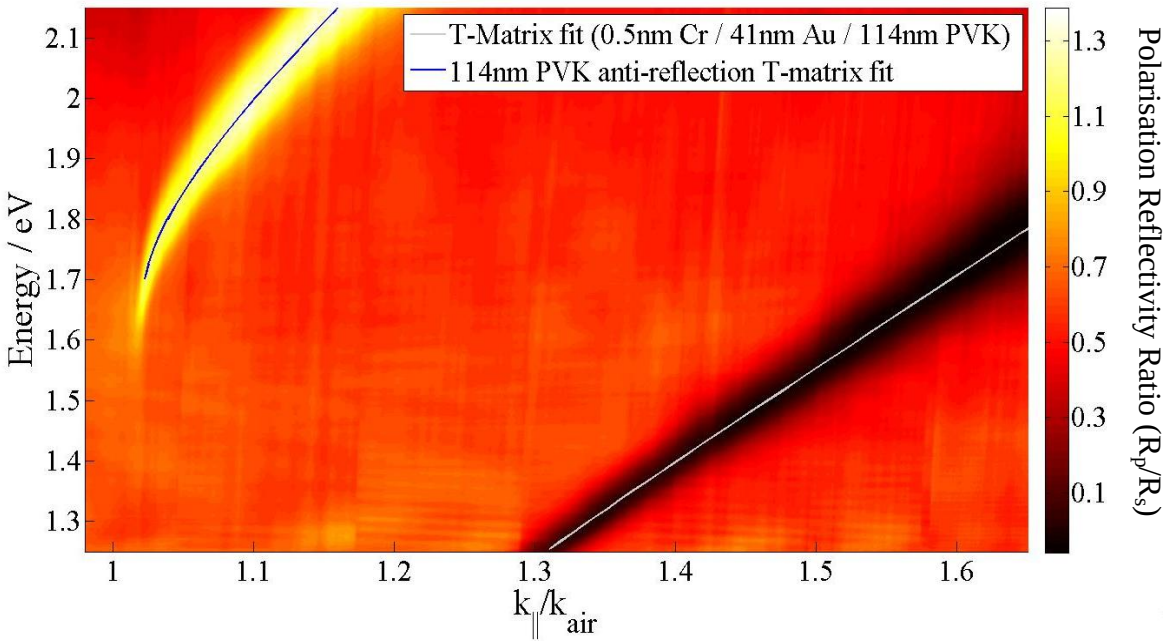

Figure 4.8: A colour contour plot of the ATR spectrum for a PVK coated Au film. The PVK layer also acts as an anti-reflection coating for s-polarised light; therefore, the plot shows this region with a polarisation reflectivity ratio greater than 1. Both the SPP and the anti-reflection peak are predicted by the T-matrix theoretical model. Hence, when determining the PVK thickness there are two data points to fit at each SPP energy, increasing the fits accuracy. Sample differs to *figure 5.6-7*.

Initially this would be of a concern; however, we need to consider the normalisation method in acquiring the data from our ATR apparatus. The data is normalised by the TE reflection spectrum. Hence, a polarisation reflectivity ratio greater than unity is possible, if the TE reflectivity is less than unity. For TE light incident at angles greater than the TIR angle it is expected that the reflectivity be maximised and close to unity or the normalisation method would not be valid. This is clearly not true for all wavelengths at all angles. The reason for this peak is from a dip in the TE reflection spectrum due to the thin PVK layer acting as a medium that supports guided modes. Because of the arrangement of the layers, only the TE polarised light is coupled into a guided mode. This effect is also predicted with the T-matrix reflection spectrum for TE polarised light. Therefore, it provides a second curve that can be fitted with the only variable the PVK thickness. As *figure 4.8* demonstrates, the thickness required to predict the guided mode is identical to the SPP dispersion fitting, therefore increasing our confidence in the measurements accuracy. The value obtained agrees with the ellipsometry thickness to within 1nm; however, the measurement takes significantly longer than either ellipsometry or UV-VIS spectroscopy so is only acquired for one sample in a batch to confirm the accuracy of the measurements from the other two methods.

4.1.4 The Effects of the Surface Roughness Caused by Rubbing the PVK Layer

During fabrication, the PVK layer is rubbed to align the liquid crystal. Excessive roughness will damage the layer as described in *figure 3.14-15* and render the sample useless. However, even a mild amount of rubbing sufficient to align the liquid crystal without removing the PVK layer will generate a rough surface. Surface roughness is known to reduce the coupling of energy into a SPP by scattering into the coating medium [213]. Therefore, the effect of our rubbed polymer layers on the SPP mode needs to be determined.

The ATR spectrum for a Rubbed PVK layer is displayed in *figure 4.9*. The SPP mode was first determined prior to rubbing as a reference. This sample was then rubbed to the level that is usually sufficient to align the liquid crystal molecules in our samples. The SPP mode does not broaden or become diminished with this level of rubbing. Therefore, we conclude that this level of rubbing to the PVK is not detrimental in our samples. This is likely because the PVK prior to rubbing is not completely smooth and has a similar roughness profile. The rubbing just provides the necessary ‘macroscopic, statistically significant chemical bond asymmetry’ required [212] to align the liquid crystal. However, the wavevector of the mode is slightly reduced because of a small amount of the polymer being removed. This reduces the thickness of the polymer by less than 1nm (calculated from fits, not shown). It is unknown how even this material removal is, though the ATR spectrum shown would suggest that the removal is even across the surface.

This sample is then rubbed again in the same direction more heavily, though not to the extent demonstrated in *figure 3.14*, and an ATR spectrum acquired. The SPP mode then begins to show the effect of significant surface roughness as the resonance dip is slightly diminished.

Therefore, this rubbing level provides an upper limit to the rubbing of the sample that is allowed for quality control. The SPP wavevector does not noticeably shift any further, suggesting little or no removal of any additional PVK. This could indicate that the initial rubbing simply removes 'loosely' attached particulates on the top of the layer, instead of removing part of the bulk. A desirable outcome if this hypothesis is true, though not important enough to merit further investigation.

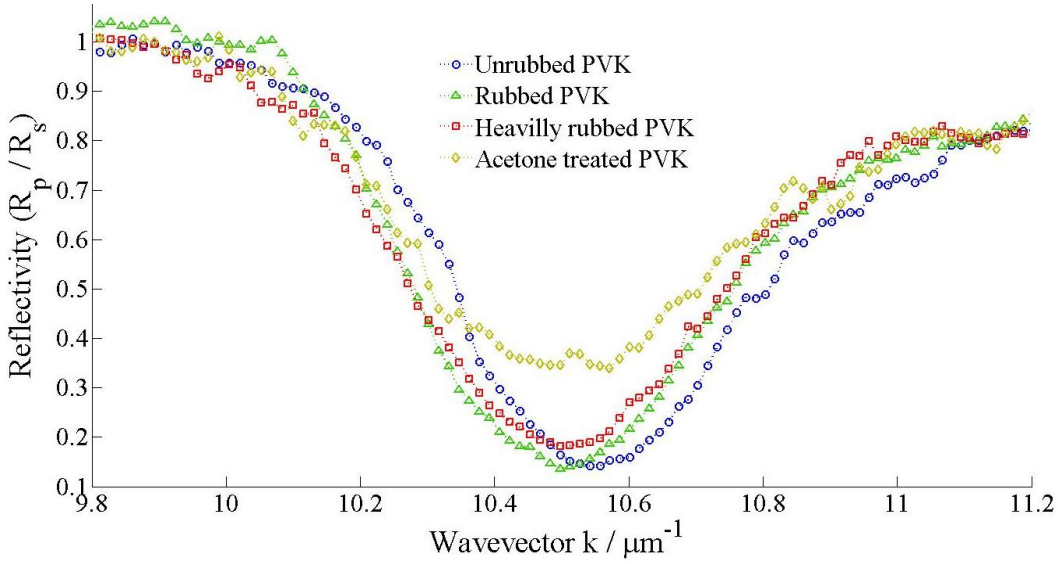

Figure 4.9: The effect of rubbing on the SPP. A rubbed surface that is used for alignment of the liquid crystal in our samples appears to have no detrimental effect on the SPP. Increasing the level of rubbing or surface roughness decreases the amount of energy coupled into the mode (either not initially coupled in or re-radiated back through scattering). Δ_{PVK} = 114nm.

The PVK surface is then roughened further by pressing an acetone soaked optic tissue onto the sample to demonstrate an extreme case of surface roughness in our samples. Acetone is notorious for damaging certain polymer materials and PVK is no exception. Hence, this treatment generates a noticeably rough surface without removing any further material from the polymer layer. The effect on the SPP is clear; the coupling into the mode is diminished and the resonance broadened, thus reducing the SPP propagation length. As the level of rubbing required to align the liquid crystal molecules does not noticeably alter the SPP mode, the surface roughness of the PVK layer does not need to be accounted for in the theoretical simulations.

4.1.5 The PVK-C_{60} Absorption Spectrum

The last characterisation step of the photoconducting layer is to determine the absorption of the C_{60} dopant. Attempts to determine the C_{60} absorption with UV-VIS spectroscopy for a polymer film deposited onto a sample, provide no evidence of any noticeable absorption, see *figure 4.7*. This is likely a result of the polymer layer being too thin to contain a sufficient

amount of C_{60} to be detectable by this technique. However, UV-VIS of the solution used to deposit the layer, *figure 4.10*, does highlight the absorption spectrum of the C_{60}.

To acquire the optical density of the solutions, a custom cuvette was fabricated with a mean path length of 220±10μm through the solution. The solution of interest filled one cuvette, and was placed into the sample channel of the UV-VIS. Another cuvette was filled with Chlorobenzene (CB), the solvent the compounds are dissolved in, and placed in the reference channel. This use of a CB reference cuvette removes any absorption or Fresnel reflections due to the solvent and glass cuvette from the data, therefore the optical density acquired is from the dissolved material alone.

The optical density of the PVK solution shows no peaks in the visible spectrum. Therefore, visible light has insufficient energy to excite the polymers electronic states. This is consistent with the literature that PVK requires a sensitizer to demonstrate photoconductive behaviour with visible light [152, 215-217]. The small non-zero value for the optical density arises from a slight change in the refractive index of the solution, increasing the magnitude of the transmission loss due to Fresnel reflections.

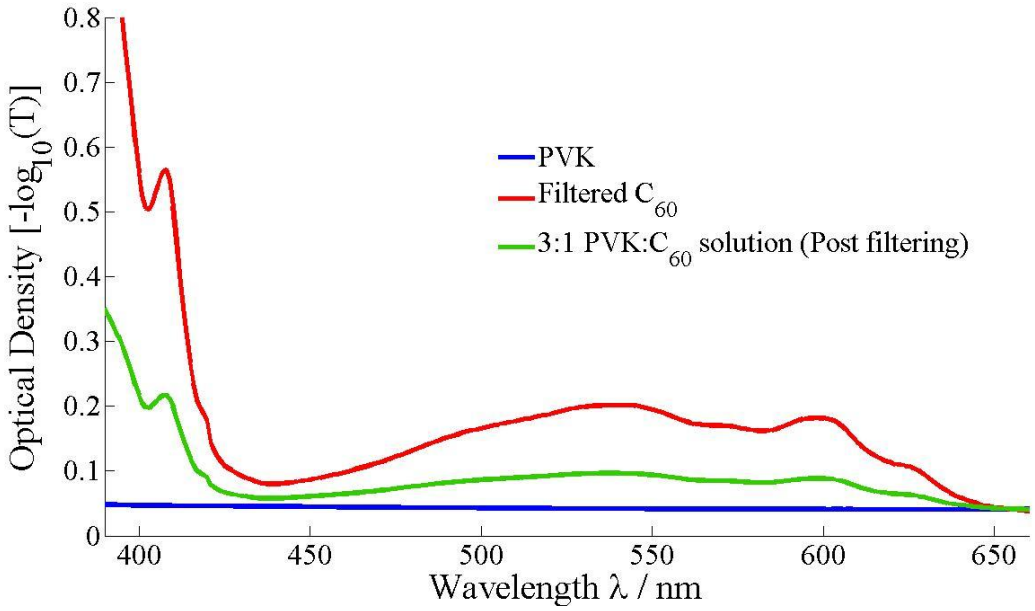

Figure 4.10: The optical density of the PVK:C_{60} solution spin coated during sample fabrication. This displays the preferable absorption wavelengths of the C_{60} dopant are 407nm, 540nm and 600nm.

The C_{60} solution shows an absorption peak in the visible spectrum at λ = 407nm and an absorption band in the 500-620nm region. Therefore, it is ideal for a dopant to sensitise the PVK to visible light [215] through a charge-transfer complex. The broad absorption peak at 540nm is particularly useful as it allows a standard wavelength 532nm laser to be used to excite the PVK, while minimising the reflected light from the thin Au film (see *figure 4.2*). A greater light sensitivity could be achieved by using a 405nm laser, as there would be a greater

excitation of the C_{60}. However, this effect would be cancelled due to the increased reflection or absorption from the Au and glass at this wavelength. The C_{60} solution is filtered to prevent undissolved particulates in the almost saturated solution [218] scattering light to create a false reading in the optical density of the solution.

The last solution examined is the mixture used during spin coating of the polymer layer. The optical density shows a weaker version of the same spectrum as the C_{60}. This is to be expected as the absorbing C_{60} solution is diluted with a non-absorbing PVK solution. The identical spectrum indicates that no obvious chemical reaction has taken place between the two compounds. Therefore, the deposited polymer film is a blend of the two chemicals. This solution does not separate during a storage time greater than 3 months. Therefore, the film should be a homogenous blend of the photoconductor and sensitizer, maximising the photoconductive response of the film.

The percentage weight ratio of PVK:C_{60} to CB for the spin-coated solution used to determine the optical density (~2.2%, see *section 3.3.2* for solution details) suggests that 220μm of the solution contains enough PVK:C_{60} for a ~5μm polymer film, assuming the density is constant. Hence, a 5μm PVK layer contains enough C_{60} to absorb 0.25% of the light at 532nm. Therefore, a 100nm polymer layer film will absorb approximately 0.005% of the light at 532nm and a laser intensity of several $mWcm^{-2}$ will be required excite all the C_{60} to generate significant photorefractive effects. This low absorption is ideal in a two-beam energy transfer device, as only a small fraction of the incident energy is required to generate the refractive index grating in the liquid crystal.

4.1.6 SPPs Interacting with a Liquid Crystal Layer

In order to understand photorefractive effects in our cells we first need to fully determine the dispersion of the SPP in these cells without any illumination, i.e. in the dark. Due to the birefringence of the liquid crystal material, the dispersion relations are more complex than for an isotropic material; particularly when the director of the liquid crystal is not either parallel or perpendicular to the SPPs in-plane wavevector. The equations describing the SPP mode in a birefringent medium are similar to those presented in *section 2.1* and can be found here [219].

An approximate analytic theory for the SPP dispersions for the general case of a uniform director and an SPP propagating in any direction are given in [220]. In the case that the director of the liquid crystal is parallel or perpendicular to the SPPs in-plane wavevector, the results can be qualitatively understood by considering the electric field associated with an SPP in an isotropic media and assuming that the birefringence is a relatively small perturbation; even in our case when the contrast between n_e and n_o is ~0.2. Unlike a travelling wave, a SPP has an electric field component parallel to its wavevector, in addition to a component in a direction normal to its wavevector. Thus an SPP samples the dielectric

response of the liquid crystal in two directions at once. The net effective refractive index for the SPP mode will therefore be some intermediate value between the refractive indexes associated with two plane waves whose electric fields are in the direction of the SPP in-plane wavevector $n_{\|}$ and a direction normal to the Au/PVK interface $n_{\perp}$. There is of course some weighting factor associated with the relative magnitudes of the SPP's electric fields in these two directions. In the case where the director is perpendicular to the SPP wavevector and parallel to the interface then the effective refractive index associated with the liquid crystal layer will be n_o. In the case that the director is either parallel to the SPP wavevector or the interface then the effective refractive index associated with the LC layer will be intermediate between n_e and n_o with, in general, a different weighting in each case. Other liquid crystal orientations (not parallel or perpendicular to the SPP wavevector) are more complex to interpret as there is some TM-TE mode mixing with SPP in anisotropic materials [172].

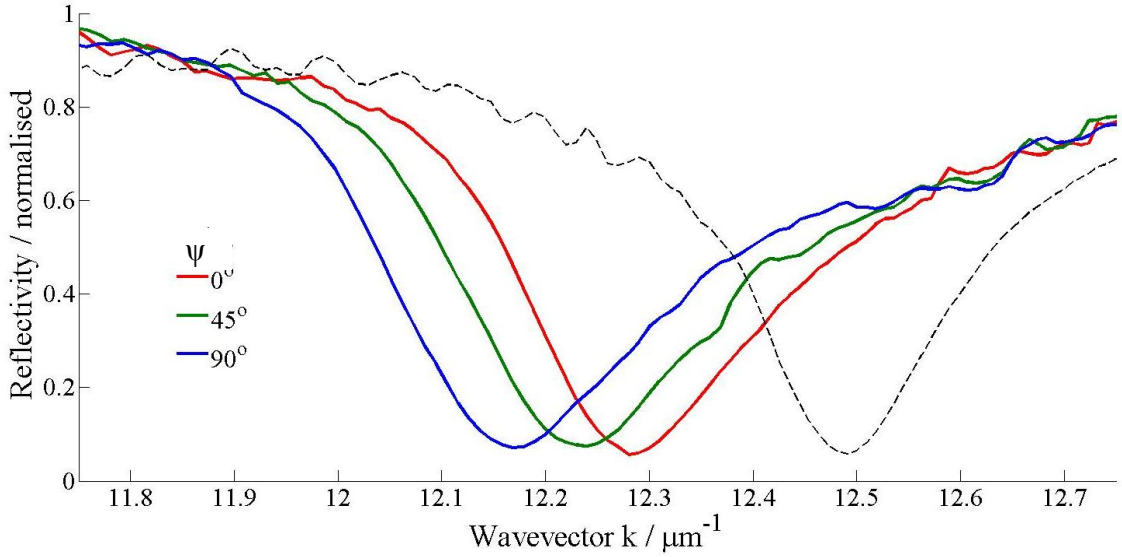

Figure 4.11: The ATR spectrum of SPP for three different values of $\psi = 90^o$, 45^o and 0^o. The black dashed line is the ATR spectrum for a ϑ_{LC} re-alignment achieved by applying a 15V electrical potential to cell ($\psi = 0^o$). $\Delta_{PVK} = 80nm$.

When SPP probes the liquid crystal layer of our cells, they demonstrate an increased wavevector (k =12.4μm^{-1}, *figure 4.12a*) than an SPP probing a cell without a liquid crystal layer ($k \approx 10.5\mu m^{-1}$, *figure 4.5*). Hence, the PVK layer deposited in our cells is sufficiently thin for the SPP to interact with the electro-optical material that will control their dispersion. The thickness of the liquid crystal layer in the cell is ~12μm, so the layer is considered to be semi-infinite in the SPP optical system and the layer thickness is not a factor in the SPP dispersion, unlike the PVK layer.

Examples of how the liquid crystals birefringence influences the dispersion of SPP modes within our cells are presented in *figure 4.11*.The lowest wavevector SPP (*blue* curve) corresponds to when the director is parallel to the interface and perpendicular to the SPP in-plane wavevector. Therefore, $n_{\|} = n_{\perp} = n_o$. The dispersion of SPP within our cells for this

director alignment can effectively be considered isotropic with a refractive index n_o throughout the layer. This wavevector is the lowest possible wavevector for a 1.46eV SPP in this cell; hence, all other director orientations will increase the SPP wavevector. For the *red* dispersion in *figure 4.11*, the director is parallel to the SPP in-plane wavevector and parallel to the interface; hence, $n_\perp = n_o$, $n_\parallel = n_e$. The SPP wavevector for this director alignment has increased by ~1.5μm^{-1}. The *green* dispersion represents $n_\perp = n_o$ and $n_\parallel$ as an intermediate value between n_e and n_o; consequently, the SPP wavevector is an intermediate value between the *blue* and *red* dispersions.

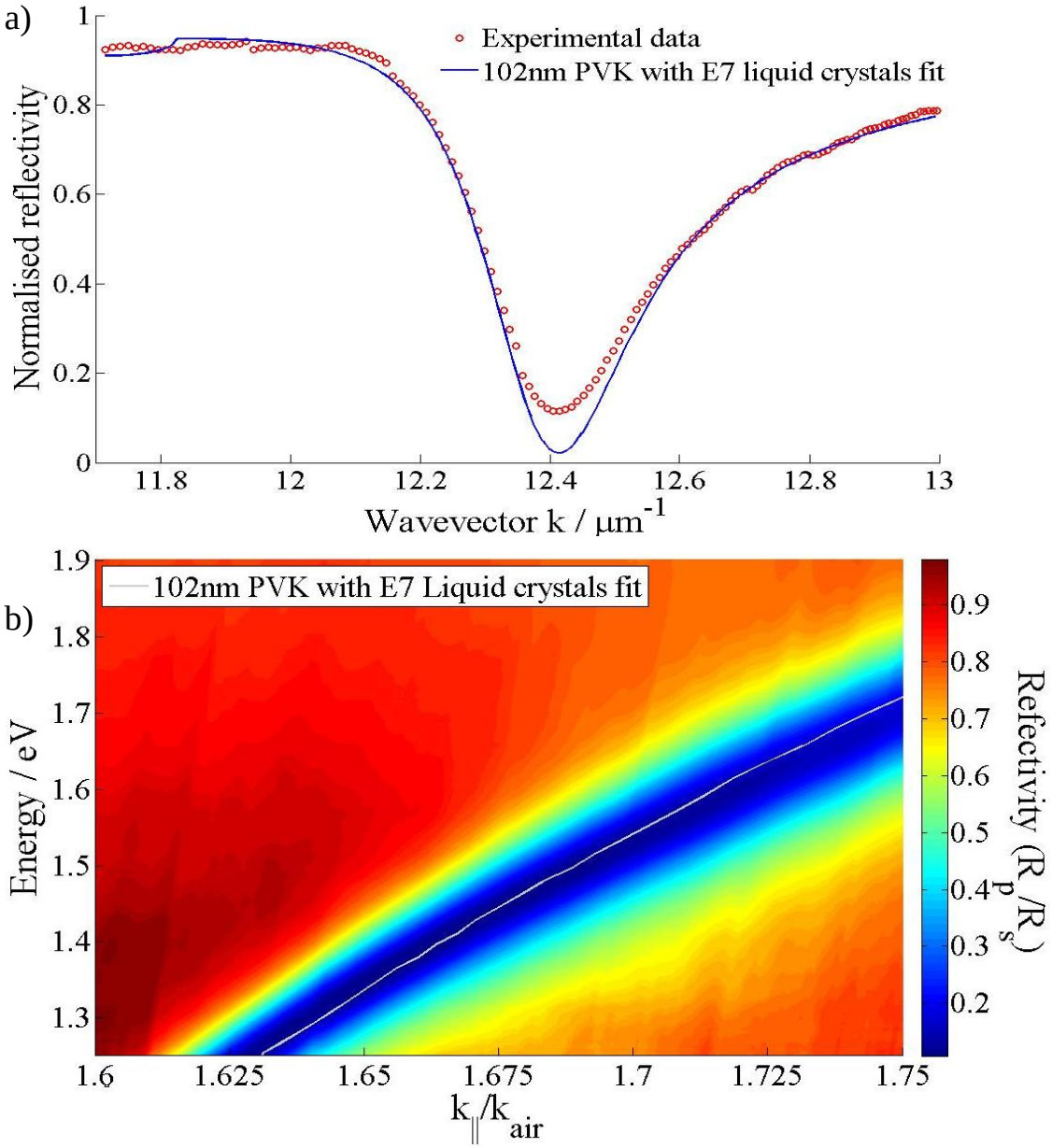

Figure 4.12: a) The ATR reflection spectrum for 1.462eV light in a fully constructed sample with an E7 liquid crystal layer. b) The dispersion of SPP within this sample when no potential is applied to the cell. Hence, the liquid crystal has a planar alignment throughout the entire layer. The white line is the theoretical SPP wavevector prediction over a significant spectral range. Δ_{PVK} = 102nm, $\psi = 45^o$.

A director alignment perpendicular to the PVK throughout the entire liquid crystal layer cannot be examined in our cells, due to the surface anchoring of the liquid crystal. However, we can generate an alignment that closely approximates this director orientation by applying a 15V potential. The director is then perpendicular to the PVK in the bulk of the layer, though the director has a spatially dependent alignment near the PVK-liquid crystal interface; the consequence of this and its effect on the SPP modes is explained in *section 4.2*. With a 15V potential applied, $n_{\perp} \approx n_e$ and $n_{\parallel} \approx n_o$, the opposite of the refractive indices for when the director is parallel to the interface and SPP in-plane wavevector. This director alignment demonstrates a noticeably larger increase in the SPP wavevector. Therefore, the effective refractive index $n_{\perp}$ is more dominant than $n_{\parallel}$ in determining the dispersion of SPP modes. This is to be expected, as considerations of the magnitude of an SPP's electric field in both directions parallel and perpendicular to the interface, *equations 2.2* and *2.3*, demonstrate that the electric field perpendicular to the interface is the largest for an SPP mode. Therefore, a greater change in the SPP wavevector is possible through a ϑ_{LC} re-orientation of the director, than with an in-plane ψ re-orientation.

The numerical simulations of the SPP-liquid crystal system described in *section 2.5* directly account for the cells birefringence and achieve an excellent agreement with the experimentally determined SPP wavevector as presented in *figure 4.12*. The numerical calculations also demonstrate a good agreement to the FWHM of the ATR spectrum, i.e. propagation length of the mode. This suggests that the liquid crystal alignment in the sample is well ordered near the PVK interface, over a length scale of the SPP propagation length. This is because a lower ordered liquid crystal alignment would broaden the SPP mode, in the same way as surface roughness and our simulations do not consider anything other than a highly ordered system. For these fits, we do not require a pre-tilt in the director alignment at the PVK interface. Hence, in general, we do not consider there to be a necessity for a director pre-tilt at the PVK interface in any of our subsequent simulations.

λ_{light} / nm	E_{SPP} / eV	k_{SPP} / µm^{-1}	d_{SPP} / µm
650	1.911	17.37$^{\alpha}$	11.9$^{\alpha}$
700	1.775	15.743	13.5$^{\alpha}$
750	1.657	14.440	16.2
800	1.553	13.325	20.2
850	1.462	12.388	24.1
900	1.380	11.578	33.1
1000	1.242	10.240	40.7

Table 4.2: Experimentally determined SPP wavevectors k_{SPP}, and propagation lengths d_{SPP}, in a photorefractive liquid crystal cell with a planar alignment and no applied potential. Δ_{PVK} = 102nm.
$^{\alpha}$ Theoretically determined value for comparison.

From the ATR spectrums in *figure 4.12b*, we also determine the propagation lengths of SPP modes for selected energies as displayed in *table 4.2*. These propagation lengths are very short and are lower than the SPP propagation lengths for an Au/air interface (*table 4.1*). This reduction in the propagation length is a result of the increased refractive index of the dielectric layers for the confining interface. A higher refractive index decreases the penetration depth of the SPP into the dielectric (*equation 2.13*). This effectively increases the confinement of the SPP's electric field to the metal layer, increasing the Ohmic losses. An increased surface roughness and lower quality layer morphology for the PVK and liquid crystal layers may also reduce the propagation length. These values can be used as a baseline for the SPP propagation length, our eventual goal of achieving SPP gain will look to significantly improve upon these values.

4.2 Liquid Crystal Response to an Electric Field

Liquid crystals are well-known electro-optic materials and various methods exist to model their behaviour. However, all of these rely upon knowing the magnitude of the potential dropped across the liquid crystal layer of the cell. Therefore, we attempted to characterise the electronic behaviour of the cell with impedance measurements in the low voltage limit. With an appropriate equivalent electrical circuit model, typical values for the resistance and capacitance of each layer can be acquired. In particular, we are interested in the resistance of the photoconductive PVK layer with increasing illumination. However, the impedance measurements cannot be used to accurately model our system, due to the non-linear electrical and illumination response of the PVK, as discussed in *section 4.2.1*.

The electro-optic response of the liquid crystal molecules re-alignment is also investigated through a crossed polariser experiment in *section 4.2.2*. This can determine the Freedericksz transition, the magnitude of the birefringence of E7 and indicate the liquid crystal orientation angel ϑ_{LC} throughout the cell as a function of the applied voltage. Finally, in *section 4.2.3*, we determine the shift in the SPP wavevector in our cells when a 1 kHz AC electric field, where the potential is dropped entirely across the liquid crystal, is applied to our cells. These measurements are used to validate the mathematical simulations for the alignment of the liquid crystal with an applied potential. They are also a direct experimental determination of the sensitivity of the SPP to the liquid crystal re-alignment.

4.2.1 Electrical Impedance Measurements

For the electrical characterisation measurements, a cells impedance is acquired in the 10^{-1}-10^{3} Hz frequency range, using eight measurement frequencies per order of magnitude. Each frequency is sampled for 10 cycles and two cycles pass after a change in frequency before impedance sampling to ensure the measurements are accurate. The AC potential is restricted to V_{peak} = 0.5V so that the measurements are in the low signal limit. At this voltage the electronic behaviour of the cell is linear [221], i.e. a small change in the magnitude of the

potential generates the same measured impedance. To ensure the equipment is correctly calibrated, after the impedance of the cell is acquired when there is no illumination, the impedance is reacquired (in the dark) with the cell in series with a 1MΩ resistor. The impedance measured then increases (to within 0.7%) by an amount corresponding to the addition of the 1MΩ resistor as expected for accurately calibrated equipment.

An example of the typical electrical behaviour acquired for our cells with increasing illumination is presented in *figure 4.13* for the magnitude of the impedance |Z| and *figure 4.14* for the phase of the impedance σ. The interpretation of this data begins with the impedance spectrum acquired in the dark (illumination level between 50-100nWcm^{-2} from background sources). At the highest frequencies examined, 300-1000Hz the impedance of the cell is dominated by capacitive effects from the liquid crystal[VII]; hence, |Z| follows 1/ω as expected for a capacitor. The impedance then demonstrates a resistive behaviour (constant |Z|) in the 10-300Hz frequency region. The dominant component in this frequency region is the resistance of the liquid crystal layer. The impedance is then dominated again by capacitive effects for the lowest frequencies examined (0.1-10Hz), as |Z| once again increases with 1/ω. However, the component that determines the behaviour in this frequency region is the capacitance of the PVK. This explanation is confirmed by the impedance phase data of *figure 4.14*. However, the phase data indicates that at no point is the electronic behaviour purely resistive ($\sigma = 0^o$) or capacitive ($\sigma = -90^o$). The most resistive behaviour occurs at ~32Hz in this sample. This frequency varies slightly between samples; however, it is always in the 10-100Hz range.

The impedance of the sample is also acquired for an increasing level of monochromatic λ = 532nm illumination of the sample. The illumination is from a 532nm laser as it is the wavelength used in our later experiments. This wavelength is also ideal for impedance spectroscopy of the cells, as there is minimal absorption from the E7 liquid crystal (<1cm^{-1} [136]), which could inadvertently heat the liquid crystal, distorting the impedance measurements at higher intensities. The beam is expanded to illuminate the entire cell. The intensity is measured by first determining the incident optical power before expanding the beam. The expanded beam's area is determined by measuring the visible diameter projected onto a screen placed at the sample position; the measured diameter is approximately 25mm. The illumination is a 2-D Gaussian intensity profile over the cell; however, as the impedance measurements determine the average impedance over the entire surface of the cell it makes sense to use the average intensity, instead of a peak intensity to describe the illumination. Therefore, the cells impedance determined at a specific average intensity may not directly correspond to the true impedance of the sample at the same un-expanded intensity in the small region experimentally probed by SPP. However, the impedance measurements will be a close approximation to the true impedance in the region of interest at the same experimental intensities. The error in the measurement of the beam diameter will result in an error of ±8% in the intensity measurement.

[VII] Determined by the impedance fits in *table 4.3*.

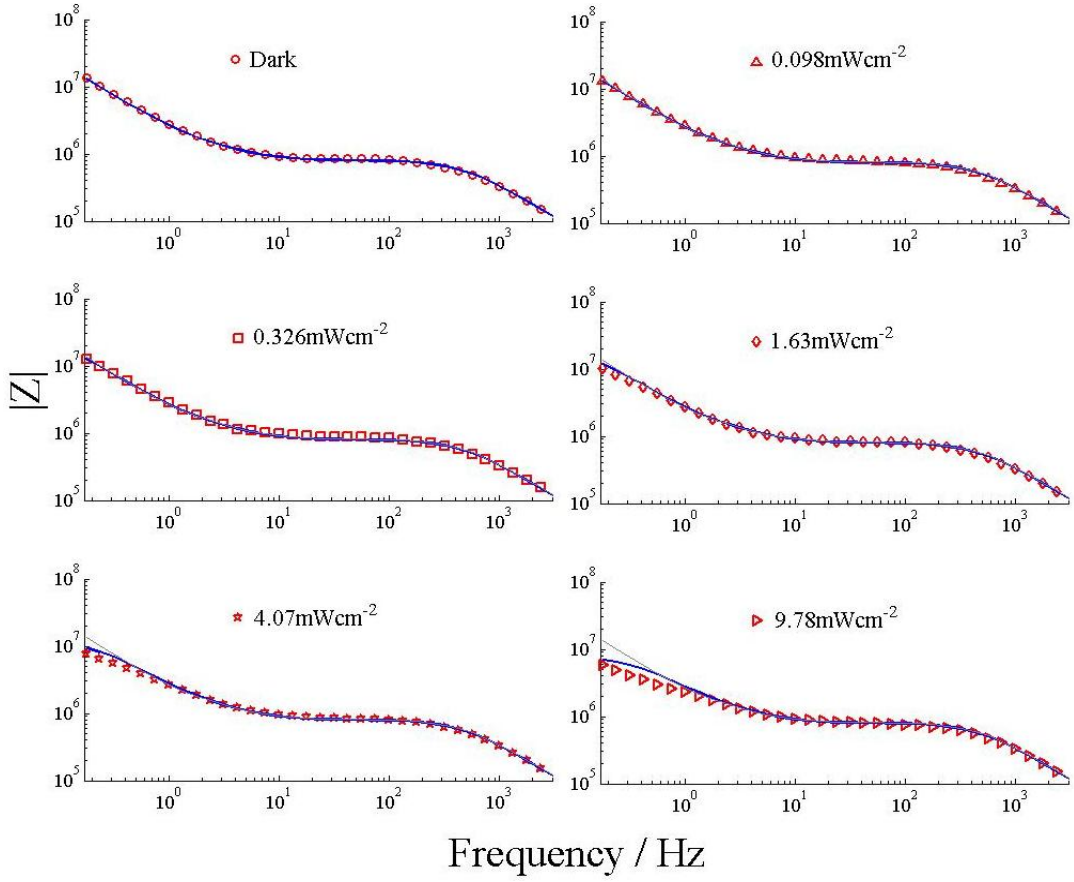

Figure 4.13: The magnitude of the impedance of the cells with increasing illumination intensity incident on the PVK. The red points are the measured impedance values, the blue line the fit with the equivalent circuit at this intensity. The grey line is the fit to the impedance of the cell in the dark for comparison. Results are typical for a functional cell.

Illuminating the sample does not appear to change the magnitude of the impedance of the cell for frequencies greater than 3Hz. In the frequency region less than 3Hz, changes are observable. The general trend of |Z| does not change. However, the magnitude of |Z| changes from 13.3MΩ in the dark to 5.7MΩ for an intensity of 9.78mWcm^{-2} at a frequency of 0.17Hz. The change in |Z| is not linear with intensity. The phase delay of the impedance signal with increasing illumination remains constant for frequencies greater than 8Hz. The effect of illumination changes the impedance phase in the 0.1-8Hz frequency region from a curve to an approximate straight line for intensities greater than 3mWcm^{-2}. The value of σ at 0.17Hz changes from -80^{o} in the dark, to -56^{o} with an illumination intensity of 9.78mWcm^{-2}; this indicates that the impedance spectrum when illuminated is more resistive and less capacitive.

To assist our analysis we fit these impedance spectrums to an equivalent circuit described in *section 3.2.4* and *figure 3.7*. This form of equivalent circuit was chosen as liquid crystal cells have been analysed with impedance spectroscopy before [222-224], using RC circuits to describe each layer. An RC circuit is used for each polymer alignment layer (these were non-photoconducting layers) and an RC circuit is used for the liquid crystal. The impedance of a related PVK system in an organic light-emitting-diodes has also been examined [225], using a

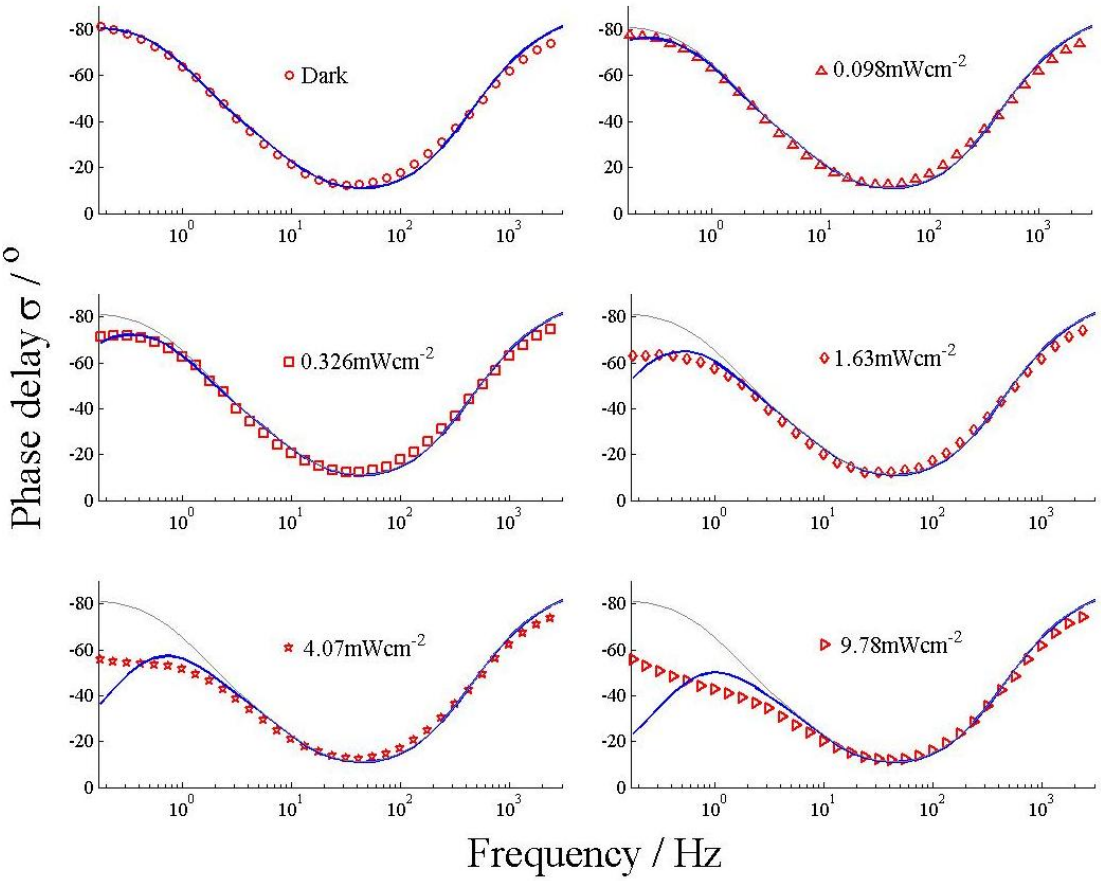

Figure 4.14: The phase delay of the electrical impedance of the cells with increasing illumination incident on the PVK. The red points are the measured impedance values, the blue line the fit with the equivalent circuit at this intensity. The grey line is the fit to the impedance of the cell in the dark for comparison. Results are typical for a functional cell.

simple RC circuit for the polymer. Hence, the equivalent circuit proposed in *figure 3.7* should be appropriate. A best fit is acquired to the impedance data using this circuit with an iterative program *Z-plot* using initial values of 10MΩ for each resistor and 100nF for each capacitor. The impedance is initially fitted to the dark data set with all the resistors and capacitors being freely fitted. The fitted values are presented in *table 4.3*. When illuminated, only the resistance of the photoconductive PVK layer should change. Hence, the capacitance of each layer and the resistance of the PI and E7 liquid crystals are fixed, leaving only the PVK resistance as a fitting variable for the illuminated data sets (these fitted values are also presented in *table 4.3*).

The fitting curves for $|Z|$ and σ calculated by the equivalent circuit with the resistance and capacitance values of *table 4.3* are plotted with their corresponding data sets in *figures 4.13* and *4.14*. In both figures, the fit to the cells impedance in the dark is also plotted to demonstrate how significant the change in the impedance data is with increasing illumination. The fit to the dark data set is exceptional, as one would expect considering the equivalent circuit is based on previously published works and all resistance and capacitance values are

freely fitted. The fits also agree well for AC frequencies above 10Hz at higher illuminations. However, below 10Hz the fits to the impedance data when the cell is illuminated do not completely agree. The calculated impedance appears to slightly over-predict |Z| for the slowest frequencies for cell illuminations above 4mWcm^{-2} and a significant divergence is demonstrated between the equivalent circuit fit and the experimental data for the phase response of the cell below 10Hz at the higher illumination intensities. The equivalent circuit fit for the impedance phase not only fails to be in quantitative agreement but the general trend predicted is also significantly divergent from the experimental data. This lack of agreement at low frequencies and higher illumination levels is an indicator that the proposed equivalent circuit model is not a complete description of the cells electronic behaviour; it is only a valid approximation in the low intensity limit.

Light / mWcm^{-2}	R_{PVK} / MΩ
0.0003	176
0.033	113
0.098	79.8
0.163	66.3
0.326	45.0
0.815	27.5
1.63	21.4
2.93	13.1
4.07	11.4
6.52	9.06
9.78	6.89

C_{PVK}	R_{LC}	C_{LC}	R_{PI}	C_{PI}
67.4nF	0.806MΩ	0.435nF	0.301MΩ	137nF

Table 4.3: Equivalent circuit fit values for the electrical impedance of the cells. Only the resistance of the PVK layer is dependent on light. Light is the calculated intensity of a λ = 532nm laser onto the PVK layer, not the intensity incident onto the sample, ~16% transmission through the Au.

Therefore, we need to determine which layer is incorrectly modelled. From the equivalent circuit fits, the frequency region demonstrating a constant |Z| is due to the liquid crystal layers resistance dominating the overall impedance of the cell. The fitted capacitance values for each layer also suggest that at the highest frequencies the electronic behaviour is dominated by the capacitance of the liquid crystal. Hence, almost all (99.3%) of the potential is dropped across the liquid crystal in this frequency regime and the PVK and PI alignment layers are effectively bypassed. This explains why photorefractive effects cannot be observed in this type of cell when a fast AC potential is applied. In the frequency region dominated by the liquid crystal layers impedance (>10Hz) the equivalent circuit model achieves a good fit.

Therefore, the liquid crystal layer must be accurately modelled and the fitted resistance and capacitance values correct for this cell.

As the PI alignment layer is not photoconductive, its impedance should not be affected by illumination. An observation confirmed by a similar investigation undertaken by Herrington [221]. Therefore, we must assume that the PI layer is correctly modelled and the discrepancies in our model fit are due to the electrical behaviour of the PVK when illuminated. The equivalent circuit used for the PVK layer is based on previous work [225] where the electrical impedance is only examined in the dark. In the dark, the RC circuit approximation also achieves good agreement with our system. Hence, to first approximation it correctly describes the layer. However, the photoconductive behaviour of PVK cannot be modelled under the assumption we made in the equivalent circuit that the polymers resistance is the only intensity dependent variable. The equivalent circuit to explain the photoconductive properties is more complicated.

The additional complexities of the equivalent electrical circuit for the PVK could be the result of several factors; an alteration of the conduction band energies from a metal semi-conductor boundary, a variation in the conductivities for ions, electrons and holes or a demonstration of non-Ohmic electrical behaviour such as a diode[VIII]. Using an unphysical constant phase element [226] can achieve a good fit. However, there is no physical justification for such an element in our system. As the measurements were acquired in the low signal limit, the effects of a metal semi-conductor boundary and the possibility of non-Ohmic behaviour are limited. Hence, it is our belief that the failure to account for a difference in the conductivities of the PVK for ions, electrons and holes (a difference that is known in the literature [152, 227, 228]), results in the strongest disagreement between the equivalent circuit and the experimental data. It could be expected that a more complicated model would then be proposed to fit the impedance data; however, a more complicated model that accounts for the additional electronic factors has not yet been determined. In addition, an improved electrical model would introduce significantly more unconstrained fitting variables that would pose serious questions to the validity of the model and the fit as a large number of unconstrained fitting parameters can match almost any impedance data.

A further indicator that the PVK's impedance is not correctly modelled is in the value of the light dependent resistance. In the dark where our circuit is in good agreement the PVK's resistance is two orders of magnitude larger than the liquid crystals. For slow AC or DC potentials the impedance of the cell should be determined only by the resistance of each layer. This would suggest that the potential dropped across the liquid crystal is almost zero. This is an inconsistent analysis with the subsequent observations of the operation of these types of cell in *sections 4.2.3, 4.3, 5.3* and *5.6*. However, the impedance fits do demonstrate that the PVK:C_{60} layer is significantly photoconductive when illuminated by λ = 532nm light, as the layers resistance can be reduced to less than 4% of its original resistance in the dark. Hence,

[VIII] A diode like behaviour is observed in later experiments in *section 5.3*.

the cells should operate as expected. However, we will not be able to numerically simulate there electronic behaviour as the there is insufficient confidence in the equivalent circuit fits to incorporate it into the model.

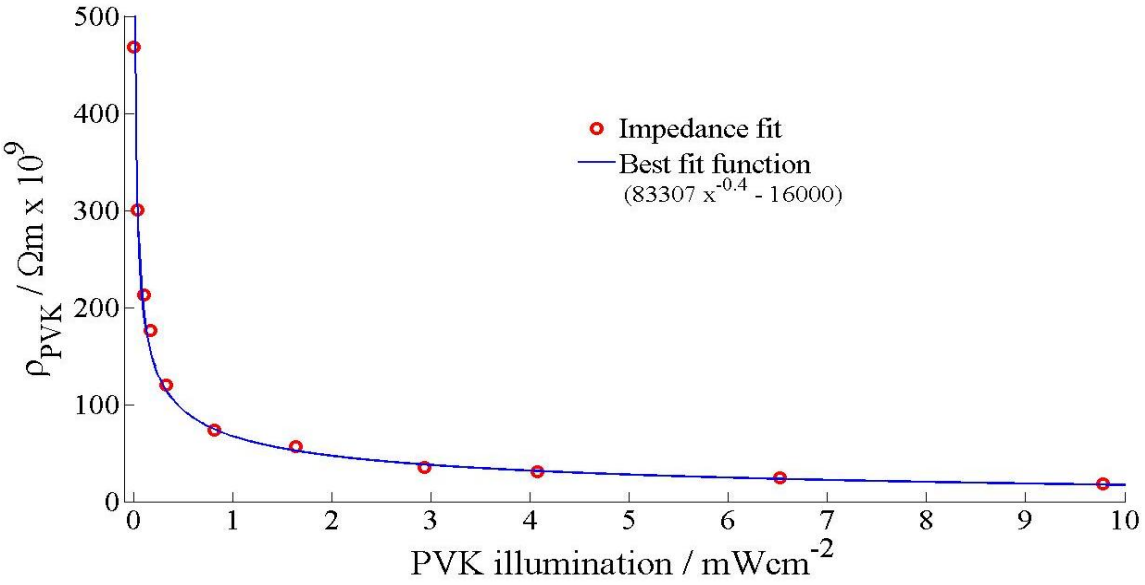

Figure 4.15: A graph illustrating how the PVK's resistivity decreases with illumination. The fit (general function, not theoretical prediction) clearly shows the value of R_{PVK} is a non-linear function with illumination intensity. PVK sample area is 400mm^2 with a thickness of 150nm.

The change in the layers resistance with illumination is also non-linear as presented in *figure 4.15*. The resistance drops rapidly with little illumination then levels out to an almost constant value for intensities higher than 3mWcm^{-2}. Interestingly, it is at this intensity that the equivalent circuit begins to demonstrate a noticeable disagreement with the experimental data. The inability to account for this non-linear intensity dependent behaviour may result in our numerical simulations over or under-predicting any photorefractive effects from a spatially modulated intensity profile.

The data presented in *figures 4.13* and *4.14* is for a single cell with a 150nm PVK layer, 11.85µm liquid crystal layer. This data is typical of the impedance spectrum of all functional cells before electronic aging (use under experimental conditions). The only variation between cells is a slight change in the frequencies of each part of the impedance spectrum; the general trends remain the same. The impedance spectra after electronic aging, is significantly dependent on the sample and its electronic history due to ionic movements within the cell. However, an aged sample generally demonstrates an impedance spectrum in the dark similar to those observed with higher illumination intensities before electronic aging. This further stresses the inadequacies of the simple proposed equivalent electronic circuit. Measurements of a cell's impedance after electronic aging are still important as they can easily indicate if the sample is damaged or if a significant change in the electronic nature of the cell has occurred and that the sample should stop being used in further measurements.

The presented impedance measurements are in the low signal limit. Using a potential with a magnitude comparable to later experiments (typically 15V) demonstrates a slightly changed impedance spectrum, *figure 4.16*. The equivalent circuit fits to this data require the same values for the capacitance as the low signal limit data; however, the resistances of each of the layers decreases (values listed in figure). The change in the liquid crystals resistance is due to the re-orientation of the liquid crystal director. Whereas a change in the PVK and PI layers resistance indicates that the electrical behaviour of the polymers is non-Ohmic. This could be due to the injection of free charges into these layers [229]. As impedance measurements require the system to be Ohmic for accurate determination of systems electronic properties, we cannot confidently say that the values listed in *figure 4.16* truly represent the equivalent electrical system. Hence, the impedance measurements can only be used to indicate that photoconductive effects are indeed present in the system as designed, or to determine if a significant change in the electrical behaviour has occurred.

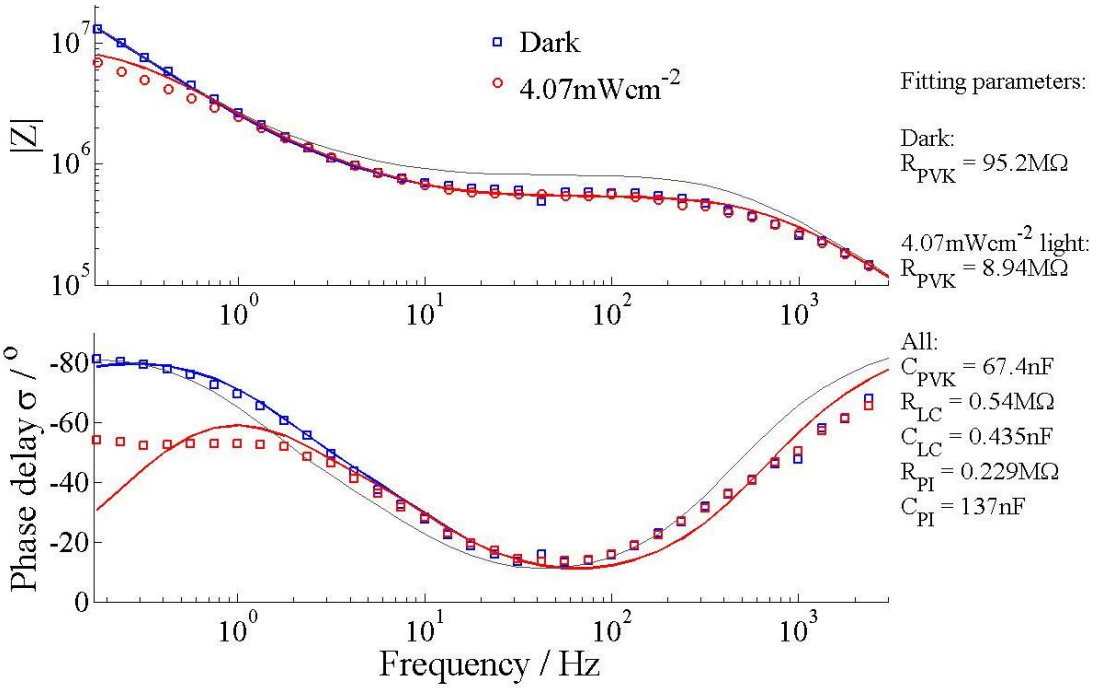

Figure 4.16: The impedance data of a sample when the applied AC potential is 15V. The solid blue and red lines are the impedance data fits using the parameters listed on the right hand side of the figure. The sample is the same one as used in *figures 4.13-15*. For comparison, the fit to the dark data acquired with a 0.5V potential is also plotted (light grey line).

4.2.2 Crossed Polariser Measurements

Applying a sufficiently strong electric field to a liquid crystal cell will result in the liquid crystals director re-orientating. As the director determines the refractive index of the layer, the orientation of the director throughout the cell as a function of the applied voltage needs to be identified. Experimentally, this is achieved with crossed polariser transmission spectroscopy and a comparison to a theoretical model as discussed in *section 3.2.2*.

We first examine the crossed polariser transmission of our cells when we apply a 1 kHz AC potential. A typical example of the crossed polariser data for one of our cells at wavelengths of 532nm, 632nm and 850nm is presented in *figure 4.17*. This data demonstrates the expected behaviour of a planar liquid crystal re-orientating to the applied potential. The initial transmittance is determined by the wavelength of the probe light, the birefringence and the thickness of the cell (11.85µm in this example). Therefore, the initial transmittance can be any value between 0-1; however, we have chosen to present wavelengths where the initial transmission is ~1 for convenience. When the applied potential is small (<0.7V_{rms}), the transmittance remains constant as the applied potential generates an electrical force that is insufficient to overcome the elastic forces within the liquid crystal layer for any distance through the cell. When V reaches a value of ~0.75V_{rms} the transmittance of the cell begins to change. This potential is the Freedericksz transition (threshold) for this cell. At this potential the electrical forces begin to exceed the elastic forces and re-define the liquid crystal alignment. As the initial liquid crystal alignment is planar and determined by anchoring forces from the surface treatment of the confining polymer interfaces, the initial re-orientation of the director at the Freedericksz threshold only occurs at the mid-point of the layer where the elastic forces are weakest. The slight re-orientation alters the transmittance, as it adjusts the phase delay between the orthogonal polarisations states as described in *section 3.2.2*.

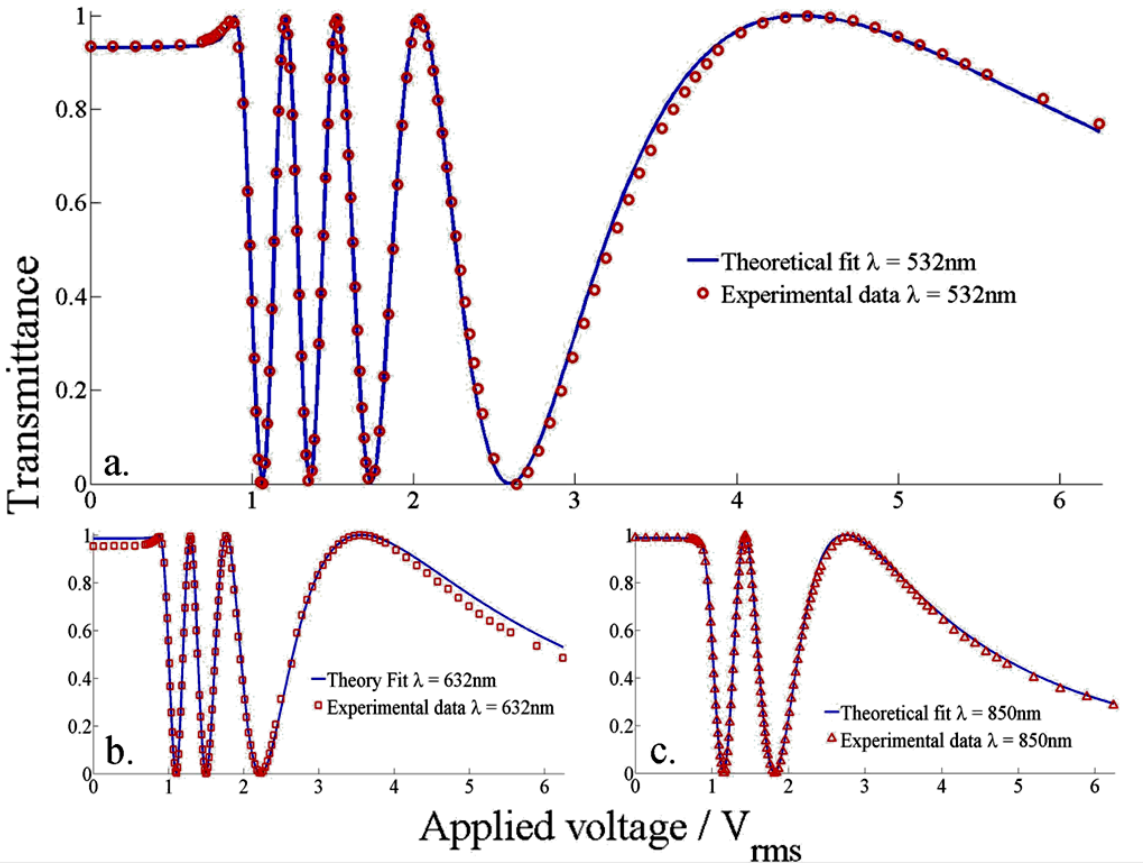

Figure 4.17: The crossed polariser transmission through a sample with a 1 kHz AC potential applied to the cell. a) Wavelength of light λ = 532nm, b) λ = 632nm, c) λ = 850nm. Cell thickness d_z = 11.85µm.

The initial change in the transmittance when the potential begins to exceed the Freedericksz threshold is not as sharp as one would expect at the transition. The transition demonstrates a slight curve; this curve is most clearly observed in *figure 4.17c* and indicates that a pre-tilt in the cells alignment is present. This pre-tilt could be on either or both of the confining interfaces as this experimental method cannot identify which side of the cell it is present on. However, a pre-tilt of 2^{o} is expected at the PI interface [230] and zero pre-tilt is expected at the PVK interface [231]. As we have no information to contradict these observations from the literature, we will assume these are the pre-tilts at each interface within our cell.

The transmittance then changes rapidly, demonstrating a periodic behaviour with multiple minima. The number of minima observed increases for shorter wavelengths. This rapid changing region between $0.75V_{rms}$ and $2V_{rms}$ is due to large re-orientations of the director within the bulk (*figure 4.18*: $0.75\text{-}2V_{rms}$). The periodicity of the transmittance minima is not constant as the director's re-orientation and the phase delay of the layer are not linear responses. The change in the transmittance for potentials between $2V_{rms}$ and $5V_{rms}$ is still large; however, the rate of the transmittance change is reduced. This is because the director in the bulk region of the layer begins to fully align itself to the applied potential (*figure 4.18*: $2\text{-}5V_{rms}$). Therefore, it does not contribute further to the change in the phase delay of the layer. The additional transmittance change is a result of the additional director re-orientations from the smaller regions near the polymer interfaces.

For potentials above $5V_{rms}$ the additional change in the transmittance is very gradual as the entirety of the bulk region of the layer (1-11μm region in *figure 4.18*) is fully aligned to the potential. If the potential were increased further than in the experimental data presented, the transmittance would approach zero as the entirety of the liquid crystal layer becomes aligned to the potential and there would then be zero phase delay between the polarisation components of the probing light.

The crossed polariser transmittance data indicates that there is a maximum phase shift between polarisation components of $5\text{-}9\pi$ depending on the wavelength of the probing light. This is due to the fact that the E7 liquid crystals within the cell demonstrate a large birefringence.

The crossed polariser data is fitted by first determining the liquid crystals director orientation profile for the applied potential with the model describe in *section 2.5,* as presented in *figure 4.18* for several example potentials. From the impedance measurements we know that at a frequency of 1 kHz the potential is only dropped across the liquid crystal layer. The unknown electrical behaviour of the PVK layer will not influence the magnitude of the applied potential across the liquid crystal. This calculated director profile combined with a measurement of the cells thickness[IX] is fitted to the data, with the magnitude of the anisotropy

[IX] Determined by an independent measurement using the interference fringes from UV-VIS transmission.

between the ordinary and extra-ordinary refractive indices as the only fitting variable. The fits acquired (blue lines in *figure 4.17*) demonstrate a remarkable agreement with the experimental data. Hence, the liquid crystal model must incorporate all the physics of the director's alignment when the potential is applied across the liquid crystal. These fits are then used to determine the extra-ordinary refractive index n_e, of the E7 liquid crystals. The values of n_e for E7 in the literature are not used, as the specific ionic chemistry within each cell structure requires us to independently determine n_e. The dispersion of n_e is determined by the wavelength dependent fits acquired in *figure 4.17* and a value for n_o from the literature [232].The refractive indices obtained are expressed as Cauchy relations in *Appendix B*. The slight disagreements between the fits and experimental data are a result of using a Cauchy approximation to describe the liquid crystals true dispersion.

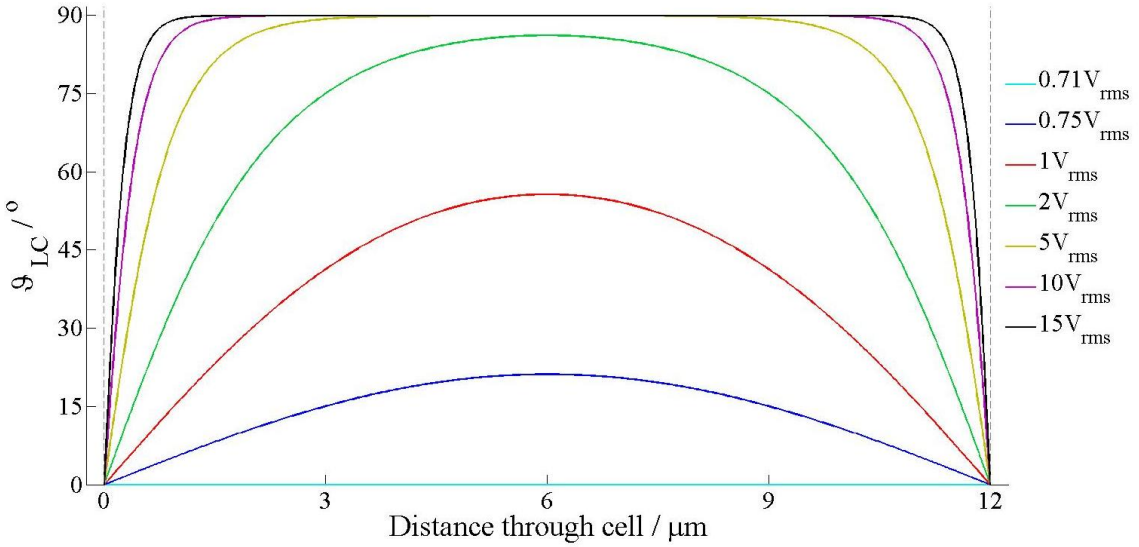

Figure 4.18: The orientation of the liquid crystal director from the alignment interfaces (ϑ_{LC}) as a function of distance into the cell, for the several V_{rms}. At the re-orientation threshold of $0.71V_{rms}$ the deformation is small (not noticeable in figure) above this threshold the re-orientation is significant in the bulk (1-11μm region of the figure). Cell thickness is 12μm; the cells boundaries are indicated by the dashed grey lines.

Though a 1 kHz frequency cannot be used to demonstrate photorefractive effects, the characterisation of the system with a 1 kHz field provides more reliable information about the liquid crystals response than the crossed polariser data from a slow 0.5Hz AC potential, *figure 4.19*, as it bypasses the effects of the PVK. A slow 0.5Hz AC potential is used instead of a DC potential to demonstrate photorefractivity due to stability issues (as explained in *section 5.3*). The crossed polariser transmittance for a slow AC potential demonstrates the same general behaviour as the 1 kHz AC data[X]. However, due to the PVK resistance, the features (Freedericksz threshold and minima) occur at higher potentials. In addition, the transmittance minima and maxima in the |V| = 4-6V region do not reach 0 or 1 respectively.

[X] The slow AC data is also identical (within experimental error) to the crossed polariser data for a DC potential

This is likely a consequence of a non-uniform electrical resistance for the PVK over a ~0.5mm length scale (diameter of the probe beam) examined in this experiment. Only a very small change in resistance is necessary for noticeable effects in the transmittance contrast of the crossed polariser signal in the 4-6V potential region. It may be difficult to remove the non-uniformality in the electrical resistance as it could be a result of spin-coating variations in the polymer thickness, C_{60} dispersion in the polymer or from the physical rubbing of the layer. Another experimental problem with a slow AC potential is that the transmittance takes a noticeable length of time (~30-60s) to reach an almost stable state due to ionic charging. Also the presence of an electrical bias (discussed in *section 5.3*) results in a hysteresis effect between the potential being ramped up and ramped down. Consequently the slow AC data is not fitted with the theoretical model; however, it does indicate the range the magnitude of the potential needs to be in order to demonstrate SPP manipulation (>7.5V for noticeable effects).

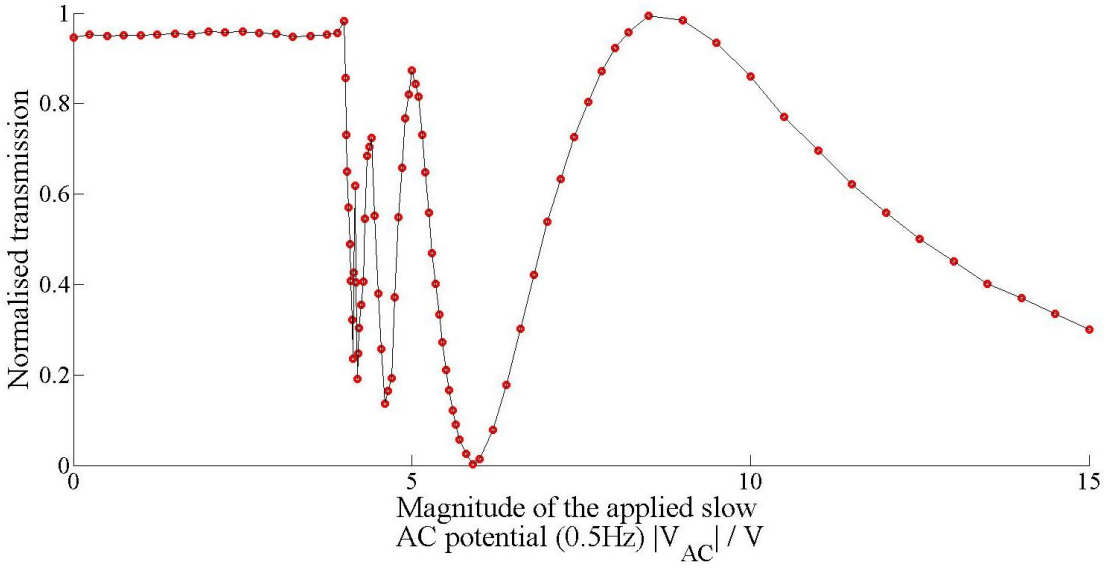

Figure 4.19: The crossed polariser transmission through a sample for 532nm light when a slow 0.5Hz AC potential is applied to the cell. The crossed polariser transmittance is determined only at the phase ($\pi/2$), corresponding to +|V| being instantaneously applied to the cell. This is to remove the effects of the liquid crystals dynamic behaviour, as discussed in *section 6.3*, from the data. The black line is a guide for the eye only as the first transmission minima/maxima are hard to resolve.

4.2.3 Electrical Control of the SPP Wavevector

The crossed polariser measurements clearly demonstrated that the orientation of the liquid crystal director can be controlled with an electric field applied across the layer. This re-orientation of the director will change the layer's effective refractive index and therefore will alter the wavevector of the SPP mode. We characterise the change in a SPPs wavevector when a 1 kHz AC potential is applied to the cell, where the entirety of the potential is dropped across the liquid crystal layer, to determine the amount of control we can exert over the SPP with this type of device. This data is then compared to the full numerical simulations of the

theoretical SPP wavevector to confirm that the liquid crystals electronic response in our model is accurate in the region of the layer that a SPP interacts with.

The ATR spectrums of 1.462eV SPP modes in our cells when an increasing 1 kHz potential is applied to the sample are presented in *figure 4.20*. As the applied potential increases so too does the wavevector of the SPP mode. For potentials below $5V_{rms}$ and above the Freedericksz transition at $0.75V_{rms}$ the change in the wavevector Δk is small ($<0.02\mu m^{-1}$). Noticeable changes in the wavevector of $\Delta k > 0.06\mu m^{-1}$ are possible for potentials larger than $7V_{rms}$, with a maximum observed $\Delta k = 0.42\mu m^{-1}$ for a $49V_{rms}$ potential. Larger potentials are not examined, as the potential would permanently change the liquid crystal's alignment near the interface by introducing a significant pre-tilt. In addition, the typical exposure times used to acquire the ATR spectra, result in potentials larger than $49V_{rms}$ beginning to damage the Au and PVK layers.

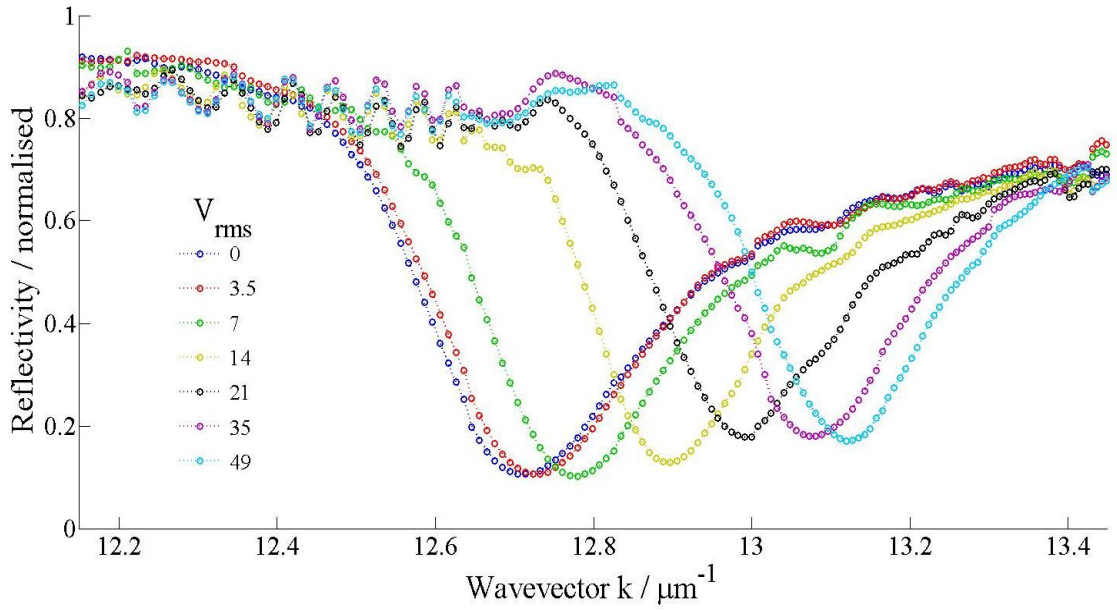

Figure 4.20: The shift of the reflection dip in the ATR spectrum when a 1 kHz AC potential of increasing magnitude is applied to the cell. Lowering or removing the potential returns the resonant SPP mode to its previous wavevector, therefore the process is reversible. Δ_{PVK} = 80nm, E_{SPP}=1.493eV.

The minimum potential required to observe a change in the SPP wavevector of $3.5V_{rms}$ is higher than the potential required for a change in the crossed polariser transmittance in this cell. As the SPP only probes the liquid crystal's director in the small (<200nm) region adjacent to the PVK layer and as *figure 4.18*indicates, the director does not begin to change noticeably in this region until potentials greater than ~2-$5V_{rms}$ are applied. A significant Δk is demonstrated for potentials $>5V_{rms}$ and this potential region corresponds to the final gradual change in the crossed polariser transmittance where the additional change in the birefringence is only due to the re-orientation of the director near the interface. Hence, the large director change in the bulk with an applied potential, which influences the crossed polariser signal does not influence the SPP wavevector as expected for a mode confined to the Au-PVK

interface. As the wavevector is only determined by the director near the interface Δk increases for potentials up to $49V_{rms}$ even though the majority of the liquid crystal layer has no additional electrical response for potentials above $10V_{rms}$.

However, the bulk alignment of the liquid crystal director does influence the ATR spectrum, as the liquid crystal layer can now act as a waveguide for guided modes. The guided modes are the cause of the periodic changes in the normalised reflectivity in the 12.2-12.7μm^{-1} region of *figure 4.20*. The liquid crystal waveguide is generated by the high effective refractive index of the bulk region acting as the waveguides core, with the lower effective refractive index regions near the PVK and PI interfaces acting as the cladding. The presence of guided modes in the ATR spectrum of SPP interacting with liquid crystals has been previously observed [157, 158], where the guided modes are a series of sharp changes in the reflectivity that can overlap the broad SPP resonance. Guided modes are also predicted in our numerical simulations of the ATR spectrum (see the inset of *figure 5.5* for an example) and they demonstrate that almost 100% of the light can theoretically couple into the guided mode. The modes observed in our experimental data and in the previous papers referenced do not demonstrate 100% of the energy coupling into the mode, for example; in our data set ~10% of the light is coupled into a guided mode. There are several possible reasons for the experimental and theoretical difference in the observe excitation efficiencies;

1. The resolution of the experimental equipment is insufficient to resolve the very sharp excitations of the guided modes.
2. A liquid crystal material is not a good medium to support guided modes. Thus, generating large losses that are not modelled in the simulations.
3. The thickness of the waveguide in the sample is not spatially uniform due to slight (<0.1μm) variations in the thickness of the liquid crystal layer. This could be caused by the top PI/ITO coated plate not being perfectly parallel to the Au/PVK substrate as assumed in the theoretical model. In addition, the boundary between core and cladding in a liquid crystal may not be well defined.

However, in our samples the guided modes do not overlap the 1.462eV SPP resonance examined. Therefore, the presence of guided modes does not adversely affect the operation of the cell and they are not generally considered. Guided modes do, however, become a significant problem in our cells when examining SPP with energies below 1.3eV. In principle we can remove the guided modes by re-designing the cell structure by having a homotropic alignment for the liquid crystal at the PI interface and by using our high refractive index glass for the top plate of the sample. This is an additional design feature that we will likely later introduce into our cell design.

Using a potential applied to a liquid crystal to control the SPP wavevector has been demonstrated before [157, 158, 162, 163] and is the subject of several patents[XI]. Hence,

[XI] For example U.S. patents no[o]: 5,451,980 for a variant of the flat panel display and 6,738,194 as tuneable optical filter.

control of SPP through a liquid crystal director is not a novel application. However, it is an important characterisation step of our devices when demonstrating our novel photorefractive control of SPP using a hybrid photorefractive liquid crystal cell.

We then compare the numerically calculated SPP wavevector determined by the dip in the theoretical ATR spectrum generated by our optical model of the cell without using any fitting parameters to our experimental data in *figure 4.21*. This additional comparison is made because though the description of the layers birefringence on the SPP modes (*figure 4.12*) and the bulk director alignment of the cell (*figure 4.17*) has been successfully predicted, we need to confirm that the theoretical liquid crystal alignment near the interface and the Berreman model used for the optical simulations in this region of the layer is correct. The theoretical prediction of the SPP modes presented in *figure 4.21* is a close approximation to the experimentally determined SPP wavevector. The slight discrepancy could be due to an implicit error in the perturbation expansion used to describe the liquid crystals birefringence [220]. However, as the discrepancy is an almost constant value we believe an almost perfect fit for all potentials would be possible if a fitting parameter for the PVK thickness is used i.e. a layer 82nm thick instead of the 80nm layer thickness assumed.

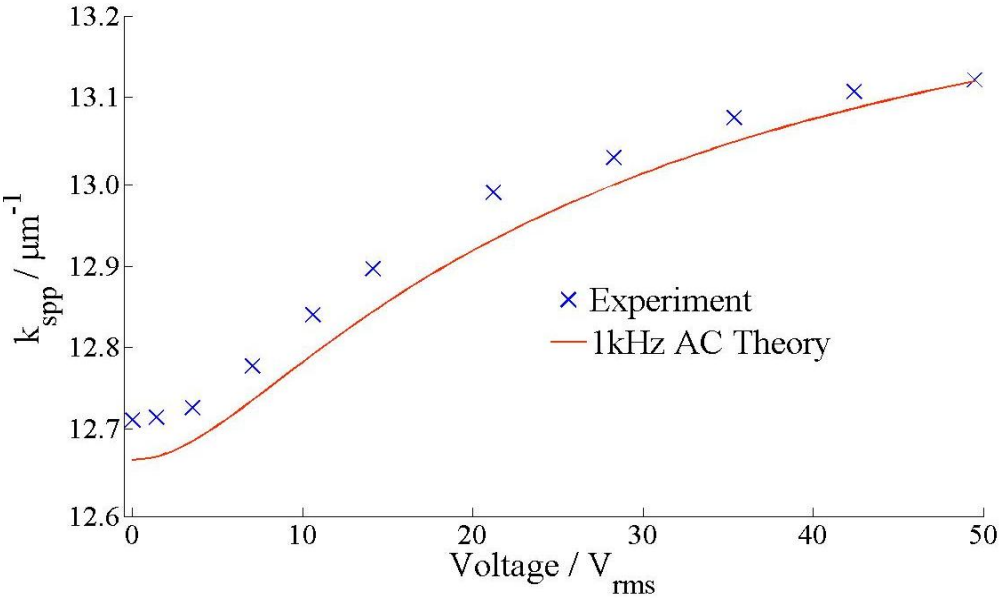

Figure 4.21: Comparison of the experimentally determined wavevector of the SPP in a sample with an 80nm thick PVK layer and the theoretical prediction using our liquid crystal model. The fit could be improved upon by using the PVK thickness as a fitting parameter. The theoretical SPP wavevector was calculated by Dr. K. Daly and Dr. G. D'Alessandro. E_{SPP} = 1.493eV. No fitting parameters were used.

From *figure 4.21* we can determine that the change in the SPP wavevector with a small change in the potential is greatest at ~15V_{rms}. Therefore, later photorefractive measurements should use a 15V potential to demonstrate the best Δk sensitivity for the system. In addition, the SPP wavevector appears to reach an asymptote for potentials greater than 49V_{rms}. This may be why we begin to observe damage in our cells at potentials higher than 49V_{rms}, as the

entirety of the liquid crystal including the anchored region is aligned as much as possible to the applied potential.

4.3 Photorefractive Control of SPP with Uniform Illumination

The final characterisation of our cells is of their photorefractive properties. To characterise the photorefractive effects of our samples, we will analyse the shift of the SPP wavevector. The shift of the SPP wavevector is used instead of TBG measurements to quantify the photorefractivity as it is more appropriate for our application. TBG measurements determine the photorefractive response of the entire cell and most notably the bulk region, whereas the SPP wavevector shift only determines the photorefractive response of the sample in the surface region of interest.

For photorefractive effects to be demonstrated in our cells, the applied potential must be partially dropped across the PVK layer. Therefore, the potential applied to the cell must be at a low frequency (<5Hz), due to the capacitance of the various layers of the cell. Photorefractive effects are normally achieved in this type of sample with a DC potential. However, for electronic stability reasons, discussed in *section 5.3*, we use a slow 0.5Hz AC potential instead. Consequently, this makes the system dynamic, as the liquid crystal's response time is quicker than a change in the instantaneous applied potential at this frequency. The dynamic effects of the liquid crystal are also dealt with in *section 5.3*. In this section we do not consider any dynamic processes; i.e. we can conceptually consider the applied potential to be DC. This is an approximation that is valid when the peak positive potential of the AC waveform is examined, as is the case in the following experimental data.

To characterise the typical photorefractive effects of the cells we first need to determine the wavevector of a SPP when the cell is in the dark. The wavevector of SPP in a typical cell in the dark is presented in *figure 4.22*, for 0.5Hz potentials from 0-20V. The potentials quoted are the magnitude of the slow AC |V|, not a V_{rms} measurement that is normally used to describe AC potentials. A measurement of |V| is used for all photorefractive measurements in the remainder of this chapter and *Chapter 5*.

The SPP wavevector within a sample when a 0.5Hz AC potential is applied demonstrates similar behaviour to that observed for a 1 kHz potential. This simple observation is contrary to the impedance data acquired in *section 4.2.1*, as the equivalent circuit fit (which was found to only be appropriate in the dark) indicated that the PVK resistance is two to three orders of magnitude larger than the liquid crystal layer. Hence, we would expect there to be almost zero potential dropped across the liquid crystal and no re-orientation of the director or shift in the SPP wavevector. However, our observations indicate that this is not true and that a significant potential is dropped across the liquid crystal. This observed shift without illumination is not ideal in the designed operation of the cell, as it will limit the refractive index contrast between light and dark that defines the photorefractive properties of a material. Though a comparison

to the SPP wavevector shifts with a 1 kHz AC potential[XII], indicates that the PVK layer is at least partially reducing the potential across the liquid crystal layer as an equal magnitude potential does not shift the wavevector as much with a 0.5Hz AC potential. Hence, it is still possible to observe photorefractive effects, even with this undesirable wavevector shift without any illumination.

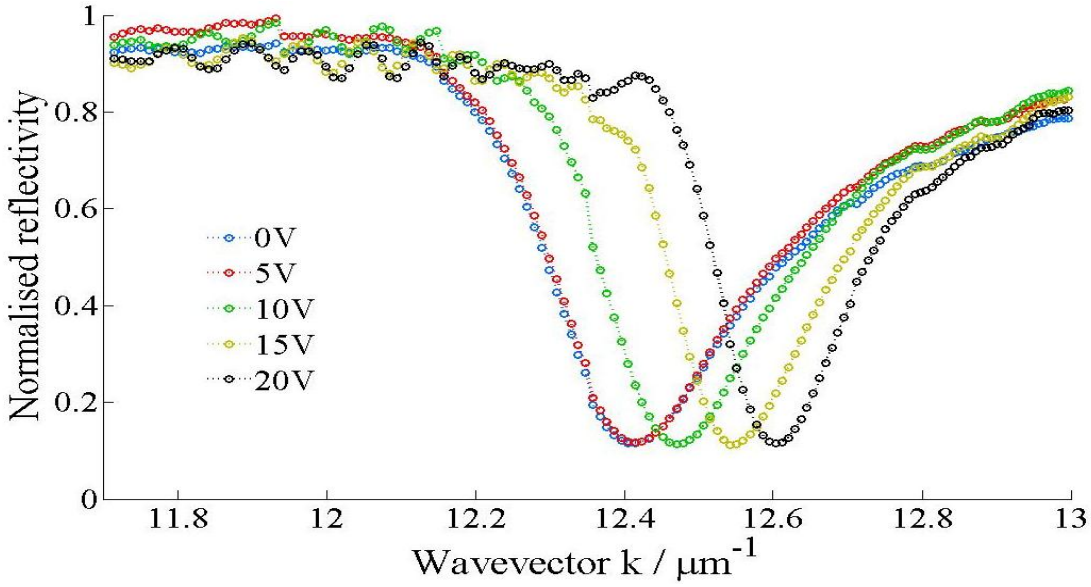

Figure 4.22: The shift of the SPP resonance in the ATR spectrum with a 0.5Hz AC potential for 1.462eV light. Δ_{PVK} = 102nm.

The ATR spectra for a 0.5Hz AC potential also demonstrate that guided modes can be partially supported within the liquid crystal layer. The modes do not have a large reflectivity contrast for the same reasons described in *section 4.2.3*. As these modes do not overlap the SPP resonance for the 1.462eV light that we typically examine, we will not consider them further.

Photorefractivity within our samples is observed by an additional SPP wavevector shift Δk when the cell is uniformly illuminated with ample λ = 532nm laser light. There is no observable change in the SPP wavevector with illumination if no potential is applied; therefore, the sample is not directly photorefractive as expected for this cell design. With an applied potential, the wavevector of the SPP demonstrates an additional shift with illumination that is comparable to the initial wavevector shift observed by applying a potential without illumination, *figure 4.23*, $\Delta k \approx 0.08\mu m^{-1}$. By illuminating the cell, the additional wavevector shift indicates that the effective refractive index of the liquid crystal layer has further increased. The increase in the effective refractive index is due to further re-orientation of the liquid crystals director away from the PVK interface (a ϑ_{LC} re-orientation). The magnitude of the wavevector for a 1.462eV SPP in this sample with illumination is $12.54\mu m^{-1}$; a 1.462eV SPP with this same wavevector can also be achieved by the application

[XII] The same data set as *figure 4.19*; however, for E_{SPP} = 1.462eV instead of E_{SPP} = 1.493eV.

of a larger potential, ~15V. Hence, Δk is caused by an increased potential across the liquid crystal layer. This is only possible due to a reduction in the PVK resistance. Therefore, the qualitative description of the operation of this type of cell (i.e. PVK as a light dependent resistor) is fundamentally true, even though we failed to quantitatively describe the electrical behaviour with our impedance measurements.

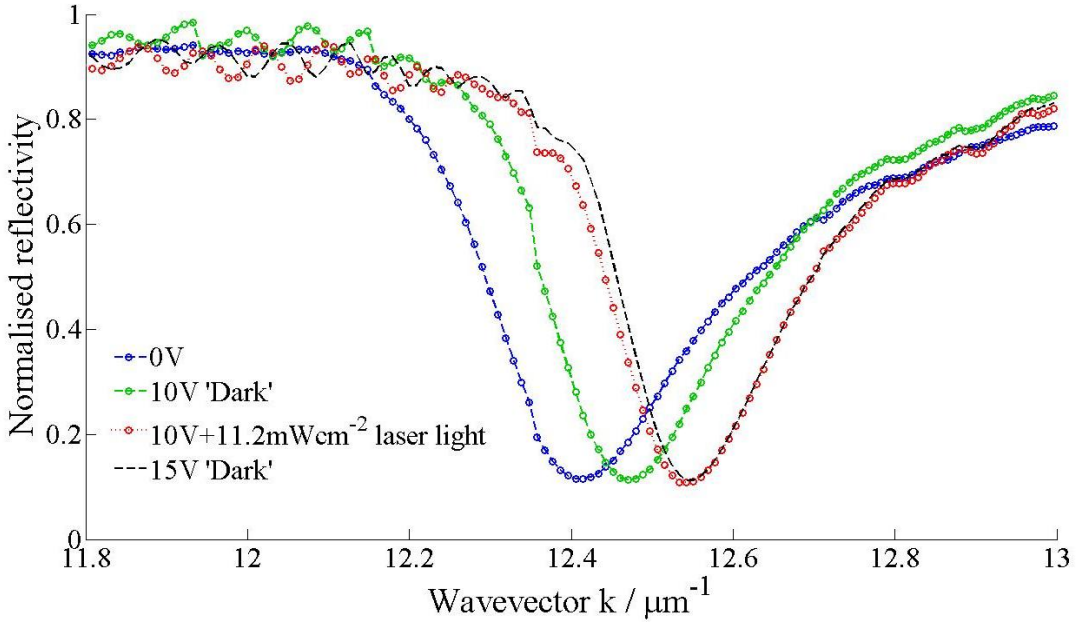

Figure 4.23: The additional shift in the SPP resonance in the ATR spectrum when the cell is illuminated with 11.2mWcm^{-2} laser light when a 0.5Hz potential is applied to the cell. The additional wavevector shift is comparable to applying a 15V potential in the dark. E_{SPP}=1.462eV, Δ_{PVK}=102nm.

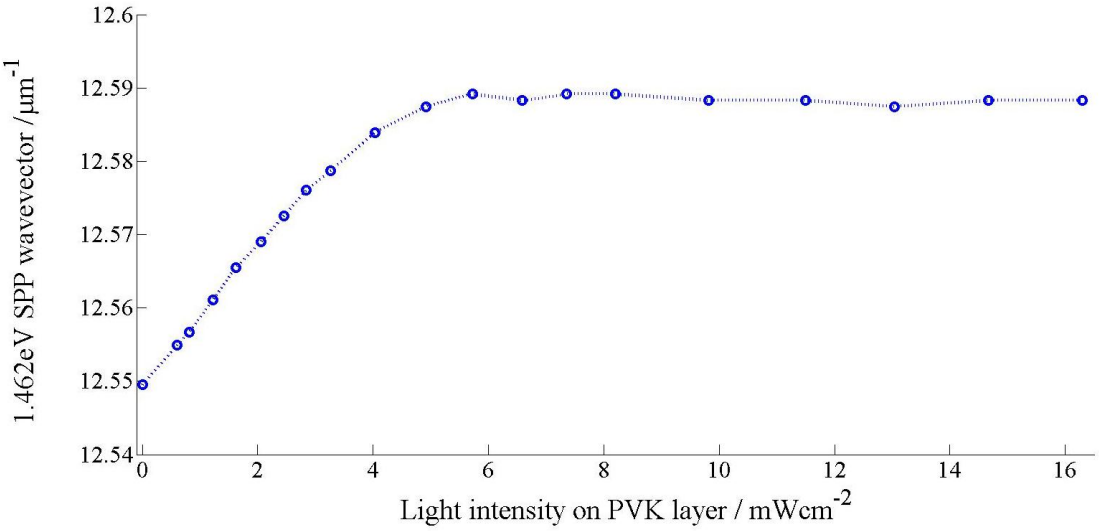

Figure 4.24: The photorefractive shift of a 1.462eV SPP with increasing illumination intensity. The wavevector shift is clearly linear with intensity until saturation. Δ_{PVK} = 102nm, |V| = 15V.

Having demonstrated the photorefractive effects typically observed within our cells, we then determine what influences the magnitude of Δk. We first examine how the SPP wavevector is dependent on the intensity of the monochromatic $\lambda = 532$nm laser light source, *figure 4.24*. A change in the SPP wavevector is observed with only a low intensity illumination $<0.7\text{mWcm}^{-2}$. This low or zero intensity threshold is expected; as a noticeable change in the cells overall impedance is observed with low intensities in the impedance measurements, due to a reduced resistance of the PVK. The wavevector of the SPP then linearly increases with increasing illumination intensity until at $\sim 5\text{mWcm}^{-2}$ the wavevector reaches a constant value. The linear increase in the wavevector cannot be simply interpreted as the actual light dependent impedance of the PVK is unknown and the liquid crystal is a non-linear system. Hence, the apparent linear trend is likely a convenient co-incidence within a highly complicated electro-optical system. The wavevector does not increase further for intensities above 5mWcm^{-2} as the C_{60} dopant used to sensitise the PVK to visible light is photo-saturated (all molecules excited) at this intensity. Further increases in the PVK's conductivity and the potential dropped across the liquid crystal are therefore not possible as no more free charges can be generated through the charge-transfer complex with the C_{60}. Hence, to maximise photorefractive effects in this type of cell, the intensity should be greater than 5mWcm^{-2}. This intensity would of course have to be re-evaluated if either a different photo-sensitizer or dopant concentration is used. Higher intensities in the $8\text{-}16\text{mWcm}^{-2}$ region are examined in *figure 4.24* to confirm that no further change in Δk occurs with intensities larger than the photo-saturation intensity of the C_{60} dopant in the sample. The constant wavevector at these intensities also indicates that no obvious electro-optical damage has occurred in the sample when exposed to these intensity levels whilst typical applied potentials and exposure times are used.

We then examine how the photorefractive control of the SPP wavevector is dependent on the magnitude of the applied potential, *figure 4.25*. Without an applied potential there are no photorefractive effects, as expected. No change in the SPP wavevector is observed in the dark until the potential is ≥ 5V, as from *figure 4.18* we know that for a 0.5Hz AC potential the typical effective Freedericksz threshold is at ~4V. However, with illumination there is a change in the SPP wavevector with a potential of 2.5V. A wavevector shift arises at this lower potential because the actual Freedericksz threshold is the potential applied only to the liquid crystal layer and is ~1V (*figure 4.17*). As we measure the total applied potential to the cell we need to factor in the resistance of the PVK when using a slow AC potential. Therefore, the effective Freedericksz transition (potential applied to the entire cell) is higher and intensity dependent.

The photorefractive wavevector shift Δk then increases rapidly until it appears that Δk is a constant value for potentials greater than 7.5V. The approximately constant value of Δk is due to the non-linear response of the liquid crystal and thus the SPP wavevector to a potential, as demonstrated in *figure 4.21* for a 1 kHz AC potential. The same non-linear behaviour also applies to the slow AC photorefractive system. As a consequence of this non-linear behaviour, Δk appears to remain constant at $\sim 0.07\mu\text{m}^{-1}$, though is in fact slightly larger at

~10V (~0.08μm^{-1}). At the highest potentials examined Δk begins to decrease as more of the liquid crystal layer is fully aligned to the potential in the dark; therefore, increasing the potential across the liquid crystal by illuminating the sample has a reduced effect as there is less of the layer that has an additional re-orientation response.

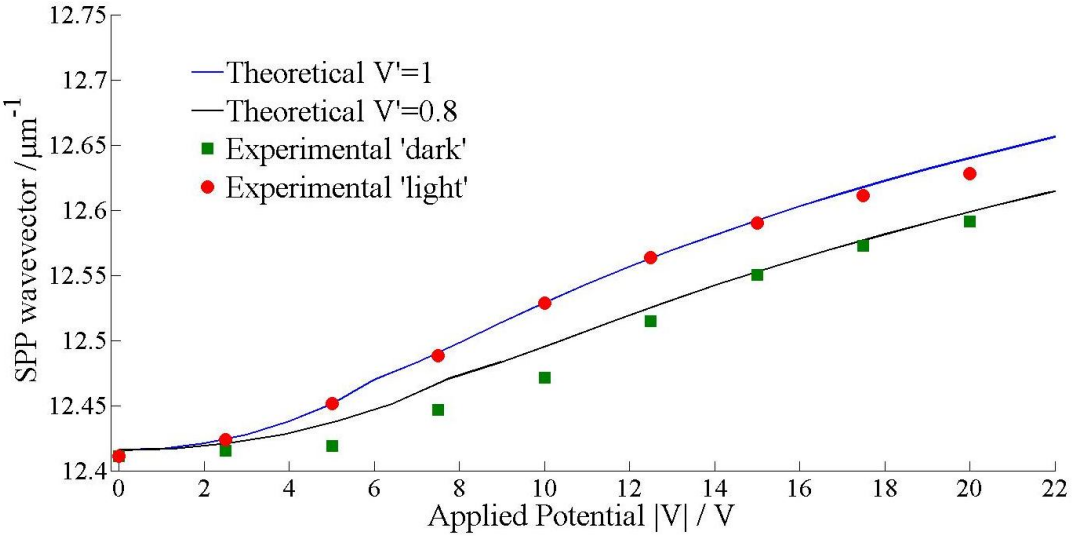

Figure 4.25: The wavevector of a 1.462eV SPP in a cell in the dark and with illumination (intensity ≈ 11mWcm^{-2}). The wavevector difference between the points demonstrates the photorefractive wavevector shift achieved with 0.5Hz potential of increasing magnitude. The theoretical SPP wavevectors using the V′ scaling factor described in the text are also presented. Δ_{PVK}=102nm.

We then compare the theoretical SPP wavevector, calculated with the full numerical simulations of the liquid crystal, to the experimental data to determine the fraction of potential that is applied across the liquid crystal when the cell is illuminated and in the dark.
As the electrical properties of the PVK layer are not directly modelled in the simulations, we assume the effect of the PVK can be described by a scaling factor V′, which describes the fraction of the potential across the liquid crystal compared to the total potential applied across the cell. This value will differ in the light and dark. Initially, we assume that V′ = 1, i.e. the PVK has a negligible electrical resistance and predict k_{SPP} for |V| = 0 to 22V. The numerically predicted SPP wavevectors can then be scaled to the experimental data using $0 \leq V' \leq 1$. The theoretical SPP wavevector with V′= 1 is presented as the *blue* line in *figure 4.24* and is a remarkably close fit to the experimentally determined wavevectors when the cell is illuminated, suggesting that V′ ≈ 1 and that the PVK resistance when illuminated is negligible. A fit to the SPP wavevector in the dark at ~15V (potential that is typically examined), requires V′ = 0.79 (*black line*), indicating that a large fraction of the potential is always applied across the liquid crystal. The V′ = 0.79 fit does not go through all the experimental points in the dark especially for the lowest potentials (<10V). This indicates that a simple linear scaling factor cannot fully describe the general operation of this device and is likely due to non-Ohmic behaviour in our system. The values of V′ fitted to the data are highly significant as they allow us to quantify the photorefractive effects that are relevant to

our application in our latter numerical simulations when we consider a non-uniform illumination profile. The required values of V′ for a fit to the experimental data are quite surprising as the impedance data for this type of device indicated that the PVK's resistance is significantly higher than the liquid crystal, thus we expected a lower V′ fit. In particular for the V′ fit for the SPP wavevector in the dark.

The theoretical fits suggest that between 20-30% of the applied potential across the liquid crystal can be controlled with illumination in our cells. Ideally, we would like a 100% modulation of the potential. Therefore, there is a significant improvement possible in these cells photorefractive properties by optimising the photoconductive layer. However, the 20-30% of the applied potential that we can control with light is significant enough to demonstrate noticeable photorefractive effects. Hence, the optimisation of this device is left for future investigations.

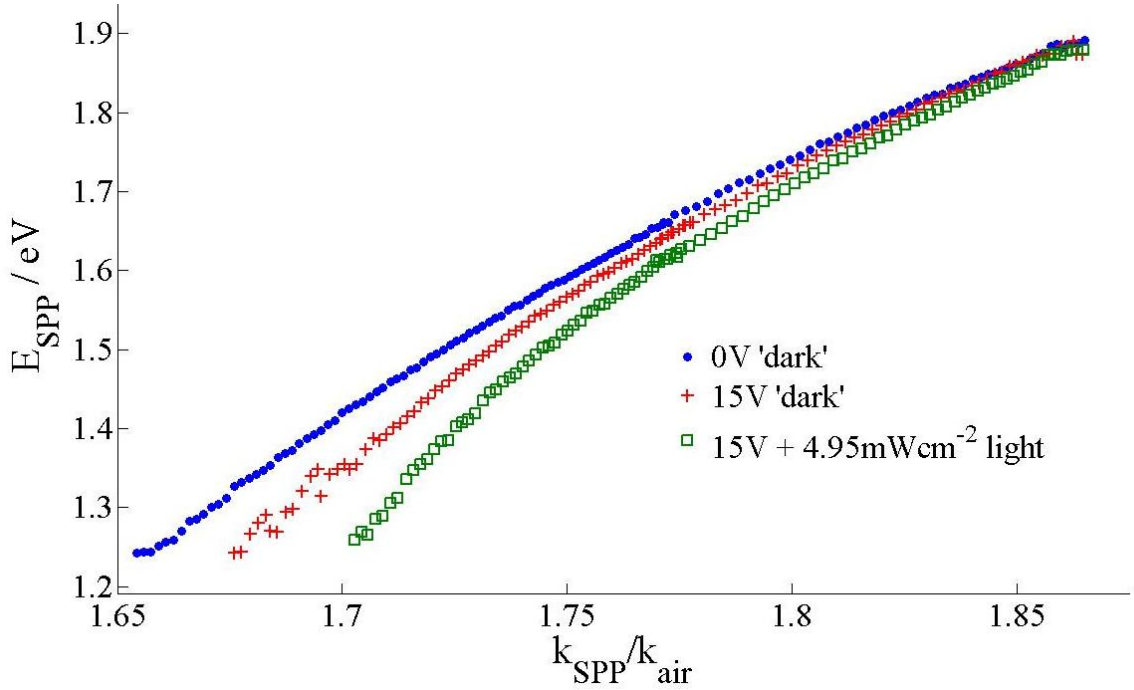

Figure 4.26: The dispersion of SPP modes in our samples when a 0.5Hz potential is applied with and without illumination. The 15V 'dark' data set is noisy for energies below 1.38eV due to the presence of guided modes interfering with the SPP resonance. Δ_{PVK} = 80nm

The final parameter investigated when examining the photorefractive properties of our cells is the dependence on the energy of the SPP mode (E_{SPP}). This is achieved by examining Δk in the E_{SPP} = 1.24eV to 1.9eV region as presented in *figure 4.26*. This clearly demonstrates an increased Δk due to photorefractive effects for lower E_{SPP}. This is the opposite of the shift that is predicted by a simple Drude free electron model with an increasing refractive index of the dielectric layer *figure 2.2*, where higher energy SPPs have an increased Δk. This significant discrepancy is because the Drude model does not account for the multi-layer structure of our samples, where the refractive index change of the liquid crystal occurs a

small distance away from the Au-PVK interface. As the penetration depth of SPP modes is energy dependent (*equation 2.13*), high E_{SPP} modes do not probe a sufficient distance from the Au-PVK interface to interact with the changing refractive index of the liquid crystal. Whereas lower energy SPP modes probe a further distance and their electric field overlaps more with the liquid crystal (see *figure 5.18* for an example) increasing the level of photorefractive control with this type of photorefractive device. In addition, due to surface anchoring there is a greater liquid crystal re-orientation further from the interface, causing an additional increase in Δk with an increased penetration depth.

Having determined the |V|, illumination intensity and E_{SPP} dependence of the photorefractive control of a SPP's wavevector Δk, we need to quantify the significance of the magnitude of Δk that is observed in our samples. While it is obvious that a larger Δk will result in greater photorefractive control of an SPP in a sample, we require a minimum value for Δk that may be necessary for practical uses of this device as an optical switch or for the observation of detectable non-linear effects. For use as an optical switch, Δk must ideally be large enough so that the photorefractive switching can completely turn off the mode. This shift is approximately equal to the FWHM of the SPP resonance i.e. enough to change the reflectivity of the sample at the angle θ_{SPP} from ~0% to ~100% in an ATR experiment. As the FWHM estimates the propagation length of the SPP δ_{SPP}, we compare the propagation length to a phase shift length scale p, determined by

$$p = 2\pi/\Delta k. \tag{4.1}$$

For an optical switch $p \leq \delta_{SPP}$ is our ideal requirement. However, for detectable non-linear effects such as the SPP diffraction examined in *chapter 5* we generally consider a larger maximum value for p as our requirement,

$$p \approx 2\delta_{SPP} \tag{4.2}$$

Equation 4.2 essentially states that the minimum requirement is that Δk is approximately equal to the half-width-half-maximum of the SPP resonance.

We then use *equations 4.1* and *4.2* to evaluate the photorefractive effects observed in our samples. As the comparison is against the propagation length of the SPP there is an energy dependence to the minimum wavevector shift required. Higher energy SPP will require a larger Δk, for the device to meet our requirements as δ_{SPP} is noticeably less.

Using *equations 4.1* and *4.2* to evaluate the photorefractive control of the sample presented in *figure 4.26*, a 1.24eV SPP which has a propagation length δ_{SPP} = 40.7μm (*table 4.2*), has a phase shift length scale of p = 30.3μm. Hence, as $p < \delta_{SPP}$, good photorefractive control of a 1.24eV SPP should be possible with this sample. By comparison, a 1.78eV SPP with a propagation length of 13.5μm has a value of p = 139μm in this sample. Therefore as $p \gg \delta_{SPP}$, the photorefractive control of 1.78eV SPP is expected to be extremely poor.

However, due to issues involving the overlapping of guided modes with the SPP resonance, a SPP mode with an energy of 1.462eV is typically examined. For SPP at this energy δ_{SPP} = 24.1μm and p = 53μm; hence, the photorefractive wavevector shift of a 1.462eV SPP in this sample just about demonstrates the minimum photorefractive control that we believe is required for the observation of sufficient non-linear SPP effects at this energy.

The benefit of optimising the samples further to increase the observed photorefractive control of SPP is obvious; time constraints did not permit this. The values used in the above example represent the typical photorefractive effects observed in all samples; there will of course be a small amount of sample to sample variation, though noticeably poor samples are not worthwhile examining. For practical photorefractive applications of this device, SPP with energies in the infra-red spectrum (<1.3eV) are likely to be required.

Chapter 5

SPP Interactions with a Refractive index Grating

Practical applications of a photorefractive SPP system with uniform illumination are limited to the switching of SPP modes. However, these devices can often be achieved without photorefractive effects; for example, a colour selective absorbing mirror [162, 163]. Far greater potential exists with the photorefractive devices developed in this thesis for demonstrating non-linear effects such as SPP gain. For gain we require a periodic refractive index profile to be generated in the liquid crystal layer using the interference pattern generated by two interfering electromagnetic waves. For a full demonstration of SPP gain this interference pattern would have to be generated by the SPP themselves. However, prior to developing a system to demonstrate SPP gain we must first establish and understand the mechanisms that determine the formation of the refractive index grating near the photoconductor interface, which will be subtly different from those that determine the TBG signal that generally occurs in the bulk region of the liquid crystal layer. In addition, we require the details of how the SPP would subsequently interact with the liquid crystals refractive index grating.

To acquire this knowledge, we examine a system where we observe the diffraction efficiency of a single SPP interacting with a refractive index grating. The grating is generated in the liquid crystal by using two external writing beams from the photorefractive TBG system described in *figure 3.8*. However, where a TBG system seeks to maximise the coherent energy transfer between the gratings writing beams, we will use the refractive index grating to transfer energy from a SPP mode into a new SPP mode. Therefore, we are examining a photorefractive grating out-coupler device. The experimental geometry of the grating out-coupler is displayed in *figure 5.1a*. The input beam is the white light source exciting the SPP modes and is incident at an angle ϑ to the normal of the sample's Au surface. The wavevector of the grating with pitch Λ, is orientated in the liquid crystal layer at an angle γ to the *y*-axis. The additional wavevector component supplied by the grating, then diffracts some of the energy in the SPP mode at an angles $\pm n\varphi$ with respect to the input beam's reflection, where n is an integer. The apparatus used to excite SPP and subsequently detect the diffracted signal is presented in *figure 3.2.* The intensity of the out-coupled light detected at angles $\pm n\varphi$ will determine the strength of the interaction of a SPP with the grating.

A clearer description of the operation of the SPP grating out-coupler device examined in this chapter is achieved with a *k*-space representation, shown in *figure 5.1b*. The refractive index grating is used to supply the additional wavevector component necessary to re-direct energy from a pump (input) SPP into a signal (diffracted) SPP. The signal SPP has the same photonic energy (E_{SPP}) as the input SPP; however, it propagates in a different direction. The magnitude of wavevector $|k_{SPP}|$ for the signal and pump SPP is assumed to be the same. The slight difference in $|k_{SPP}|$ due to the liquid crystals birefringence is negligible, as φ is typically between 3-10^{o}. This assumption is later proven to be appropriate in *section 5.4*.

There are seven notable variables in this system: the pitch Λ, and orientation γ, of the refractive index grating which determines $\underline{k}_{\Lambda}$; the energy of the SPP (E_{SPP}), as this influences the strength of the photorefractive interaction with the liquid crystal layer (*figure 4.26*) and partially determines $\underline{k}_{SPP}$; there are also several variables from the liquid crystal cell's photorefractive response that influence the grating formation and therefore the energy transfer of SPP; the magnitude of the applied potential |V|; the writing beam intensity I and the initial director orientation ψ_0 of the liquid crystal with respect to the SPP propagation direction. In addition, for long-term repeatability and stability of the device, the electric field that aligns the liquid crystal needs to be a slow AC potential. Therefore, the frequency of the slow AC field is also examined along with the consequential dynamic behaviour of the photorefractive liquid crystal system.

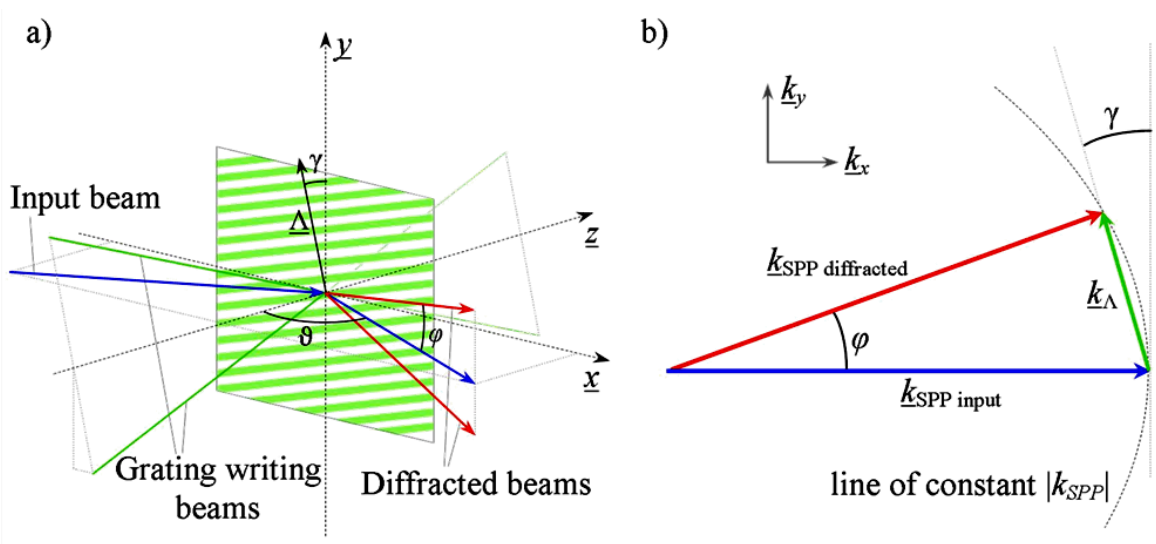

Figure 5.1: A refractive index grating coupler for use of SPP control. a) The geometry of the experiment. Note that the illumination creating the grating is over a significantly larger area than the SPP excitation beam, therefore the grating can be considered global. b) The 'k-space' representation of the grating coupler.

By analysing how the SPP diffraction efficiency depends on each of the variables listed, we can determine the ideal experimental parameters that maximise the SPP energy transfer in this system and future related SPP gain systems. In addition, this analysis will also provide details of the grating formation mechanisms in the region near the interface that is examined.

The data for this chapter will be presented as followed: first, we prove that a refractive index grating is written into the liquid crystal layer. Then we prove that the SPP interaction with this grating results in diffraction of the SPP and not scattering from surface roughness or poor surface alignment. Details are then presented about the experimentally observed dynamics of the diffraction efficiency when using a slow AC potential and theoretical reasoning for this behaviour. We then consider the dependence of SPP diffraction for each of the remaining variables; the orientation of the grating, the energy of the SPP mode, the magnitude of the slow AC potential, the intensity of the illumination generating the refractive index grating and the pitch of the grating. Finally, the SPP diffraction efficiency dependence on the initial in-plane director orientation ψ_0, with respect to the SPP propagation direction and grating is examined.

The experimental data provided is for several conditions for most of the variables examined. A complete review of the SPP diffraction efficiency over the entire variable space is not conducted due to the immense size of the variable space and time limitations. However, sufficient data has been obtained to determine the general variable dependence and the physical mechanisms responsible for the observed trends. The data presented is typical for samples with a slight difference in the thickness of the PVK layer; therefore, it represents the general response of these devices with these materials. We compared the experimental data to the full numerical simulations of SPP diffraction in our cells, using the theoretical model described in *section 2.5*. The numerical simulations are used to assist us, where possible, in isolating the mechanisms that determines the observed behaviour or to validate a qualitative description of a plausible mechanism.

The last section provides a brief summary of the optimum parameters for coupling energy between SPP based on the optimum parameters for SPP diffraction into the first diffraction order.

5.1 Refractive Index Grating Formation

The refractive index grating in the liquid crystal layer is generated by illuminating the PVK layer with the interference pattern from two crossed coherent λ = 532nm laser beams, when a potential is applied across the cell. The optics described in *figure 3.8* creates the periodic interference pattern with a pitch Λ, given by *equation 3.8*. The illumination of the photoconductive layer is from the Au side of the sample[XIII]. This is to prevent the non-uniform liquid crystal alignment distorting the wavefront of the two beams and complicating the form of the interference pattern. Illumination from the front of the sample results in the beams only passing through plane interfaces, into uniform isotropic materials before illuminating the PVK layer. Therefore, we conclude that the intensity profile can be accurately described by a $sin^2(k_\Lambda x)$ function.

[XIII] Considered the 'front' of the sample and the PI/ITO top plate the 'back', refer to *figure 3.11*.

The two-beam energy transfer that occurs within photorefractive materials as described in *sections 2.2.1 and 3.2.5*, confirms the presence of a grating in the liquid crystal layer. An example of the photorefractive gain possible with one of our cells, for a 24µm pitch grating and a cell rotation of 25°, is presented in *figure 5.2*. Until ~8V, no energy transfer is observed. Then at the DC Freedericksz threshold, both beams display a loss due to scattering from the initially chaotic liquid crystal alignment. Further increases in the potential then allow the grating to be formed; there is then a net energy transfer between the two beams. The gain co-efficient reaches a maximum of 300cm^{-1} at ~12V, before energy transfer into higher diffraction orders (self-diffraction) competes with the gain process.

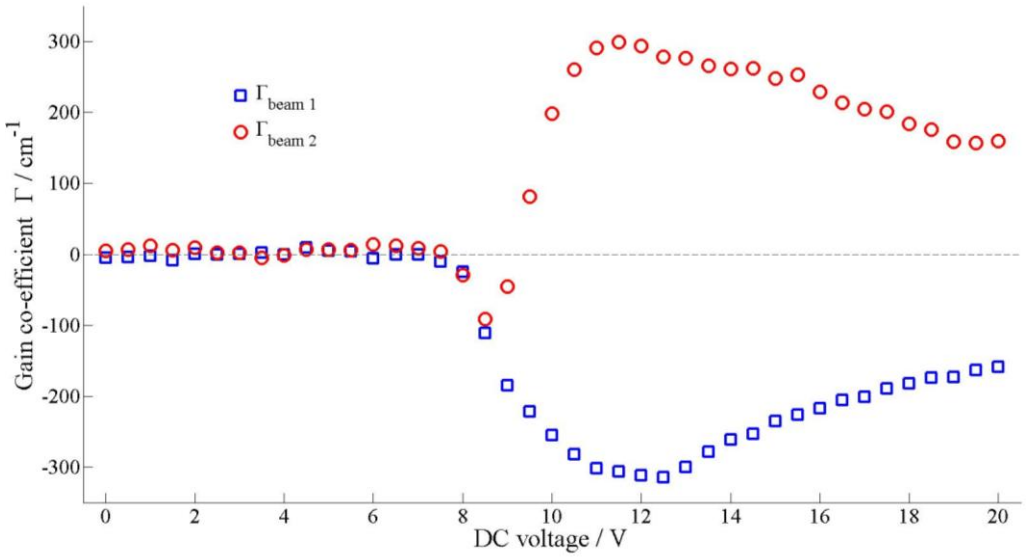

Figure 5.2: The photorefractive gain co-efficient for each of the λ = 532nm grating writing beam's for an increasing DC potential, for one of our samples. The cell is orientated at β = 25° and the grating pitch is 24µm. The initial intensity of both beams was the same. The intensity of beam 1, probe, increases at the expense of beam 2, pump, due to the formation of a refractive index grating in the liquid crystal layer of the sample.

The magnitude of the maximum gain measured in one of our cells is typically about Γ ≈ 250-300cm^{-1}. This value compares favourably with the literature for this type of photorefractive structure when an undoped liquid crystal is used. Gain values for an undoped E7 liquid crystal layer are listed at approximately 100-200cm^{-1} [147, 233]. The improvement in our cells compared to the literature is likely due to the level or distribution of the C_{60} doping in the photoconductive layer. Our C_{60} solution was filtered to remove large undissolved particulates; this may improve the PVK's diffusion and trapping of charges as the polymer layer is a more even blend of the two chemicals. Investigations into the level of the C_{60} doping or even using a C_{60} derivative such as *[6,6]-phenyl C61- butyric acid methyl ester* (PCBM) could improve the photorefractive effects of the cells [234]. However, the cells demonstrate noticeable gain so this method of cell optimisation was not investigated.

An alternative method of confirming the formation of a refractive index grating is to observe the self-diffraction of the writing beams. An example is displayed in *figure 5.3*. The self-

diffracted beams are even present when there is no cell tilt ($\beta = 0$), so allow confirmation of the formation of the grating under the same conditions used for the SPP diffraction experiments. The number of diffraction orders observed depends on the pitch of the grating. A pitch of 4μm shows self-diffraction up to the second order and a grating pitch of 10μm shows diffraction up to the fourth or fifth orders. However, gratings with a pitch less than 2μm do not demonstrate self-diffraction as these pitches are in the Bragg regime ($\Lambda << \delta_{LC}$) [113]. When the writing beams, after passing through the cell, are projected onto a piece of card or the wall, a line passing through all the self-diffracted orders and writing beams can be used as a measurement of the angle γ, the in-plane orientation of the grating.

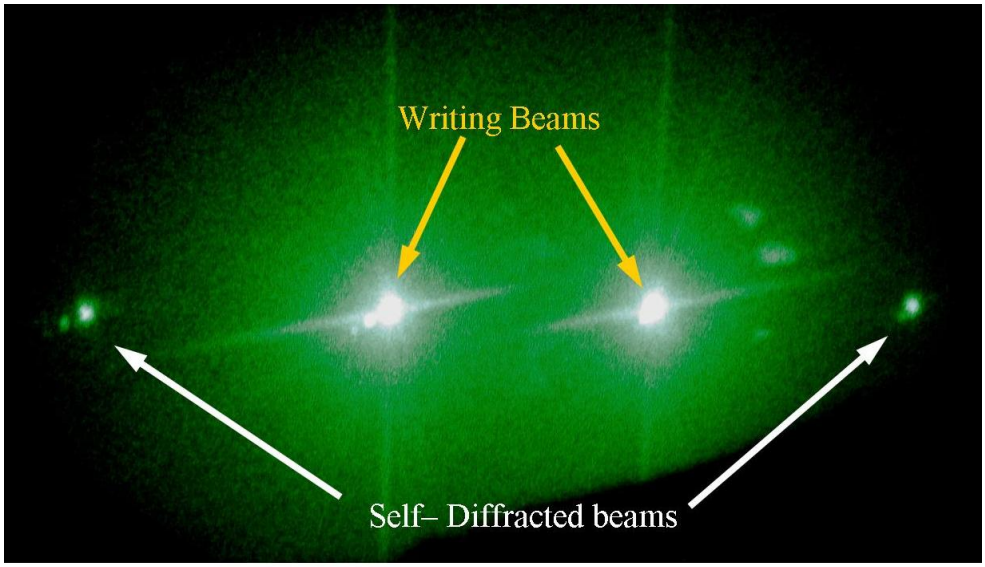

Figure 5.3: Image indicating the first order self-diffracted beams from a refractive index grating written into the liquid crystal layer. This observation is a quick method of confirming the formation of a refractive index grating in the liquid crystal layer. However, it cannot quantify the photorefractive response of the cell. Laser wavelength = 532nm, grating pitch = 4μm.

5.2 SPP Diffraction

The photorefractive two-beam gain and self-diffraction in our samples prove the grating is formed, however they probe the entire volume of the liquid crystal and interact more with the bulk or mid-point of the layer. Consequently, the results may not indicate the formation of a grating in the anchored region of the liquid crystal layer near the interface that interacts with the SPP. It is possible that in this region the liquid crystal alignment is chaotic, as the electrical forces that form the grating just exceed the elastic forces. If the thickness of this chaotic region is significant, greater than 50nm, then it could result in the SPP being scattered, in the same way surface roughness disperses the SPP energy [213].

It is unlikely that surface roughness from the rubbed PVK layer causes the SPP to be significantly scattered. As the amount of rubbing used to align the liquid crystal in our cells

does not introduce a significant broadening or reduce the coupling of light into SPP modes (see *figure 4.9*). A small amount of scatter is possible, though this will present itself as a global signal in *k*-space as there is not a single defined *k*-vector associated with the roughness. The periodicity of the roughness may also be large compared to the pitch of the grating and the SPP propagation length, limiting the interaction and our ability to resolve this effect.

We determine the SPP interaction with a light defined refractive index grating by mapping the detected spectrometer signal in *k*-space. For this we limit the SPP to propagate along the k_x axis, therefore $|k_y| = 0$, by introducing a 0.5mm width horizontal slit to the rail holding the SPP excitation optics displayed in *figure 3.2*. The finite width of the slit will result in a finite broadness to the detected signal. The broadness can be restricted by reducing the width of the slit at the expense of a greatly reduced signal received by the detection fiber. The coupling of energy into the SPP mode (excitation efficiency) is then determined over a small region of *k*-space, $k_y \approx$ -0.5-0.5, $k_x \approx$ 11.45-11.95, as displayed by the colour plot in between the horizontal white lines in the *figures 5.4 and 5.11*. In the figures the coupling of light into the SPP mode is zero for dark blue regions and is ~92% for the dark red region, the labelled colour scale is for the magnitude of the SPP diffraction efficiency not the excitation efficiency of the SPP mode.

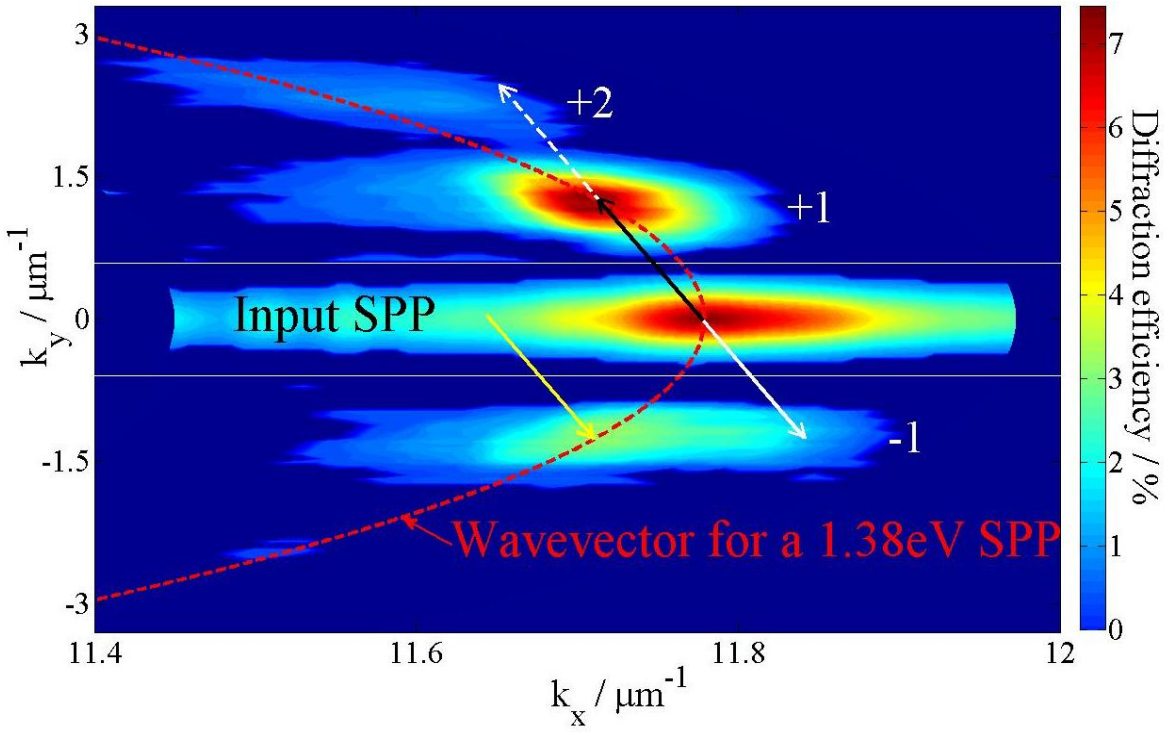

Figure 5.4: Diffraction from a 5µm grating aligned at 3.2° with respect to the k_y axis. Energy is coupled directly into the +1 order, black arrow. Energy is also coupled into other orders, the +2 and -1 order; however, the wavevector does not match the allowed wavevector for this 1.38eV SPP mode. Therefore, the yellow arrow demonstrates a more effective coupling that takes place as the grating is global. The dashed red line is in fact a circle in k-space if the k_x- and k_y-axes are scaled identically. Δ_{PVK} = 107nm, V = 15V.

The effect of the SPP interacting with a refractive index grating is determined by the presence of a detected signal in a *k*-space region where the SPP is not excited. For this experiment, the grating is written with its *k*-vector orthogonal or slightly tilted from being orthogonal to the SPP propagation direction, i.e. almost parallel to k_y. Therefore, any diffraction is away from the light exciting the SPP mode, which would otherwise saturate the spectrometer signal. Presented in *figure 5.4* is the detected signal for a 1.38eV SPP when a 4μm grating is written into the liquid crystal layer. The calculated wavevector of the grating is displayed by the arrow annotations.

Firstly, we notice that the detected signal is localised in *k*-space. This is the signature of diffraction. Therefore, the refractive index grating diffracts and does not globally scatter the SPP. If there is any scattered light, it is not resolvable over the background electronic noise from the spectrometer.

The grating in the *figure 5.4* example is orientated at 3.5^o with respect to the k_y axis and energy is clearly transferred into three different diffraction orders. The orientation of this grating corresponds to direct coupling into the +1 order. Surprisingly the detected signal for the other diffraction orders does not correspond to a point in *k*-space one would intuitively expect, as displayed by the white arrows in the figure.

The reason for this is that the SPP can only have a wavevector permitted by the dashed red line. For gratings not aligned for direct coupling, there is a wavevector mismatch, a concept discussed in *section 5.4*. As the SPP mode is excited by ATR the resonant coupling into the mode does not have a single value for *k*, therefore a more effective diffraction process is possible by the yellow arrow. This is possible as the grating is positioned globally in *k*-space.

The localisation of all the diffraction orders to a position on the dashed red line of *figure 5.4* proves that the diffraction of SPP is into other equal energy SPP modes propagating in different directions. If this were not the case, and the energy is coupled out directly as photons, then the diffraction spots would be localised at *k*-space positions at the end of each arrow annotation.

To significantly decrease the measurement time for all further measurements, only a single point in *k*-space is used to determine the diffraction efficiency. This point is the position of maximum diffraction for the order of interest. For example, the +1 order measurement point will be at the end of the black arrow at $k_x \approx 11.7$, $k_y \approx 1.44$, in the system presented in *figure 5.4*. This is done instead of acquiring a signal map of the *k*-space region of interest. This could lead to our results slightly underestimating the diffraction efficiency, if the measurement point in *k*-space is not perfect for the conditions examined. However, a manual search of several points in a small *k*-space region near the theoretical diffraction position is conducted to maximise the observed experimental signal, thus minimising any errors from the quicker measurement method.

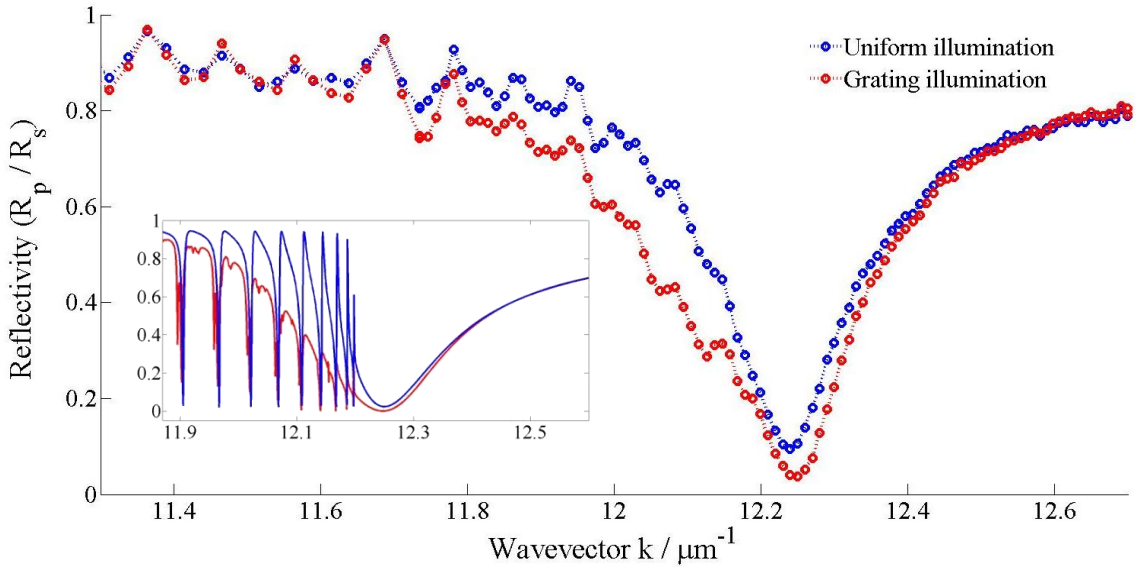

Figure 5.5: The ATR spectrum for a SPP when the illumination is uniform (blue) and when a grating (red) with the same average illumination intensity is written into the liquid crystal layer. The grating is orthogonal to the SPP propagation direction. (Inset) The behaviour predicted by our mathematical simulations. The experimentally predicted guided modes are not resolvable in the experimental data. $\Lambda = 4\mu m$, $|V| = 15V$, $E_{SPP} = 1.462eV$.

The generation of a refractive index grating in the liquid crystal also modifies the ATR spectrum of the SPP mode compared to when the sample is uniformly illuminated, *figure 6.5*. When the average beam intensity (I_{light} + I_{dark} /2) writing the grating is the same as the uniform illumination intensity, as is the case in *figure 5.5*, then the SPP wavevector is the same. This is because the SPP wavevector when a grating is written into the liquid crystal is the average between the wavevector of an SPP propagating in the dark and propagating in the illuminated regions (as the grating is approximately orthogonal to the SPP propagation direction). This effect combined with some energy being diffracted out of the mode results in the ATR spectrum of the SPP broadening. This behaviour is also predicted by our mathematical simulations of the system, inset *figure 5.5.*

5.3 Dynamics of the SPP Diffraction to a Slow AC field

To demonstrate photorefractive effects in our samples the electrical impedance of each layer of our hybrid photorefractive liquid crystal cells results in a requirement to use a DC or slow frequency AC potential. Unfortunately, it was discovered that a DC potential does not generate a stable and repeatable electrical environment for our measurements. Ionic charging in the cell, which occurs on the minute timescale, significantly changed the electronic response of a sample, sometimes increasing or decreasing a device's effectiveness. This charging required several hours to properly discharge and long-term damage was found to occur in the cells, significantly reducing a samples lifetime to 2-10 hours of operation.

Therefore, we decided to use a slow AC field to prevent the long-term build up ions in the liquid crystal that slowly alter its behaviour. This stabilised the electronic response whilst still allowing us to demonstrate photorefractive effects in our cells. Hence, repeatable measurements can be acquired and the sample lifetime increases to several months. However, the period of the slow AC waveforms used is much larger than the liquid crystal response time (~23ms for E7 [235]). Consequently, the liquid crystals alignment, and its effective refractive index, will follow in time the sinusoidal AC waveform. Therefore, the SPP wavevector becomes dynamic and needs to be accounted for.

The slow AC field is generated by a signal generator that is phase and frequency locked by a lock-in-amplifier to a chopper placed in the SPP excitation optics rail. The chopper wheel has a single slit that allows light to pass for $1/40^{th}$ of a rotation. The diode detector of the chopper can be rotated to introduce a phase delay between the AC field and the illumination of the sample. The phase delay between the probe light and AC waveform is determined by the trace of an oscilloscope. An example of the probe beam intensity in relation to the AC waveform is presented in *figure 5.6a.*

By changing the phase delay between the probe beam and the AC waveform, the dynamic behaviour of the SPP wavevector to the slow AC field is examined, *figure 5.6b*. We observe that the magnitude of the SPP wavevector follows the magnitude of the applied AC waveform in time, and is never a constant value. As the SPP wavevector is never constant in time, this indicates that the liquid crystal molecules near the PVK interface are always in motion and there is no apparent threshold potential for the initial re-orientation of the liquid crystal molecules. In a liquid crystal cell, the inversion symmetry of the liquid crystal results in the refractive index of the layer being controlled by the magnitude of the applied potential, not its direction. Therefore, the magnitude of the SPP wavevector is always larger with the application of a non-zero potential than the SPP wavevector when no potential is applied, regardless of the direction of the potential. However, the dynamic response of the SPP wavevector to the slow AC does displays a small asymmetry in the magnitude of the maximum SPP wavevector between the positive[XIV] and negative phases of the waveform. Hence, there may be a small electrical bias within the system. However, its affect on the SPP wavevector is sufficiently small that we can ignore this effect without a significant loss in accuracy.

In addition, the dynamic response of the SPP wavevector appears to slightly precede the applied AC waveform, as the phase of the waveform with the largest SPP wavevector is ~0.42π, whereas the maximum applied potential is at 0.5π. This is a consequence of the cell's electric impedance response at this frequency; with the phase shift being generated from the capacitance (complex impedance) of the various layers within the cell.

[XIV] The convention used is that a positive potential corresponds to the positive electrode of an equivalently applied DC field being attached to the Au side of the cell.

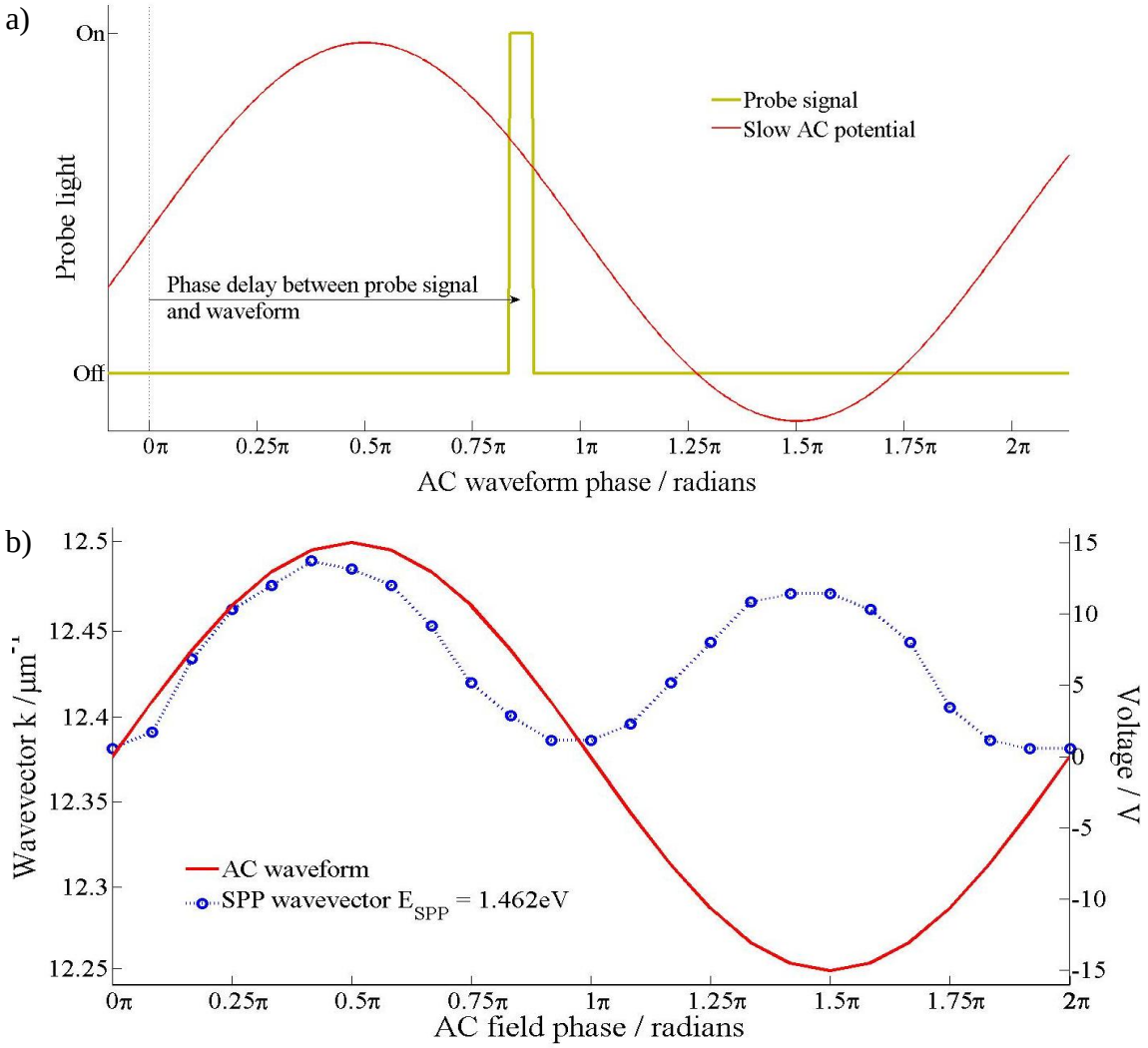

Figure 5.6: a) A demonstration of the probe signal in relation to the phase of the AC waveform. The phase delay can be controlled by our apparatus. b) With a slow, 0.5Hz AC potential the liquid crystal alignment oscillates with the applied potential. This results in the wavevector of the SPP also oscillating in time with the phase of the potential. The wavevector of the 1.462eV SPP when no potential is applied is 12.375μm^{-1}, slightly lower than the minimum wavevector for a 0.5Hz AC potential. Sample illuminated with a 4μm grating.

Using a slow AC potential will also result in the diffraction of SPP becoming dynamic, as the formation of a grating is dependent on the magnitude of the applied potential (*section 5.6*). The diffraction of SPP and the SPP wavevector shift have different dynamic behaviour to the slow AC field, as observed in *figure 5.7*. The magnitude of the diffraction of SPP also follows the AC waveform; however, there are noticeable differences compared to how the SPP wavevector follows the AC waveform. The most obvious is the clear asymmetry between the positive and negative parts of the applied waveform. This asymmetry is much larger than that observed for the SPP wavevector. The rise and decay of the diffraction, and therefore the grating formation, is also sharper than the SPP wavevector's dynamic behaviour. In addition, the diffraction shows regions of zero SPP diffraction, indicating a threshold effect. The threshold for the positive potentials appears to be ~5V and ~10V for the

negative potentials. Like the SPP wavevector the SPP diffraction dynamics also appear to slightly precede the applied potential.

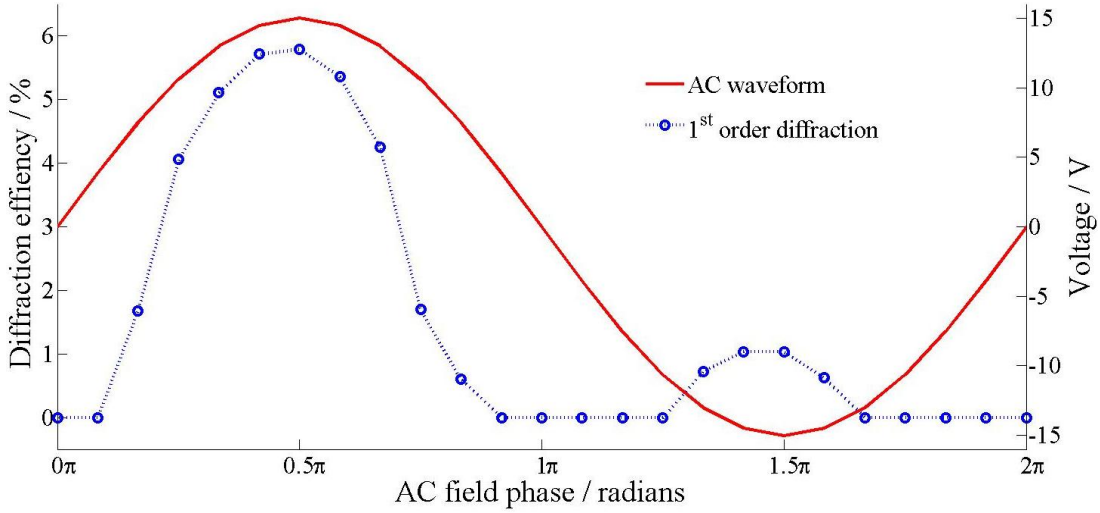

Figure 5.7: The magnitude of the diffraction signal as a function of the slow 0.5Hz AC waveform phase for a 4µm pitch grating. There is a clear asymmetry between the positive and the negative potentials of the waveform. E_{SPP} = 1.462eV, Δ_{PVK} = 80nm.

The variation in the dynamics between the SPP wavevector and the SPP diffraction efficiency can be explained from the magnitude of the elastic torques for the different liquid crystal deformation's that determine the wavevector and diffraction. The torque Γ, on a liquid crystal molecule is given by,

$$\underline{\Gamma}_K = \underline{\hat{n}} \times \underline{F}, \tag{5.1}$$

where $\underline{\hat{n}}$ is the liquid crystal director and $\underline{F}$ is the elastic force acting on a liquid crystal molecule from the intermolecular forces due to a local deformation of the director profile. Using the single elastic constant approximation the force can be shown to be [236],

$$\underline{F} = K \nabla^2 \underline{\hat{n}}, \tag{5.2}$$

with K as the single elastic constant. Therefore,

$$\underline{\Gamma}_K = \underline{\hat{n}} \times K\nabla^2\underline{\hat{n}}. \tag{5.3}$$

The form of *Equation 5.3* is difficult to directly interpret; however, it can be simplified by considering the case that the director is restricted to a single plane. The deformation is then characterised by an angle ϑ_{LC}, between the current orientation of the director and the director's equilibrium orientation (which is set parallel to one of the axis of the plane). For example, we consider that the deformation of the director is limited to the *x*-*z* plane, and the director is characterised by the angle ϑ_{LC} to the *x*-axis such that,

$$\underline{\hat{n}} = \begin{pmatrix} cos\left(\vartheta_{\mathrm{LC}}(\underline{r})\right) \\ 0 \\ sin\left(\vartheta_{\mathrm{LC}}(\underline{r})\right) \end{pmatrix}, \tag{5.4}$$

where we have directly introduced the spatial dependence of the deformation angle. It follows that,

$$\underline{\Gamma}_{\mathrm{K}} = \underline{\hat{n}} \times \mathrm{K}\nabla^2\underline{\hat{n}} = -\mathrm{K}\nabla^2\vartheta_{\mathrm{LC}}. \tag{5.5}$$

In order to interpret the dynamics of the system let us consider the liquid crystals impulse response to the instantaneous removal of the applied electrical torque generating the deformation, i.e. the liquid crystals relaxation from a deformed state to its equilibrium state when no electrical forces act on the molecules. The rotation of the liquid crystals director as it relaxes will be impeded by the viscous forces; hence, an additional torque acts upon the liquid crystal molecules,

$$\underline{\Gamma}_{\mathrm{vis}} = \xi\frac{\partial\vartheta_{\mathrm{LC}}}{\partial t}, \tag{5.6}$$

where ξ quantifies the liquid crystals rotational viscosity. As the change in angular momentum is negligible, we use the torque balance equation on our system [130],

$$\mathrm{K}\nabla^2\vartheta_{\mathrm{LC}} = \xi\frac{\partial\vartheta_{\mathrm{LC}}}{\partial t}. \tag{5.7}$$

The function that describes $\vartheta_{\mathrm{LC}}(\underline{r})$ in our system is complicated and is often unknown without using a numerical method. However, the function can be described by a Fourier series,

$$\vartheta_{\mathrm{LC}}(\underline{r}) = \sum_k \mathrm{A}_k(\mathrm{t})\sin(\underline{k}.\underline{r}), \tag{5.8}$$

where k is a wavevector component for a deformation over a length scale L, i.e. $k = \pi/L$. Substituting *equation 5.8* into *equation 5.7* for each k results in,

$$\frac{\partial \mathrm{A}_k(t)}{\partial t} = -\mathrm{A}_k(t)\frac{\mathrm{K}k^2}{\xi}. \tag{5.9}$$

Therefore,

$$\mathrm{A}_k(t) = \mathrm{A}_{k,0}e^{-\mathrm{K}k^2t/\xi}. \tag{5.10}$$

The relaxation time τ, of each deformation component is determined by $\tau = \xi/Kk^2$. Hence, the relaxation time is proportional to the square of the length scale of the deformation ($\tau \propto L^2$).

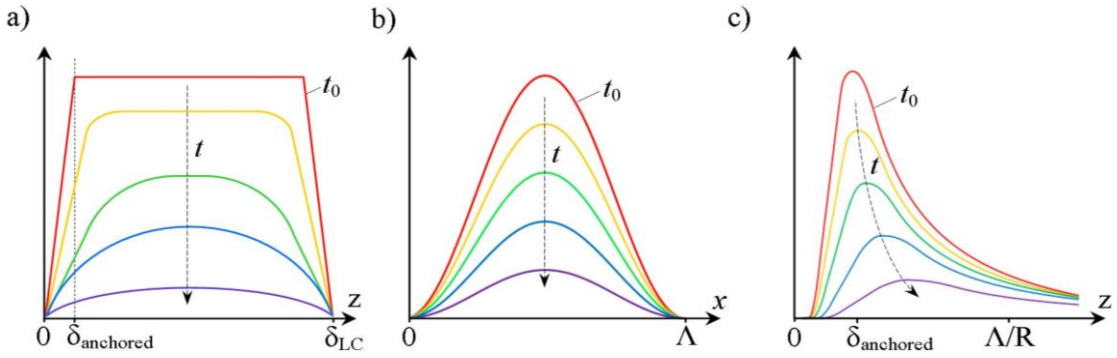

Figure 5.8: The magnitude of the director deformations in the liquid crystal. a) The bulk-deformation throughout the liquid crystal layer that determines the SPP wavevector. b) The magnitude of the grating deformation parallel to the interface for a single grating period. c) The magnitude of the grating deformation away from the interface. The combined deformations of (b) and (c) determine the SPP diffraction efficiency. The lines labelled t_0 are the initial deformations with a large applied potential and the figure illustrates how these deformations relax in time. *N.B*: The deformation relaxations are illustrations, not actual calculations.

The dynamics of the SPP wavevector are determined by the relaxation of the bulk-deformations in the liquid crystal, *figure 5.8a*. As the wavevector of an SPP is determined by the average between the dark and illuminated regions, *figure 5.5*, we do not need to consider the grating deformations for the SPP wavevector dynamics (*figures 5.8b, 5.8c*). When a large potential is applied the director profile of the liquid crystal is of the form illustrated by the red line in *figure 5.8a*. This is considered the initial bulk-deformation at time t_0 when we remove the electrical potential to allow the liquid crystal director to relax. This bulk-deformation has Fourier components with a short length scale associated with the size of the anchored region, ~100nm, which relax very quickly. It also has components with a long length scale associated with the thickness of the liquid crystal layer, δ_{LC} (~12μm), with a slower relaxation time. Therefore, the director profile changes shape as the various Fourier components of the deformation relax over different time scales, until only the δ_{LC} length scale component is required to describe the bulk-deformation, the blue and purple lines of *figure 5.8a*. The dynamic behaviour of the SPP wavevector is a result of this variation in the relaxation time. The SPP only interacts in a region near the interface (the first 200-300nm), where the short length-scale components dominate the liquid crystals bulk-deformation. These components relax quickly and allow the SPP wavevector to follow the AC waveform when the bulk-deformation is large. However, after the short-scale deformations have relaxed the SPP wavevector is determined only by the slight deformation in the probe region from the δ_{LC} length-scale deformation with its long relaxation time. Hence, the SPP wavevector is only slightly larger than the SPP wavevector when there is no applied potential. In addition, because the relaxation time of the δ_{LC} length-scale deformation is longer than the time scale for a change in the instantaneous applied potential from the slow AC waveform, *figure 5.9*,

the liquid crystal is never able to fully relax into its equilibrium state in the bulk. The molecules are therefore always above the applied potential threshold for director re-orientation. Hence, when the potential is re-applied by the slow AC, the molecules are able to immediately re-orientate as observed in *figure 5.9*.

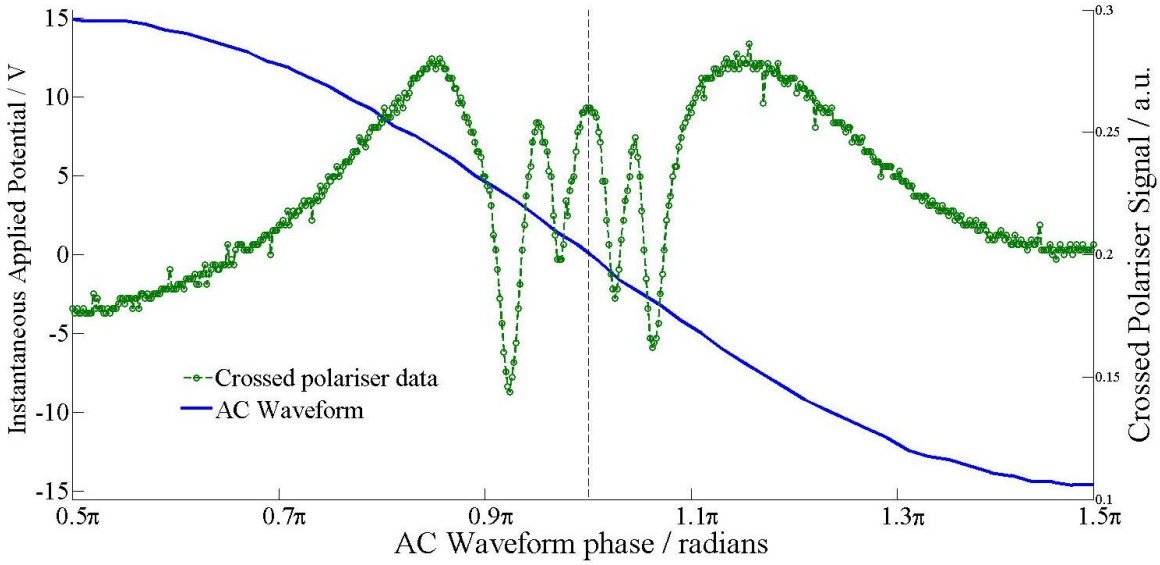

Figure 5.9: Oscilloscope trace of the time dependent crossed polariser transmission intensity with an 0.5Hz applied potential. When the applied potential is at 0V (π radians) the crossed polariser signal has not relaxed fully as it only demonstrates two transmission minima during the ramp down period. For full relaxation we should observe four transmission minima, as demonstrate in the crossed polariser data in *figure 4. 19*, where |V| is examined at π/2 instead of the time dependence of a |V| = 15V potential. As the system has not fully relaxed the system is able to immediately respond to the application of a non-zero potential in the negative potential phase, even if the instantaneous potential is less than the 4V Freedericksz threshold of this system.

By contrast the diffraction efficiency is determined by the formation of a grating in the probe region. The grating-deformations are over a constant length scale of Λ parallel to the PVK/liquid crystal interface, *figure 5.8b*, and a length scale of $\sim\Lambda/R$[XV] away from the interface, *figure 5.8c*. Therefore, the deformations relax at an approximately constant rate. These deformations relax quicker than the change in the instantaneous applied potential from the slow AC waveform. Hence, the SPP diffraction closely follows the AC waveform. In the presented experimental data on the dynamics, $\Lambda = 4\mu m$ and $\delta_{LC} \approx 12\mu m$; therefore, $\tau_{\delta LC} \approx 9\,\tau_{\Lambda}$. Therefore, complete relaxation of the grating-deformations is significantly faster than the bulk-deformations. In our system this results in the grating-deformations completely relaxing to their equilibrium states, below the applied potential threshold for director re-orientation to form the grating. Thus we observe a threshold potential and regions of no SPP diffraction.

[XV] Mathematically determined from *equation 5.25* in *section 5.8. R* is the square root of the ratio of the liquid crystals low frequency dielectric constants parallel and perpendicular to the director.

The large asymmetry in the diffraction efficiency is explained by a DC bias within the cell. The physical origin of a DC bias in our cells is unknown. Possible origins are from the formation of a space charge field due to either ionic charging on a time scale faster than the slow AC potential, or from the rectifying properties of a metal-semiconductor junction [237] altering the impedance of the PVK layer. Our experimental data indicates that the DC bias assists grating formation for the positive potential phase of the slow AC and impedes grating formation for the negative phase. The affect of the DC bias can be thought of as effectively lowering the threshold potential required for grating formation for the positive phase. Whereas, the DC bias effectively increases the threshold potential for the negative phase of the slow AC. The DC bias has little to no effect on the SPP wavevector dynamics as the molecules are never fully relaxed and are always above the threshold potential required for the deformations responsible for the SPP wavevector. The affect of the bias field is only observed in the small asymmetry in the maximum SPP wavevector between the positive and negative potential phases. We conclude from this that the DC bias within the cell is quite small; however, it is significant compared to the additional potential required to form a grating. As *equations 5.5* and *5.9* indicate that a shorter length scale deformation requires a larger torque to deform the director alignment. Therefore, the threshold for the grating (L = 4μm) is slightly higher than the threshold for the initial bulk-deformation (L = 12μm).

The data demonstrated in *figures 5.6* and *5.7* is for an AC field with a frequency of 0.5Hz; however, the phase response of the SPP wavevector to the AC waveform is typical for all frequencies below 10-20Hz. At frequencies above 20Hz, the AC field varies too quickly for the E7 liquid crystals to respond to the phase of the waveform and there is no dynamic behaviour, only a single value for the SPP wavevector is then observed.

The frequency dependence on the SPP diffraction efficiency is also investigated and as *figure 5.10a* shows, the magnitude of the diffraction is frequency dependent. The asymmetric diffraction efficiency behaviour between the positive and negative applied potentials is observed up to 5Hz. Above 5Hz little or no diffraction is observed to determine if the asymmetry is present. The peak diffraction efficiency occurs at ~0.5Hz, corresponding to a phase shift between the maximum diffraction and the maximum positive potential of the AC waveform of ~0π.

A similar frequency dependent behaviour has also recently been observed by our colleagues in Prof. Kaczmarek's liquid crystal group with the two-beam gain of a photorefractive liquid crystal [233]. In this work, they observe a peak in the photorefractive gain, for a similar type of cell, at 2Hz with similar tail-off at higher and lower frequencies. They explain this behaviour using a semi-analytical impedance ladder model and demonstrate theoretically a range of frequencies exist close to zero Hz (DC) that improve the gain. The mechanism behind the frequency dependence is the same for our cells even though the peak is not in quantitative agreement. Several possibilities exist for the disagreement:

1. A slightly differing sample structure, in particular the PVK thickness.

2. Our experiments examine the anchored region where alignment forces are present and not the bulk region of the liquid crystal.
3. The experimental conditions affect the frequency response, for example pitch of the grating or the magnitude of the applied potential (Prof. Kaczmarek's group use a 24µm pitch where we use a 4µm pitch).

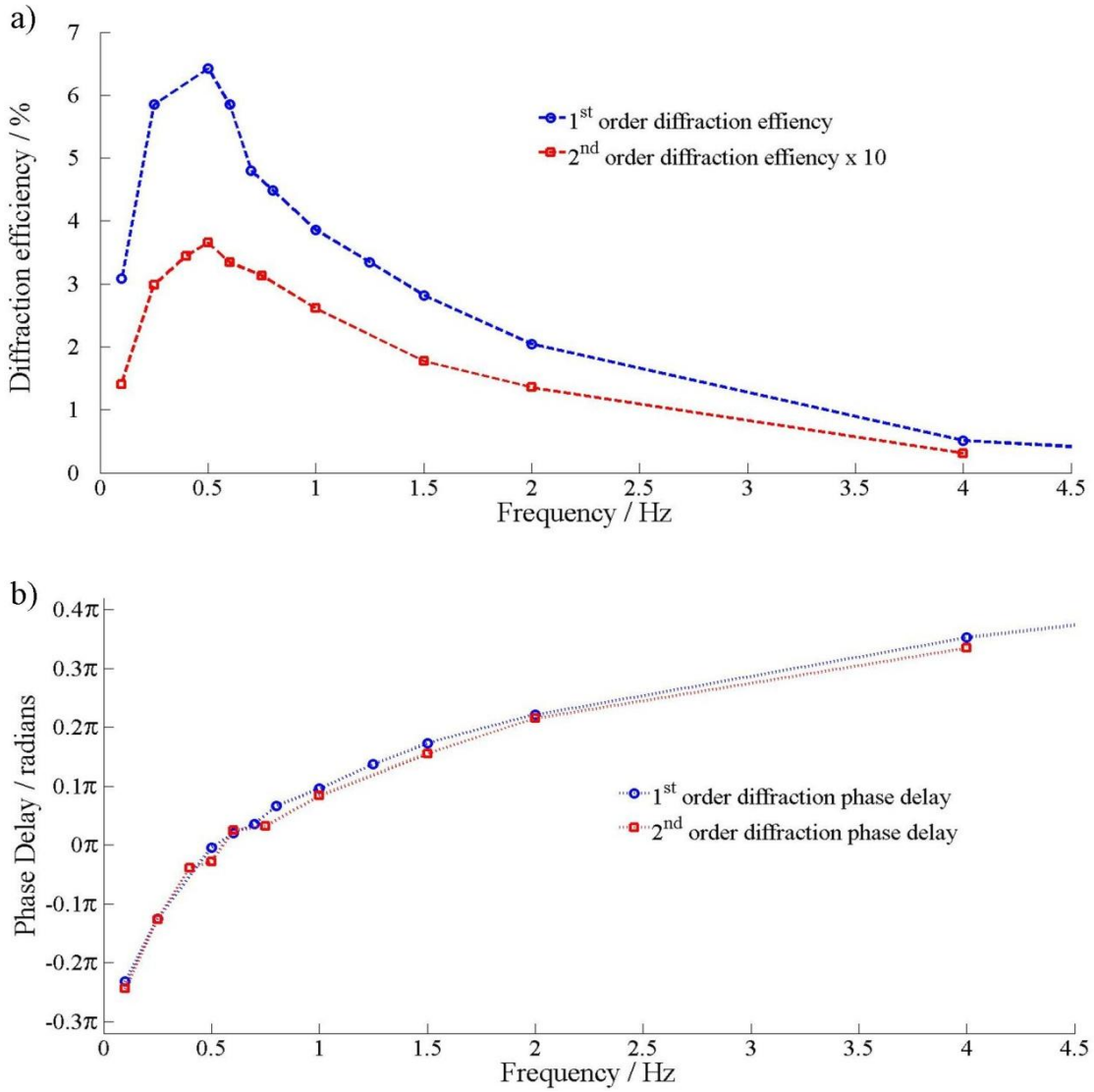

Figure 5.10: a) Frequency dependence on the diffraction efficiency for a 4µm pitch grating. Maximum diffraction occurs at ~0.5Hz hence this is the frequency investigated thereafter. b) The maximum diffraction signal corresponds to a phase delay between the diffraction and AC waveform of 0π. E_{SPP} = 1.462eV, |V| = 15V, Λ = 4µm, Δ_{PVK} = 120nm.

For the purpose of all further measurements, the diffraction efficiency is measured at a single frequency of 0.5Hz at a phase of 0.47π, the phase demonstrating maximum diffraction. It is assumed that there is no additional frequency dependence on any of the trends observed with the other experimental parameters for SPP diffraction, i.e. the third possible reason for our quantitative disagreement with the bulk two-beam gain frequency dependence is false;

though this has not been experimentally verified. Ideally we would like to investigate any possible frequency dependence. However, due to time constraints this was not possible. It is unlikely that the general trends observed with the other SPP diffraction variables would significantly change with frequency, though quantitative variations in thresholds, peaks and diffraction efficiencies are possible.

During experiments with a slow AC potential, the phase delay between the probe signal and the AC waveform should be selected to maximise the observed SPP diffraction efficiency. For example, the phase that shows the maximum diffraction in *figure 5.7* is ~π/2; therefore, the phase delay between the probe and waveform also needs to be ~π/2 for the best SPP diffraction efficiency observations. As the SPP diffraction efficiency follows the waveform of the slow AC field we assume the liquid crystals behaviour can at any single point in time be approximated by a DC potential of equivalent magnitude. For example, a 15V slow AC potential at a point in the waveform with a phase π/4, can be approximated by a DC potential of $15sin(\pi/4) = 10.6$V.

5.4 Phase Matching Condition for SPP Diffraction

The first variable investigated to maximise the SPP diffraction efficiency is how the orientation of the grating, γ, relative to the SPP wavevector, affects the magnitude of the coupling. Our convention is that γ has a value of 0^o when the grating is perpendicular to the SPP wavevector (*figure 5.11b*). A positive rotation is an anti-clockwise motion, the resultant grating orientation then diffracts more energy into a SPP diffraction order in the '+' k_y region of *k*-space.

As the grating orientation is changed the magnitude of the diffraction efficiency can either increase or decrease, this is presented in *figure 5.11*.The increase or decrease in diffraction efficiency as a function of γ, is different for each diffraction order. This indicates that there is an optimum value of γ for coupling into another SPP mode. The γ dependence is experimentally demonstrated for the +1 order in *figure 5.12*, for a 5μm grating. From a grating orientated at $\gamma = -2^o$ the diffraction steadily increases with increasing γ until a maximum diffraction efficiency is observed at $+2^o$. Further increasing γ then begins to reduce the coupling into this diffraction order. The γ dependence on the SPP diffraction efficiency is also observed in the mathematical simulations of this system. However, the magnitude of the diffraction efficiency in our simulations is not in quantitative agreement.

The γ dependence on the diffraction efficiency can be explained by a wavevector mismatch term in the coupling between SPP modes. Just like the excitation of the initial SPP mode by ATR, energy transfer into another SPP mode is only permitted when there is wavevector conservation. Some diffraction is possible without exact wavevector conservation as SPP are not singly defined in *k*-space and a broad range of wavevectors can excite the mode, hence the broad FWHM of the ATR excitation.

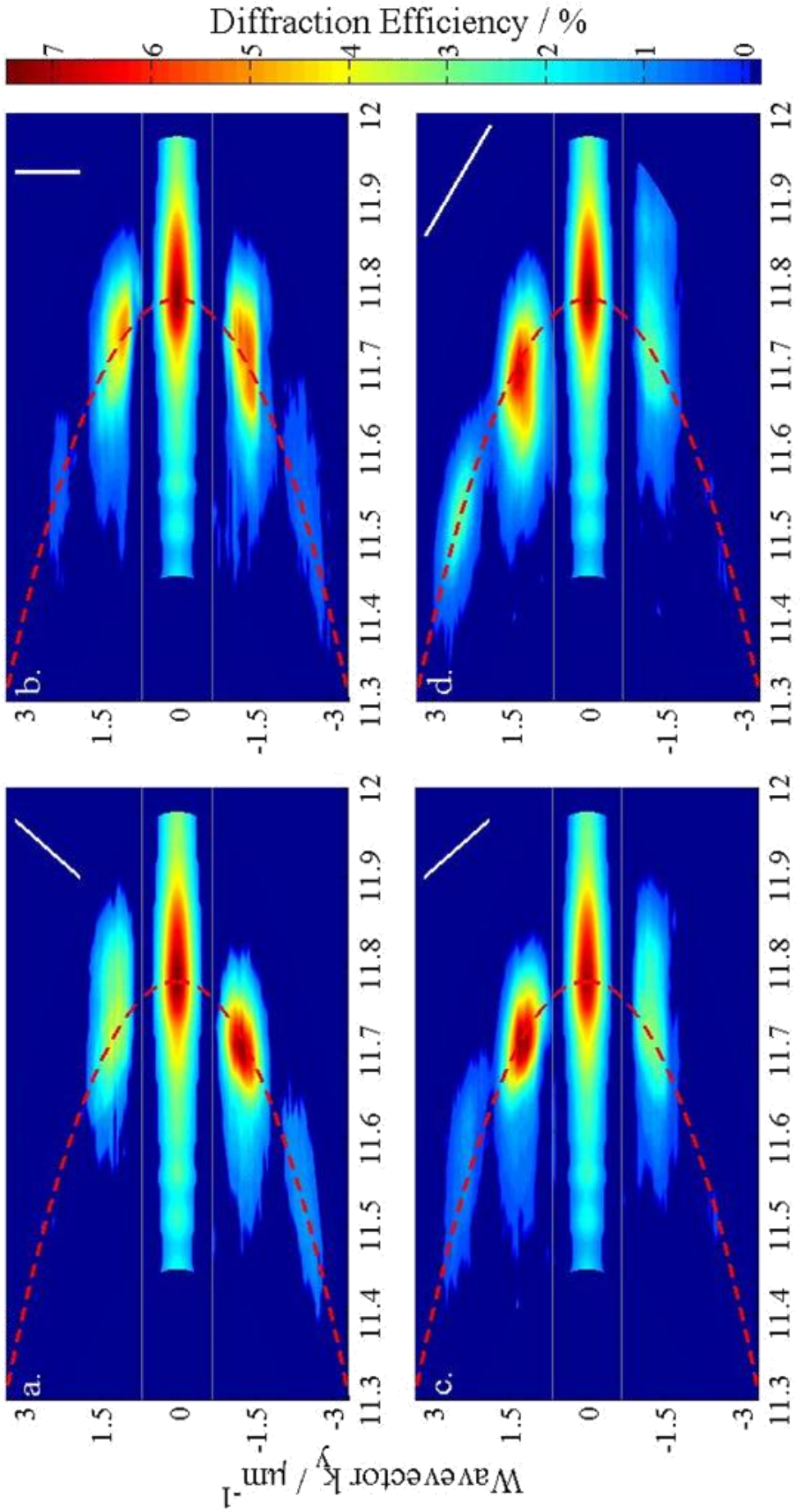

Figure 511: k-space 'maps' of the SPP diffraction. In each graph the region around $k_y = 0$ between the white lines represents the input energy into a 1.38eV SPP mode with a wavevector of $k_x = 11.78\mu m^{-1}$ (Dashed red line). The region outside these lines is the detected diffraction signal for a 5μm grating aligned to couple energy into a) the '-1' order, b) vertical grating, c) '+1' order and d) the '+2' order, this is displayed as the white line in the top right corner of each plot. The dashed red line is in fact a circle in k-space if the k_x- and k_y-axes are scaled identically.

Conversely, light exciting the SPP mode with a wavevector slightly off-resonance can couple into the diffracted SPP modes with an exact wavevector match, if γ is not orientated for direct coupling between SPP. As less energy is initially stored in the SPP where k_x is not resonant, there is less energy to transfer into other modes by this method. This is the process described by the yellow arrow of *figure 5.4*. With our experimental equipment and theoretical model both of these effects are possible when determining the diffraction efficiency. Examples of wavevector mismatches are displayed in *figure 5.13*.

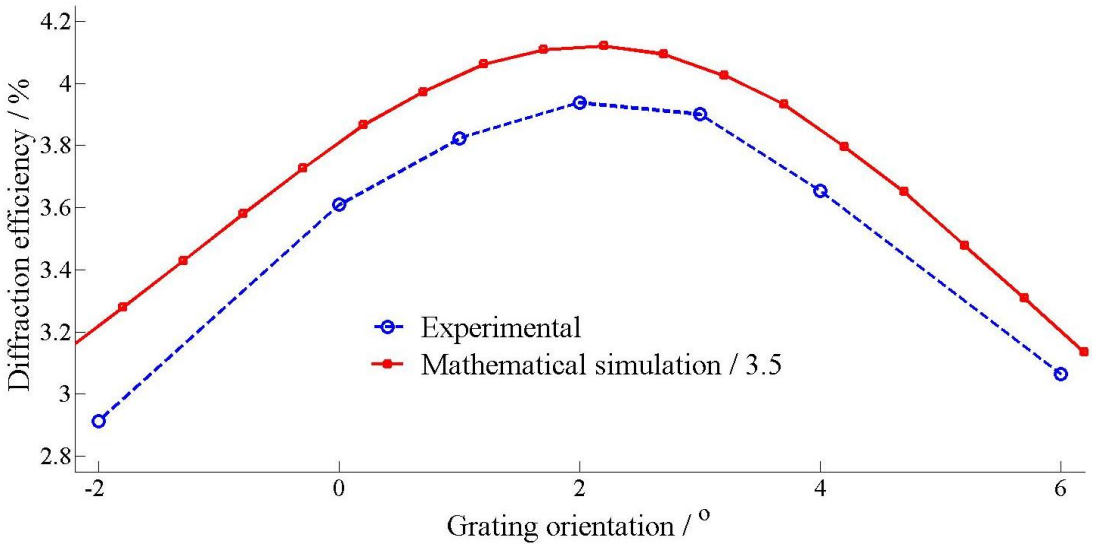

Figure 5.12: The experimentally determined diffraction efficiency for a 5μm pitch grating (blue), highlighting that the optimum diffraction occurs at 2.1°. This angle is theoretically predicted by the analytical approximation of *equation 5.11* and is determined by the full mathematical simulations for this system (red). E_{SPP} = 1.462eV, V = 15V, Δ_{PVK} = 80nm.

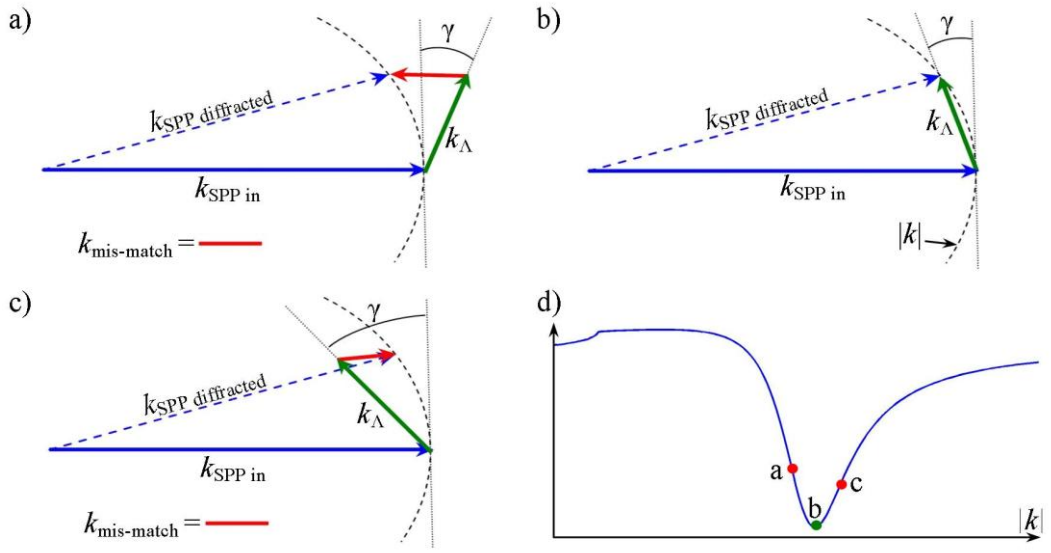

Figure 5.13: Examples of the grating mismatch wavevector in k-space. a) $\gamma < \gamma_{SPP}$, b) direct coupling between SPP modes $\gamma = \gamma_{SPP}$, c) $\gamma > \gamma_{SPP}$. d) The region of the ATR excitation of a SPP mode that couples to the ideal SPP wavevector for examples a-c.

When the diffraction is maximised by the orientation of the grating we state the SPP coupling is phase matched to that diffraction order and $\gamma = \gamma_{SPP}$. When determining the influence of the other SPP diffraction efficiency variables, the grating is always phase matched to maximise the energy transfer. For our future experiments to achieve photorefractive gain of SPP, by interfering two SPP modes to form the refractive index grating, the phase matching requirement will inherently be achieved.

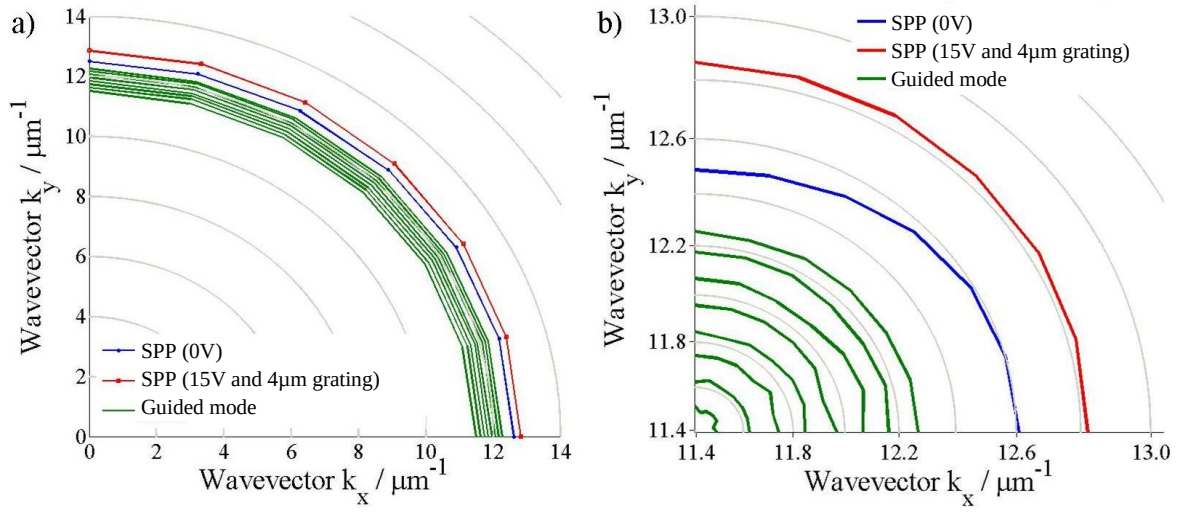

Figure 5.14: The birefringent effects on the SPP wavevector. The in-plane liquid crystal director angle ψ is the polar angle in the above plots. When $\psi = 0^o$, the wavevector only has a k_x component. a) To first approximation the SPP wavevector forms a circle in *k*-space, as do the guided modes. b) Closer inspection shows that the SPP wavevector forms an ellipse with a small eccentricity as expected for a birefringent material. The eccentricity is less when a potential and illumination are applied. The guided modes appear unaffected as they propagate in the bulk, which is completely aligned to the electric field. $E_{SPP} = 1.462$eV, $\Delta_{PVK} = 94$nm.

The value of γ required for phase matching can be analytically determined by simple geometry. After a measurement of k_{SPP} is acquired, the angle γ_{SPP} is determined from the angles within an isosceles triangle, *equation 5.11*, assuming that the dispersion of SPP approximates a circle and the value of k_{SPP} is therefore the same for both the original and diffracted SPP mode (a valid approximation, confirmed by *figure 5.13*).

$$\gamma_{SPP} = \tan^{-1}\left(\frac{mk_{\Lambda}/2}{k_{SPP}}\right), \tag{5.11}$$

where m = -2, -1, 1, 2, is the diffraction order and k_Λ is the wavevector of the grating.

The diffraction as a function of γ also demonstrates the symmetry between the positive and negative diffraction orders. As shown in *figure 5.15*, the magnitude of γ that is resonant for the +1 order is the same as the -1 order. Offsetting γ from γ_{SPP} also displays complete symmetry. Therefore, only the positive diffraction orders are considered in our experiments and simulations, as there is no loss in generality of the behaviour of the system.

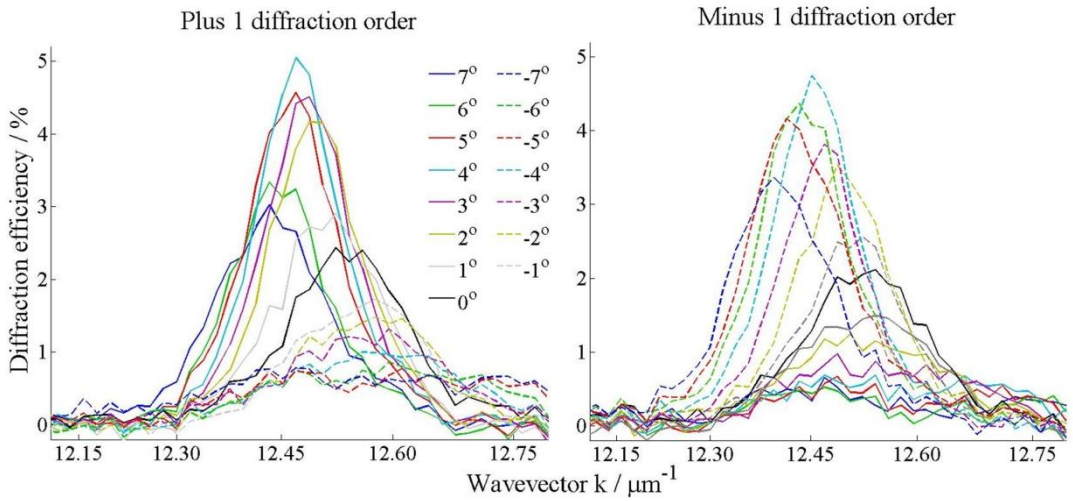

Figure 5.15: The SPP diffraction as a function of the angle γ for a 3μm pitch grating. There is a clear preferential angle for which SPP diffraction occurs (~4° in this example). This angular dependence is symmetrical between the positive and negative diffraction orders. Hence, a diffraction order may be characterised by only the positive order. E_{SPP} = 1.462eV, V = 15V.

5.5 SPP Energy Dependence on the Diffraction Efficiency

As a consequence of a variation in the SPP penetration depth into the dielectric mediums, the magnitude of the photorefractive SPP wavevector shift demonstrated a dependence on the energy of the SPP mode (*figure 4.26*). Therefore, it can be expected that the SPP diffraction will also show an SPP energy dependence.

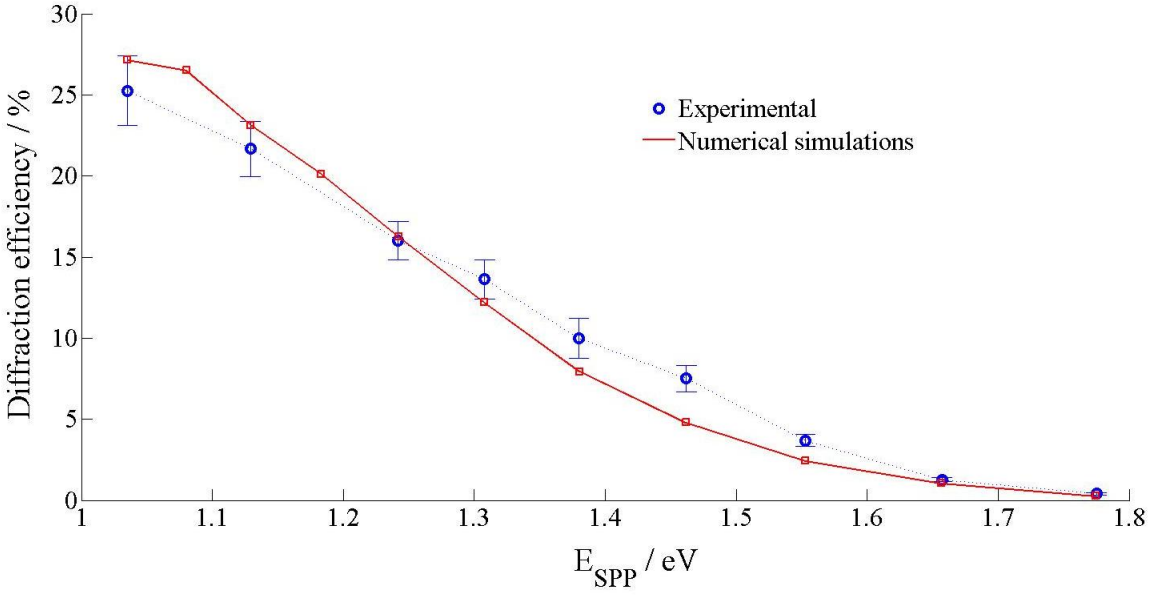

Figure 5.16: The first SPP diffraction order dependence on the energy of the SPP mode. For lower energy SPP there is a significant increase in the diffraction efficiency. This behaviour is confirmed in the simulations. Λ = 4μm, V = 15V, Δ_{PVK} = 80nm.

The experimentally determined SPP energy dependence on the SPP diffraction efficiency with a 4μm pitch grating is presented in *figure 5.16*. It is quite clear that the lower the energy of the SPP mode the greater the SPP diffraction efficiency. For energies lower than 1.656eV the increase in the diffraction efficiency is linear, with no maximum observed in the energy range examined. Energies lower than 1.03eV are experimentally difficult to examine due to the presence of guided modes within our samples with a wavevector similar to the SPP. In all of our experimental data where a variation in the SPP energy is examined (*figures 5.28* and *5.35*), a lower energy SPP has always demonstrated an increased diffraction efficiency. Therefore, we believe that this energy dependence is independent of all other SPP diffraction variables, though this has not been rigorously tested.

The energy dependence is observed in the numerical simulations, *figure 5.16*. However, to observe the experimentally determined trend of an increasing diffraction efficiency with decreasing SPP energy, with all other parameters matching the experimental conditions, the modulation of the potential between the light to dark regions must be reduced to $V' = 0.96 + 0.04\sin^2(kx)$. Usually, we use a function with a larger modulation of $V' = 0.8 + 0.2\sin^2(kx)$, as this form of the potential is indicated by the experimentally determined magnitude of the shift in the SPP wavevector in the light and dark (*figure 4.25*). If the experimentally determined V' is used, the simulations predict the energy dependence displayed *figure 5.17*. With an identical voltage to the experiment (15V), the diffraction efficiency remains constant at approximately 25% for energies below ~1.46eV. Reducing the magnitude of the potential lowers the SPP energy required to observe the constant diffraction efficiency level. Therefore, we conclude that the energy dependence is correctly predicted within our simulations. However, the simulations predict a saturation level in the diffraction efficiency that is not experimentally verified in our samples.

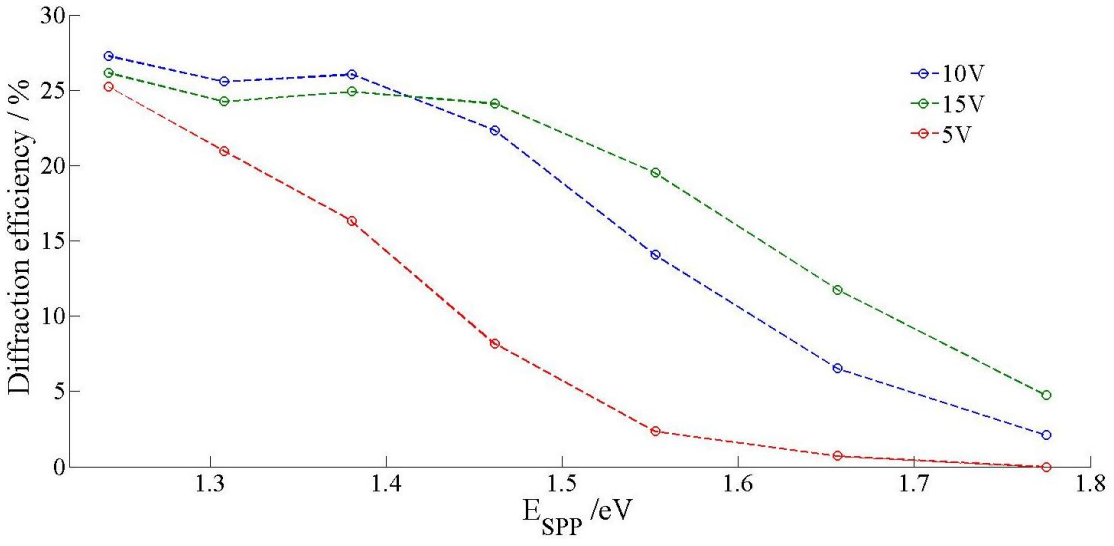

Figure 5.17: The mathematical simulation of the energy dependence. This demonstrates the same behaviour as experimentally determined, when there is a low theoretical voltage. However, as the simulations over-predict the diffraction: increasing the voltage saturates the diffraction at ~25%.

Two possibilities exist for the physical mechanism for the increased diffraction efficiency with lower energy SPP. With decreasing energy, the SPP penetrates further into the dielectric layers and propagates a further distance along the interface increasing the interaction time. We can attempt to determine which of these two length scales increases the most with a change in the SPP energy by comparing the penetration depth and propagation length for two different energies, 1.38eV and 1.66eV. The propagation lengths of SPP determined experimentally and listed in *table 4.2* indicate that a 1.38eV SPP has a propagation length of ~33μm, which is twice that of a 1.66eV SPP, ~16μm. The penetration length *l*, the distance for which the SPPs electric field decays to a value of E_0e^{-1}, can be calculated by *equation 2.13* and using an approximate value of $\varepsilon_d = 2.56$ ($n_d = 1.6$) for the dielectric layers, a 1.38eV SPP has a decay length $l \approx 320$nm and $l \approx 215$nm, for a 1.66eV SPP. We then consider that the portion of the SPP's electric field within the PVK layer does not interact with a grating and cannot be diffracted. Therefore, for SPP with equally sized electric fields at the Au/PVK interface, the electric field overlap with the liquid crystal (*figure 5.18*) for the lower 1.38eV energy SPP mode is 3.2 times more than the 1.66eV SPP. Hence, reducing the energy of a SPP increases the relative electric field overlap with the grating more than the SPP propagation length, so we would expect the change in the SPP penetration depth to be more significant in determining the diffraction efficiency. However, we experimentally observe that a 1.38eV SPP has a diffraction efficiency five times larger than the 1.66eV SPP. Hence, it is likely that the diffraction efficiency cannot be explained by an independent increase in either of these length scales, assuming the dependence on each is linear.

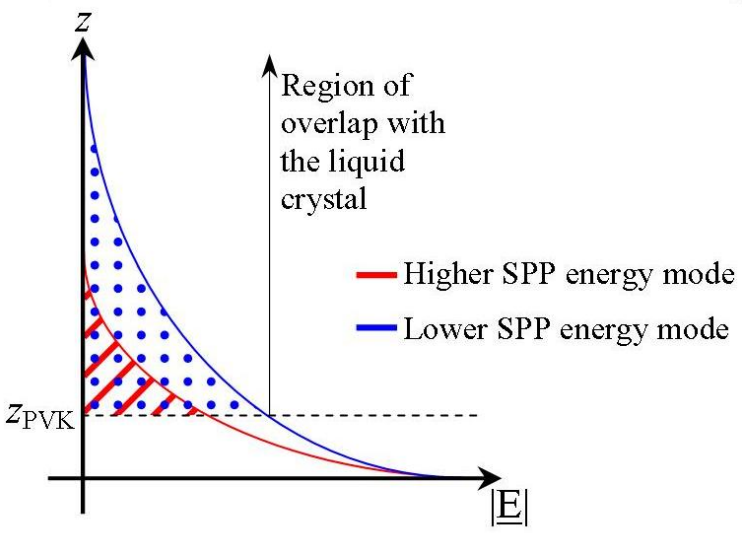

Figure 5.18: The increased overlap of a lower energy SPP mode with a longer e^{-l} decay length into the liquid crystal layer. Note: The electric fields presented are illustrations not calculations.

We cannot use our numerical simulations to isolate if either the propagation length or penetration depth is more significant in the observed energy dependence, as they both share common parameters in their theoretical description (equations 2. and 2.). Though in principle we could adjust variables to independently increase one parameter whilst keeping the other

fixed, the resulting dielectric constants would not describe our physical system so would be of limited use. However, we believe that the penetration depth is the most significant property as we must also consider that the strength of the grating is dependent on the distance from the PVK-liquid crystal interface. Therefore, SPP that probe further into the liquid crystal interact with a stronger refractive index grating and could display an increased diffraction efficiency as a result. Our interpretation that the penetration depth is more significant is also reinforced by the fact that the increased penetration depth of lower energy modes was identified as the mechanism behind the energy dependence of the increased photorefractive effects observed for lower energy SPP modes in *figure 4.26*, where the propagation length is not a factor.

The saturation level observed in the numerical simulations can be explained by the magnitude of the coupling co-efficients for the energy transfer into and out of a diffraction order. For all diffraction orders, energy transferred into an order can itself be subsequently transferred into another diffraction order or back into its original diffraction order. Mathematically, one would describe this process by a series of rate equations within a matrix that describes the coupling between all diffraction orders, i.e. terms describing the coupling between the $0^{th} \rightarrow \pm1^{st}$, $+1^{st} \rightarrow -1^{st}$, $0^{th} \rightarrow \pm2^{nd}$, etc. The magnitude of each of these terms is dependent on the extent of the SPP's interaction with the refractive index grating and the size of the wavevector mismatch term (*section 5.4*) in the grating coupling. The observed diffraction efficiency is the net energy transfer from solving the rate equations for each diffraction order. For lower energy SPP, the increased overlap of the electric field with the liquid crystal increases the energy coupled out of the order by a similar amount as the energy transferred in. Hence, a saturated diffraction efficiency is observed in the simulations.

Our experimental results do not display this saturation level as the coupling co-efficients, which are dependent on the magnitude of the gratings modulation, are likely too low to reach the stage where increased energy transfer into the order is offset by additional energy transfer out of the order. In the full numerical simulations of the system when we use the experimentally expected V′ from *section 4.3* (*figure 5.17*) these co-efficients are sufficient to display a saturation level behaviour. Hence, a reduced modulation (and therefore a reduced coupling) is required to allow the numerical simulations to predict a more accurate energy dependence. This helps explain why the simulations over-predict the diffraction efficiency, as the simulated modulation is larger than in our physical system. The consequences of this over-prediction are discussed in more detail in the conclusions of *Chapter 6*.

5.6 SPP Diffraction Efficiency Dependence on the Magnitude of the Slow AC potential

The next variable investigated is how the magnitude of the slow AC potential influences the diffraction efficiency. As our samples are not directly photorefractive, and the photorefractive like effects are caused by modulating the applied potential, there will be a voltage dependence on the grating formation and therefore, the SPP diffraction efficiency.

The effect of the magnitude of the applied potential on the SPP diffraction efficiency with a 6μm grating for two different PVK layer thickness samples is presented in *figure 5.19*. No SPP diffraction is observed until a potential of ~4-5V is applied to the cell. The diffraction efficiency then linearly increases until an applied voltage of 10-11V. Further increases are then observed in the diffraction efficiency until a peak value at 16V for the 80nm PVK layer and 19V for a 94nm layer. This additional increase in the diffraction is not linear. After the peak diffraction at either 16V or 19V the diffraction efficiency begins to drop off. Our experimental equipment prevents us from examining voltages greater than 20V for a 0.5Hz AC potential.

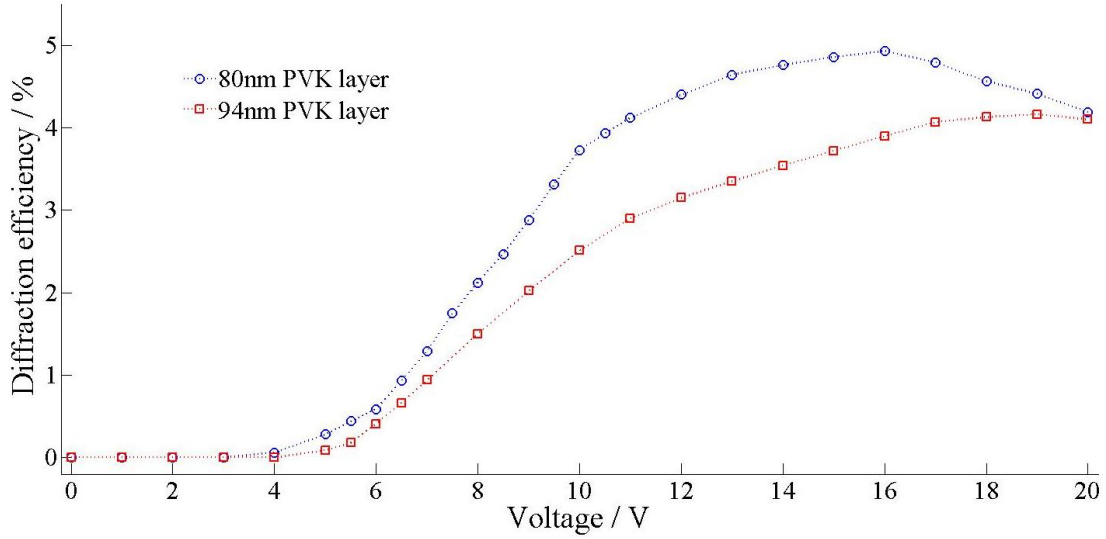

Figure 5.19: The first SPP diffraction order dependence on the magnitude of the applied potential for a 6μm grating. Increasing the PVK thickness shifts the position of the peak to a higher voltage as well as reducing the maximum observed diffraction efficiency. E_{SPP} = 1.462eV, Λ = 6μm.

In addition, we also observe the diffraction efficiency dependence on the magnitude of the potential for a 4μm pitch grating, *figure 5.20*. The same general trend is observed with the 4μm grating as observed for the 6μm gratings. However, the potential required to maximise the diffraction efficiency is lower for the 4μm grating (13V) than the 6μm grating (16V). Then after a small reduction, the diffraction efficiency appears to settle to a constant value of ~7.5%.

We have also investigated the second SPP diffraction order dependence on the magnitude of the potential for a 6μm grating, *figure 5.21*. The same form of the voltage dependence as seen for the first diffraction order is observed for this higher order. There are however, a few quantitative differences between the first and second diffraction orders voltage dependence. No diffraction is observed until an applied potential of 8V for the second order, whereas diffraction is initially observed at 4-5V for the first diffraction order. In addition, the peak diffraction appears to reside out of our equipment range of 20V.

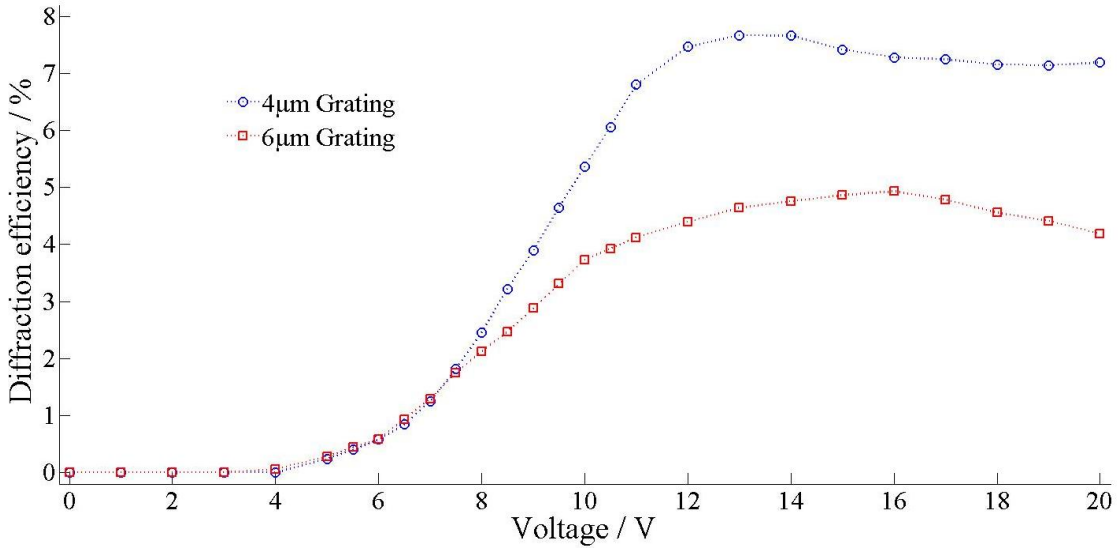

Figure 5.20: The first SPP diffraction order dependence on the magnitude of the applied potential for different grating pitches with an 80nm PVK thickness sample. The smaller pitch grating reaches a maximum in the diffraction with a lower potential. E_{SPP} = 1.462eV, Δ_{PVK} = 80nm.

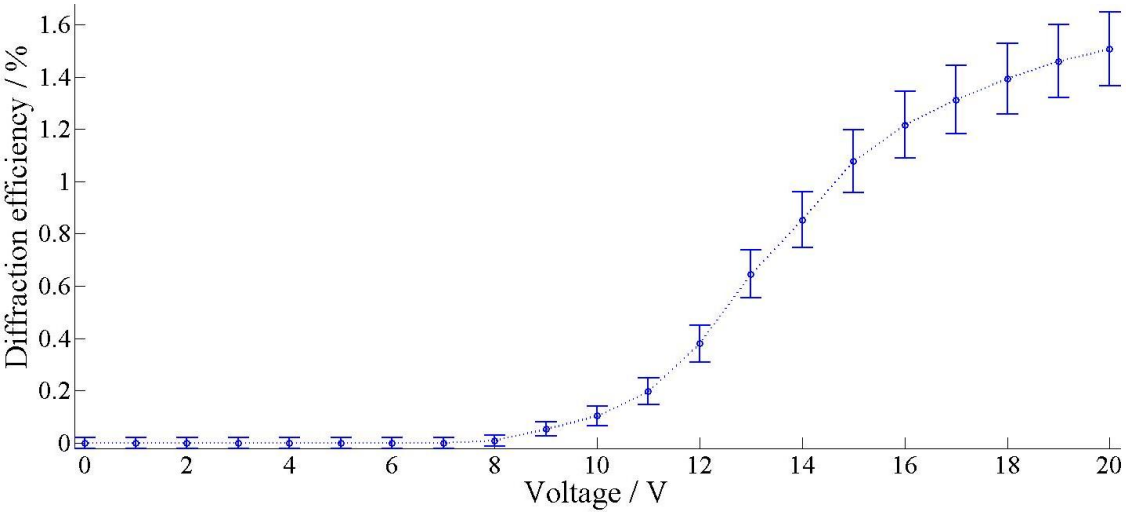

Figure 5.21: The second SPP diffraction order dependence on the magnitude of the applied potential. This demonstrates the similar behaviour as the first order. However, the peak voltage appears to be outside of our experimental equipment. E_{SPP} = 1.462eV, Λ = 6μm, Δ_{PVK} = 80nm.

The 4-5V potential that is required to initially demonstrate SPP diffraction into the first diffraction order is comparable to the slow AC Freedericksz transition at 4V, observed by the crossed polariser data presented in *figure 4.19* for a similar cell. Therefore, there is no SPP diffraction and no grating is formed in the liquid crystal for applied potentials lower than a grating formation threshold potential. This threshold is an expected behaviour for a cell structure where the liquid crystal is not directly photorefractive. The higher potential required to initially demonstrate SPP diffraction into the second order (~8V) suggests that the potential needs to be noticeably larger to generate a significant second harmonic component to the refractive index grating than required for the first harmonic.

The diffraction efficiency peaks at 16V and 19V for the 80nm and 94nm thick PVK layer samples respectively, correspond to when the refractive index difference between the light and dark regions is greatest. Initially, the increase in the potential for maximum diffraction was thought to be a result from the increase in the PVK thickness resulting in a larger PVK resistance and a lower potential drop across the liquid crystal layer. Therefore, a larger potential needs to be applied across the liquid crystal so that the same optimum potential forms the grating. Indeed, the V_{peak}/δ_{PVK} ratio is approximately constant for both samples at ~0.2Vnm^{-1}. However, this behaviour is not predicted by a simple resistance ladder model of the system. The fraction of the potential across the liquid crystal (V_f) is given by,

$$V_f = \frac{1}{1+\frac{Z_{PVK}}{Z_{LC}}}. \tag{5.12}$$

From the experimental data for the SPP wavevector (*section 4.3*), $V_{f\_dark} \approx 0.8$ in the dark and $V_{f\_light} = 1$ when illuminated, i.e. implying that Z_{PVK} is negligible when the cell is illuminated. Hence, in the gratings 'dark' regions, $Z_{PVK}/Z_{LC} = 0.25$ for a sample with a PVK thickness of 102nm. Linearly scaling Z_{PVK} for the 80 and 94nm samples leads to $V_{f\_dark80} = 0.83$ and $V_{f\_dark94} = 0.81$. However, the modulated component ($V_{mod} = V_{f\_light} - V_{f\_dark}$) which we presumed is entirely responsible for the grating formation, shows the opposite PVK thickness dependence, i.e. V_{mod} increases with the PVK thickness from 0.17 to 0.19. Hence, the resistance ladder model may not be an accurate description of the system (a consistent conclusion with our impedance data). This is likely a result of not accounting for the true non-Ohmic and capacitive behaviour of the PVK layer. However, if the actual electronic behaviour of the system is similar to the resistance ladder model, then the experimental observation of an increased potential for the optimum diffraction efficiency with increasing PVK thickness has an important consequence. The magnitude of the uniform component of the potential (the potential component V_{f_dark}) is then significant in the grating formation mechanism. Hence, we cannot explain the grating formation by only the magnitude of a modulated potential component, the uniform potential component must also be considered.

The diffraction efficiency dependence on the magnitude of the potential is also examined with our numerical model of the system, *figure 5.22*. The simulations display the same voltage dependence for both the first and second order as experimentally observed. However, the potential of the initial and peak diffraction is not in quantitative agreement. The initial diffraction in the simulations is at a slightly lower theoretical voltage; this is likely from the simulations over-predicting the diffraction efficiency, making this point more noticeable than in the experiments. In the simulations, the potential with the maximum diffraction efficiency is larger than experimentally determined; this is likely from not all of the liquid crystals electronic behaviour being accounted for in the model. In particular, the possibility of free charges in the liquid crystal. The small reduction in the diffraction efficiency after a peak value is not obvious in the figure; however, close inspection of the numerical values show that

this behaviour is present. The good match in the observed trends between the simulations and experiment indicates that this dependence is a result of the liquid crystals response to the applied potential and is not a result of the PVK's electrical behaviour, which is not accounted for in the model.

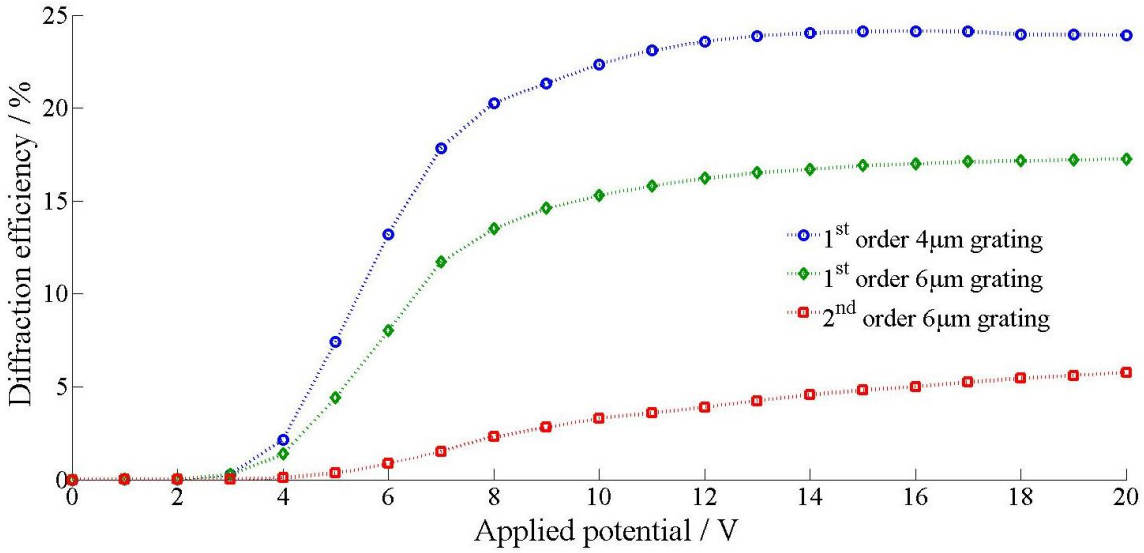

Figure 5.22: Mathematical simulation of the dependence of the first SPP diffraction order efficiency on the magnitude of the applied voltage. The rise in the diffraction efficiency matches the experimental data. E_{SPP} = 1.462eV.

A similar voltage dependence has also been previously observed from this type of photorefractive liquid crystal cell in the related applications of photorefractive two-beam gain [147] and for the first order diffraction efficiency of a probe beam examining the strength of the grating written into the liquid crystal layer [17]. In these works the peak gain occurred at 10V and 7V respectively. There is however, a noticeable difference, after the maximum gain or diffraction efficiency the voltage dependence tends to zero for higher potentials in these works, whereas our diffraction efficiency shows evidence for a stable level. Though a different physical effect is examined in all three cases, the voltage dependence should be determined by the same mechanism; the liquid crystals response to a modulated potential. The different sample conditions would likely only change the quantitative behaviour, not the general form of the potential dependence. The significant difference in our experiments is that only the liquid crystal near the interface is probed and in the other experiments the entire layer is probed where the behaviour is mostly determined by the bulk alignment.

The SPP diffraction efficiency dependence on the magnitude of the applied potential can be explained by a simple qualitative model based on the relative refractive index of the grating in the light (n_{light}) and dark (n_{dark}) illumination regions with an increasing potential. The electric field within the liquid crystal is a combination of both a modulated and a larger uniform component normal to the cell and a modulated lateral component (experimentally indicated in *section 4.3* and mathematically explained in *section 5.8*). The refractive index at all points in

the liquid crystal layer is determined by the relative strength of the electric field of all the components. Prior to the Freedericksz threshold the combined electric field components are insufficient to generate an electrostatic force significant enough to re-orientate the liquid crystal molecules. Hence, no grating is formed and no SPP diffraction is observed. Slightly above the threshold, the larger applied potential in the illuminated grating regions from the modulated electric field components, allows n_{light} to be greater than n_{dark}. Therefore, a grating is formed with a strength characterised by $\Delta n = n_{light} - n_{dark}$ and SPP diffraction is observable. The diffraction efficiency then increases with larger applied potentials as Δn becomes larger.

Due to the large uniform component of the electric field normal to the interface, n_{dark} will increase with larger potentials as well as n_{light}, though at a lesser rate. As increasing the potential scales both the uniform and modulated electric field components. Hence, n_{light} will still increase faster until the peak diffraction efficiency when Δn is largest.

For the potential range of 4-10V, the linear diffraction efficiency increase region, the magnitude of Δn is mostly determined by the difference between the light and dark regions in the director alignment angle away from the interface, ϑ_{LC}. As this range of potentials corresponds to the region where the slow AC crossed polariser transmission (*figure 4.19*) varies the most rapidly from re-orientations away from the interface. In the region between 11V and the potential with the largest diffraction efficiency the grating modulation is determined by a combination of the out-of-plane ϑ_{LC} variation and the in-plane ψ variation of the director. As the lateral electric field component begins to have a significant effect on the liquid crystal alignment.

After Δn and the diffraction efficiency is maximised, the drop in diffraction efficiency is a result of the applied potential beginning to fully align the liquid crystals director normal to the PVK interface in the gratings 'light' regions, maximising n_{light}, whilst n_{dark} can still increase. If there were only an electric field component normal to the interface, then further increases in the applied potential would result in the diffraction efficiency tending to zero. As the uniform component becomes significant enough to re-orientate the liquid crystal in the dark regions so that $n_{dark} \rightarrow n_{light} = n_e$, effectively erasing the grating. The modulated normal electric field component then has a reduced effect. This is the behaviour observed in the literature. However, near the interface we also have a modulated lateral electric field component. This component is significant as it affects both the liquid crystals in-plane ψ and its out-of-plane ϑ_{LC} director orientation. Therefore, there is always a grating present to diffract SPP as there is no uniform lateral component to erase the grating at higher potentials. We conclude that because the diffraction efficiency is then at a constant level, the value of Δn caused by the lateral field does not vary significantly in this potential region. In *section 5.8* we will show that the lateral electric field will decay away from the interface, therefore it is always present for our experiments, allowing us to observe a constant level in the diffraction efficiency. However, the experiments in the literature probe the entire layer where the majority of their examined behaviour occurs in the bulk region, where the lateral electric field has decayed to an insignificant value. They still observe some behaviour from the

contributions of the grating formed near the PVK interface. The variations in the magnitude of the applied potential dependence with different pitch gratings is from the magnitude of the modulated electric field being pitch dependent and $E_{mod4\mu m} > E_{mod6\mu m}$, this is proven in *section 5.8*.

Experimentally we have determined that to maximise the SPP diffraction by using an optimum voltage the applied potential should be at the peak of the curves in *figures 5.19-21*. However, without prior determination of the position of this peak, which is sample dependent, a potential of 15V is ideal. At 15V the diffraction efficiency is near maximum for almost all gratings with a PVK layer thickness of 80nm. If a sample has a different PVK thickness the ideal potential should be scaled accordingly.

5.7 Writing Beam Intensity Dependence of the Grating Formation

The previous section demonstrated that the magnitude of the applied potential (the total of the combined uniform and modulated components) affects the diffraction efficiency by influencing the strength of the grating formation in the liquid crystal layer. By increasing the magnitude of the potential both the uniform or modulated component are scaled equally. However, the magnitude of the modulated component can be separately increased, without changing the magnitude of the uniform component, by increasing the illumination intensity in the light regions of the PVK. As the difference between the light and dark regions of the intensity dependent PVK conductivity determines strength of the modulated component. We can therefore expect the intensity of the illumination incident on the PVK layer to influence the SPP diffraction efficiency.

Our initial hypothesis for the intensity dependence is that the diffraction will increase with illumination, until a maximum efficiency when the conductivity of the PVK in the illuminated regions is at its highest possible value. The related intensity dependence of the SPP wavevector shift with uniform illumination, *figure 4.24*, suggests that the increase should be linear. Further increasing the incident intensity after maximising the PVK conductivity in the light region should, if the SPP diffraction efficiency follows the same trend as the SPP wavevector, display a constant diffraction efficiency.

The experimentally determined intensity dependence for the first SPP diffraction order is presented in *figure 5.*23. A low intensity beam is all that is required to observe the effect of a difference in the PVK conductivity. In this case the formation a modulated potential component that generates the grating to diffract an SPP. The low or zero intensity threshold behaviour is also demonstrated by the SPP wavevector shift with uniform illumination. The initial rise with increasing illumination intensity is linear as hypothesised, until a peak value is approached at ~2.5mWcm^{-2}. For higher intensities, the diffraction efficiency is slightly different to our initial hypothesis, in that it does not remain constant but gradually reduces. Interestingly, the intensity dependence for the second diffraction order, *figure 5.24*, displays a

continued increase in the diffraction efficiency for intensities greater than 2.5mWcm^{-2}. In addition, the continued rate of increase in the diffraction efficiency for the second order is reduced after 2.5mWcm^{-2}. Therefore, at higher intensities the mechanism for grating formation must reduce the diffraction efficiency of the first order while increasing energy transfer into higher diffraction orders. However, the reduction of energy into the first order is not necessarily a consequence of an increased energy transfer into higher orders.

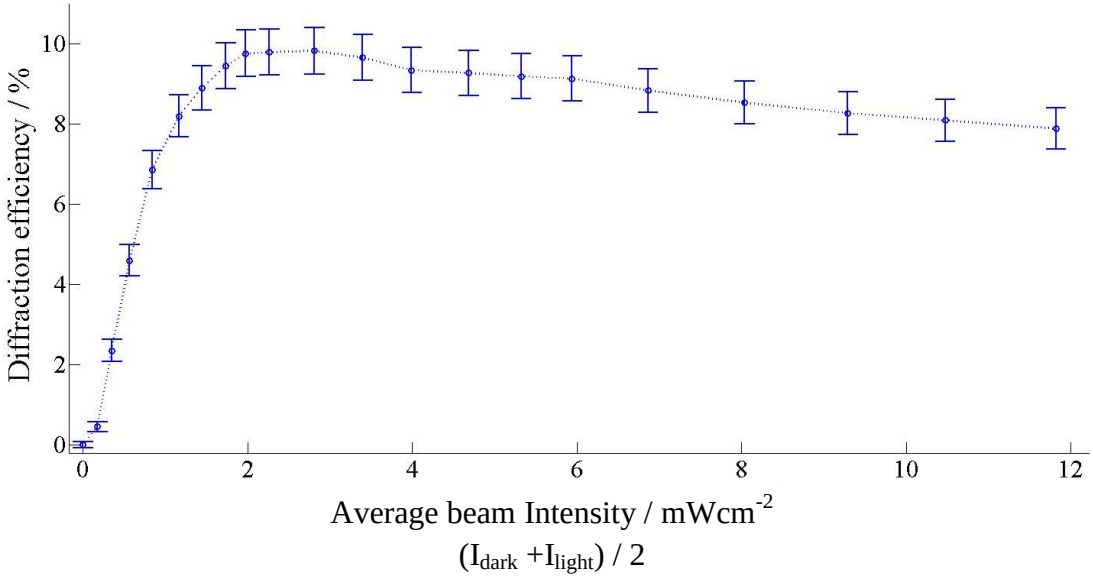

Figure 5.23: First order SPP diffraction efficiency dependence on the average illumination intensity. The diffraction appears to increase linearly until a saturation point. The diffraction then reduces with further increases in the average beam intensity. E_{SPP} = 1.462eV, Λ = 3µm, V =15V, Δ_{PVK} = 80nm.

Comparison to the mathematical simulations of the intensity dependence for SPP diffraction is not possible directly, as the intensity dependent conductivity of the PVK is not explicitly accounted for in the model. However, we propose a simple model about how the form of the spatially modulated potential at the PVK interface determines the intensity dependence. The observed behaviour is then explained from how the components of the refractive index gratings Fourier transform change in magnitude with illumination intensity.

We describe the form of the refractive index grating at low intensities by a $\sin^2(k_\Lambda x)$ function, *figure 5.25a*. This function is an approximation as we have assumed that the PVK conductivity and therefore the potential at the PVK interface, linearly follows the interference pattern of the crossed beams writing the grating. This is of course not true, as suggested by the impedance data for the PVK layer (*section 4.2.1*). The refractive index grating would also have second or higher harmonic components to its Fourier transform due to the non-linear response of the liquid crystal to a potential. However, as an approximation to the true form of

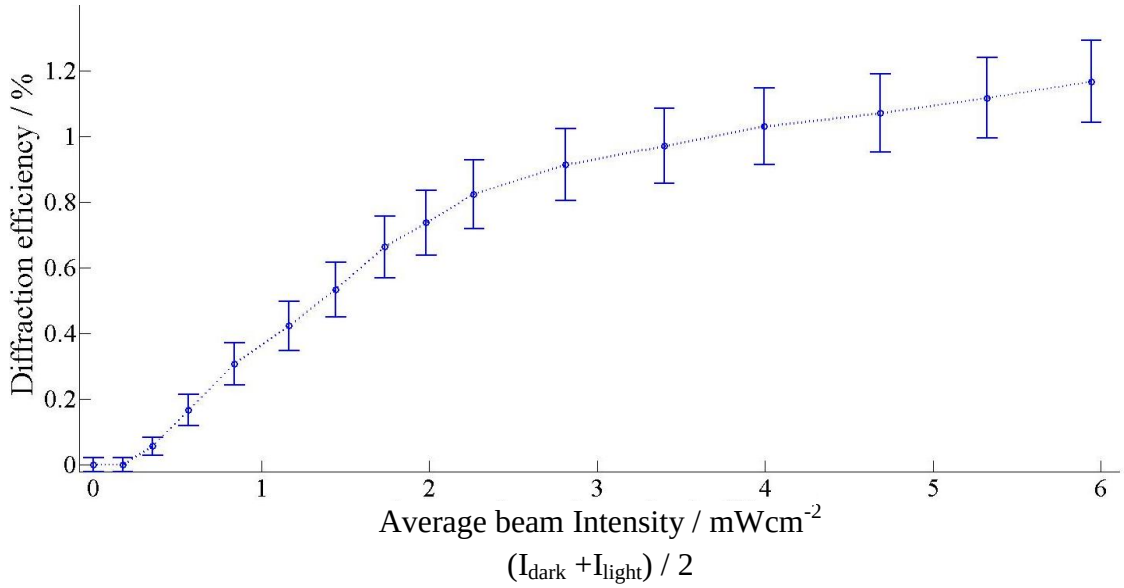

Figure 5.24: Second order SPP diffraction efficiency dependence on the average illumination intensity. The increase is linear with beam intensity in two different regimes. The changing point between regimes is at an intensity of ~2.5mWcm^{-2} the same intensity as the peak diffraction efficiency for the first order SPP diffraction. E_{SPP} = 1.462eV, Λ = 3µm, V =15V, Δ_{PVK} = 80nm.

the grating in our simple model it is correct to the leading order solution of the real grating function. From zero illumination, the refractive index modulation of the grating increases linearly with intensity until the intensity that displays the maximum first order diffraction efficiency. At this point, the PVK conductivity is considered to be at its maximum possible value at the positions of the PVK interface where the intensity of the interference pattern is largest (I_{light}), *figure 5.25b*. Further increasing the intensity then begins to maximise the PVK conductivity in a region larger than just where I_{light} is incident on the PVK interface. The effect on the grating is that it can no longer be fully described by a $\sin^2(k_\Lambda x)$ function, as the top of the modulation levels out to a constant refractive index, as visually represented in *figure 5.25c*.

Mathematically the intensity dependent form of the grating is described by the function, $n_{LC}(x) = A(I)\sin^2(k_\Lambda x)$. Where A(I) is an intensity dependent scaling function. The range of x is set from 0 to 200π (effectively semi-infinite), so the Fourier transform is not significantly influenced by the boundary conditions. The function n_{LC} (x) is also passed through an algorithm that sets n_{LC} =1, if n_{LC} (x) is > 1, to describe the photo-saturation of the PVK conductivity. The intensity dependence is then explained by the magnitude of the harmonics of the Fourier transform of this mathematical expression for the region between A(I) = 0 (no illumination) and A(I) = 2. At A(I) = 1, the PVK conductivity and the refractive index are maximised in the regions of I_{light} only. The intensity dependence of the Fourier transform of the model, *figure 5.25d*, displays the same trend for the intensity dependence of the first diffraction order. Indicating this model correctly describes the intensity dependence. The second diffraction order is not entirely predicted correctly, as we have not included a second

harmonic component in the low intensity regime that, in reality, would be present due to the non-linearity of the liquid crystal's re-orientation to a potential.

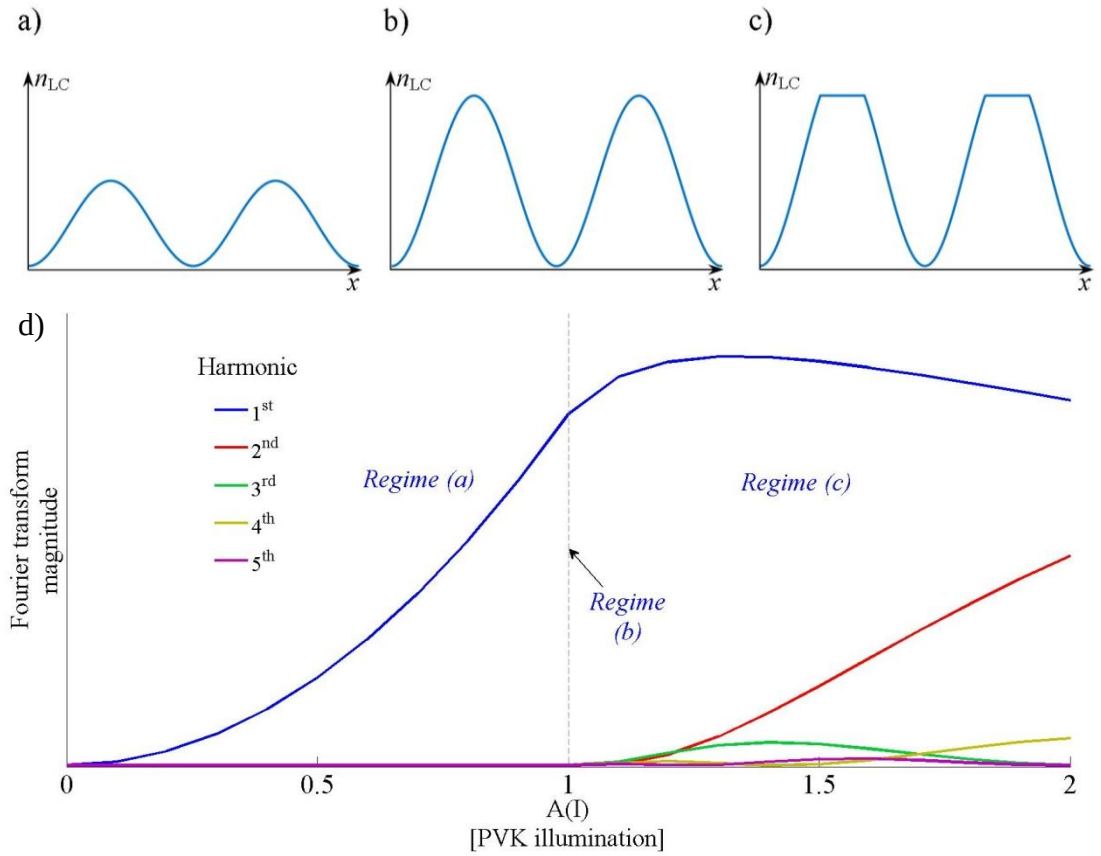

Figure 5.25: The approximation of the refractive index grating profile in the liquid crystal with increasing illumination. The intensity of the interference pattern is; (a) lower than the intensity required to maximise the PVK conductivity in any region, (b) the intensity maximises the conductivity in the brightest regions only and c) the conductivity of the PVK is maximised in a region larger than just the brightest part of the interference pattern. The liquid crystals refractive index is assumed to follow this conductivity profile. (d) The change in the Fourier transform for this grating profile with increased illumination.

Further confirmation of this model can then be determined by our mathematical simulations for the full liquid crystal system using the results of the Fourier transform. We simulate the intensity dependence in two regimes; the first, for the low intensities regime, the voltage scaling function V' across the liquid crystal is described by a constant plus a sinusoidal modulated component. The form of the potential is a result of an interpretation of the data acquired for to the SPP wavevector shift observed with uniform illumination (*figure 4.24b*), the value of the constant is therefore 0.8. The magnitude of the modulated component, α, is experimentally equivalent to the difference in the PVK's conductivity as a result of the non-uniform illumination. When $\alpha = 0$ there is no illumination and when $\alpha = 0.2$ the illumination has maximised the PVK's conductivity only where I_{light} is the incident intensity on the PVK. In the higher intensity regime, when the PVK conductivity is maximised in regions larger

than just where I_{light} is the incident intensity, the refractive index profile described by *figure 5.25c* cannot be programmed into the full simulations. Therefore, we simulate this intensity regime with the voltage scaling function $V' = (1-\beta) + \beta\sin^2(kx)$. With this function, the modulation of the grating reduces with lower β and the applied voltage in the I_{light} region is independent of β, i.e. constant. This does not simulate the higher intensity region correctly for our hypothesised model. However, it is sufficient to simulate the consequence of a reduced first harmonic component in our simulations as the Fourier transform of our model in *figure 5.25d* indicates. The results of these simulations are displayed in *figure 5.26*. This curve agrees with the observed first SPP diffraction order efficiency, confirming that the magnitude of the harmonic of the Fourier transform determines the diffraction efficiency. Physically, the Fourier transform of the grating is then a measure of the refractive index modulation, i.e. Δn, for each harmonic.

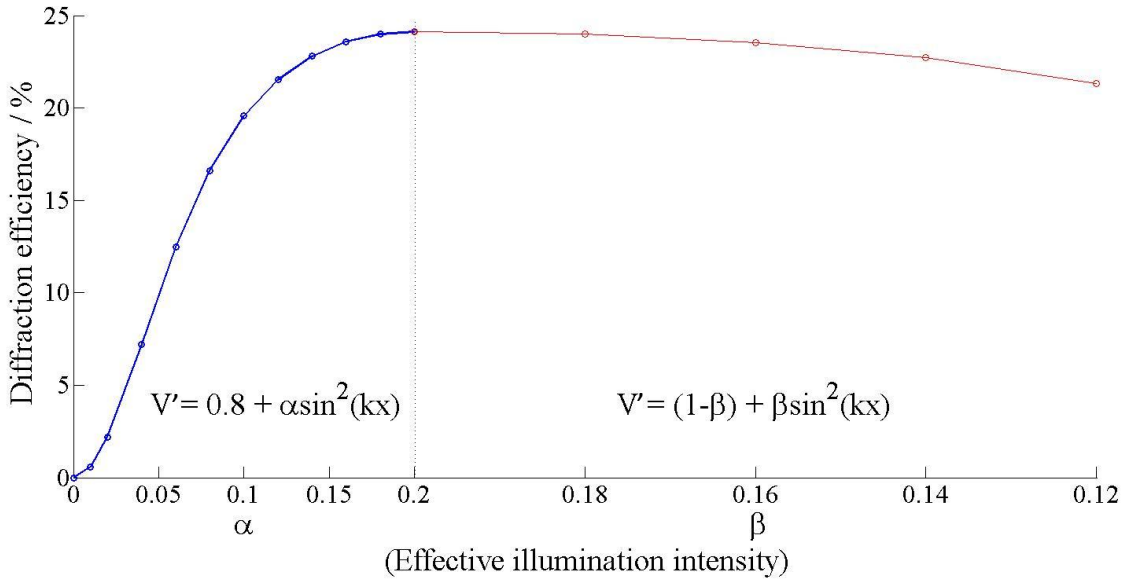

Figure 5.26: Mathematical simulation of the intensity dependence of the first diffraction order. The simulations do not directly account for the intensity dependent conductivity of the PVK; however, we can simulate this behaviour using expressions for the voltage profile across the liquid crystal. The simulated potential is 15V multiplied by the functions for V' displayed.

We experimentally observed that the maximum first order SPP diffraction occurs at an average intensity of ~2.5mWcm^{-2}. At this intensity, the C_{60} dopant is believed to be photo-saturated and no further increase in the PVK conductivity is possible through a charge-transfer complex. As the intensity in the dark region of the interference pattern is considered to always be zero[XVI], I_{light} is double this value, ~5mWcm^{-2}. Therefore, the C_{60} photo-saturation intensity in the illuminated regions is the same for both the intensity dependence of

[XVI] Experimentally this is not true due to the existence of internal reflections within the cell. The low intensity of the internal reflections allows us to normally ignore their existence. However, they could be significant when we consider the PVK's conductivity in the dark regions.

the SPP wavevector and SPP diffraction. A consistency one would expect for the intensity dependence of two related effects in samples for the same PVK batch.

In general, unless otherwise stated, we used an intensity of ~1.25mWcm^{-2} for each writing beam. This is the beam intensity after transmission through the Au, which is 16-20% transparent. Therefore, the brightest regions of the interference pattern should be photo-saturating the C_{60} in the PVK layer, maximising the grating contrast. As the amount of light absorbed is only a tiny fraction of the beam (0.005%), a different PVK thickness for another sample will not affect this optimum intensity. A change in the C_{60} doping level would change the optimum illumination intensity.

5.8 Pitch Dependence on the Diffraction Efficiency

In this section, I examine how the pitch of the refractive index grating affects the SPP diffraction efficiency.

5.8.1 Experimental Observations

The pitch dependence of the SPP diffraction efficiency for the first diffraction order is presented in *figure 5.27*, for a 120nm PVK layer sample. We observe a clear peak in the diffraction efficiency at a pitch of approximately 4µm. The efficiency drops sharply either side of this optimum pitch, tending to zero for pitches less than 1µm and to a value of 4.5% for a 6µm pitch. The diffraction efficiency then drops very gradually for pitches greater than 6µm. The apparent increase in the diffraction for a pitch greater than 30µm is an artefact from

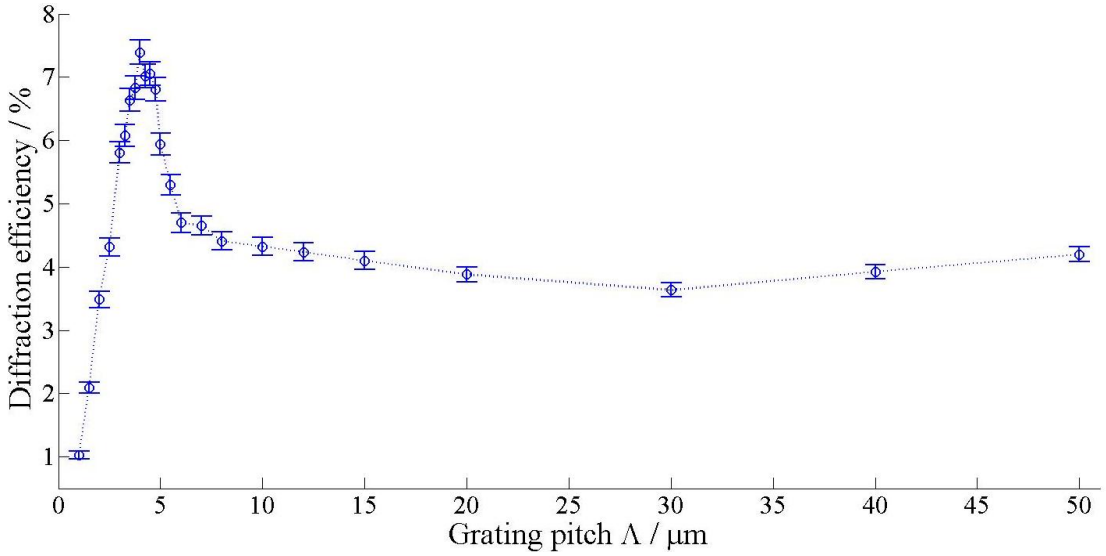

Figure 5.27: Grating pitch dependence of the diffraction efficiency for the first diffraction order. A sharp increase in the diffraction efficiency is observed in the 2-6µm region, for this δ_{PVK} = 120nm sample. The peak efficiency is at 4µm. For pitches larger then 6µm, the diffraction efficiency appears to gradually decrease. V = 15V, E_{SPP} = 1.462eV.

the measurement to determine the diffraction efficiency. For large grating pitches, higher diffraction orders (+2 and +3) begin to significantly overlap the +1 order examined, due to the broadness of the diffraction spots in *k*-space, see *figure 5.4*.

Having observed that the diffraction efficiency peaks at a differing magnitude potential with different pitches, *figure 5.20*, we examine how the pitch dependence varies when we change the magnitude of the applied potential. The general trend observed in *figure 5.28* is the same as observed before, regardless of the potential, i.e. an increasing diffraction efficiency with decreasing pitch until a maximum value, then a sharp drop in efficiency for the smallest pitches. However, the black dashed line indicates that the optimum pitch moves to smaller pitches for higher potentials. The change in the peak pitch is small, as doubling the potential from 10V only shifts the peak by ~0.5µm. A more significant effect is the enhancement in the diffraction efficiency at the peak pitch by increasing the potential. At 10V, the maximum diffraction with a 4.5µm grating diffracts 26% more energy than a 8µm grating. Equivalently at 20V the maximum diffraction with a 4µm grating, couples 68% more energy than at 8µm. Therefore, we conclude that the mechanism for generating the peak is dependent on the applied potential, though the position of this peak is only weakly dependent.

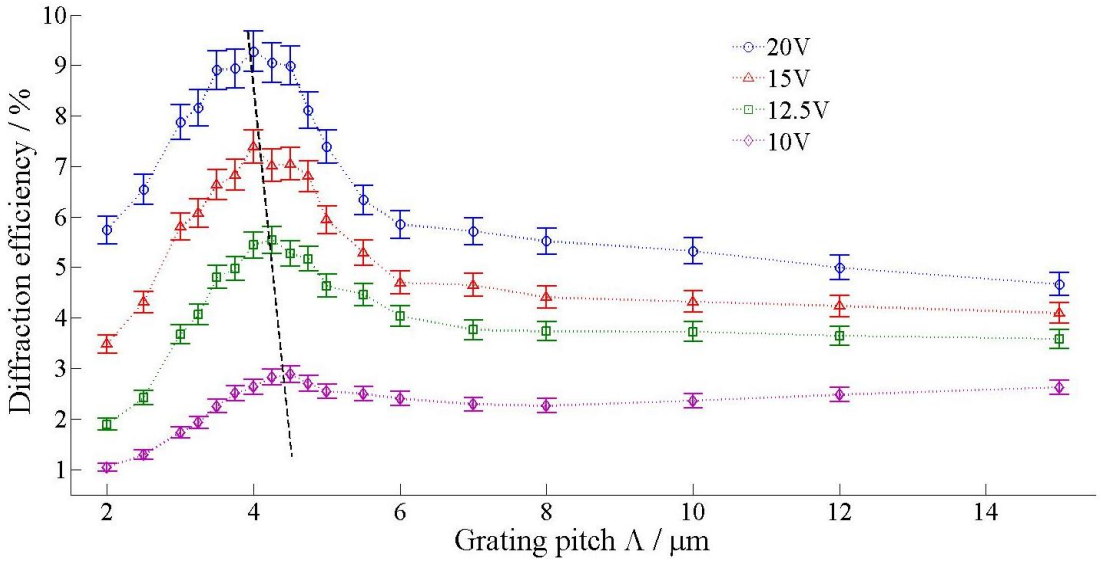

Figure 5.28: Pitch dependence of the first SPP diffraction order for an increasing magnitude of the applied potential. Increasing the potential across the liquid crystal shifts the peak in the pitch dependence a small amount to a lower grating pitch. δ_{PVK} = 120nm, V = 15V, E_{SPP} = 1.462eV.

As liquid crystal cells are well known for large variations in behaviour between samples, we have investigated how the pitch dependence varies from cell to cell. The variation in the pitch dependence between two cells fabricated several months apart is displayed in *figure 5.29a*. A peak in the diffraction is observed with both batches, though the optimum pitch is not the same. The newer batch displays a peak at 3µm instead of 4µm. The decrease in diffraction efficiency for larger pitches is less curved for the newer samples. Hence, the peak is not as sharp as observed in the older samples. It is unknown if this is of significance.

Within a single batch, we also investigated if the thickness of the PVK layer alters the pitch dependence, *figure 5.29b*. The data shows the same general pitch dependent behaviour for all examined PVK layer thicknesses. There is no obvious variation in the optimum pitch for PVK layers between 80 and 107nm thick. We conclude that the mechanism behind the pitch dependence is not directly related to the PVK layer thickness.

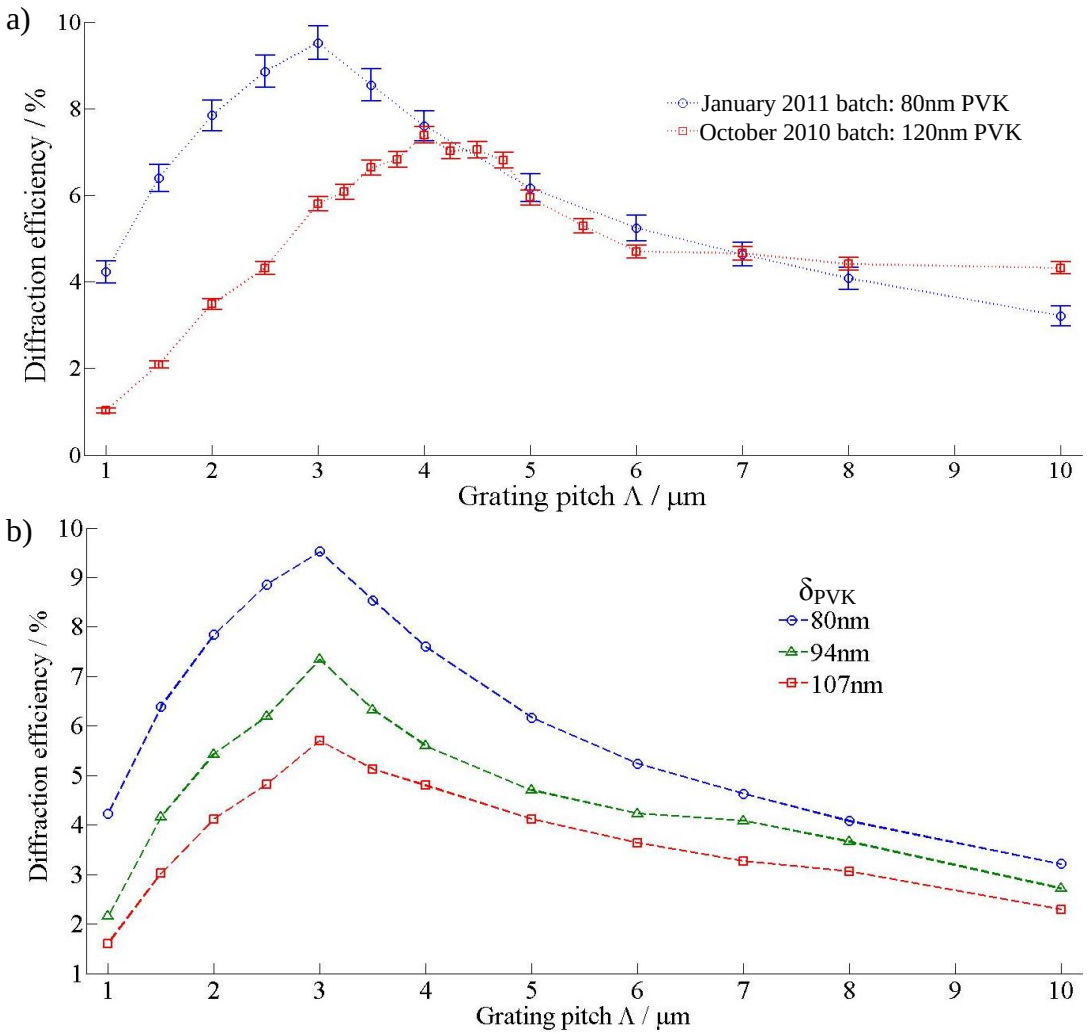

Figure 5.29: The pitch dependence of the diffraction efficiency into the first order for a) two different batches of samples, b) samples from the same batch with a differing PVK layer thickness. The same pitch dependence is seen in all samples; however, the maximum diffraction efficiency is at slightly different pitches between batches. V = 15V, E_{SPP} = 1.462eV.

We then investigate if the energy of the SPP influences the pitch dependence of the first diffraction order, as presented in *figure 5.30*. The data indicates that the observed optimum pitch is approximately constant within a sample over the range of energies that we typically examine. The general shape of the pitch dependence is the same for all examined energies, though the peak at 3μm for a 1.656eV SPP is not as sharp and could be slightly shifted to a pitch between 3-3.5μm.

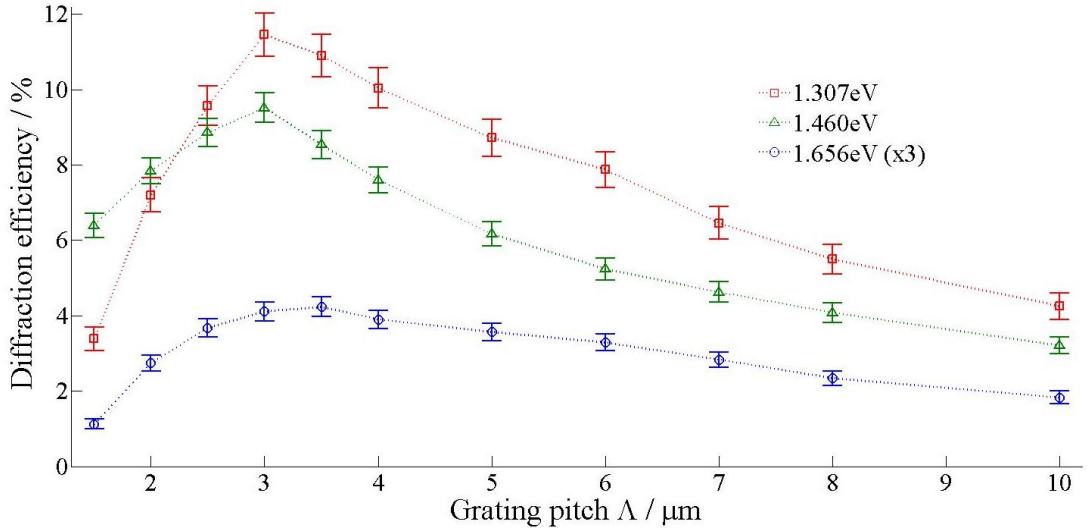

Figure 5.30: Pitch dependence of the first diffraction order for SPP modes with different energies. The same pitch dependence is seen regardless of the SPP energy. The 1.307eV data underestimates the diffraction efficiency due the detection sensitivity of the spectrometer used. This does not affect the shape of the pitch dependence, only its magnitude. δ_{PVK} = 80nm, V = 15V.

To rule out the possibility that at short pitches the energy may be diffracted into other diffraction orders, instead of the first order, we examined the pitch dependence for the -1 and +2 diffraction orders when the grating is phase matched to the +1 order. Moreover, as *figure 5.31* displays, diffraction into other orders is not the reason for the drop in coupling efficiency at small grating pitches. In fact, when the grating is phase matched to the +1 order, the diffraction efficiency for the other diffraction orders begins to decrease at a larger grating pitch, ~5-6μm. Only the +1 order then displays a sharp peak in the diffraction efficiency. This is because the wavevector mismatch term for diffraction into other orders becomes significantly larger as the pitch of the grating is reduced, limiting diffraction as described in *section 5.4*. The small increase in diffraction at 5μm for the -1 order, compared to larger pitches, suggests that the peak in the +1 order is not a result of energy preferentially being transferred into the +1 order.

Lastly, we examine how the pitch influences coupling of energy into the second diffraction order (when the grating is phase matched to the +2 order). The pitch dependence for the second order, *figure 5.32*, is noticeably different to the first order in that a peak in the diffraction efficiency is not clearly observed. Little or no diffraction is experimentally observed for grating pitches less than 2.5μm. The diffraction steadily rises until a maximum at 7μm, before slightly decreasing. Unlike the first diffraction order, the maximum diffraction efficiency is not a sharp peak. In addition, we note that the diffraction into the second order is much lower than the first order.

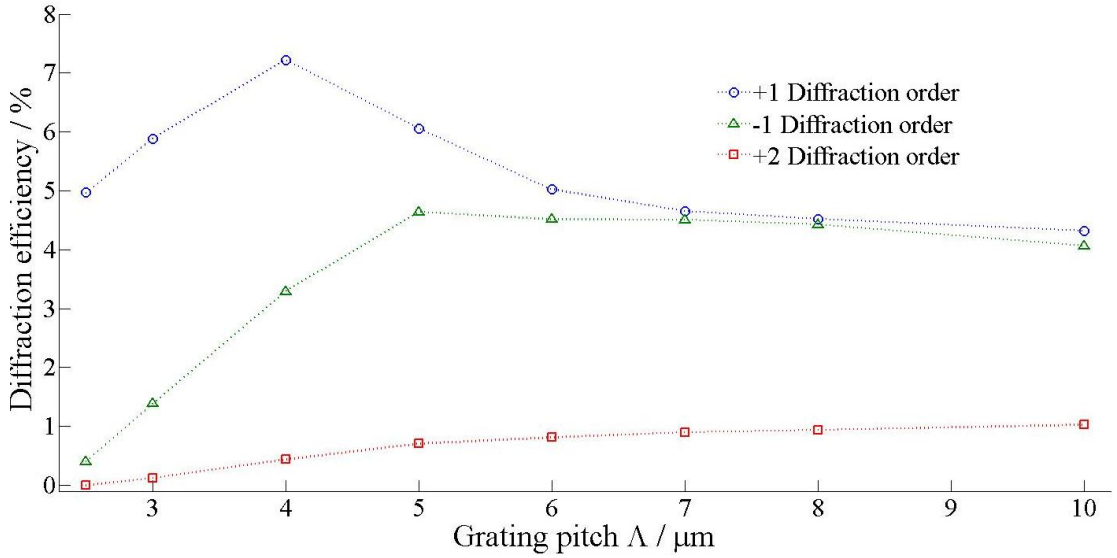

Figure 5.31: Pitch dependence of the diffraction into different diffraction orders when the grating orientation angle γ, is phase matched to the first order. The '-1' order shows similar trends to the '+1' order, however the wavevector mismatch term becomes significantly larger for smaller pitches hence the drop off in efficiency appears to occur at a larger value. The pitch dependence for the '+2' order shows that the drop in diffraction efficiency for the '+1' order, for pitches lower the 4μm, is not due to the transfer of energy into higher orders. δ_{PVK} = 120nm, V=15V, E_{SPP}=1.462eV.

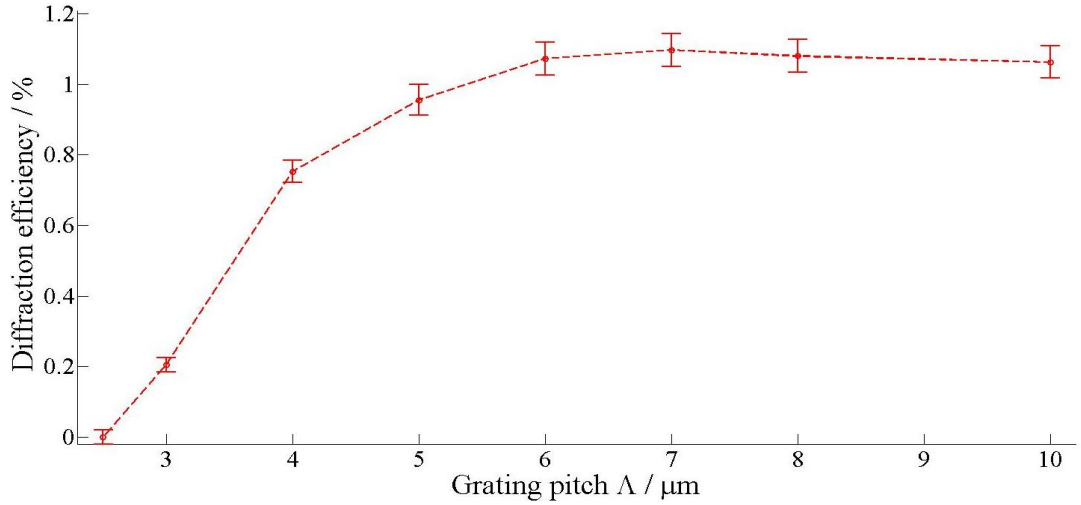

Figure 5.32: Pitch dependence of the second order diffraction efficiency. The peak appears at ~7μm, slightly higher than the first order. The mechanism that causes this dependence must therefore be dependent on the specific grating harmonic. δ_{PVK} = 120nm, V = 15V, E_{SPP}= 1.462eV.

5.8.2 Review of the Pitch Dependence for Diffraction from Bulk Photorefractive Gratings in Hybrid Liquid Crystal Systems

A related pitch dependence has been observed for the first order diffraction efficiency of a probe beam examining gratings written into the bulk region of photorefractive liquid

crystal layer. Khoo reports an optimum grating spacing of 60μm [167], roughly twice the thickness of his cell and attributes the effect to the doped photorefractive liquid crystals ability to trap charges forming the internal space charge field. In the results reported by Khoo, there is not a clear peak in the diffraction efficiency at the optimum value, unlike our observations; his reported pitch dependence shows a similar trend to our observations of the pitch dependence for the second order SPP diffraction efficiency. The difference in his peak values is likely a result of his cell using a liquid crystal that is directly photorefractive and not using photoconducting layers.

Other groups have also examined the pitch dependence [238, 239] in a cell structure similar to ours and demonstrate a peak diffraction for a grating pitch of 25-30μm. Ono indicates that the reduced diffraction efficiency for pitches smaller than ~15μm is because these gratings are not purely in the Raman-Nath grating regime, hence are limited in displaying first order diffraction [238]. Therefore, a direct comparison to our results is not entirely appropriate, as the Raman-Nath and Bragg diffraction regimes are less meaningful in our experiments. The experiments of Khoo and Ono probe the bulk grating formation. The grating formation near the surface may have a subtly different mechanism, which could explain the significant discrepancy in their reported optimum diffraction pitch compared to our observations.

A similar value for the peak in the pitch dependence, in the related effect of photorefractive two-beam gain, is observed in a unique variation on a photorefractive liquid crystal cell, where a photorefractive crystal Ce:SBN is used instead of photoconductive layers [240]. This type of cell demonstrates an optimum two-beam gain for a grating pitch of ~2μm, similar to our observations. In their experiments, they do not apply a potential across the liquid crystal layer. They explain that their observed pitch dependence is due to the magnitude of the space-charge field from the Ce:SBN crystal at the interface. This space charge field penetrates into the liquid crystal layer to modulate the director, enhancing the photorefractive gain of the Ce:SBN crystal. They propose that the magnitude of the space-charge field increases with decreasing pitch, as the same potential is dropped across a smaller length. The reduced diffraction efficiency for pitches smaller than 2μm is then the result from the grating pitch becoming comparable to the Debye screening length in this crystal of 1.6μm; therefore preventing sufficient trapping of the charges in the non-illuminated regions to generate a good photorefractive grating. They do not consider the details of the response of the liquid crystal to the electric field. The model they propose ignores the fact that the magnitude of the electric field varies with distance from the interface.

5.8.3 Numerical Simulations of the Pitch Dependence

The mathematical simulations were then used to confirm if the observed pitch dependence can be explained by the SPP interacting with a modulated refractive index in a liquid crystal layer. The numerical simulations of the pitch dependence are displayed in *figure 5.33a*, for the first diffraction order and *figure 5.33b* for the second diffraction order. The

simulations demonstrate the same behaviour that we experimentally observe, though the position of the peak is not in quantitative agreement. For both the first and second diffraction order, the predicted optimum pitch is slightly smaller than the experimentally observed pitch. The simulations over-predict the magnitude of the diffraction for all pitches for both diffraction orders.

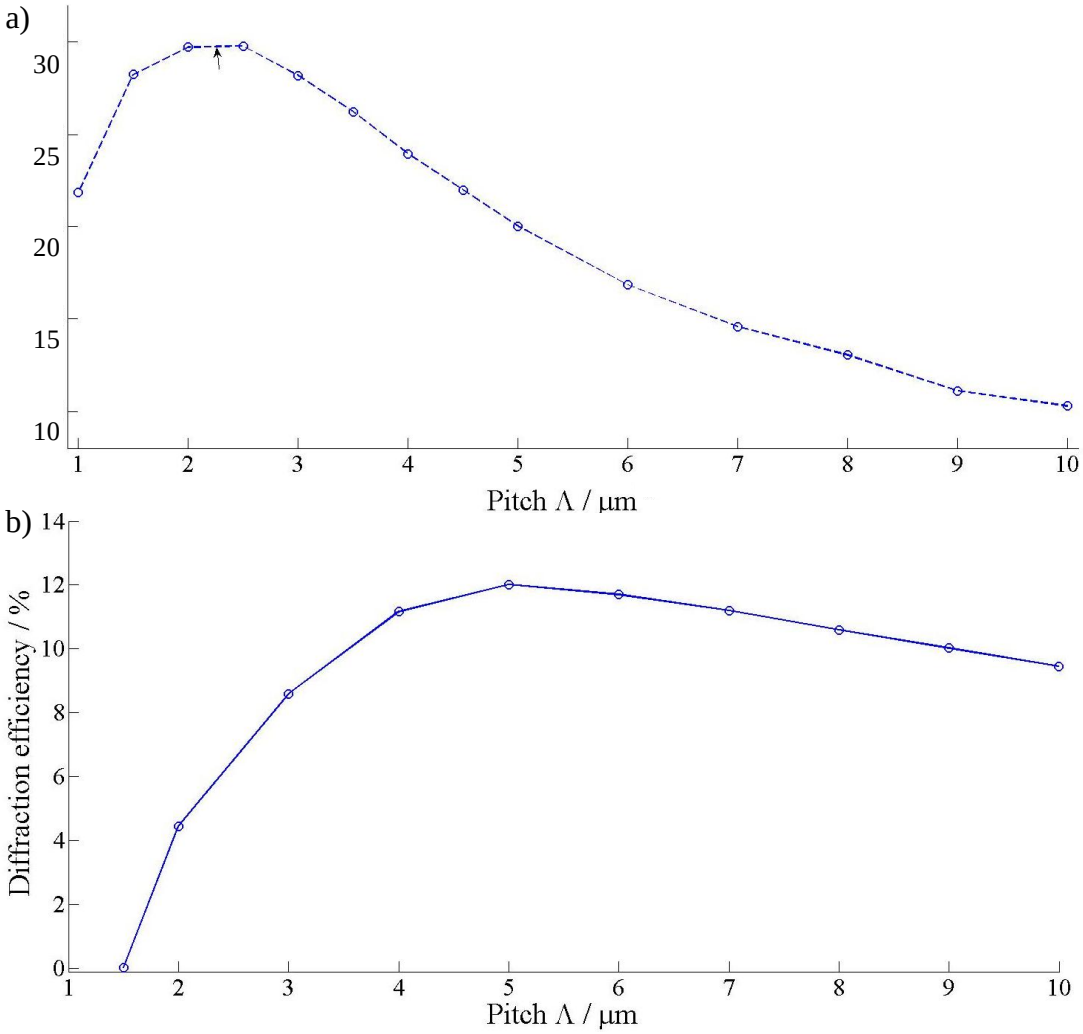

Figure 5.33: Mathematical simulation of the pitch dependence on the first diffraction order (a), second diffraction order (b). However, the value of the peak pitch is not the same, the general pitch dependent behaviour is accounted for in the model. δ_{PVK} = 107nm, V = 15V, E_{SPP}= 1.462eV.

The match to the experimental behaviour indicates that the peak is not due to the charge dynamics in the PVK being dependent on pitch. This fact combined with the experimental observation that the peak in diffraction efficiency does not depend on SPP energy, and therefore the details of how the SPP interacts with the LC grating, strongly suggests that the variation of the diffraction efficiency with pitch is solely due to the response of the liquid crystal to the photo-induced spatially modulated electric field.

5.8.4 Approximate Analytic Model to Explain the Pitch Dependence

We propose a simplified model for the pitch dependence that is based on two underlying effects;

1. The spatial dependence of the modulated electric field within the liquid crystal layer, generated by the photo-induced potential profile at the PVK-liquid crystal interface.
2. The magnitude of the re-orientation of the liquid crystal molecules is dependent on the distance into the cell. Directly at the PVK-liquid crystal interface there is a boundary layer where the molecules are rigidly anchored. Whereas away from the interface, in the bulk region of the layer, the liquid crystal is relatively free to rotate in response to the electric field.

In order to predict the pitch dependence of the SPP diffraction efficiency we first develop an approximate analytic expression for the electric field in the photo-excited cell. We then combine this with a simple model of an extreme version of the boundary layer in the liquid crystal, where an initial thickness of the liquid crystal, δ_{fixed}, does not respond to the electric field to form a grating and outside of this region, the liquid crystal responds fully to the electric field. This model clearly does not encompass all the physics of the system, as discussed in more detail later; however, the insights it gives are still valid in the real situation.

Approximate analytical expression for the electric field.

Maxwell's equations in the absence of free charges state,

$$\underline{\nabla} \cdot \underline{\underline{\varepsilon}}\, \underline{E} = 0 \tag{5.13}$$

where $\underline{\underline{\varepsilon}}$ denotes the anisotropic dielectric tensor of the liquid crystal. To allow an approximate analytic solution of this equation we will assume that the LC is unaffected by the electric field, i.e. the director is aligned in-plane, parallel to the PVK-LC interface. Whilst the true electric field will differ from that calculated here due to this approximation the general form of the solution is not be significantly different. The electric field is determined by the gradient of the electrostatic potential,

$$\underline{E} = -\underline{\nabla}\, \phi. \tag{5.14}$$

Combining *equations 5.13* and *5.14* leaves us the following equation to solve,

$$\underline{\nabla} \cdot \underline{\underline{\varepsilon}}\, \underline{\nabla}\, \phi = 0. \tag{5.15}$$

For our system, the domain of the potential is rectangular with a width of a single grating period and with a length equal to the thickness of the liquid crystal layer, d. The grating in our cell is periodic in the *x*-direction, resulting in the obvious periodic boundary condition,

$$\phi(x, z) = \phi(x+\Lambda, z). \tag{5.16}$$

In the *z*-direction, there is a modulated potential at the PVK interface. We propose that the form of the potential at the PVK interface has a uniform component plus a modulated component, which to first order is described by a sine function,

$$\phi(x, 0) = \phi_0 + \phi_1 \sin(k_\Lambda x). \tag{5.17}$$

With ϕ_0 and ϕ_1 as constants describing the magnitude of the uniform and modulated potentials. As our cells only have one photoconductive layer, the potential at the PI interface is considered to be zero

$$\phi(x, d) = 0. \tag{5.18}$$

As *equation 5.15* is linear, it can be solved using the method of separation of variables. Moreover, from the boundary conditions of our system, *equations 5.16-5.18*, we find that the potential has the form,

$$\phi(x,z) = \varphi_0(z) + \varphi_1(z)\sin(k_\Lambda x) \tag{5.19}$$

where,

$$\varphi_0(z) = \frac{\phi_0}{d}(d - z) \tag{5.20}$$

$$\varphi_1(z) = \tfrac{1}{2}\,\phi_1 [(1 - \coth(k_\Lambda d))e^{k_\Lambda R z} + (1 + \coth(k_\Lambda d))e^{-k_\Lambda R z}] \tag{5.21}$$

and the constant $R = (\varepsilon_x/\varepsilon_z)^{1/2}$ (for an E7 liquid crystal, $R = [19.54/5.17]^{1/2}$), has been introduced to account for the liquid crystals dielectric anisotropy. Thus the electric field components in the *x* (lateral) and *z* (normal) directions are given by,

$$E_x = -\tfrac{1}{2}\phi_1 k_\Lambda [(1+\coth(k_\Lambda d))e^{-k_\Lambda R z} + (1-\coth(k_\Lambda d))e^{k_\Lambda R z})]\cos(k_\Lambda x) \tag{5.22}$$

$$E_z = \tfrac{1}{2}\phi_1 R k_\Lambda [(1+\coth(k_\Lambda d))e^{-k_\Lambda R z} - (1-\coth(k_\Lambda d))e^{k_\Lambda R z})]\sin(k_\Lambda x) + E_0 \tag{5.23}$$

where $E_0 = \phi_0/d$. Since $k_\Lambda d \geq 2\pi$ for the gratings we examine, $\coth(k_\Lambda d) \approx 1$, these equations then simplify to,

$$E_x = -\phi_1 k_\Lambda e^{-k_\Lambda R z} \cos(k_\Lambda x) \tag{5.24a}$$

$$E_z = \phi_1 R k_\Lambda e^{-k_\Lambda R z} \sin(k_\Lambda x) + E_0. \tag{5.24b}$$

Visualising the combined effect of these electric fields on the liquid crystal alignment is not trivial. However, we can still determine the pitch dependence by considering the effect of the constant E_0 term in *equation 5.24b*. Provided that the value of E_0 is large enough to align the director parallel to z, then the additional modulated component of the normal field has a limited effect on the liquid crystal alignment. The modulation of the liquid crystals director is then a result of the lateral electric field of *equation 5.24a*. The modulation follows the same pitch dependence in the *x*-direction as the photo-induced potential, with a phase shift of $\pi/2$, as expected. The magnitude of the lateral electric field then determines the strength of the grating formation and is given by,

$$|E_x| = \phi_1 k_\Lambda e^{-k_\Lambda Rz}. \tag{5.25}$$

Hence, the magnitude of the lateral electric field is dependent on both the pitch and the distance from the interface.

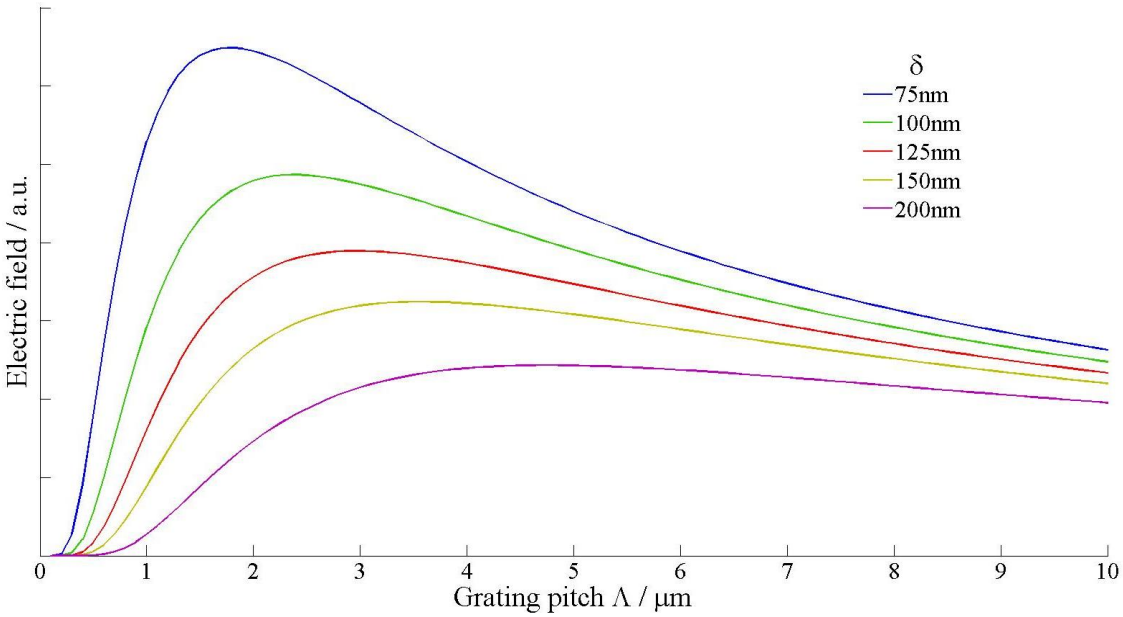

Figure 5.34: The pitch dependence on the electric field described by *equation 5.25*.

The magnitude of the lateral electric field is plotted as a function of pitch in *figure 5.34*, for several distances into the cell $z = \delta$, close to the PVK interface. For finite distances away from the PVK interface the lateral electric field initially increases as the pitch decreases. This is because the same photo-excited potential difference is dropped over a shorter distance for shorter pitches. However, at some point the exponential decay of the field with distance from the PVK begins to dominate and it is for this reason that the electric field magnitude decreases with pitch for short pitches.

The boundary layer in the liquid crystal.

As a consequence of the anchoring forces, the liquid crystal molecules adjacent to the PVK are oriented parallel to the interface and the electrical forces generating the grating cannot rotate the director[XVII]. The effect of the anchoring forces is propagated for a certain distance into the cell due to the elastic response of the liquid crystal to spatial variations of the director. This effect decreases with distance away from the interface. However, a thin layer of the liquid crystal, called the boundary region, will have a reduced rotation with the applied electric field. Whilst in reality, in the boundary region the liquid crystal director varies continuously from the direction at the interface to the direction in the bulk of the liquid crystal, we will treat it, in order to simplify the situation, as a region in which the liquid crystal is not able to re-orientate and that just outside the boundary region the effect of the anchoring forces is zero. That is to say, we split the liquid crystal layer into a boundary region between $\delta = 0$ and $\delta = \delta_{fixed}$ with no grating formation and a bulk region $\delta > \delta_{fixed}$ which responds to the electric fields. This approximation and the likely real system are demonstrated in the inset of *figure 5.35*. This means that the diffraction efficiency will follow a curve similar to those shown in *figure 5.34*, not a $1/\Lambda$ function and that this is the reason for the experimental pitch dependence.

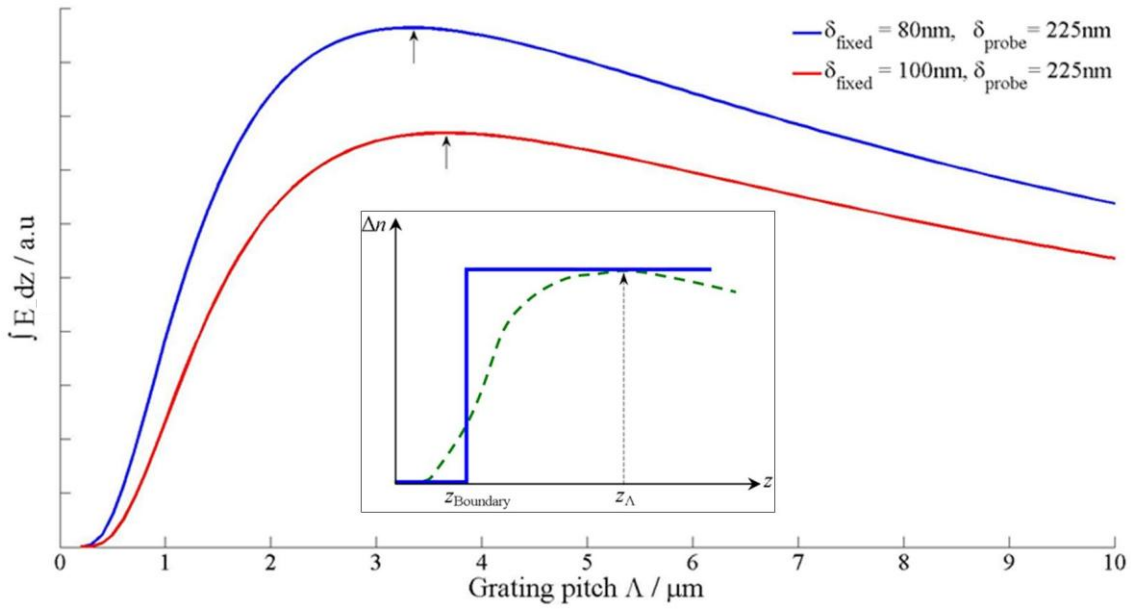

Figure 5.35: The pitch dependence on the integral of *equation 5.25*, between the values of δ_{fixed} and δ_{probe} described in the text. The pitch with the largest electric field closely matches the experimentally determined optimum pitch. *Inset*: The boundary layer approximation used (solid *blue* line) and an illustration of the actual physical effect of the boundary layer (dashed *green* line).

Whilst the magnitude of the approximate electric field of *equation 5.25* predicts the general form of the pitch dependence correctly it predicts the peak of the diffraction efficiency will be

[XVII] Under normal operating conditions. A very large potential will cause a small re-orientation and could also permanently damage the sample.

at a shorter pitch than observed experimentally. One possible explanation for this is that the SPP probes the orientation of the liquid crystal for a reasonable distance into the liquid crystal. To approximate this we can integrate the result given in *equation 5.25* from δ_{fixed} to a distance δ_{probe}. Whilst in principle this integral should be weighted with the SPP mode intensity as a function of distance, this is a complication that does not make sense considering the other approximations we have made. The value of δ_{probe} can be determined by the distance the SPP penetrates into the dielectric determined by *equation 2.13* where the average refractive index of the liquid crystal layer ($n \approx 1.6$) has been used as an approximation for the dielectric mediums; the PVK thickness is then subtracted. Therefore, for the 1.462eV SPP typically used in our experiments, $\delta_{probe} \approx$ 205-225nm, depending on the sample.

The size of the boundary region is generally considered to be ~100nm [143]. Our observations of the photorefractive shift of the SPP dispersion in *figure 4.26* also indicate a similar value. No dispersion modification is observed, in the light or dark, for SPP with energies higher than 1.9eV. An SPP with this energy would penetrate ~80nm into the liquid crystal; hence we also have an experimentally determined approximate value for the thickness of the boundary region.

The integral of the magnitude of the lateral electric field already discussed, as a function of grating pitch, is plotted in *figure 5.35* for both values of δ_{fixed}. The peak of this integral is 3.3μm for the 80nm boundary region and 3.5μm for a 100nm region, in very good agreement with the experimentally observed optimum pitches for the SPP diffraction in the samples. Reducing δ_{fixed} lowers the pitch of the maximum for this integral and increasing δ_{probe} raises the pitch. Changing δ_{fixed} shifts the pitch of the maximum more the changing δ_{probe} by the same amount.

In addition to explaining the general form of the pitch dependence of the SPP diffraction efficiency, this simplified model provides an explanation for the changes in the pitch dependence with an increasing potential. A larger potential will increase the magnitude of both the modulated electric field and the uniform electric field E_0. A larger modulated electric field component will not alter the shape of the pitch dependence. However, an increase in the uniform electric field will decrease the thickness of the boundary layer, which, as shown by *figure 5.35*, will shift the peak to shorter pitches.

This model can also help explain the weak variation of the pitch dependence of the diffraction efficiency with SPP energy. A slight variation in the optimum pitch of the SPP energy is expected, as lower energies probe further into the liquid crystal changing δ_{probe}. The expected theoretical change in δ_{probe} between the 1.46 and 1.66eV SPP is ~35nm. This change in δ_{probe} can only generate a small change in the optimum pitch of ~0.35μm, a similar shift to that observed in the experimental data. The change in δ_{probe} between the 1.46 and 1.31eV SPP is insufficient for a noticeable shift in the optimum pitch.

The difference in the pitch for optimum SPP diffraction between batches can be explained with this approximate model by a variation in the thickness of the boundary layer. A match to the optimum pitch for the October 2010 batch (peak at 4μm) would require δ_{fixed} = 124nm, and the January 2011 batch (3μm), δ_{fixed} = 73nm. A possible cause for the physical change in the size of the boundary region between batches is that the anchoring strength of the liquid crystal to the PVK interface varies. As the anchoring strength is dependent on the nature of the interaction with the polymer surface [236], in particular the macroscopic chemical bond asymmetry [212] and the van der Waals forces between the alignment layer and liquid crystal [241, 242]. During fabrication there may be a variation in the rubbing strength of the PVK; this may significantly affect the anchoring energy. In addition, it is a possibility that between batches the ionic conductivity of the liquid crystal varies from the addition of impurity ions; this could noticeably affect the strength of the intermolecular anchoring forces, therefore influencing the boundary layer thickness. Either of these is possible and both are hard to quantify for an accurate comparison between experiment and a theoretical model.

Validity of the approximations in this model.

Clearly there are gross approximations within the model set out above. In particular we have not dealt with the non-linear response of the liquid crystal to the electric fields. This means that the forms of the spatially modulated electric fields we have determined are not quantitatively correct. However, in reality the modulated electric field will still decay rapidly away from the PVK interface, which is the key to the success of this simplified model. In addition we have used a very simple approximation to the true boundary layer behaviour that contains the fundamental truth that the liquid crystal near the PVK interface is dominated by the anchoring effects.

If we wished to simplify the model further we could say that the pitch dependence of the diffraction efficiency exists in two regimes, which are given by the comparison of two length scales. The first length scale is the distance over which the combined modulated and uniform electric fields change direction significantly. Because the exponential decay of the modulated electric field component normal to the interface is much more rapid than the lateral variation of the electric field, it is the former that gives this electric field directional change length scale. The second length scale is an elastic length scale for the minimum distance the liquid crystal deformations can occur over, without an elastic force requirement in excess of the electrical force provided. In our model the anchoring at the PVK interface forming the boundary layer determines this length scale. If the electric field directional change length scale is much greater than the elastic length scale then the pitch dependence is due to the fact that the lateral electric field is effectively the magnitude of the photo-induced modulation of the PVK surface potential divided by the pitch. This describes the increase in diffraction efficiency with decreasing pitch. If the electric field directional change length scale is much less than elastic length scale then no grating will form and this is the reason why the diffraction efficiency falls so rapidly with decreasing pitch for small pitches. This further

simplified model suggest that even if we did not have anchoring of the liquid crystal at the PVK interface, we would still see a peak in the diffraction efficiency at some pitch determined by the fundamental elastic properties of a non-anchored liquid crystal.

The aim of developing the simplified model was to gain a better understanding of the underlying processes of the pitch dependence and full predictions require the full numerical simulations.

5.9 Liquid Crystal Rubbing Direction Dependence of the SPP Diffraction Efficiency

Lastly, we consider how the initial orientation of the in-plane liquid crystal director (the director orientation when no potential is applied) at the PVK interface, ψ_0, affects the diffraction efficiency. The orientation of the director is measured relative to the SPP propagation direction. When ψ_0 is parallel to the SPP propagation direction, $\psi_0 = 0^o$. The grating is then approximately orthogonal to the director with this alignment. All previous data sets presented have $\psi_0 = 0^o$. Assuming the cell has been fabricated with zero twist, ψ_0 should be parallel to the rubbing direction marked on the PI coated substrate (*figure 3.16*). This method of measuring ψ_0 has a systematic error of up to 5^o associated with it; however, once placed into the experimental apparatus the cell can be rotated to an accuracy of 0.5^o.

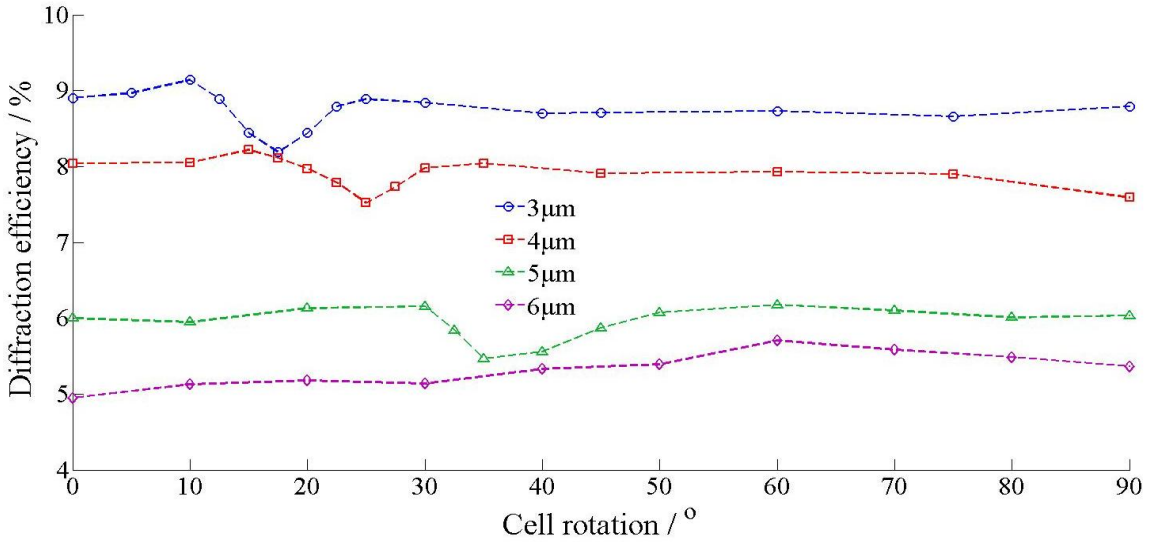

Figure 5.36: First order diffraction efficiency dependence on the initial (before an applied voltage) in-plane director of the liquid crystal molecules. In general, there is no rotational dependence, with the exception of a dip in the efficiency at certain cell orientations. This dip is dependent on the pitch of the grating. δ_{PVK} = 80nm, V = 15V, E_{SPP}= 1.462eV.

Presented in *figure 5.36* are the results of the ψ_0 dependence on the diffraction efficiency for several pitch gratings. In general, there is no dependence on ψ_0 and a constant diffraction efficiency is observed. This is consistent with our simplified model of the system described

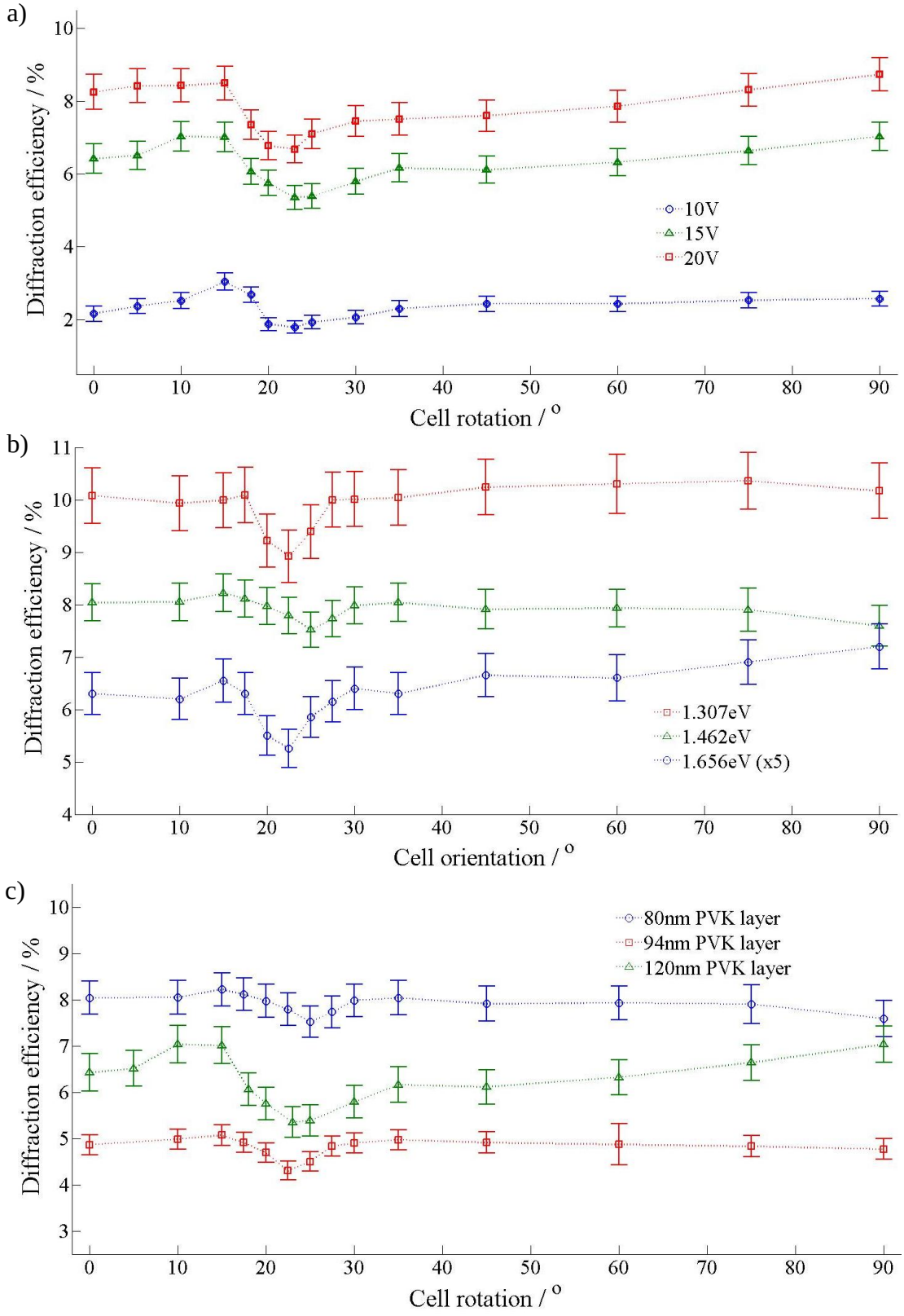

Figure 5.37: The in-plane director dependence on the first order diffraction for a 4μm pitch grating for a) several applied voltages, b) different SPP energies and c) various samples with different PVK layer thicknesses (δ_{PVK} = 120nm from a different batch than the others shown). Therefore, we conclude that this behaviour is entirely a liquid crystal alignment effect and is not dependent on the cells manufacture or the SPP. Unless otherwise stated δ_{PVK} = 80nm, V = 15V, E_{SPP}= 1.462eV.

for the pitch dependence in *section 5.8*. In our model we proposed that the director orientation outside the boundary layer, the region where a grating can form, is in general orthogonal to the PVK interface. Hence, there is no in-plane director dependence. In the boundary layer where the director is entirely in-plane, where a ψ_0 dependence would be expected, no grating can form; so this does not influence the SPP diffraction efficiency. The slight variation experimentally observed with ψ_0 is from the contributions to the SPP diffraction from the intermediate region between the boundary layer and bulk that in reality exists.

Surprisingly for specific ψ_0, there are clear drops in the diffraction efficiency. The drops in the SPP diffraction efficiency are small, reducing the diffraction by only 1-1.5%. These dips all occur over a similar angular spread of ~15°, though the angle at which the dips occur is clearly dependent on the pitch of the grating. The angle of ψ_0 for the dips in the SPP diffraction efficiency is lower for a reduced grating pitch. No dips are observed for grating pitches above 6µm. This observed dip in the diffraction efficiency for a particular pitch and ψ_0 is observed regardless of the magnitude of the applied potential, SPP energy, the PVK thickness or sample batch, as displayed in *figure 5.37*. The second diffraction order dependence on ψ_0 is also determined in *figure 5.38*. This also shows the dip in diffraction at the same angle as the first diffraction order for the 4µm grating shown. Therefore, this must be an entirely liquid crystal based effect dependent on the formation of the grating when the director has a specific initial in-plane alignment.

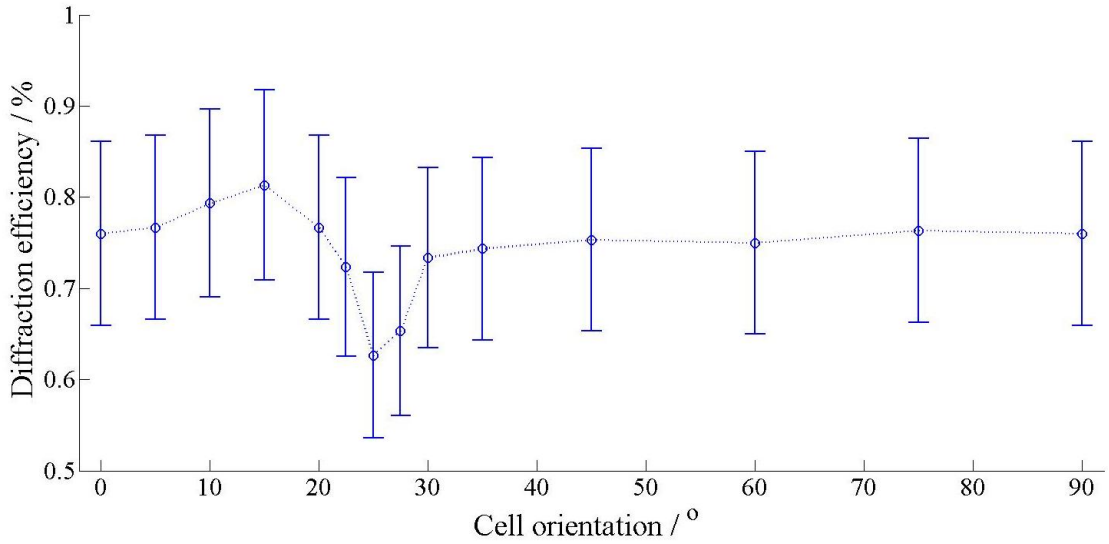

Figure 6.38: Second order diffraction efficiency dependence on the in-plane director orientation for a 4µm grating. The same behaviour is demonstrated as observed for the first order. δ_{PVK} = 120nm, V = 15V, E_{SPP}= 1.462eV.

We use our mathematical simulations of the system to determine if the observed ψ_0 dependence is an expected behaviour of this type of cell. Unfortunately, as *figure 5.39* displays, this behaviour is not theoretically predicted. The general non-dependence on ψ_0 for the diffraction efficiency is predicted by the simulations. However, the simulations predict that for a certain region of ψ_0 the diffraction should slightly increase (+0.5%), the opposite of

our experimental data. The angular spread of this region is larger and its peak is not in quantitative agreement with the angle of the experimentally observed dips. Therefore, the slight increase in the numerical predictions diffraction efficiency is unlikely to be generated by the same mechanism as the observed experimental dips in the diffraction efficiency.

The hybrid photorefractive liquid crystal we use is a highly complex non-linear system. Therefore, it is entirely possible that we have not attributed correct values to all of the initial input parameters for the liquid crystal layer in our simulations. In particular, a pre-tilt at the PVK surface and the twist in the cells in-plane alignment, both are normally believed to be 0^o. Changing either of these parameters to 5^o, though not both at the same time, slightly altered the ψ_0 dependence on the diffraction efficiency as displayed in *figure 5.39*. However, neither of these changes resulted in the experimentally observed dip in the diffraction efficiency.

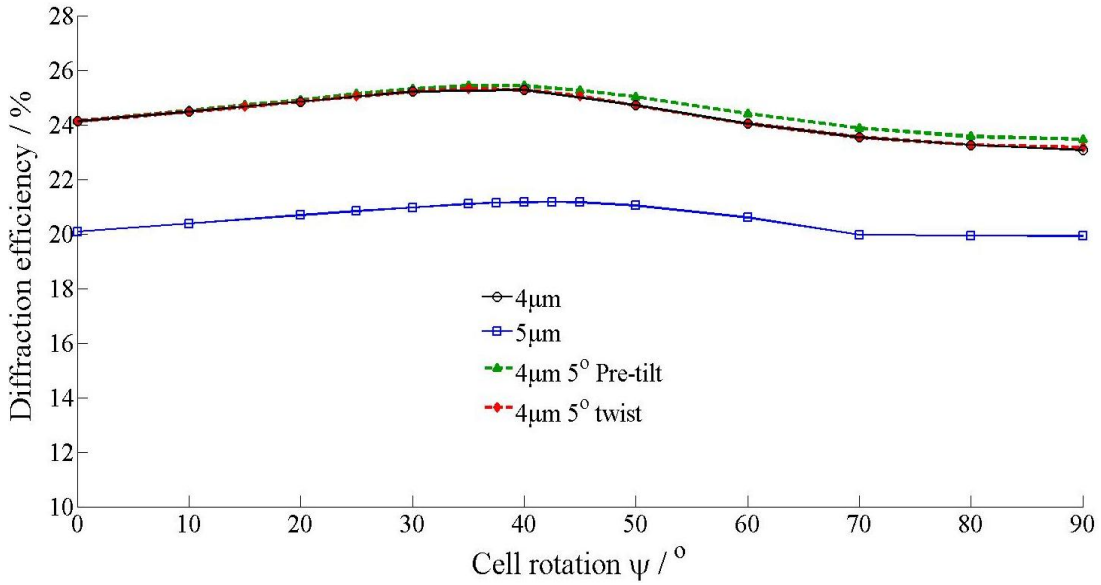

Figure 5.39: Mathematical simulation of the initial in-plane director dependence on the diffraction efficiency for a 4μm and 5μm grating. The simulations fail to predict the dips experimentally observed, however the lack of a general rotation dependence on the diffraction (flat line) is observed. A pre-tilt or twist in the liquid crystal is not responsible for this behaviour.

A possible explanation for the diffraction efficiency dip is that the spatial modulation profile of the refractive index grating at certain ψ_0 does not match the assumed $\sin^2(k_\Lambda x)$ profile of the interference pattern. Thus changing the magnitude of the gratings Fourier components and the grating strength; therefore, lowering the SPP diffraction efficiency. An example would be the formation of a saw-tooth grating with the same fundamental pitch instead of a sinusoidal grating. However, we do not believe that the actual grating formed would diverge from the expected sinusoidal grating as severe as a saw-tooth. Alternatively, the dip could be the result of the formation of a defect near the PVK interface, disrupting but not preventing the liquid crystals director modulation to form the grating. The current failure of the mathematical simulations to predict this behaviour may be due to the model's inability to determine the behaviour of a system where defects in the liquid crystal alignment have formed. The model

should warn of the formation of a defect and no warning in the simulations was observed. It is possible that the formation of a defect in the real liquid crystal system is because the non-linear system converges to a local solution, instead of the global solution that the simulations determine.

Though the existence of these dips cannot yet be theoretically predicted and understood, their presence in the experimental data is promising for the long-term goal of research into photorefractive gain of SPP. The dips could present a symmetry breaking mechanism in the photorefractive energy transfer between two SPP modes. An essential mechanism if this type of system is going to demonstrate SPP gain. The significance of a symmetry breaking mechanism and a review of the potential methods to achieve a net SPP photorefractive gain are discussed in the thesis conclusions in *Chapter 6*.

As a final confirmation of this effect, we re-examined the pitch dependence on the diffraction for two additional ψ_0 values. The pitch dependence at $\psi_0 = 20^o$ or 40^o shown in *figure 5.40* is noticeably different to the original $\psi_0 = 0^o$ trend. The pitch dependence now displays a double peak in the diffraction efficiency. The pitches that have a reduced diffraction at these newly examined ψ_0 values are in agreement with the pitches that display a reduced diffraction efficiency for these values of ψ_0 in *figure 5.36*. Therefore, the model used to describe the pitch dependence is still valid, though the possible formation of a defect state proves to be an effect that dominates the liquid crystal behaviour under specific conditions.

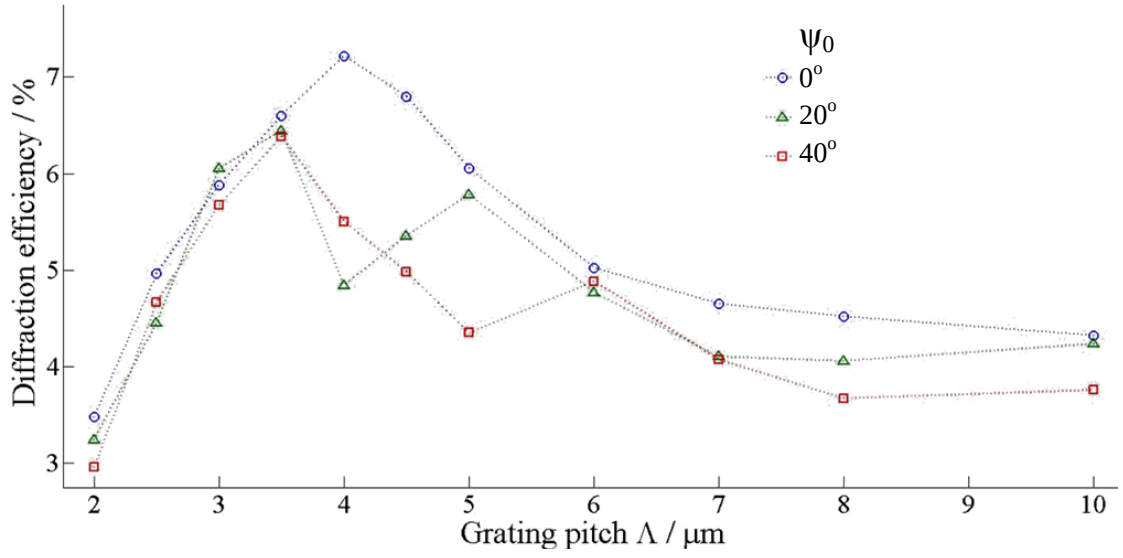

Figure 5.40: Pitch dependence of the first diffraction order for different initial in-plane director orientations. Dips appear in the pitch dependence that are consistent with the reduced diffraction observed at certain cell orientations for specific pitches. δ_{PVK} = 120nm, V = 15V, E_{SPP}= 1.462eV.

5.10 Chapter Conclusions

In this chapter, I have demonstrated that a SPP can probe and interact with a spatially dependent refractive index profile written into the liquid crystal layer with an external light source. In particular, a refractive index grating generated by two coherent interfering beams. The short penetration depth (~200-400nm) of SPP, results in the SPP probing the region of the liquid crystal layer nearest to the PVK. In this region, the re-orientation of the liquid crystal molecules is limited from the additional forces of the surface anchoring to the rubbed PVK layer, which could have seriously impeded the effectiveness of this novel device. However, the modulation of the liquid crystals refractive index between the illuminated and dark areas is shown to be sufficient to diffract a significant amount of energy from a SPP mode.

To generate a stable and repeatable electronic environment, so we can accurately examine how the SPP diffraction efficiency is dependent on all known experimental parameters, a slow frequency AC field is used. The use of the slow AC potential results in a dynamic liquid crystal system. We simplify the effects of a slow AC potential by considering only a single phase of the applied potential, when SPP diffraction is maximum, and approximate the liquid crystal behaviour with a static DC potential. Using a slow AC field instead of a DC field also enhanced the SPP diffraction efficiency; however, a DC field would have to be used with a liquid crystal with a fast response time, if photorefractive liquid crystals are to become the leading device for SPP manipulation. The long-term electronic stability of the liquid crystal to a DC potential would also have to be addressed.

The experimental data clearly indicates that the diffraction efficiency can be significantly increased by using a lower energy SPP mode. However, reducing the SPP energy reduces the confinement of the SPP to the interface [43]. This may limit some practical applications for this device where a highly confined mode is desirable, so is not necessarily a desirable way to increase the SPP diffraction efficiency. The SPP diffraction efficiency dependence on the magnitude of the applied slow AC potential, the illumination intensity and the pitch of the grating were all shown to be explained by how well or strong a grating can be formed in the SPP interaction region of the liquid crystal layer.

In addition, in the experimental data we observe a variation in the magnitude of the diffraction efficiency with PVK thickness in *figure 5.19, 5.29b and 5.37c*. This indicates that the diffraction efficiency can be improved significantly by optimising the dimensions of the samples layers. The increased diffraction efficiency, with decreasing PVK thickness, cannot be entirely explained by an increased potential drop across the liquid crystal due to a thinner, less resistive PVK layer. A portion of the diffraction efficiency increase is a result of the SPP probing further into a liquid crystal region where a good refractive index modulation is possible. Further optimisation of the diffraction efficiency can be achieved by using a PVK layer thinner than 80nm, the thinnest layer we have examined. It is unknown how thin we can

make the PVK layer while improving SPP diffraction, as a thinner layer will reduce the photorefractivity of the sample.

For each parameter, we have determined the optimum value or conditions that maximise the SPP diffraction from a limited examination of the variable space. The observed trends in any parameters dependence on the SPP diffraction efficiency are believed to represent the trends throughout all of the variable space. However, a full examination of all of the variable space is an excessive workload for the time available in this project. A summary of the optimum parameters is presented in *table 5.1*; most of these parameters have a slight dependence on the sample dimensions and the materials used. Unless otherwise stated in the figure captions of the presented data, these were the parameters used for all the SPP diffraction efficiency measurements.

Experimental Parameter	Symbol	Optimum value
Grating orientation	γ	*Equation 6.11*
Energy of SPP	E_{SPP}	1.24eV or lower
Slow AC frequency	ω	0.5Hz
Magnitude of Potential	$\|V\|$	15V
Illumination intensity	I_{light}	$5mWcm^{-2}$
Grating pitch	Λ	3-4μm
In-plane director	ψ_0	No general dependence
PVK thickness	δ_{PVK}	80nm or less

Table 5.1: The optimum parameters experimentally determined for SPP diffraction.

To assist us in determining the physics of the liquid crystals response to a modulated potential we have used the mathematical simulations described in *section 2.5*. The simulations have successfully predicted most of the observed trends in the SPP diffraction efficiency for the experimental parameters investigated. However, the simulations do not achieve quantitative agreement with the experimental data. The only trend not to be observed in the simulations is the dips in the diffraction efficiency for the initial ψ_0 dependence. Both of these may be the result of the simulations not fully describing all components of the cell correctly. Several possible unaccounted mechanisms may be responsible for the discrepancies observed: For example, the diffusion of free charges in the cell, the non-linear response of the PVK or noise and defects in the liquid crystal alignment. A description of the possible unaccounted physics and the methods required to implement them in the model is discussed in *Chapter 6*, where the theoretical model is reviewed. The current simulations of the photorefractive liquid crystal system are still an invaluable tool in determining the operation of this device, allowing us to determine a qualitative description of the mechanisms behind each parameter dependence on maximising the SPP diffraction efficiency. In addition, for the pitch dependence they have

allowed us develop a semi-analytical mathematical model to describe the origin of this behaviour.

By using hybrid photorefractive liquid crystals to manipulate SPP, we have used the SPP to determine the liquid crystal's behaviour in our cells and characterise the mechanics of the grating formation, in particular near the PVK interface. This information will allow us to develop an experimental system to demonstrate SPP gain.

Chapter 6

Conclusions and Future Work

In this thesis, we have demonstrated that SPP can interact with the liquid crystal layer of a novel hybrid photorefractive plasmonic liquid crystal device. The wavevector of the SPP is determined by the alignment of the liquid crystals director near the PVK-liquid crystal interface. Though anchoring forces limit the re-orientation of the liquid crystal in the region near the interface, they do not prevent the device from operating as intended. The thickness of the photoconductive layer is also sufficiently thin to allow the SPP to interact with the liquid crystal and is still be able to generate significant photorefractive effects through a noticeable change in the layers electrical resistance with illumination.

To understand our devices we have characterised the cells electrical and optical behaviour. The optical reflection and transmission of the cells are as expected and conforms to the predicted optical behaviour of a multilayer T-matrix simulation. This allows us to determine the thickness of each layer of our devices between fabrication steps to ensure the sample meets our specifications. Through the optical characterisation, we demonstrate that the surface treatment of the PVK required in order to align the liquid crystal does not negatively influence the SPP modes in the structure. In addition, the wavelengths absorbed by the C_{60} (λ<650nm, *figure 4.10*) do not correspond to the wavelengths we excite SPP modes in a fully fabricated sample (λ>750nm). As the device is highly reflective at a non-normal incidence angle when SPP are not excited, the light used to excite SPP does not inadvertently photo-excite the PVK, which would generate additional unquantifiable photorefractive effects that we do not desire when analysing our cells operation.

The electrical response of the cells is in qualitative agreement with the general description of the operation of this class of photorefractive device, i.e. the light dependent resistance of the photoconductor determines the liquid crystal alignment. This behaviour has been experimentally demonstrated with the electrical impedance measurements in *section 4.2.1* where a ~100nm PVK layers resistance is reduced from 174MΩ to 6.9MΩ with 9.8mWcm^{-2} of λ=532nm illumination. However, the simple equivalent circuit model used to obtain these values and to explain the impedance data is not appropriate for our devices under standard operating conditions. Because the model always fits the data at frequencies above 10Hz, where the capacitance of each layer results in the potential drop only being across the liquid crystal, we infer that the discrepancies are due entirely to the electrical behaviour of the PVK. We cannot however determine the exact electrical behaviour of PVK through impedance

measurements. This is because the true electrical behaviour of PVK is likely non-linear (with both |V| and illumination), non-Ohmic and history dependent. It is possible that with an extended more complicated equivalent circuit we could have fitted this data. However, we would have to introduce so many additional unconstrained electrical components (variables), we would completely erode our confidence in such a fit. Despite our inability to fully characterise the electrical properties of PVK, the electrical re-orientation characterisation of the liquid crystal determined by crossed polarisers (*section 4.2.2*) was in agreement with that predicted by our mathematical model. We subsequently demonstrated that the SPP wavevector could be controlled electrically in this system with a wavevector shift of up to $0.4\mu m^{-1}$. Therefore, though it would be desirable to understand the PVK, in particular to assist us in optimising these devices, it did not prevent us from designing the photorefractive SPP device we required.

The photorefractive control of SPP in our cells was demonstrated to be sufficient for SPP at the typically examined energy of 1.46eV, i.e. a wavevector shift of $0.21\mu m^{-1}$. The magnitude of the photorefractive wavevector shift demonstrated an SPP energy dependence associated with the penetration depth of SPP modes into the dielectric layers. This energy dependence makes this device more appropriate for controlling lower energy SPP. In addition, we were also able to characterise the intensity dependence of the photorefractive effects and were able to determine the saturation intensity of $\sim 5mWcm^{-2}$ for a 10% weight C_{60} doped PVK layer. The most surprising result is that the numerical predictions of the SPP wavevector indicate that when the sample is illuminated above the saturation intensity, the entire potential is dropped across the liquid crystal, thus indicating that the PVK has a negligible resistance when illuminated. This is in stark contrast to the impedance measurements. However, as the photorefractive wavevector shift is a direct measure of the effects we want in our cells, we use this as the basis of the spatially dependent potential profile used in subsequent SPP diffraction simulations.

By using uniform illumination, this device could operate as a light triggered SPP switch, though it would require further optimisation to become a practical application. In particular, the cell structure would have to be modified to remove the guided modes. This could be achieved by using a hybrid aligned liquid crystal cell where the director is homotropically aligned on the PI side of the cell and planar aligned on the PVK side. Also the applied potential would have to be DC instead of a low frequency AC. Currently, the electronic stability issues with a DC potential are the biggest limitation of this device. Developing an electrically stable system is a area for future study.

The eventual aim after developing this photorefractive SPP device is to demonstrate SPP gain. As a step towards demonstrating this effect, we examine the diffraction efficiency of a single SPP interacting with an independently generated refractive index grating. This was done so that we know the optimum parameters of this type of system (listed in *table 6.1*) and to determine the physical mechanisms behind the grating formation near the PVK interface. The SPP diffraction efficiency is dependent on three key properties; the SPP electric field

overlap (interaction) with the grating; the difference in the refractive index for the light or dark regions of the grating (grating formation) near the interface; and the orientation of the grating. The last of these is the phase matching requirement that will be inherently achieved in a SPP gain system. The SPP electric field overlap explains the observed energy dependence of the SPP diffraction. The most complicated property is the formation of the refractive index grating. The simplest explanation is that the formation of the grating is dependent of the magnitude of the modulated component of the electric field (*equations 5.24a* and *5.24b*). This therefore explains the |V|, intensity and pitch dependence. However, for the pitch dependence we must also consider that a layer of the liquid crystal approximately 100nm thick near the interface will not respond to the electric field due to the large elastic energies associated with a re-orientation in this region. In these experiments, we demonstrated a maximum diffraction efficiency of 25.3 ± 2.03% for a 1.03eV SPP from a 4μm grating. This could be further improved upon with additional optimisation of the sample such as by using a liquid crystal with a lower anchoring strength to the PVK layer or by using a thinner PVK layer, δ_{PVK}=50nm for example.

While developing the physical samples we simultaneously worked with Dr. Keith Daly and Dr. Giampaolo D'Alessandro to develop a full numerical simulation of the system to assist in our analysis of the cells operation (*section 2.5*). The diffraction efficiency predicted by these simulations agrees with experimentally observed trends for the grating orientation, pitch, |V|, illumination intensity and the energy of the SPP dependence. The only trend not observed is the reduction in the diffraction efficiency at certain director orientations in *section 5.9*. Therefore, we conclude that all the fundamental physics of the system is incorporated into the model. There are however, notable areas of disagreement, such as the simulations over-prediction of the magnitude of the diffraction efficiency. This over-prediction could be removed by using a reduced modulation factor for V′, i.e. using $V'=0.95+0.5\sin^2(k_\Lambda x)$ instead of $V'=0.8+0.2\sin^2(k_\Lambda x)$. While this is easy to implement, it has important consequences when describing our physical system. The original modulation was determined by the separate fits to the SPP wavevector in the light and dark (*figure 4.24*). By using a reduced modulation, this would indicate that the electrical properties of the PVK in the dark regions of the grating are not truly 'in the dark'. There are a few possible reasons for this:

1. The assumption that the scattered light or back reflections in the system are negligible is false, thus the dark regions in fact represent a non-insignificant light level;
2. The diffusion of the charges in either the photoconductor or liquid crystal is comparable to the pitch of the grating structures. Therefore, the lateral drift of charges results in a partial screening effect. Thus, the modulation of the conductivity profile generated in response to the intensity grating will be reduced;
3. The electrical conductivity response of the PVK is non-linear. Therefore, there is a reduced fundamental wavevector component in the Fourier transform of the grating.

All three of these are likely to be factors in the physical system. However, we believe that the second listed reason is likely to be more dominant. That is to say the inaccuracies in the predictions of the SPP diffraction efficiency are due to the model's non-inclusion of the

electrical behaviour of the cells. This non-inclusion is entirely due to our inability to characterise the electrical behaviour of the PVK and is not a result of a necessary assumption in order to develop the model. This generalisation is further reinforced by the fact that our simulations fit all the data for systems where the electrical properties of PVK do not need to be considered, i.e. 1 kHz AC data.

Including the electrical behaviour of the layers in the numerical simulations may also fix the other noticeable discrepancy with the simulations; that the position of thresholds or peaks is not in perfect quantitative agreement with the experimental data. However, the predicted peaks and thresholds are close to the experimental observations; therefore, this is a relatively minor concern. As the predictions are a close approximation, this may be potentially solved by using different parameters for the liquid crystal layer. In particular, changing the thickness of the liquid crystal layer or using all three of the liquid crystal's elastic constants instead of a single elastic constant term. However, there may always be a small disagreement between theory and experiment due to the presence of defects in a sample, which cannot be accounted for in the liquid crystal model.

The samples used in this thesis are un-optimised. The structure was only developed to a point where the photorefractive effects were sufficient to demonstrate the effects described in *Chapter 5*. The optimisation of the samples is left as an ongoing future project. Possible optimisation routes include, but are not limited to; detailed studies on the diffraction efficiency of SPP by changing the thickness of either the PVK or liquid crystal layers; using different liquid crystals or photoconductive materials; using a different photosensitising dopant or optimising the dopant level. In addition, doping the liquid crystal with certain nanoparticles such as $BaTiO_3$ has demonstrated an improvement in the photorefractive properties of this class of photorefractive device [243].

The research undertaken in this thesis has demonstrated that good photorefractive control of SPP modes, in particular those with energies <1.3eV, is possible with a hybrid photorefractive liquid crystal cell. When the refractive index of the liquid crystal has a periodic profile, we demonstrate that significant diffraction of SPP into other SPP modes is possible. Using the SPP's response to the modulated liquid crystal, we have determined the details of the mechanisms behind the grating formation in this type of device and have shown that they are subtly different to those in the related bulk liquid crystal systems used for TBG. This is due to the extra significance of the anchoring forces near the interface in our system. The information obtained will be used to develop a photorefractive SPP system capable of demonstrating gain. Therefore, to conclude this thesis we presented a brief discussion of the further advances required for SPP gain to be demonstrated with a photorefractive liquid crystal system. In this section, we do not presume that any of the improvements that we could possibly make to our samples have been implemented.

6.1 Photorefractive Gain of SPP

For gain of SPP by a similar mechanism as TBG for light, we would require two interfering SPP to generate the refractive index grating with their interference pattern. However, the form of the electric fields of SPP is noticeably different to light waves, so the interference pattern will also differ. We now consider two SPP propagating in the *x*-*y* plane that cross at an angle α with their bisector parallel to the *x*-axis, the electric fields of the SPP in the dielectric layer are then,

$$\underline{\mathrm{E}}_q = \underline{\tilde{\mathrm{A}}} e^{\left(i|k|\cos\left(\frac{\alpha}{2}\right)x \ +(-1)^q i|k| sin\left(\frac{\alpha}{2}\right)y \ -k_z z \ -i\omega t\right)}, \tag{6.1}$$

where q=1, 2 is used to label the two SPP modes, $\underline{\tilde{\mathrm{A}}}$ is the complex amplitude of the SPPs polarisation components and $|k|$ is the magnitude in-plane SPP wavevector and is equivalent to k_x in *equation 2.2*. The magnitude of k_z and $|k|$ are determined by *equations 2.3* and *2.6* respectively. Following the same mathematical steps as *equations 2.15-2.17* to determine the intensity of the interfering SPP we find that,

$$\mathrm{I} = 2\underline{\tilde{\mathrm{A}}}^* \underline{\tilde{\mathrm{A}}} e^{-2k_z z}\left[\ 1 + \cos\left(2|k| sin\left(\tfrac{\alpha}{2}\right)y\right)\ \right]. \tag{6.2}$$

From *equation 6.2* we observe that two interfering SPP also generate a periodic intensity profile with the same pitch as two light waves crossing at an angle α. The difference is that the intensity grating is now bound to the interface due to the exponential term. This exponential term indicates that the electric field of interfering SPP decays over a shorter distance into the dielectric, compared to the decay of a single SPP (*equation 6.1*). This is partially offset by a larger field to begin with; however, this may limit the SPPs electric field overlap with the liquid crystal for higher energy SPP modes. Hence, we should use SPP with energies of 1-1.25eV (infrared wavelengths) to increase the likelihood of demonstrating SPP gain with a photorefractive liquid crystal system.

The photorefractive material or more specifically for our samples, the photo-conductive layer, must then absorb the energy from the SPP as it does from photons to generate free charges. As SPP have the same ω as a photon, if a photon has sufficient energy to generate charges in the photoconductor, then SPP can as well. The dynamics of the free charges are independent of their generation method; hence, a refractive index grating will be formed in the liquid crystal layer by the same mechanisms described in this thesis and the same optimum parameters we have determined here will be used in any future system. It must be noted that the requirement of SPP absorption to form the refractive index grating could be an additional loss mechanism for the SPP modes. Hence, the required energy transfer between modes to demonstrate gain will be slightly higher. This is not thought to be a significant limitation as the absorption of the C_{60} dopant used in the photoconductive layer of our tested samples was negligible at only 0.005% for λ = 532nm. However, this absorption may

significantly differ, as we will require a different dopant to absorb light at the infrared wavelengths we will use.

In addition to this, we require a symmetry breaking mechanism to demonstrate SPP gain.
Due to the restricted geometry of the SPP (the SPP will always propagate in the same plane as the photoconductor), we cannot rotate the cell relative to the bisector in the same way that is used to achieve TBG, i.e. setting the bisector at a non-normal incidence angle. Fortunately, the investigations in this thesis on the SPP diffraction efficiency dependence on the liquid crystals rubbing direction (*section 5.9*) relative to the SPP propagation direction, presented a possible symmetry breaking mechanism. This is because we can design a system where the two SPP propagate in different directions relative to the director, i.e. we rotate the cells in-plane director relative to the bisector. This possible method of SPP symmetry breaking does not have the disadvantage of a wavevector mismatch term like TBG. If the director is aligned at an angle relative to the SPP near the observed dip for one beam, for example at ~18^o when a 3μm grating is used, the other beam is then at an angle of ~22^o to the director and from *figure 5.36* we know that each SPP will then have an asymmetric energy transfer. Currently this asymmetry would only result in a net energy transfer of 1%, i.e. the magnitude of the decrease in the dip. This amount of enhancement for one SPP would be insignificant for any applications, though it would be sufficient to prove that photorefractive gain of SPP is possible. Though this symmetry breaking method may work in principle, as the mechanism behind the observed dip is not understood this may not be the best symmetry breaking method to pursue, in particular if the ~1% asymmetry cannot be improved upon.

An alternative method to establish a symmetry breaking mechanism is to use a dynamic grating method [244]. In this method, one of the laser beams used to excite one of the SPP modes will have a piezoelectric actuator attached to its steering mirror. The piezo will be used to adjust the beams path length by a few microns. This small spatial extension of the beam path will translate the beams wavefront (phase) and hence, the interference pattern. If the motion of the piezo is characterised by a saw-tooth wave then the refractive index grating generated in the photorefractive material is forced to have a phase shift in the direction of the piezo's motion (time-averaged direction). Thus, this will force the system to have an asymmetry even though the bisector is in the plane of the liquid crystal interface, which according to *equation 2.23* is enough to demonstrate gain.

From the work carried out in this thesis and the additional considerations presented in this section, we have reaffirmed our hypothesis that SPP photorefractive gain is possible. Future work will be to establish an experimental geometry that can demonstrate measureable SPP gain, though there are no fundamental reasons why we could not be successful. However, the amount of SPP gain demonstrated or the apparatus used could be inadequate for subsequent practical applications.

Appendix A

Experimental Equipment Specifications

This appendix lists the relevant specifications of the analytical apparatus used in this thesis. Each experimental device has the section listed detailing the operation and use of the equipment.

Surface Plasmon Excitation and Analysis Experiment (*section 3.1*):

n_{prism}:	1.833 at 850nm	(Schott N-LaSF9)
$n_{indexfluid}$:	1.8900 at 589.3nm	(Cargille)

White light source spectral range:	Tungsten Halogen lamp:	450-1500nm
Photorefractive writing beam wavelength:	Diode laser, Coherent:	532nm

Spectrometer:	Ocean optics HR4000		
	Detection range:	200-1100nm	
	Wavelength resolution:	1nm	
	Photon Control SPM-002-NIR1700		
	Detection range:	900-1700nm	
	Wavelength resolution:	3.5nm	
Broadband polariser: Thorlabs, LP-VIS			
	extinction ratio:	$>10^5$:1	550-1200nm spectral range

ATR illumination range:	~10° within the ϑ = 25°-80° region.	
Rotation stage detection range:	ϑ axis:	0 to 90°
	φ axis:	+90 to -60°
Rotation stage minimum step:	ϑ axis:	0.002°
	φ axis:	0.005°

Detector resolution*:	200μm core fiber:	0.11°
	50μm core fiber:	0.03°
	5.3μm core fiber:	0.003°

* Fiber optic detector is fixed 50mm from ATR focus.

UV-VIS Spectrophotometer (*section 3.2.1*):

Jasco V-570 UV-VIS spectrometer.

- Double beam instrument with single monochromator.

Wavelength range:	D_2 Lamp:	190-350nm
	Halogen Lamp:	330-2500nm
Wavelength Accuracy:	±0.3nm (VIS)	±1.5nm (NIR)
Wavelength reproducibility:	±0.1nm (VIS)	±0.4nm (NIR)
Spectral Bandwidth:	1nm (VIS)	4nm (NIR)
Resolution:	0.1nm (VIS)	0.5nm (NIR)
Detector:	Photomultiplier tube:	190-900nm
	PdS photocell:	750-2500nm

Photometric accuracy:	±0.3% Transmission
Photometric reproducibility:	±0.15% Transmission
Scanning speed:	200nm/min
Baseline flatness:	±0.15% Transmission
Baseline stability:	±0.06% Transmission/hour

Ellipsometer (*section 3.2.3*):

M-2000DI Woollam Variable-Angle Spectroscopic Ellipsometer (VASE)

- Rotating analyzer with auto-retarder
- Auto tilt and height alignment

Angular range:	15-90^o automatically aligned with 0.01^o accuracy.	
	Typical measurements at:	50^o, 55^o, 60^o
Wavelength range:	193-1690nm	
	Typical examined range:	400-1050nm
Measurement time:	0.1-20s depending on required accuracy	(Typical: 5s)
Fitting Software:	CompleteEASE version: 4.39	

Impedance Analyser (*section 3.2.4*):

Solartron 1260 Impedance/Gain - phase analyser

Frequency range:		10μHz to 32MHz
Frequency resolution (max):		10μHz
Error:		± 100ppm
AC Amplitude:		0 to $3V_{rms}$
Maximum AC resolution:		5mV
Integration time:		10cycles
Voltage detection:		0-30mV scale used
Maximum resolution:		1μV
Connections:		Differential BNC
Impedance ranges:	Capacitance:	1pF to 10mF
	Resistance:	10mΩ to 100MΩ
	Inductance:	100nH to 1000H
Impedance resolution:		0.001dB, 0.01^{o}

Appendix B

Determining the optical constants of the Au and PVK layers

The wavevector of a surface plasmon polariton (SPP) is well known for its dependence on the refractive index of the dielectric medium and is utilised as a method of detection in chemical or biological systems [245]. The work in this thesis theoretically fits the SPP resonance of an attenuated total reflection (ATR) experiment to acquire details about the SPP and its interaction with the confining structure. Therefore, it is essential that accurate data for the optical constants of the materials interacting with the SPP is known.

The optical constants of a thin Au layer are often quoted from established texts and articles such as Palik's, *Handbook of optical constants of solids* [246] or Johnson and Christy's, *Optical constants of the Nobel metals* [24]. Alternatively an analytical model [247] of the optical constants of Au could be used instead of the Drude model for metals. However, there is significant variation in the optical constants published by various groups [24, 248-250]. The origin of this variation can be attributed to two factors; the thickness and the morphology of the Au film [251]. Oxidation is not considered a problem, as Au is a noble metal so there is little atmospheric contamination.

The deposition conditions for thin Au films created by thermal evaporation are known to affect the film structure and morphology [251]. For example, the rate of deposition determines the granular structure of the film [252]. Also the nature and orientation of the film can be significantly influenced by the substrate material and temperature [251].

Furthermore, the optical properties of a thin Au film are thickness dependent for layers thinner than 80nm [253]. In general, the value of n is higher and the value of k is lower than the values for a bulk Au layer [251]. The variation in the optical constants for thin layers with increasing thickness is not linear and is wavelength dependent. Therefore, accurate optical constants obtained from the literature are only possible for films fabricated under the same conditions to the same specifications. Hence, we determine the optical properties of the 40nm Au films used in this thesis, ourselves.

A number of methods exist to determine the optical constants of a material, a comprehensive list and explanation can be found here [246]. For our measurements of the optical properties of Au we used a 39.5nm Au layer evaporated onto an N-LaSF9 disc, with no Cr adhesion layer. The thickness of the Au is at first estimated by the *T*-matrix fit to the transmission

spectrum using the optical constants listed in Palik's, *Handbook of optical constants of solids* as initial values. This thickness is then used to determine the wavelength dependent refractive index of the Au using ellipsometry. An iterative process is then used between the fits to the data acquired by these two measurements to converge on a set of optical constants. The constants acquired are displayed in *table B.1* for selected wavelengths.

λ / nm	E / eV	*n*	*k*
400	3.106	1.628	1.863
450	2.761	1.513	1.824
500	2.485	0.882	1.758
532	2.335	0.457	2.216
550	2.259	0.349	2.483
600	2.071	0.203	3.122
656	1.894	0.135	3.754
700	1.775	0.118	4.207
750	1.657	0.125	4.690
800	1.553	0.142	5.143
850	1.462	0.176	5.573
900	1.380	0.212	6.073
1000	1.242	0.245	6.877
1100	1.129	0.166	7.657
1200	1.035	0.171	8.432
1300	0.956	0.193	9.213
1400	0.887	0.325	9.955
1500	0.828	0.370	10.719

Table B.1: Refractive index data for a 40nm Au film at selected wavelengths.

The photorefractive effects in our samples are created indirectly by the polymer poly-N-vinylcarbazole (PVK). This layer is deposited directly onto the Au; therefore, the SPP will always probe it and alter the SPP wavevector. Unfortunately, there is little information on the refractive index of this polymer in the literature and only a value at λ = 532nm of $n \approx 1.7$ [254] was found. Also our PVK layer is doped with C_{60} ($n \approx 1.96$ [218]) and it is unknown how this would change the refractive index. Therefore, we acquired a Cauchy series approximation of the refractive index of our polymer blend using ellipsometry.

A PVK layer (~260nm) was spin coated at 500rpm onto a semi-infinite (~300nm) Au film. No light is transmitted through the Au and the bulk optical constants of this layer [24] were used. As the sample is opaque a reflection spectrum of this sample was acquired by a UV-VIS spectrometer at an incidence angle of 85^{o}. The thickness of the PVK generated sufficient interference fringes in the reflection to allow an estimation of the thickness assuming $n = 1.7$. This thickness was used in the ellipsometer fit. An identical iterative method to that used to

determine the Au refractive index, was then used to determine a Cauchy series for the refractive index of the polymer that is accurate to 0.001. The ellipsometer also acquired a fit for an approximation to the wavelength dependent absorption of the layer. Both these functions are displayed in *table B.2*.

$n = a + b/\lambda^2 + c/\lambda^4$	$k = d\exp(-e\lambda)$
a = 1.65400	d = 0.02553
b = 0.01145	e = 1.12500
c = 0.00152	

Table B.2: Cauchy function data for the refractive index of PVK.
The wavelength of light λ must be in μm.

For completeness *table B.3* lists the Sellmeier function to determine the refractive index of the N-LaSF9 glass used for the high refractive index prism and sample substrates. In addition, the Cauchy co-efficients for the ordinary and extra-ordinary refractive indices of E7 are listed in *table B.4*. The E7 Cauchy functions were determined by the crossed polariser transmission fits of *figure 5.16*.

$$n^2 = 1 + \frac{B_1\lambda^2}{\lambda^2 - C_1} + \frac{B_2\lambda^2}{\lambda^2 - C_2} + \frac{B_3\lambda^2}{\lambda^2 - C_3}$$

B_1	2.00029547
B_2	0.298926886
B_3	1.80691843
C_1	0.012142602
C_2	0.053873624
C_3	156.530829

Table B.3: Sellmeier formula and co-efficients for the N-LaSF9 High refractive index glass substrate as listed in the Schott material catalogue [214]. The wavelength of light λ must be in μm.

$n_o = a + b/\lambda^2 + c/\lambda^4$	$n_e = d + e/\lambda^2 + f/\lambda^4$
a = 1.4990	d = 1.6673
b = 0.0072	e = 0.0159
c = 0.0003	f = 0.0010

Table B.4: Cauchy function for the n_o and n_e refractive index of the liquid crystal E7.
The wavelength of light λ must be in μm.

References

1. Raether, H., *Surface plasmons on smooth and rough surfaces and on gratings*. 1987, Berlin ; New York: Springer-Verlag.

2. Zayats, A.V., I.I. Smolyaninov, and A.A. Maradudin, *Nano-optics of surface plasmon polaritons.* Physics Reports-Review Section of Physics Letters, 2005. **408**(3-4): p. 131-314.

3. Lal, S., S. Link, and N.J. Halas, *Nano-optics from sensing to waveguiding.* Nature Photonics, 2007. **1**(11): p. 641-648.

4. Lezec, H.J., J.A. Dionne, and H.A. Atwater, *Negative refraction at visible frequencies.* Science, 2007. **316**(5823): p. 430-432.

5. Melville, D.O.S. and R.J. Blaikie, *Super-resolution imaging through a planar silver layer.* Optics Express, 2005. **13**(6): p. 2127-2134.

6. LPVIS, *Silver ellipsoidal nanoparticle doped linear polarisers.* Thorlabs Product Catalogue, 2011. **V21**: p. 910-911.

7. Baker, G.A. and D.S. Moore, *Progress in plasmonic engineering of surface-enhanced Raman-scattering substrates toward ultra-trace analysis.* Analytical and Bioanalytical Chemistry, 2005. **382**(8): p. 1751-1770.

8. Muhlschlegel, P., et al., *Resonant optical antennas.* Science, 2005. **308**(5728): p. 1607-1609.

9. Ozbay, E., *Plasmonics: Merging photonics and electronics at nanoscale dimensions.* Science, 2006. **311**(5758): p. 189-193.

10. Kuttge, M., et al., *Loss mechanisms of surface plasmon polaritons on gold probed by cathodoluminescence imaging spectroscopy.* Applied Physics Letters, 2008. **93**(11): p. -.

11. Caldwell, M.E. and E.M. Yeatman, *Surface-Plasmon Spatial Light Modulators Based on Liquid-Crystal.* Applied Optics, 1992. **31**(20): p. 3880-3891.

12. MacDonald, K.F., et al., *Ultrafast active plasmonics.* Nature Photonics, 2009. **3**(1): p. 55-58.

13. Hsiao, V.K.S., et al., *Light-driven plasmonic switches based on Au nanodisk arrays and photoresponsive liquid crystals.* Advanced Materials, 2008. **20**(18): p. 3528-+.

14. Jones, D.C. and G. Cook, *Theory of beam coupling in a hybrid photorefractive-liquid crystal cell.* Optics Communications, 2004. **232**(1-6): p. 399-409.

15. Khoo, I.C., H. Li, and Y. Liang, *Observation of Orientational Photorefractive Effects in Nematic Liquid-Crystals.* Optics Letters, 1994. **19**(21): p. 1723-1725.

16. Wiederrecht, G.P., *Photorefractive liquid crystals.* Annual Review of Materials Research, 2001. **31**: p. 139-169.

17. Bartkiewicz, S., et al., *High gain of light in photoconducting polymer-nematic liquid crystal hybrid structures.* Optics Communications, 2001. **187**(1-3): p. 257-261.

18. Ritchie., R.H., *Plasma losses by fast electrons in thin films.* Phys. Rev., 1957. **106**(5): p. 874-881.

19. Powell, C.J., Swan, J.B., *Origin of the characteristic electron energy losses in aluminum.* Phys. Rev., 1959. **115**(4): p. 869-875.

20. Powell, C.J., Swan, J.B., *Origin of the characteristic electron energy losses in magnesium.* Phys. Rev., 1959. **116**(1): p. 81-83.

21. Kretschmann, E.R., H., *Radiative decay of nonradiative surface plasmons excited by light.* z. Naturforsch. A, 1968. **23**: p. 2135–2136.

22. Otto, A., *Excitation of nonradiative surface plasma waves in silver by the method of frustrated total reflection.* Z. Phys., 1968. **216**: p. 398.

23. Stern, E.A., Ferrell, R.A., *Surface plasma oscillations of a degenerate electron gas.* Phys. Rev., 1960. **120**(1): p. 130-136.

24. Johnson, P.B. and R.W. Christy, *Optical-Constants of Noble-Metals.* Physical Review B, 1972. **6**(12): p. 4370-4379.

25. Maier, S.A., et al., *Local detection of electromagnetic energy transport below the diffraction limit in metal nanoparticle plasmon waveguides.* Nature Materials, 2003. **2**(4): p. 229-232.

26. Xie, Z.H., et al., *Plasmonic Nanolithography: A Review.* Plasmonics, 2011. **6**(3): p. 565-580.

27. Blaber, M.G., M.D. Arnold, and M.J. Ford, *Search for the Ideal Plasmonic Nanoshell: The Effects of Surface Scattering and Alternatives to Gold and Silver.* Journal of Physical Chemistry C, 2009. **113**(8): p. 3041-3045.

28. Kretschmann, E., *Atr Method with Focused Light - Application to Guided Waves on a Grating.* Optics Communications, 1978. **26**(1): p. 41-44.

29. Gu, J.H., et al., *Determination of thickness and optical constants of thin metal films with an extended ATR spectrum.* Journal of Physics D-Applied Physics, 2008. **41**(15): p. -.

30. Hecht, E., *Optics*. 4th ed. 2002, Reading, Mass.: Addison-Wesley. vi, 698 p.

31. Devaux, E., et al., *Launching and decoupling surface plasmons via micro-gratings.* Applied Physics Letters, 2003. **83**(24): p. 4936-4938.

32. Wood. XLII, R.W., *On a remarkable case of uneven distribution of light in a diffraction grating spectrum.* Philosophical Magazine Series 6, 1902. **4**(21): p. 396-402.

33. Wood, R.W., *R.W. Wood. Anomalous diffraction gratings.* Phys. Rev., 1935. **48**(12): p. 928-936.

34. Preist, T.W., N.P.K. Cotter, and J.R. Sambles, *Periodic Multilayer Gratings of Arbitrary Shape.* Journal of the Optical Society of America a-Optics Image Science and Vision, 1995. **12**(8): p. 1740-1748.

35. Hooper, I.R. and J.R. Sambles, *Surface plasmon polaritons on thin-slab metal gratings.* Physical Review B, 2003. **67**(23).

36. Hooper, I.R. and J.R. Sambles, *Coupled surface plasmon polaritons on thin metal slabs corrugated on both surfaces.* Physical Review B, 2004. **70**(4).

37. Sambles, J.R., Z. Chen, and I.R. Hooper, *Strongly coupled surface plasmons on thin shallow metallic gratings.* Physical Review B, 2008. **77**(16).

38. Song, S.H., et al., *Surface-plasmon photonic band gaps in dielectric gratings on a flat metal surface.* Journal of Applied Physics, 2003. **94**(1): p. 123-129.

39. Park, S., et al., *Resonant coupling of surface plasmons to radiation modes by use of dielectric gratings.* Optics Letters, 2003. **28**(20): p. 1870-1872.

40. Fischer, B., B. Rothenhausler, and W. Knoll, *Surface-Plasmon-Enhanced Diffraction Orders in Polymer Gratings.* Thin Solid Films, 1995. **258**(1-2): p. 247-251.

41. Wu, F.Q., et al., *Complete surface plasmon-polariton band gap and gap-governed waveguiding, bending and splitting.* Journal of Physics-Condensed Matter, 2009. **21**(18).

42. Rothenhausler, B. and W. Knoll, *Total Internal Diffraction of Plasmon Surface-Polaritons.* Applied Physics Letters, 1987. **51**(11): p. 783-785.

43. Barnes, W.L., *Surface plasmon-polariton length scales: a route to sub-wavelength optics.* Journal of Optics a-Pure and Applied Optics, 2006. **8**(4): p. S87-S93.

44. Barber, D.J., Freestone, I. C., *An Investigation of the Origin of the Colour of the Lycurgus Cup by Analytical Transmission Electron Microscopy* Archaeometry, 1990. **32**(1): p. 33-45.

45. Garnett, J.C.M., *Colours in metal glasses and in metallic films.* Philos. Trans. R. Soc. London, 1908(203): p. 377.

46. Haes, A.J. and R.P. Van Duyne, *A unified view of propagating and localized surface plasmon resonance biosensors.* Analytical and Bioanalytical Chemistry, 2004. **379**(7-8): p. 920-930.

47. Frey, B.L., et al., *Control of the Specific Adsorption of Proteins onto Cold Surfaces with Poly(L-Lysine) Monolayers.* Analytical Chemistry, 1995. **67**(24): p. 4452-4457.

48. Berger, C.E.H., et al., *Surface plasmon resonance multisensing.* Analytical Chemistry, 1998. **70**(4): p. 703-706.

49. Heaton, R.J., A.W. Peterson, and R.M. Georgiadis, *Electrostatic surface plasmon resonance: Direct electric field-induced hybridization and denaturation in monolayer nucleic acid films and label-free discrimination of base mismatches.* Proceedings of the National Academy of Sciences of the United States of America, 2001. **98**(7): p. 3701-3704.

50. Homola, J., *Present and future of surface plasmon resonance biosensors.* Analytical and Bioanalytical Chemistry, 2003. **377**(3): p. 528-539.

51. Liedberg, B., C. Nylander, and I. Lundstrom, *Biosensing with Surface-Plasmon Resonance - How It All Started.* Biosensors & Bioelectronics, 1995. **10**(8): p. R1-R9.

52. Rich, R.L. and D.G. Myszka, *Advances in surface plasmon resonance biosensor analysis.* Current Opinion in Biotechnology, 2000. **11**(1): p. 54-61.

53. Szabo, A., L. Stolz, and R. Granzow, *Surface-Plasmon Resonance and Its Use in Biomolecular Interaction Analysis (Bia).* Current Opinion in Structural Biology, 1995. **5**(5): p. 699-705.

54. Simon, H.J., D.E. Mitchell, and J.G. Watson, *Optical Second-Harmonic Generation with Surface Plasmons in Silver Films.* Physical Review Letters, 1974. **33**(26): p. 1531-1534.

55. Sipe, J.E., et al., *Analysis of 2nd-Harmonic Generation at Metal-Surfaces.* Physical Review B, 1980. **21**(10): p. 4389-4402.

56. Tsang, T.Y.F., *Surface-plasmon-enhanced third-harmonic generation in thin silver films.* Optics Letters, 1996. **21**(4): p. 245-247.

57. Xu, H.X., et al., *Spectroscopy of single hemoglobin molecules by surface enhanced Raman scattering.* Physical Review Letters, 1999. **83**(21): p. 4357-4360.

58. Miyazaki, H.T. and Y. Kurokawa, *Squeezing visible light waves into a 3-nm-thick and 55-nm-long plasmon cavity.* Physical Review Letters, 2006. **96**(9): p. -.

59. Fang, N., et al., *Sub-diffraction-limited optical imaging with a silver superlens.* Science, 2005. **308**(5721): p. 534-537.

60. Pendry, J.B., *Negative refraction makes a perfect lens.* Physical Review Letters, 2000. **85**(18): p. 3966-3969.

61. Atwater, H.A., et al., *The new "p-n junction". Plasmonics enables photonic access to the nanoworld.* Mrs Bulletin, 2005. **30**(5): p. 385-389.

62. Barnes, W.L., A. Dereux, and T.W. Ebbesen, *Surface plasmon subwavelength optics.* Nature, 2003. **424**(6950): p. 824-830.

63. Maier, S.A. and H.A. Atwater, *Plasmonics: Localization and guiding of electromagnetic energy in metal/dielectric structures.* Journal of Applied Physics, 2005. **98**(1).

64. Lin, S.Y., et al., *Low-loss, wide-angle Y splitter at similar to 1.6-mu m wavelengths built with a two-dimensional photonic crystal.* Optics Letters, 2002. **27**(16): p. 1400-1402.

65. Ditlbacher, H., et al., *Two-dimensional optics with surface plasmon polaritons.* Applied Physics Letters, 2002. **81**(10): p. 1762-1764.

66. Pile, D.E.P. and D.K. Gramotnev, *Plasmonic subwavelength waveguides: next to zero losses at sharp bends.* Optics Letters, 2005. **30**(10): p. 1186-1188.

67. Bozhevolnyi, S.I., et al., *Channel plasmon-polariton guiding by subwavelength metal grooves.* Physical Review Letters, 2005. **95**(4): p. -.

68. Lamprecht, B., et al., *Surface plasmon propagation in microscale metal stripes.* Applied Physics Letters, 2001. **79**(1): p. 51-53.

69. Nikolajsen, T., et al., *Polymer-based surface-plasmon-polariton stripe waveguides at telecommunication wavelengths.* Applied Physics Letters, 2003. **82**(5): p. 668-670.

70. Berini, P., et al., *Characterization of long-range surface-plasmon-polariton waveguides.* Journal of Applied Physics, 2005. **98**(4): p. -.

71. Maier, S.A. and H.A. Atwater, *Plasmonics: Localization and guiding of electromagnetic energy in metal/dielectric structures.* Journal of Applied Physics, 2005. **98**(1): p. -.

72. Brongersma, M.L., J.W. Hartman, and H.A. Atwater, *Electromagnetic energy transfer and switching in nanoparticle chain arrays below the diffraction limit.* Physical Review B, 2000. **62**(24): p. 16356-16359.

73. Maier, S.A., P.G. Kik, and H.A. Atwater, *Observation of coupled plasmon-polariton modes in Au nanoparticle chain waveguides of different lengths: Estimation of waveguide loss.* Applied Physics Letters, 2002. **81**(9): p. 1714-1716.

74. Hao, F. and P. Nordlander, *Plasmonic coupling between a metallic nanosphere and a thin metallic wire.* Applied Physics Letters, 2006. **89**(10).

75. Markel, V.A. and A.K. Sarychev, *Propagation of surface plasmons in ordered and disordered chains of metal nanospheres.* Physical Review B, 2007. **75**(8).

76. Atwater, H.A., et al., *Plasmonics - A route to nanoscale optical devices.* Advanced Materials, 2001. **13**(19): p. 1501-+.

77. Coyle, S., et al., *Confined plasmons in metallic nanocavities.* Physical Review Letters, 2001. **87**(17).

78. Viitanen, A.J., I.S. Nefedov, and S.A. Tretyakov, *Waves along chains of nanopores in noble metals.* Metamaterials Iii, 2008. **6987**.

79. Nezhad, M.P., K. Tetz, and Y. Fainman, *Gain assisted propagation of surface plasmon polaritons on planar metallic waveguides.* Optics Express, 2004. **12**(17): p. 4072-4079.

80. Seidel, J., S. Grafstrom, and L. Eng, *Stimulated emission of surface plasmons at the interface between a silver film and an optically pumped dye solution.* Physical Review Letters, 2005. **94**(17): p. -.

81. Zhu, G., et al., *Elongation of surface plasmon polariton propagation length without gain.* Optics Express, 2008. **16**(20): p. 15576-15583.

82. Bergman, D.J. and M.I. Stockman, *Surface Plasmon Amplification by Stimulated Emission of Radiation: Quantum Generation of Coherent Surface Plasmons in Nanosystems.* Physical Review Letters, 2003. **90**(2): p. 027402.

83. Dionne, J.A., et al., *PlasMOStor: A Metal-Oxide-Si Field Effect Plasmonic Modulator.* Nano Letters, 2009. **9**(2): p. 897-902.

84. Atwater, H.A., *The Promise of Plasmonics.* Sci. Am., 2007. **296**: p. 56-63.

85. Ashkin, A., Boyd, G. D., Dziedzic, J. M., Smith, R. G., Ballman, A.A., Levinstein, J. J., Nassau, K., *Optically-induced refractive index inhomogeneities in LiNBO3 and LiTaO3.* Applied Physics Letters, 1966. **9**(1): p. 72-74.

86. Feinberg, J., et al., *Photorefractive Effects and Light-Induced Charge Migration in Barium-Titanate.* Journal of Applied Physics, 1980. **51**(3): p. 1297-1305.

87. Breer, S. and K. Buse, *Wavelength demultiplexing with volume phase holograms in photorefractive lithium niobate.* Applied Physics B-Lasers and Optics, 1998. **66**(3): p. 339-345.

88. Orlowski, R., L.A. Boatner, and E. Kratzig, *Photorefractive Effects in the Cubic Phase of Potassium Tantalate-Niobate.* Optics Communications, 1980. **35**(1): p. 45-48.

89. Odoulov, S. and O. Oleinik, *Photorefractive Barium Sodium Niobate.* Ferroelectrics, 1989. **92**: p. 227-232.

90. Kumar, J., et al., *Enhanced 2-Beam Mixing Gain in Photorefractive Gaas Using Alternating Electric-Fields.* Optics Letters, 1987. **12**(2): p. 120-122.

91. Guenther, R.D., *Modern optics*. 1990, New York ; Chichester: Wiley. xvi,696p.,[4]p.of plates.

92. Houlier, B. and F. Micheron, *Photoinduced Charge-Transfer Process in Plzt Ceramics.* Journal of Applied Physics, 1979. **50**(1): p. 343-345.

93. Moerner, W.E., A. GrunnetJepsen, and C.L. Thompson, *Photorefractive polymers.* Annual Review of Materials Science, 1997. **27**: p. 585-623.

94. Fischer, B. and M. Segev, *Photorefractive Wave-Guides and Nonlinear Mode-Coupling Effects.* Applied Physics Letters, 1989. **54**(8): p. 684-686.

95. Wang, Q.N., R.M. Brubaker, and D.D. Nolte, *Photorefractive Phase-Shift Induced by Hot-Electron Transport - Multiple-Quantum-Well Structures.* Journal of the Optical Society of America B-Optical Physics, 1994. **11**(9): p. 1773-1779.

96. Sutter, K. and P. Gunter, *Photorefractive Gratings in the Organic-Crystal 2-Cyclooctylamino-5-Nitropyridine Doped with 7,7,8,8-Tetracyanoquinodimethane.* Journal of the Optical Society of America B-Optical Physics, 1990. **7**(12): p. 2274-2278.

97. Khoo, I.C., et al., *Coherent beam amplification with a photorefractive liquid crystal.* Optics Letters, 1997. **22**(16): p. 1229-1231.

98. Tziraki, M., et al., *Photorefractive holography for imaging through turbid media using low coherence light.* Applied Physics B-Lasers and Optics, 2000. **70**(1): p. 151-154.

99. Gunter, P., *Holography, Coherent-Light Amplification and Optical-Phase Conjugation with Photorefractive Materials.* Physics Reports-Review Section of Physics Letters, 1982. **93**(4): p. 199-299.

100. Weiss, S., S. Sternklar, and B. Fischer, *Double Phase-Conjugate Mirror - Analysis, Demonstration, and Applications.* Optics Letters, 1987. **12**(2): p. 114-116.

101. Segev, M., et al., *Spatial Solitons in Photorefractive Media.* Physical Review Letters, 1992. **68**(7): p. 923-926.

102. Cronin-Golomb, M., Fischer, B., White, J. O., Yariv, A., *Theory and Applications of Four-Wave Mixing in Photorefractive Media.* Ieee Journal of Quantum Electronics, 1984. **20**(1): p. 12-30.

103. Sternklar, S., et al., *Beam Coupling and Locking of Lasers Using Photorefractive 4-Wave-Mixing.* Optics Letters, 1986. **11**(8): p. 528-530.

104. Günter, P., J.P. Huignard, and A.M. Glass, *Photorefractive materials and their applications*. 1988, Berlin ; New York: Springer-Verlag.

105. Imbert, B., et al., *High Photorefractive Gain in 2-Beam Coupling with Moving Fringes in Gaas-Cr Crystals.* Optics Letters, 1988. **13**(4): p. 327-329.

106. Meerholz, K., et al., *A Photorefractive Polymer with High Optical Gain and Diffraction Efficiency near 100-Percent.* Nature, 1994. **371**(6497): p. 497-500.

107. Kim, K.H., et al., *Effects of applied electric field on orientational photorefraction in porphyrin : Zn-doped nematic liquid crystals.* Applied Physics Letters, 2004. **85**(3): p. 366-368.

108. Liu, D.T.H., et al., *Photorefractive Gain in Gaas under a Dc Electric-Field.* Applied Physics Letters, 1988. **53**(15): p. 1369-1371.

109. Gookin, D.M., *Optical Switch Using the Photorefractive Effect and Ferroelectric Polarization Reversal.* Optics Letters, 1987. **12**(3): p. 196-198.

110. Daly, K.R., G. D'Alessandro, and M. Kaczmarek, *Regime independent coupled-wave equations in anisotropic photorefractive media.* Applied Physics B-Lasers and Optics, 2009. **95**(3): p. 589-596.

111. Mach, P., et al., *Switchable Bragg diffraction from liquid crystal in colloid-templated structures.* Europhysics Letters, 2002. **58**(5): p. 679-685.

112. Gaylord, T.K. and M.G. Moharam, *Thin and Thick Gratings - Terminology Clarification.* Applied Optics, 1981. **20**(19): p. 3271-3273.

113. Moharam, M.G., T.K. Gaylord, and R. Magnusson, *Criteria for Bragg Regime Diffraction by Phase Gratings.* Optics Communications, 1980. **32**(1): p. 14-18.

114. Daly, K.R., *Light-Matter Interaction in Liquid Crystal Cells.* Ph.D thesis, School of Mathematics, University of Southampton, 2011.

115. Evans, D.R., G. Cook, and M.A. Saleh, *Recent advances in photorefractive two-beam coupling.* Optical Materials, 2009. **31**(7): p. 1059-1060.

116. Cook, G., C.J. Finnan, and D.C. Jones, *High optical gain using counterpropagating beams in iron and terbium-doped photorefractive lithium niobate.* Applied Physics B-Lasers and Optics, 1999. **68**(5): p. 911-916.

117. Burland, D.M., et al., *Photorefractive Polymers - a Status-Report.* Pure and Applied Chemistry, 1995. **67**(1): p. 33-38.

118. Krasavin, A.V., A.V. Zayats, and N.I. Zheludev, *Active control of surface plasmon-polariton waves.* Journal of Optics a-Pure and Applied Optics, 2005. **7**(2): p. S85-S89.

119. Krasavin, A.V., et al., *High-contrast modulation of light with light by control of surface plasmon polariton wave coupling.* Applied Physics Letters, 2004. **85**(16): p. 3369-3371.

120. Abb, M., et al., *All-Optical Control of a Single Plasmonic Nanoantenna-ITO Hybrid.* Nano Letters, 2011. **11**(6): p. 2457-2463.

121. Chen, J., et al., *Observation of surface-plasmon-polariton transmission through a silver film sputtered on a photorefractive substrate.* Journal of Applied Physics, 2007. **102**(11).

122. Pacifici, D., H.J. Lezec, and H.A. Atwater, *All-optical modulation by plasmonic excitation of CdSe quantum dots.* Nature Photonics, 2007. **1**(7): p. 402-406.

123. Smolyaninov, I.I., et al., *Single-photon tunneling via localized surface plasmons.* Physical Review Letters, 2002. **88**(18).

124. Reinitzer, F., *Contributions to the Knowledge of Cholesterol.* Liquid Crystals, 1989. **5**(1): p. 7-18.

125. Lehmann, O., *On flowing crystals.* Zeitschrift Fur Physikalische Chemie, 1889. **4**: p. 462-472.

126. Friedel, G., *The mesomorphic states of matter.* Ann. Phys., 1922. **18**: p. 273-474.

127. deBroglie, M., Friedel, E., *Diffraction of X-rays by smectic substances.* Comptes rendus de l'Academie des Sciences, 1923. **176**: p. 738-740.

128. Collings, P.J. and M. Hird, *Introduction to liquid crystals : chemistry and physics*. 1997, London: Taylor & Francis. xi,298p., [4]p. of plates.

129. Sluckin, T.J., D. Dunmur, and H. Stegemeyer, *Crystals that flow : classic papers from the history of liquid crystals*. 2004, London: Taylor & Francis. xxii, 738 p.

130. Khoo, I.-C., *Liquid crystals*. 2nd ed. ed. 2007, New York ; Chichester: Wiley-Interscience. xiv, 368 p.

131. Albrecht, O., et al., *Monolayers of Rod-Shaped and Disk-Shaped Liquid-Crystalline Compounds at the Air-Water-Interface.* Colloid and Polymer Science, 1986. **264**(8): p. 659-667.

132. Bushby, R.J. and O.R. Lozman, *Discotic liquid crystals 25 years on.* Current Opinion in Colloid & Interface Science, 2002. **7**(5-6): p. 343-354.

133. Yeh, P. and C. Gu, *Optics of liquid crystal displays*. 1999, New York ; Chichester: Wiley. xii,438p.

134. Li, J., et al., *Infrared refractive indices of liquid crystals.* Journal of Applied Physics, 2005. **97**(7): p. -.

135. Pedrotti, F.L. and L.S. Pedrotti, *Introduction to optics*. 2nd ed. ed. 1993: Prentice-Hall International. xxii,602p.

136. Khoo, I.-C., *Liquid crystals : physical properties and nonlinear optical phenomena*. 1995, New York, N.Y. ; Chichester: Wiley & Sons. xvi,298p.

137. Wu, S.-T. and D.-K. Yang, *Reflective liquid crystal displays*. Wiley SID series in display technology. 2001, Chichester [Eng.] ; New York: Wiley. xvi, 335 p.

138. Collings, P.J. and J.S. Patel, *Handbook of liquid crystal research*. 1997, New York ; Oxford: Oxford University Press. xv,600p.

139. Gennes, P.-G.d. and J. Prost, *The physics of liquid crystals*. 2nd ed. ed. 1993, Oxford: Clarendon Press. xvi,597p.

140. Gu, Y.D. and N.L. Abbott, *Observation of Saturn-ring defects around solid microspheres in nematic liquid crystals.* Physical Review Letters, 2000. **85**(22): p. 4719-4722.

141. Eakin, J.N., et al., *Zero voltage Freedericksz transition in periodically aligned liquid crystals.* Applied Physics Letters, 2004. **85**(10): p. 1671-1673.

142. Barbero, G., L.R. Evangelista, and N.V. Madhusudana, *Effect of surface electric field on the anchoring of nematic liquid crystals.* European Physical Journal B, 1998. **1**(3): p. 327-331.

143. Sheng, P., *Boundary-Layer Phase-Transition in Nematic Liquid-Crystals.* Physical Review A, 1982. **26**(3): p. 1610-1617.

144. Blake, G.I., T. Mullin, and S.J. Tavener, *The Freedericksz transition as a bifurcation problem.* Dynamics and Stability of Systems, 1999. **14**(3): p. 299-331.

145. Chandrasekhar, S. and N.V. Madhusudana, *Liquid-Crystals.* Annual Review of Materials Science, 1980. **10**: p. 133-155.

146. Rudenko, E.V. and A.V. Sukhov, *Photoinduced Electrical-Conductivity and Photorefraction in a Nematic Liquid-Crystal.* Jetp Letters, 1994. **59**(2): p. 142-146.

147. Buchnev, E., et al., *Enhanced two-beam coupling in colloids of ferroelectric nanoparticles in liquid crystals.* Journal of the Optical Society of America B-Optical Physics, 2007. **24**(7): p. 1512-1516.

148. Ono, H. and N. Kawatsuki, *Orientational holographic grating observed in liquid crystals sandwiched with photoconductive polymer films.* Applied Physics Letters, 1997. **71**(9): p. 1162-1164.

149. Kajzar, F., S. Bartkiewicz, and A. Miniewicz, *Optical amplification with high gain in hybrid-polymer-liquid-crystal structures.* Applied Physics Letters, 1999. **74**(20): p. 2924-2926.

150. Mun, J., et al., *Transport and trapping of photocharges in liquid crystals placed between photoconductive polymer layers.* Applied Physics Letters, 2001. **79**(13): p. 1933-1935.

151. Qian, J., et al., *Optical characteristic of PVK/C-60 films fabricated by physical jet deposition.* Chemical Physics Letters, 1996. **257**(5-6): p. 563-568.

152. Kaczmarek, M., et al., *The role of surface charge field in two-beam coupling in liquid crystal cells with photoconducting polymer layers.* Journal of Applied Physics, 2004. **96**(5): p. 2616-2623.

153. Pagliusi, P. and G. Cipparrone, *Surface-induced photorefractive-like effect in pure liquid crystals.* Applied Physics Letters, 2002. **80**(2): p. 168-170.

154. Sprokel, G.J., R. Santo, and J.D. Swalen, *Determination of the Surface Tilt Angle by Attenuated Total Reflection.* Molecular Crystals and Liquid Crystals, 1981. **68**(1-4): p. 977-986.

155. Sprokel, G.J., *The Reflectivity of a Liquid-Crystal Cell in a Surface-Plasmon Experiment.* Molecular Crystals and Liquid Crystals, 1981. **68**(1-4): p. 987-993.

156. Welford, K.R., J.R. Sambles, and M.G. Clark, *Guided Modes and Surface Plasmon-Polaritons Observed with a Nematic Liquid-Crystal Using Attenuated Total Reflection.* Liquid Crystals, 1987. **2**(1): p. 91-105.

157. Welford, K.R. and J.R. Sambles, *Detection of Surface Director Reorientation in a Nematic Liquid-Crystal.* Applied Physics Letters, 1987. **50**(14): p. 871-873.

158. Yang, F., L.Z. Ruan, and J.R. Sambles, *Exploration of the surface director profile in a liquid crystal cell using coupling between the surface plasmon and half-leaky optical guided modes.* Applied Physics Letters, 2008. **92**(15).

159. Innes, R.A., S.P. Ashworth, and J.R. Sambles, *Large Optical Bistability in a Nematic Liquid-Crystal Using Surface Plasmon-Polaritons.* Physics Letters A, 1989. **135**(6-7): p. 357-362.

160. Innes, R.A. and J.R. Sambles, *Optical Non-Linearity in Liquid-Crystals Using Surface Plasmon-Polaritons.* Journal of Physics-Condensed Matter, 1989. **1**(35): p. 6231-6260.

161. Dickson, W., et al., *Electronically controlled surface plasmon dispersion and optical transmission through metallic hole arrays using liquid crystal.* Nano Letters, 2008. **8**(1): p. 281-286.

162. Wang, Y., S.D. Russell, and R.L. Shimabukuro, *Voltage-induced broad-spectrum reflectivity change with surface-plasmon waves.* Journal of Applied Physics, 2005. **97**(2).

163. Wang, Y., *Voltage-Induced Color-Selective Absorption with Surface-Plasmons.* Applied Physics Letters, 1995. **67**(19): p. 2759-2761.

164. Yang, F.Z. and J.R. Sambles, *Microwave liquid crystal wavelength selector.* Applied Physics Letters, 2001. **79**(22): p. 3717-3719.

165. Lee, C.H., et al., *Sensitization of the Photoconductivity of Conducting Polymers by C-60 - Photoinduced Electron-Transfer.* Physical Review B, 1993. **48**(20): p. 15425-15433.

166. Hu, H.L., et al., *Influence of poly3-octylthiophene (P3OT) film thickness and preparation method on photovoltaic performance of hybrid ITO/CdS/P3OT/Au solar cells.* Solar Energy Materials and Solar Cells, 2010. **94**(1): p. 29-33.

167. Khoo, I.C., *Orientational photorefractive effects in nematic liquid crystal films.* Ieee Journal of Quantum Electronics, 1996. **32**(3): p. 525-534.

168. Hikmet, R.A.M., *Electrically Induced Light-Scattering from Anisotropic Gels.* Journal of Applied Physics, 1990. **68**(9): p. 4406-4412.

169. Born, M. and E. Wolf, *Principles of optics : electromagnetic theory of propagation, interference and diffraction of light*. 6th (corrected) ed. ed. 1980, Cambridge: Cambridge University Press, 1997. xxviii,808p.

170. Simon, J.M. and V.A. Presa, *Surface Electromagnetic-Waves at the Interface with Anisotropic Media.* Journal of Modern Optics, 1995. **42**(11): p. 2201-2211.

171. Gigli, M.L. and R.A. Depine, *Excitation of eigenmodes at uniaxial crystal-metal-isotropic films.* Journal of Modern Optics, 1998. **45**(11): p. 2281-2299.

172. Elston, S.J. and J.R. Sambles, *Surface Plasmon-Polaritons on an Anisotropic Substrate.* Journal of Modern Optics, 1990. **37**(12): p. 1895-1902.

173. Daly, K.R., G. D'Alessandro, and M. Kaczmarek, *An Efficient Q-Tensor-Based Algorithm for Liquid Crystal Alignment Away from Defects.* Siam Journal on Applied Mathematics, 2010. **70**(8): p. 2844-2860.

174. Berreman, D.W., *Optics in Stratified and Anisotropic Media - 4x4-Matrix Formulation.* Journal of the Optical Society of America, 1972. **62**(4): p. 502-&.

175. Ko, D.Y.K. and J.R. Sambles, *Scattering Matrix-Method for Propagation of Radiation in Stratified Media - Attenuated Total Reflection Studies of Liquid-Crystals.* Journal of the Optical Society of America a-Optics Image Science and Vision, 1988. **5**(11): p. 1863-1866.

176. Li, L.F., *Formulation and comparison of two recursive matrix algorithms for modeling layered diffraction gratings.* Journal of the Optical Society of America a-Optics Image Science and Vision, 1996. **13**(5): p. 1024-1035.

177. Auslender, M. and S. Hava, *Scattering-matrix propagation algorithm in full-vectorial optics of multilayer grating structures.* Optics Letters, 1996. **21**(21): p. 1765-1767.

178. Moharam, M.G. and T.K. Gaylord, *Rigorous Coupled-Wave Analysis of Planar-Grating Diffraction.* Journal of the Optical Society of America, 1981. **71**(7): p. 811-818.

179. Glytsis, E.N. and T.K. Gaylord, *3-Dimensional (Vector) Rigorous Coupled-Wave Analysis of Anisotropic Grating Diffraction.* Journal of the Optical Society of America a-Optics Image Science and Vision, 1990. **7**(8): p. 1399-1420.

180. Homola, J., S.S. Yee, and G. Gauglitz, *Surface plasmon resonance sensors: review*. Sensors and Actuators B-Chemical, 1999. **54**(1-2): p. 3-15.

181. Innes, R.A. and J.R. Sambles, *Optical Nonlinearity in a Nematic Liquid-Crystal Using Surface Plasmon-Polaritons.* Optics Communications, 1987. **64**(3): p. 288-292.

182. Baba, A., et al., *Evaluation of tilt angles of nematic liquid crystal molecules on polyimide Langmuir-Blodgett films using the attenuated total reflection measurement method.* Japanese Journal of Applied Physics Part 1-Regular Papers Brief Communications & Review Papers, 1998. **37**(5A): p. 2581-2586.

183. Watanabe, J., et al., *Prism-Coupled Light-Emission from Tunnel-Junctions Containing Interface Roughness - Experiment.* Physical Review B, 1988. **38**(18): p. 12959-12965.

184. Fontana, E. and R.H. Pantell, *Characterization of Multilayer Rough Surfaces Using Surface-Plasmon Spectroscopy.* Journal of the Optical Society of America B-Optical Physics, 1986. **3**(8): p. P158-P158.

185. Engenhardt, K.M. and S. Gregory, *Surface-plasmon-polariton excitation of optical microcavities and second-harmonic emission.* Journal of the Optical Society of America B-Optical Physics, 2000. **17**(4): p. 593-599.

186. Stockman, M.I., *Nanoplasmonics: The physics behind the applications*. Physics Today, 2011. **64**(2): p. 39-44.

187. Dragoman, M. and D. Dragoman, *Plasmonics: Applications to nanoscale terahertz and optical devices.* Progress in Quantum Electronics, 2008. **32**(1): p. 1-41.

188. Skoog, D.A., et al., *Principles of instrumental analysis*. 6th ed. / Douglas A. Skoog, F. James Holler, Stanley R. Crouch. ed. 2007, Pacific Grove, Calif.: Brooks/Cole ; London : Thomson Learning [distributor]. xv, 1039 p.

189. Daly, K.R., *Light-matter interaction in liquid crystal cells.* Ph.D. thesis, School of Mathematics, University of Southampton (2011).

190. Woollam, J.A., et al *Overview of Variable Angle Spectroscopic Ellipsometry (VASE), Part I: Basic Theory and Typical Applications*. in *Optical Metrology, vol. CR72, pp 3-28*. 1999: SPIE.

191. Tompkins, H.G. and E.A. Irene, *Handbook of ellipsometry*. 2005, Norwich, N.Y.: William Andrew Pub. ; Heidelberg, Germany : Springer. xvi, 870 p.

192. Horowitz, P. and W. Hill, *The art of electronics*. 2nd ed. ed. 1989: Cambridge University Press.

193. Agilent Technologies, *Agilent Impedance Measurement Handbook: A Guide to measurement technology and techniques*. 4th Edition ed. 2009.

194. Bakshi, V., *Electronic Measurements.* Technical Publications, 2007.

195. Bahl, I.J., *Fundamentals of RF and microwave transistor amplifiers*. 2009, Hoboken, N.J.: Wiley. xxiii, 671 p.

196. Yao, F., Pei, Y., Zhang, Yu, Zhang, J., Hou, C., Sun, X., *High-resolution photorefractive gratings in nematic liquid crystals sandwiched with photoconductive polymer film.* Applied Physics B-Lasers and Optics, 2008. **92**(4): p. 573-576.

197. Bach, F.-W., A. Laarmann, and T. Wenz, *Modern surface technology*. 2006, Weinheim: Wiley-VCH. xx, 325 p.

198. Graedel, T.E., *Corrosion Mechanisms for Silver Exposed to the Atmosphere.* Journal of the Electrochemical Society, 1992. **139**(7): p. 1963-1970.

199. Zhang, S., et al., *Surface plasmon resonance characterization of thermally evaporated thin gold films.* Surface Science, 2007. **601**(23): p. 5445-5458.

200. Heising, R.A., *Quartz Crystals for electrical Circuits: Their Design and Manufacture*. 1946, New York: D. Van Nostrand Company, Inc.

201. Barrett, E.M., *Conjugated Polymer Photodetectors as Retinomorphic Imaging Devices.* Ph.D thesis, Department of Physics, Imperial College London (2006), 2006.

202. Hall, D.B., P. Underhill, and J.M. Torkelson, *Spin coating of thin and ultrathin polymer films.* Polymer Engineering and Science, 1998. **38**(12): p. 2039-2045.

203. Bornside, D.E., C.W. Macosko, and L.E. Scriven, *Spin Coating - One-Dimensional Model.* Journal of Applied Physics, 1989. **66**(11): p. 5185-5193.

204. Schubert, D.W. and T. Dunkel, *Spin coating from a molecular point of view: its concentration regimes, influence of molar mass and distribution.* Materials Research Innovations, 2003. **7**(5): p. 314-321.

205. Leneweit, G., K.G. Roesner, and R. Koehler, *Surface instabilities of thin liquid film flow on a rotating disk.* Experiments in Fluids, 1999. **26**(1-2): p. 75-85.

206. Birnie, D.P., et al., *Film Substrate Vacuum-Chuck Interactions during Spin-Coating.* Optical Engineering, 1992. **31**(9): p. 2012-2020.

207. Mittal, K.L.E. and K.W.E. Lee, *Polymer surfaces and interfaces : characterization, modification and application*. 1997: VSP.

208. Lee, B.W. and N.A. Clark, *Alignment of liquid crystals with patterned isotropic surfaces.* Science, 2001. **291**(5513): p. 2576-2580.

209. Pidduck, A.J., et al., *Control of liquid crystal alignment by polyimide surface modification using atomic force microscopy.* Applied Physics Letters, 1997. **71**(20): p. 2907-2909.

210. Chaudhari, P., et al., *Atomic-beam alignment of inorganic materials for liquid-crystal displays.* Nature, 2001. **411**(6833): p. 56-59.

211. Bahadur, B., *Liquid-Crystal Displays.* Molecular Crystals and Liquid Crystals, 1984. **109**(1): p. 1-93.

212. Stohr, J., et al., *Microscopic origin of liquid crystal alignment on rubbed polymer surfaces.* Macromolecules, 1998. **31**(6): p. 1942-1946.

213. Hornauer, D.L., *Light-Scattering Experiments on Silver Films of Different Roughness Using Surface Plasmon Excitation.* Optics Communications, 1976. **16**(1): p. 76-79.

214. SCHOTT, *Optical glass: Data Sheets.* N-LASF9 p. 62, 2008.

215. Wang, Y., *Photoconductivity of Fullerene-Doped Polymers.* Nature, 1992. **356**(6370): p. 585-587.

216. Zhang, Y.D., T. Wada, and H. Sasabe, *Carbazole photorefractive materials.* Journal of Materials Chemistry, 1998. **8**(4): p. 809-828.

217. Chen, Y., et al., *Researches on the photoconductivity and UV-visible absorption spectra of the first C-60-chemically modified poly(N-vinylcarbazole).* Polymer Bulletin, 1996. **36**(2): p. 203-208.

218. Ruoff, R.S., et al., *Solubility of C-60 in a Variety of Solvents.* Journal of Physical Chemistry, 1993. **97**(13): p. 3379-3383.

219. Stegeman, G.I., *Long-Range Surface-Plasmons in Birefringent Media.* Applied Optics, 1983. **22**(15): p. 2243-2245.

220. Daly, K.R., et al., *Theory of hybrid photorefractive plasmonic liquid crystal cells.* Journal of the Optical Society of America B-Optical Physics, 2011. **28**(8): p. 1874-1881.

221. Herrington. M., *Electrical and Optical effects in Hybrid liquid crystal cells.* Ph.D thesis, School of Physics and Astronomy, University of Southampton., 2011.

222. Costa, M.R., R.A.C. Altafim, and A.P. Mammana, *Electrical Modeling of liquid crystal Displays-LCDs.* Ieee Transactions on Dielectrics and Electrical Insulation, 2006. **13**(1): p. 204-210.

223. Macgregor, A.R., *Modeling the Optical-Properties of Twisted Nematic Guest Host Liquid-Crystals.* Journal of Physics D-Applied Physics, 1988. **21**(9): p. 1438-1446.

224. Aubourg, P., et al., *Liquid-Crystal Light Valve Using Bulk Monocrystalline Bi12sio20 as the Photoconductive Material.* Applied Optics, 1982. **21**(20): p. 3706-3712.

225. Jonda, C. and A.B.R. Mayer, *Investigation of the electronic properties of organic light-emitting devices by impedance spectroscopy.* Chemistry of Materials, 1999. **11**(9): p. 2429-2435.

226. Orazem, M.E. and B. Tribollet, *Electrochemical impedance spectroscopy*. 2008, Hoboken, N.J.: Wiley. xxxi, 523 p.

227. Ikeda, N. and T. Miyasaka, *A solid-state dye-sensitized photovoltaic cell with a poly(N-vinyl-carbazole) hole transporter mediated by an alkali iodide.* Chemical Communications, 2005(14): p. 1886-1888.

228. Fournet, P., et al., *Enhanced brightness in organic light-emitting diodes using a carbon nanotube composite as an electron-transport layer.* Journal of Applied Physics, 2001. **90**(2): p. 969-975.

229. Sonnonstine, T.J. and M.M. Perlman, *Surface-Potential Decay in Insulators with Field-Dependent Mobility and Injection Efficiency.* Journal of Applied Physics, 1975. **46**(9): p. 3975-3981.

230. Jiao, M.Z., et al., *Alignment layer effects on thin liquid crystal cells.* Applied Physics Letters, 2008. **92**(6).

231. Kaczmarek, M. and A. Dyadyusha, *Structured, photosensitive PVK and PVCN polymer layers for control of liquid crystal alignment.* Journal of Nonlinear Optical Physics & Materials, 2003. **12**(4): p. 547-555.

232. Li, J., et al., *Infrared refractive indices of liquid crystals.* Journal of Applied Physics, 2005. **97**(7).

233. Herrington, M., et al., *AC-field-enhanced beam coupling in photorefractive, hybrid liquid crystals.* Epl, 2011. **95**(1).

234. Brabec, C.J., et al., *Photovoltaic properties of conjugated polymer/methanofullerene composites embedded in a polystyrene matrix.* Journal of Applied Physics, 1999. **85**(9): p. 6866-6872.

235. Kato, T., T. Kutsuna, and K. Hanabusa, *Liquid-crystalline physical gels formed by the aggregation of trans-(1R,2R)-bis (dodecanoylamino) cyclohexane in a thermotropic nematic liquid crystal. Phase behavior and electro-optic properties.* Molecular Crystals and Liquid Crystals Science and Technology Section a-Molecular Crystals and Liquid Crystals, 1999. **332**: p. 2887-2892.

236. Simoni, F., *Nonlinear optical properties of liquid crystals and polymer dispersed liquid crystals*. 1997, Singapore ; London: World Scientific. xvii, 259p.

237. Sah, C.-T., *Fundamentals of solid-state electronics*. 1991, Singapore ; River Edge, NJ: World Scientific. xxvi, 1010 p.

238. Ono, H. and N. Kawatsuki, *Real-time holograms in liquid crystals on photoconductive polymer surfaces.* Optics Communications, 1998. **147**(4-6): p. 237-241.

239. Lee, W. and C.C. Lee, *Two-wave mixing in a nematic liquid-crystal film sandwiched between photoconducting polymeric layers.* Nanotechnology, 2006. **17**(1): p. 157-162.

240. Deer, M.J., et al., *Characterization of an inorganic photorefractive liquid crystal hybrid cell.* Journal of Physics D-Applied Physics, 2006. **39**(1): p. 36-45.

241. Stohr, J. and M.G. Samant, *Liquid crystal alignment by rubbed polymer surfaces: a microscopic bond orientation model.* Journal of Electron Spectroscopy and Related Phenomena, 1999. **99**: p. 189-207.

242. Zhuang, X., et al., *Orientation of Amphiphilic Molecules on Polar Substrates.* Physical Review Letters, 1995. **75**(11): p. 2144-2147.

243. Herrington, M.R., et al., *The Effect of the Size of BaTiO3 Nanoparticles on the Electro-Optic Properties of Nematic Liquid Crystals.* Molecular Crystals and Liquid Crystals, 2010. **527**: p. 72-79.

244. Refregier, P., et al., *2-Beam Coupling in Photorefractive Bi12sio20 Crystals with Moving Grating - Theory and Experiments.* Journal of Applied Physics, 1985. **58**(1): p. 45-57.

245. Halas, N.J., S. Lal, and S. Link, *Nano-optics from sensing to waveguiding.* Nature Photonics, 2007. **1**(11): p. 641-648.

246. Palik, E.D., *Handbook of Optical-Constants.* Journal of the Optical Society of America a-Optics Image Science and Vision, 1984. **1**(12): p. 1297-1297.

247. Etchegoin, P.G., E.C. Le Ru, and M. Meyer, *An analytic model for the optical properties of gold.* Journal of Chemical Physics, 2006. **125**(16): p. -.

248. Schulz, L.G., *The Optical Constants of Silver, Gold, Copper, and Aluminum. I. The Absorption Coefficient k.* JOSA, 1954. **44**(5): p. 357-362.

249. Theye, M.L., *Investigation of the optical properties of Au by means of thin semitransparent films.* Physical Review B-Solid State, 1970. **2**(8): p. 3060-3078.

250. Innes, R.A. and J.R. Sambles, *Optical Characterization of Gold Using Surface-Plasmon Polaritons.* Journal of Physics F-Metal Physics, 1987. **17**(1): p. 277-287.

251. Heavens, O.S., *Optical Properties of Thin Films.* Rep. Prog. Phys., 1960. **23**(1).

252. Sennett, R.S., Scott, G. D., *The Structure of Evaporated Metal Films and Their Optical Properties.* Journal of the Optical Society of America, 1950. **40**(4).

253. Male, D., Rouard, P., *Sur les déterminations des constantes optiques des métaux massifs faites au moyen des lames épaisses.* J. Phys. Radium, 1953. **14**(11): p. 584-587.

254. Reuter, R. and H. Franke, *An Integrated Organic Photoconductive Detector for Optoelectronics.* Applied Physics B-Photophysics and Laser Chemistry, 1989. **48**(3): p. 219-224.

Publications

Theory of hybrid photorefractive plasmonic liquid crystal cells

Keith R. Daly,[1,*] Stephen Abbott,[2] Giampaolo D'Alessandro,[1] David C. Smith,[2] and Malgosia Kaczmarek[2]

[1]*School of Mathematics, University of Southampton, Southampton, Hampshire, England*
[2]*School of Physics and Astronomy, University of Southampton, Southampton, Hampshire, England*
**Corresponding author: krd103@soton.ac.uk*

Received April 5, 2011; accepted June 2, 2011;
posted June 8, 2011 (Doc. ID 145419); published July 11, 2011

We use the theory of optical waveguides to study analytically the voltage-dependent response of a surface plasmon polariton (SPP) at the interface between a photorefractive liquid crystal cell and a semi-infinite gold layer. For sufficiently large electric fields the alignment of the liquid crystal can be calculated analytically. The resulting correction to the SPP dispersion relation is then determined in terms of the applied field and the liquid crystal surface alignment relative to the SPP propagation direction. The approximate analytic techniques developed here are shown to be accurate when compared to rigorous diffraction theory and experimental measurements. The approximate equations are a powerful tool of general application. They can be used to study SPP propagation at the interface between a metal and any nonhomogeneous or anisotropic dielectric and are also applicable to self-assembled monolayers and biosensing applications.

OCIS codes: 240.5420, 240.6680, 160.3710, 230.3720.

1. INTRODUCTION

An SPP is a coupled oscillation of an electromagnetic field with the electron cloud at the surface of a metal [1]. These excitations, originally predicted by Ritchie in 1957 [2], propagate along a metal–dielectric interface and have amplitude, which decays exponentially in both materials. Because of their unique properties, such as their sensitivity to small changes in dielectric constants, $\sim O(10^{-14})$ [3,4], SPPs have a wide variety of applications in both industry and academia. These include resonance sensors [5], enhanced spectroscopy techniques capable of detecting single molecules [6], waveguides [7], biosensors [8], and subwavelength optical applications, such as nanoscale lithography [9].

The ability to manipulate SPPs is essential for continued development of devices in this area. One way this can be achieved is through the use of photorefractive liquid crystal cells, a device commonly used in spatial light modulators [10] and beam couplers [11,12]. These devices consist of a planar cell containing liquid crystals sandwiched between photorefractive or photoconducting layers. In the case relevant to SPP manipulation, one of these layers consists of polyimide (PI) and the other of photoconducting polyvinyl carbazole doped with C_{60} (PVK:C_{60}), as shown in Fig. 1(a). The addition of a thin gold layer and a high refractive index optical prism allows coupling to SPPs at the metal PVK interface in the standard Kretschmann configuration [13].

A great deal of numerical and experimental work has been carried out concerning SPPs at a liquid crystal–metal interface. These studies include: SPP propagation in anisotropic materials [14], the use of SPPs to probe the surface alignment [15], SPP-induced nonlinearity [16] and bistability [17], and numerical and experimental observations of guided mode resonances and plasmonic resonance shift [18]. Liquid crystals have also been used as a means to control plasmonic transmission through metallic hole arrays [19] and color-selective absorption at metallic surfaces [20]. However, to fully utilize the properties of the photorefractive cell to manipulate SPPs, it is important to gain a good understanding of the SPP response to the liquid crystal alignment. In this paper we obtain an approximate analytical solution for the liquid crystal alignment and use waveguide perturbation techniques to describe the change in the effective index of the SPP due to the orientation of the liquid crystal molecules.

Perturbation methods have been used extensively to help understand the dispersion relation of SPP. These studies include the effects of SPP resonance width [21,22] and the change in SPP propagation vector [23,24] due to absorption and nonideal interfaces. These studies consider the standard analytic SPP resonance conditions derived for a single isotropic dielectric–metal interface as the leading order solution. This result is then perturbed due to absorption in the metal and finite width, nonideal, metal films. It is this approach that we adopt to study the SPP response to the liquid crystal alignment.

This paper is arranged as follows: in Section 2 we consider the optical problem in the context of perturbed waveguides. The leading order problem is a simple metal–dielectric interface, which supports SPP propagation, while the effects of the liquid crystal are treated as a perturbation. In Section 3 we develop an analytic approximation for the alignment of the liquid crystal layer to be used in conjunction with the perturbation techniques developed in Section 2. In Section 4 we compare the analytic approximation with the reflection spectrum calculated using rigorous diffraction theory. In Section 5 we compare the results with experimental observations and show that the approximations made here are valid. Finally in Section 6 we discuss the application of the approximation to hybrid photorefractive plasmonic liquid crystal cells.

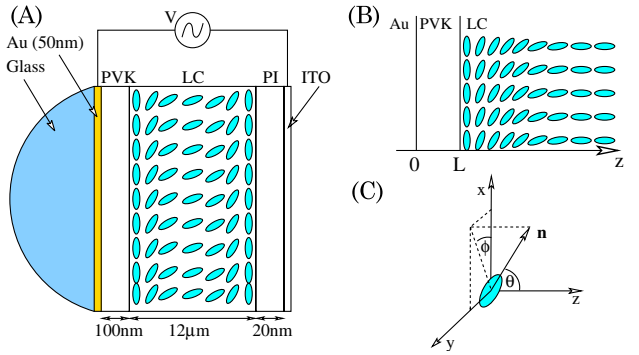

Fig. 1. (Color online) (A) Hybrid photorefractive–plasmonic liquid crystal cell with hemispherical prism to allow SPP coupling in the standard Kretschmann geometry. (B) Waveguide structure under study: the system is simplified to a three-layer structure. At leading order this simplifies further to a two-layer system where both layers are homogeneous and isotropic. (C) Definition of angles used relative to coordinate axes. The SPP propagates in the x direction and the alignment of the liquid crystal is determined in terms of the Euler angles θ and ϕ.

2. OPTICAL MODEL

A. Leading Order Plasmonic Mode

The system we study may be considered as a three-layer optical waveguide consisting of a semi-infinite gold layer, a thin alignment layer, usually an isotropic dielectric, of thickness L, and a semi-infinite liquid crystal layer, as shown in Fig. 1(b). In this section we derive the standard conditions for an SPP to propagate at the interface between a semi-infinite dielectric and a semi-infinite metal. The effects of the anisotropy and inhomogeneity, due to the liquid crystal, are then treated as a perturbation, which will affect the dispersion relation of the plasmon.

The dielectric function for this structure can be written as

$$\epsilon(z) = \epsilon_u(z) I + \eta \Delta\epsilon(z), \tag{1}$$

where $\eta \ll 1$ is a smallness parameter and I is the identity matrix. Throughout this paper we use the symbol ϵ to denote the dielectric permittivity at optical frequency. The low frequency dielectric constants used in the liquid crystal model are denoted using the symbol ε. We consider the effects of the anisotropy and inhomogeneity as a first-order perturbation, while at leading order the liquid crystal layer is optically identical to the PVK layer. Hence, the leading and first-order dielectric constants are defined as

$$\epsilon_u(z) = \begin{cases} \epsilon_m & z < 0 \\ \epsilon_d & 0 < z < L \\ \epsilon_d & z > L \end{cases},$$

$$\Delta\epsilon(z) = \begin{cases} 0 & z < 0 \\ 0 & 0 < z < L \\ \epsilon_{\mathrm{lc}}\left[\hat{\boldsymbol{n}}(z) \otimes \hat{\boldsymbol{n}}(z) - \frac{1}{3} I\right] + \epsilon_c I & z > L \end{cases}, \tag{2}$$

where ϵ_m is the dielectric constant of the metal. Here we model this using a standard Drude model [25]. The anisotropy of the liquid crystal is $\epsilon_{\mathrm{lc}} = \epsilon_{\parallel} - \epsilon_{\perp}$ and its isotropic correction to the leading order permittivity is $\epsilon_c = \frac{\epsilon_{\parallel} + 2\epsilon_{\perp}}{3} - \epsilon_d$. The Au–PVK boundary is at $z = 0$, the PVK–liquid crystal boundary is at $z = L$.

By considering the anisotropy and inhomogeneity of the liquid crystal as a perturbation, we neglect any optical modes that are guided by the alignment of the liquid crystal layer. However, due to the mode orthogonality conditions [26], there is no coupling between the optical and SPP modes. Therefore, we can neglect the guided modes and consider only the SPP mode.

To understand the effects of the perturbation on the waveguide we consider Maxwell's equations for a dielectric function of the form of Eq. (1). The perturbation is assumed to induce a small change in the propagation constant of the SPP mode, which becomes significant over a relatively large distance. Therefore, we consider two different spatial scales: the fast scale $\boldsymbol{x}_0 = k_0 \boldsymbol{x}$ and the slow scale $\boldsymbol{x}_1 = \eta k_0 \boldsymbol{x}$, where k_0 is the free space wavenumber. This gives us the expanded differential operator $\nabla = \nabla_0 + \eta \nabla_1$. We also expand the time-independent electric and magnetic fields as a power series expansion in η, $\mathcal{E} = \mathcal{E}_0 + \eta \mathcal{E}_1 + \mathrm{O}(\eta^2)$ and $\mathcal{H} = \mathcal{H}_0 + \eta \mathcal{H}_1 + \mathrm{O}(\eta^2)$. Here we have scaled the electric and magnetic fields and assumed a time dependence $\exp(-i\omega t)$. The nonscaled fields are given by $\tilde{\mathcal{E}} = \mathcal{E} e^{-i\omega t}/\sqrt{\epsilon_0}$ and $\tilde{\mathcal{H}} = \mathcal{H} e^{-i\omega t}/\sqrt{\mu_0}$, where ϵ_0 and μ_0 are the permittivity and permeability of free space, respectively. Substituting into Maxwell's equations and expanding to leading order we obtain

$$\begin{pmatrix} \mathcal{D}_0 & -i \\ i\epsilon_u & \mathcal{D}_0 \end{pmatrix} \begin{pmatrix} \mathcal{E}_0 \\ \mathcal{H}_0 \end{pmatrix} = 0, \tag{3}$$

where $\mathcal{D}_0$ is the curl operator with respect to the fast variable. The leading order of the optical modes of the waveguide are given by the nontrivial solutions to Eq. (3). In this case there is only a single bound isotropic SPP mode with magnetic field $\mathcal{H}_0(\boldsymbol{x}) = A_0(\boldsymbol{x}_1)\boldsymbol{H}_0(\boldsymbol{x}_0)$ and electric field $\mathcal{E}_0(\boldsymbol{x}) = A_0(\boldsymbol{x}_1)\boldsymbol{E}_0(\boldsymbol{x}_0)$. Here, A_0 is the mode amplitude and the leading order mode profiles are given by

$$\boldsymbol{H}_0(\boldsymbol{x}) = \begin{cases} \boldsymbol{h}^m e^{i\boldsymbol{k}^m \cdot \boldsymbol{x}_0} & z < 0 \\ \boldsymbol{h}^d e^{i\boldsymbol{k}^d \cdot \boldsymbol{x}_0} & z > 0 \end{cases}, \quad \boldsymbol{E}_0(\boldsymbol{x}) = \begin{cases} \frac{1}{\epsilon_m} \boldsymbol{e}^m e^{i\boldsymbol{k}^m \cdot \boldsymbol{x}_0} & z < 0 \\ \frac{1}{\epsilon_d} \boldsymbol{e}^d e^{i\boldsymbol{k}^d \cdot \boldsymbol{x}_0} & z > 0 \end{cases}. \tag{4}$$

The polarization and wave vectors in the region ν, where $\nu = \{d, m\}$ denotes the dielectric and metal regions, respectively, are defined as

$$\boldsymbol{e}^{\nu} = \begin{pmatrix} \pm i\beta_{\nu} \\ 0 \\ \alpha_0 \end{pmatrix}, \quad \boldsymbol{k}^{\nu} = \begin{pmatrix} \alpha_0 \\ 0 \\ \mp i\beta_{\nu} \end{pmatrix}, \quad \boldsymbol{h}^{\nu} = \begin{pmatrix} 0 \\ 1 \\ 0 \end{pmatrix}, \tag{5}$$

where we have also used the top and bottom signs for $\nu = \{d, m\}$, respectively. The leading order effective index α_0 and the decay constants in each layer β_{ν} are given by

$$\alpha_0 = \sqrt{\frac{\epsilon_d \epsilon_m}{\epsilon_d + \epsilon_m}}, \qquad \beta_m = \sqrt{-\frac{\epsilon_m \epsilon_m}{\epsilon_d + \epsilon_m}},$$
$$\beta_d = \sqrt{-\frac{\epsilon_d \epsilon_d}{\epsilon_d + \epsilon_m}}. \tag{6}$$

From Eq. (6) we obtain the constraint $|\epsilon_{m,0}| > |\epsilon_{d,0}|$ for the existence of propagating solutions. To understand the

effects of the perturbation we consider the $O(\eta)$ terms in the expansion of Maxwell's equations [26],

$$\begin{pmatrix} \mathcal{D}_0 & -i \\ i\epsilon_u & \mathcal{D}_0 \end{pmatrix} \begin{pmatrix} \mathcal{E}_1 \\ \mathcal{H}_1 \end{pmatrix} = \begin{pmatrix} -\nabla_1 \times \mathcal{E}_0 \\ -i\Delta\epsilon\mathcal{E}_0 - \nabla_1 \times \mathcal{H}_0 \end{pmatrix}. \tag{7}$$

Equation (7) is a linear system of equations of the form $M\boldsymbol{x} = \boldsymbol{b}$ for the first-order correction to the electric and magnetic fields. However, for Eq. (3) to have a solution, we require $\mathrm{Det}(M) = 0$. Therefore, Eq. (7) is singular. In order for it to have a solution we must require that the inner product $\langle \boldsymbol{b}, \ker(M^\dagger) \rangle$ is zero. Here, $\ker(M^\dagger)$ denotes the kernel of the adjoint of M. As $\ker(M^\dagger)$ is spanned by a single optical mode, we obtain the solvability condition

$$\int_{-\infty}^{\infty} \mathcal{H}_0^* \cdot \nabla_1 \times \mathcal{E}_0 - \mathcal{E}_0^* \cdot \nabla_1 \times \mathcal{H}_0 - i\mathcal{E}_0^* \cdot \Delta\epsilon\mathcal{E}_0 dz_0 = 0. \tag{8}$$

Using Eqs. (4), (5), and (8), we obtain that the correction to the effective index of the SPP is

$$n_{\mathrm{eff}}^{\mathrm{spp}} = \alpha_0 + \eta \frac{1}{P_0} \int_{k_0 L}^{\infty} \boldsymbol{E}_0^* \cdot \Delta\epsilon \boldsymbol{E}_0 dz_0, \tag{9}$$

where the mode normalization P_0 is defined as

$$P_0 = \int_{-\infty}^{\infty} \hat{\boldsymbol{e}}_x \cdot [\boldsymbol{E}_0^* \times \boldsymbol{H}_0 + \boldsymbol{E}_0 \times \boldsymbol{H}_0^*] dz_0. \tag{10}$$

Equation (9) determines the correction to the SPP wavenumber for a given variation in the liquid crystal alignment. To determine its value it is necessary to calculate the variation in the liquid crystal alignment near the gold layer for different applied fields.

3. PLASMONS AT A LIQUID CRYSTAL INTERFACE

A. Liquid Crystal Alignment

In this section we model the alignment of the liquid crystal to an applied electric field using a variational approach. The problem of liquid crystal alignment, in the case where the liquid crystal is restricted to a plane, has been studied asymptotically by Self *et al.* [27] in the context of large and small applied fields. Here, we extend this to the case relevant for SPP propagation of large applied fields in a general twisted cell.

We model the orientation of the liquid crystal on a macroscopic level in terms of a unit director $\hat{\boldsymbol{n}}$, which tells us the average alignment of liquid crystal molecules over a small sample. We define $\hat{\boldsymbol{n}}$ in terms of the first two Euler angles θ and ϕ. The liquid crystal alignment is found by minimizing the total free energy of the liquid crystal cell. This is given by $\tilde{\mathcal{F}}(\hat{\boldsymbol{n}}) = \tilde{\mathcal{F}}_d(\hat{\boldsymbol{n}}) + \tilde{\mathcal{F}}_e(\hat{\boldsymbol{n}})$, where $\tilde{\mathcal{F}}_d$ is the elastic free energy and $\tilde{\mathcal{F}}_e$ is the electrostatic free energy. The free energy can be simplified further by using the one elastic constant approach. The resulting nondimensional free energy can be written as

$$\mathcal{F} = \int_{L_0}^{L_1} \frac{1}{2}(\partial_{z_0}\theta)^2 + \frac{1}{2}\sin^2\theta(\partial_{z_0}\phi)^2 - \frac{1}{2}\chi_i(\partial_{z_0}\psi)^2 - \frac{1}{2}\chi_a \cos^2\theta(\partial_{z_0}\psi)^2 dz_0, \tag{11}$$

where $\hat{n}_z$ is the z component of the director, $L_0 = k_0 L$, $L_1 = k_0(L + L_z)$, and L_z is the thickness of the liquid crystal layer. Here $\chi_i = \frac{\varepsilon_0 \varepsilon_\perp}{K}\psi_0^2$ and $\chi_a = \frac{\varepsilon_0 \Delta\varepsilon}{K}\psi_0^2$, where $\Delta\varepsilon = \varepsilon_\parallel - \varepsilon_\perp$ is the low frequency dielectric anisotropy, K the liquid crystal elastic constant, and ε_0 the permittivity of free space. The nondimensional potential ψ is found by scaling the dimensional potential $\tilde{\psi}$ with a typical potential ψ_0, $\psi = \tilde{\psi}/\psi_0$. The liquid crystal alignment can now be determined by minimizing Eq. (11) in terms of θ and ϕ. After some manipulation we obtain the Euler–Lagrange equations for the steady state liquid crystal alignment:

$$\frac{d^2\theta}{dz_0^2} - \sin 2\theta \left(\frac{d\phi}{dz_0}\right)^2 - \frac{1}{2}\chi_a \mathcal{E}_z^2 \sin 2\theta = 0, \tag{12a}$$

$$\frac{d}{dz_0}\left[(1 - \cos 2\theta)\frac{d\phi}{dz_0}\right] = 0, \tag{12b}$$

where $\mathcal{E}_z = -\partial_{z_0}\psi$ is the z component of the electric field that aligns the liquid crystal. The surface anchoring of the liquid crystal gives us the boundary conditions $\theta(0) = \theta_{p0}$, $\theta(1) = \theta_{p1}$, $\phi(0) = \phi_{p0}$, and $\phi(1) = \phi_{p1}$. The equation for ψ is derived by either minimizing Eq. (11) with respect to ψ or substituting Eq. (1) into Maxwell's equation $\nabla \cdot \boldsymbol{D} = 0$. After some manipulation this yields

$$\frac{d}{dz_0}\left[(1 + \alpha_\theta \cos 2\theta)\frac{d\psi}{dz_0}\right] = 0, \tag{13}$$

where $\alpha_\theta = \Delta\varepsilon/(\varepsilon_\parallel + \varepsilon_\perp)$ is the electrostatic coupling strength. We want to approximate the alignment of the liquid crystal in the high voltage regime. To simplify the derivation we consider the limit of zero electrostatic coupling, $\alpha_\theta = 0$. Nonzero electrostatic coupling can be considered using a perturbation approach [27]. For a spatially homogeneous applied voltage the solution to Eq. (13) yields a nondimensional electric field with only a z component, which is constant throughout the cell and has value $\mathcal{E}_z = V/(\psi_0 k_0 L_z)$, where V is the voltage applied to the cell. This allows us to nondimensionalize Eq. (12a) to obtain

$$\frac{\partial^2\theta}{\partial z_0^2} - \sin 2\theta \left(\frac{d\phi}{dz_0}\right)^2 - \frac{1}{\delta^2}\sin 2\theta = 0, \tag{14}$$

where $\delta^2 = 1/(\mathcal{E}_z^2\chi_a) \ll 1$. This is a singular perturbation problem for the director angle θ. As such, neglecting terms $O(\delta^2)$ will not allow us to satisfy any of the boundary conditions. We split the domain into three different regions: two inner regions, $z_0 - L_0 \sim O(\delta)$ and $L_1 - z_0 \sim O(\delta)$, and an outer region where $z_0 \sim O(1)$. We now consider each region individually. The outer problem is relatively straightforward, $\sin 2\theta_o = 0$, for $\theta_o \in [0, \pi/2]$, where θ_o is the director angle in the outer region. Therefore, we obtain $\theta_o = 0$ or $\theta_o = \pi/2$. For high voltage it can be shown that the former is stable and the later is unstable. We see that $\theta_o = 0$ is a solution of Eq. (12b). This means that ϕ_o, the twist in the outer region, is undefined. This solution is valid throughout the outer region. However, it will break down near the boundaries where the director angles vary rapidly. An appropriate spatial scaling makes the two inner problems identical. We use $z_0 - L_0 = \delta\zeta$ for the boundary

near $z_0 = L_0$ and $L_1 - z_0 = \delta\zeta$ for the boundary $z_0 = L_1$. Therefore, we only consider the inner region near $z_0 = L_0$ in detail. We rescale and solve Eq. (12b) for $\frac{d\phi_i}{d\zeta}$,

$$\frac{d\phi_i}{d\zeta} = \frac{C_0}{1 - \cos 2\theta_i}, \tag{15}$$

where C_0 is an arbitrary constant and θ_i and ϕ_i are the director angles in the inner region. Substituting Eq. (15) into Eq. (14) we obtain

$$\frac{d^2\theta_i}{d\zeta^2} - \sin 2\theta_i = C_0^2 \frac{\sin 2\theta_i}{(1 - \cos 2\theta_i)^2}. \tag{16}$$

We can solve Eq. (16) using the knowledge that $\theta_i \to \theta_o$ as $\zeta \to \infty$. We multiply by $\frac{d\theta_i}{d\zeta}$ and integrate to obtain

$$\frac{1}{2}\left(\frac{d\theta_i}{d\zeta}\right)^2 + \frac{1}{2}\cos(2\theta_i) = -\frac{C_0^2}{2(1 - \cos 2\theta_i)} + C_1, \tag{17}$$

where C_1 is an arbitrary constant. Matching with the outer solution $\theta_o = 0$ requires that θ_i should vanish as ζ tends to infinity. This is only possible if $C_0 = 0$ and $C_1 = 1/2$. Substituting these values into Eqs. (15) and (16) gives $\phi_i = \phi_{p0}$ and

$$\theta_i = \arctan\left\{\frac{2C_2 e^{\sqrt{2}\zeta}}{C_2^2 e^{2\sqrt{2}\zeta} - 1}\right\}, \tag{18}$$

where C_2 is determined by the pretilt θ_{p0},

$$C_2 = \frac{1 + \sin(\theta_{p0})}{\cos(\theta_{p0})} \approx 1 + \theta_{p0} + \mathrm{O}(\theta_{p0}^2), \tag{19}$$

for $\theta_{p0} \ll 1$. Carrying out a similar calculation at the second boundary and matching the outer we obtain the composite solution for θ:

$$\theta = \arctan\left\{\frac{2(1 + \theta_{p0})e^{\sqrt{2}(z_0 - L_0)/\delta}}{e^{2\sqrt{2}(z_0 - L_0)/\delta}(1 + 2\theta_{p0}) - 1}\right\} + \arctan\left\{\frac{2(1 + \theta_{p1})e^{\sqrt{2}(L_1 - z_0)/\delta}}{e^{2\sqrt{2}(L_1 - z_0)/\delta}(1 + 2\theta_{p1}) - 1}\right\}. \tag{20}$$

The composite solution for ϕ is given by any function that satisfies the boundary conditions and has zero first derivative at the boundaries. In general, the full composite expansion is not required as we only want to understand the effects of the liquid crystal alignment near to the cell boundary. Therefore, only the inner expansion near $z_0 = L_0$ is required and the change in θ near $z_0 = L_1$ can be neglected.

B. Correction to SPP Wavenumber

We now calculate the correction to the SPP wavenumber. Using the waveguide perturbation techniques, developed in Section 2, we can obtain an expression in terms of the overlap integral of the SPP with the perturbation, recall Eq. (9). For sufficiently large cell width, typically greater than the decay length of the plasmon, we need only consider the liquid crystal alignment profile near the PVK boundary where there is zero pretilt. In this case the director can be written as

$$\hat{\boldsymbol{n}} = \frac{1}{e^{2\sqrt{2}(z_0 - L_0)/\delta} + 1}\begin{pmatrix} 2e^{\sqrt{2}(z_0 - L_0)/\delta}\cos(\phi_{p0}) \\ 2e^{\sqrt{2}(z_0 - L_0)/\delta}\sin(\phi_{p0}) \\ e^{2\sqrt{2}(z_0 - L_0)/\delta} - 1 \end{pmatrix}. \tag{21}$$

The liquid crystal orientation varies on a scale $\sim\mathrm{O}(1/\delta)$, while the SPP decays on a scale $\sim\mathrm{O}(k_0\beta_d)$. We define the shifted spatial variable, $\xi = 2\beta_d(z_0 - L_0)$, such that the liquid crystal alignment varies exponentially with ξ at a rate γ, where

$$\gamma = \sqrt{\frac{2\varepsilon_0\Delta\varepsilon}{K}}\frac{V}{k_0\beta_d L_z}. \tag{22}$$

Using this scaling and Eqs. (5) and (21) the correction to the effective index is

$$n_{\mathrm{eff}}^{\mathrm{spp}} = \alpha_0[1 + \eta(\kappa_h + \kappa_{nh})e^{-2L\beta_d}], \tag{23}$$

where the homogeneous and nonhomogeneous coefficients are

$$\kappa_h = \frac{1}{6}\left\{\frac{3\epsilon_m\epsilon_c}{\epsilon_d(\epsilon_d + \epsilon_m)} - \frac{(\epsilon_d + 2\epsilon_m)\epsilon_m\epsilon_{\mathrm{lc}}}{\epsilon_d(\epsilon_d^2 - \epsilon_m^2)}\right\}, \tag{24a}$$

$$\kappa_{nh} = \frac{2(\epsilon_d\cos^2\phi_{p0} + \epsilon_m)\epsilon_m\epsilon_{\mathrm{lc}}}{\epsilon_d(\epsilon_d^2 - \epsilon_m^2)}\int_0^\infty \frac{e^{-\xi}e^{\gamma\xi}}{(e^{\gamma\xi} + 1)^2}\mathrm{d}\xi, \tag{24b}$$

respectively. The integral in Eq. (24b) has a solution in the form of an infinite series

$$\int_0^\infty \frac{e^{-\xi}e^{\gamma\xi}}{(e^{\gamma\xi} + 1)^2}\mathrm{d}\xi = \frac{1}{\gamma}\left(\frac{1}{2} + \sum_{n=1}^{\infty}\frac{(-1)^n}{1 + n\gamma}\right), \tag{25}$$

which is asymptotic for large γ. An approximate solution can also be found for small γ using Laplace's method:

$$\int_0^\infty \frac{e^{-\xi}e^{\gamma\xi}}{(e^{\gamma\xi} + 1)^2}\mathrm{d}\xi \approx \frac{1}{4}\left(1 - \frac{1}{2}\gamma^2 + \gamma^4\right) + \mathrm{O}(\gamma^6). \tag{26}$$

Equations (22)–(26) describe the response of the SPP to the liquid crystal in terms of a perturbation to the effective refractive index of the SPP. These expressions can be used to explore the parameter dependence of the SPP on the experimentally controllable properties of the photorefractive cell and optimize parameters, such as the SPP sensitivity, to voltage. Before we discuss the predictions of this result we first explore its validity through numerical and experimental comparison.

4. NUMERICAL COMPARISON

Having developed an expression for the dependence of the SPP effective index on the parameters of the waveguide, we now wish to verify the assumptions we have made through comparison with numerical simulations based on rigorous diffraction theory [28]. The liquid crystal alignment is calculated by solving Eqs. (12a) and (12b) using a numerical relaxation method. The reflection spectrum of the device is calculated using a scattering matrix approach in which the liquid crystal is treated as a large number of homogeneous anisotropic layers [29]. The reflection spectrum of the layered device is found by writing the solutions to Maxwell's equations in each layer and solving the boundary conditions at each interface to

Table 1. Numerical Values of Constants for a Typical Hybrid Plasmonic Photorefractive LC Cell Filled with the Liquid Crystal Compound E7

$\varepsilon_0 = 8.85 \times 10^{-12}\,\mathrm{Fm}^{-1}$	$L_z = 12 \times 10^{-6}\,\mathrm{m}$	$\alpha_0 = 1.7974 + 0.0089i$
$K = 15.9 \times 10^{-12}\,\mathrm{N}$	$\lambda = 832\,\mathrm{nm}$	$\beta_d = 0.5706 + 0.0257i$
$\varepsilon_\parallel = 19.54$	$\chi_a = 5.566$	$\beta_m = 5.5196 - 0.2056i$
$\varepsilon_\perp = 5.17$	$\epsilon_d = 2.89$	$\psi_0 = 1\mathrm{V}$
$\Delta\varepsilon = 14.37$	$\epsilon_m = -30.1182 + 2.5361i$	

obtain the mode amplitudes. The result is a system of linear equations for the reflection spectrum of the cell.

The reflection spectrum for a homogeneously aligned liquid crystal will have a single minimum at the point of SPP absorption. However, for a liquid crystal with nonhomogeneous alignment it is possible to excite a large number of guided modes. These resonant modes are guided by the liquid crystal alignment [18] and, neglecting the presence of the thin gold layer, have effective index bounded by the liquid crystal refractive indices, $n_{\mathrm{eff}}^{\mathrm{opt}} < n_e$.

In order to allow easy comparison between Eq. (23) and the numerical simulation, it is important to choose the properties of the waveguide structure such that the optical mode resonances do not overlap the SPP resonance. Otherwise, it would be very difficult to distinguish between the minima associated with the optical modes and the minimum associated with the SPP resonance. This restriction is imposed only to aid comparison and is not a limitation of the model.

We consider a liquid crystal with refractive indices $n_o = 1.6$ and $n_e = 1.7$. This gives $\epsilon_c = -0.22$ and $\epsilon_{\mathrm{lc}} = 0.33$. The remaining parameters used in the equations and simulation are given in Table 1. The reflection spectrum is calculated for a range of voltages and PVK thicknesses. The minimum of the reflection spectrum is calculated and the resulting $n_{\mathrm{eff}}^{\mathrm{spp}}$ is compared with the analytic approximation. The results are shown in Fig. 2.

The results are shown to agree well with small discrepancies occurring at low voltages. However, these errors are all within the bounds of the error induced by the perturbation expansion. The SPP effective index is seen to be most sensitive to the liquid crystal alignment at lower voltages. This can be quantified by differentiating Eq. (25) twice and solving the resulting equation numerically to find the point of maximum sensitivity of the SPP response. Using the parameters given in Table 1, we determine that the SPP is most sensitive to the liquid crystal at approximately 14.6 V.

The same calculations can be done for the case of a real liquid crystal compound E7 with refractive indices $n_o = 1.5100$ and $n_e = 1.7104$ at $\lambda = 832\,\mathrm{nm}$. These indices are calculated using a Cauchy series [30,31]. These results can only be obtained for the case where the effective index of the SPP is larger than that of the highest optical guided mode, i.e., for a sufficiently thick PVK layer. This comparison is shown in Fig. 3. As this system has the same low frequency dielectric properties as the low anisotropy case, the voltage of highest sensitivity is again ≈14.6 V.

The numerical comparison presented here shows the accuracy of the analytic approximations developed here in describing the response of the SPP to the variation in the liquid crystal alignment. Calculating the theoretical point of maximum sensitivity allows us to determine the ideal conditions to obtain the maximum SPP sensitivity to the refractive index changes. Before we move on to discuss how these results can be used to help optimize the performance of the photorefractive liquid crystal cells we validate this model further through experimental comparison.

5. EXPERIMENTAL COMPARISON

As a final test of the model we compare its predictions to the experimentally measured reflection spectra for a plasmonic photorefractive liquid crystal cell. The experimental structure is identical to the one used in the numerical simulations.

A high-index glass substrate, $n = 1.833$ measured at $\lambda = 832\,\mathrm{nm}$, is coated with a $40 \pm 3\,\mathrm{nm}$ Au layer by thermal deposition in a vacuum chamber at a pressure of 8×10^{-6} torr. The PVK solution is then deposited on the Au layer by spin

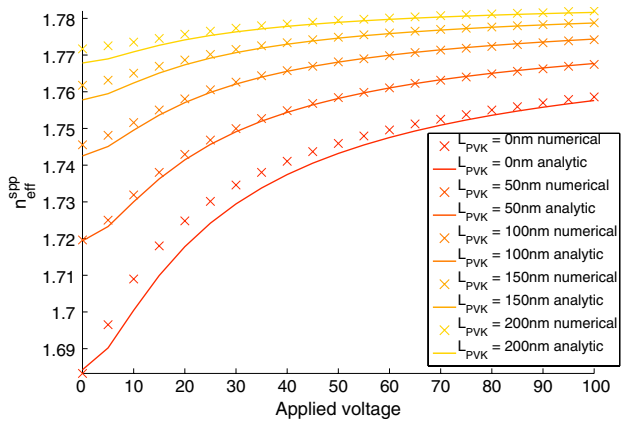

Fig. 2. (Color online) Comparison between numerical reflection spectrum and analytic approximation for the SPP effective index with $n_o = 1.6$ and $n_e = 1.7$. The numerical effective index is calculated directly from the minimum of the reflection spectrum, and the analytic approximation is given by Eq. (23).

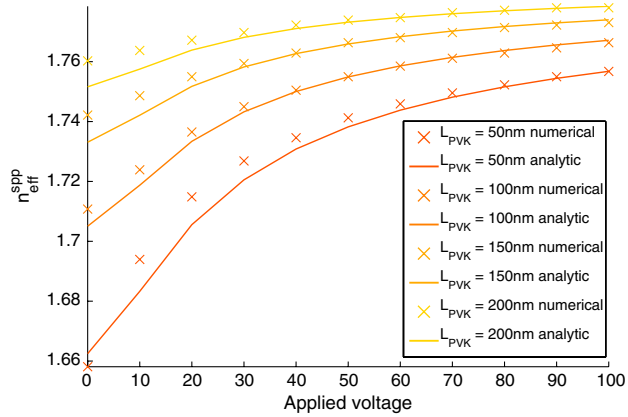

Fig. 3. (Color online) Comparison between numerical reflection spectrum and analytic approximation for the SPP effective index with $n_o = 1.5100$ and $n_e = 1.7104$. This gives $\epsilon_c = -0.39$ and $\epsilon_{\mathrm{lc}} = 0.65$. The numerical effective index is calculated directly from the minimum of the reflection spectrum, and the analytic approximation is given by Eq. (23).

coating at 3600 rpm. After spin coating, the sample is left to anneal for 1 h at 240 °C.

The PVK thickness, as determined by transmission spectra measured using a UV–Vis spectrometer, is 80 ± 3 nm. The top plate is an ITO-coated glass slide with a PI alignment layer deposited by spin coating at 4000 rpm. Both the PI and PVK polymer layers are rubbed using a velour cloth so a planar alignment can be achieved with the liquid crystal. The top plate is attached to the substrate using UV curing glue with 12 μm spacers added to it. The cell is filled with the liquid crystal mixture E7 under vacuum conditions. Uniform alignment is checked by viewing the cell through crossed polarizers. Finally, electrical contacts are added to the ITO and Au layers using a conductive epoxy.

SPPs are excited using a white light source that is collimated, polarized, and focused onto the hemispherical lens to which the samples are attached with an index matching fluid. This allows light with a range of input wave vectors to generate SPP at various energies simultaneously, see Fig. 4. The optics are mounted onto a rail that rotates about the sample and the fiber connected to the spectrometer is attached to a motorized rotation stage providing the greatest possible range of incident angles to generate SPPs. The experiments angular resolution is 0.05° and the spectrometer has a wavelength resolution of 1 nm.

Reorientation of the liquid crystal is achieved by applying a 1 kHz AC voltage of adjustable amplitude. The AC waveform is generated by a signal generator, which is connected to an amplifier capable of a peak output voltage of 70 V.

The SPP dispersion relation is determined from the analysis of the reflection spectrum measured by a fiber optic silicon CCD spectrometer connected to a motorized positioning stage. Coupling to an SPP corresponds to a minimum of the reflection spectrum as a function of the incidence angle. Its location gives the effective index of the SPP.

The comparison between the experimental and theoretical dispersion relations is shown in Fig. 5. The liquid crystal elastic constant is $K_3 = 19.5$ pN [32] and the refractive index of the PVK layer is measured at 1.68. The agreement between theory and experiment is exceptionally good as no fitting parameters were used.

There is a small discrepancy in the overall magnitude of the SPP effective index. In principle, this could be removed by using the PVK thickness or refractive index as a fitting parameter. However, as there is a small discrepancy also present in the comparison between the numerical and analytic results, it is more likely that this offset arises from the finite width of the Au layer, or from the implicit error in the perturbation expansion. This comparison demonstrates the strength of the approximation methods used in this paper and their ability to correctly predict the SPP effective index.

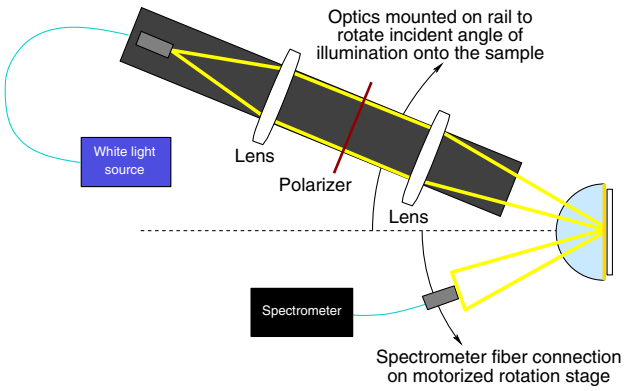

Fig. 4. (Color online) The experimental setup to generate and analyze SPP. *P*-polarized light is required to observe the dip in the reflection spectrum due to coupling to an SPP. *S*-polarized light is used to normalize the signal.

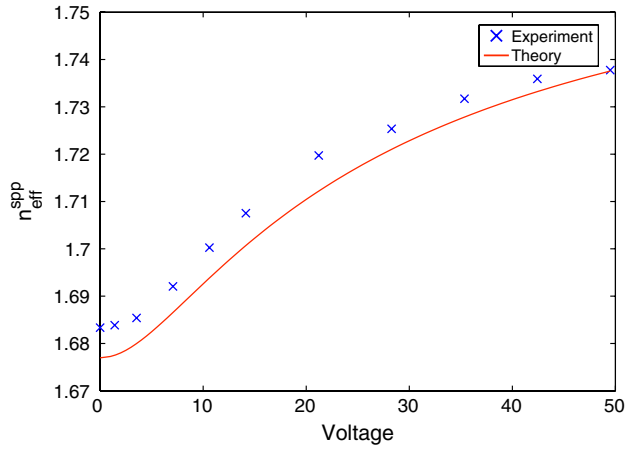

Fig. 5. (Color online) Comparison between the approximate theoretical prediction and experimental measurements of the SPP effective index with $n_o = 1.5100$ and $n_e = 1.7104$. Corresponding to $\epsilon_c = -0.39$ and $\epsilon_{lc} = 0.65$. No fitting parameters were used to obtain these plots.

6. DISCUSSION

In this paper we have derived an approximate expression for the effective refractive index of an SPP propagating along the metal–dielectric interface of a three-layer structure. The SPP propagates between a semi-infinite gold layer and a thin alignment layer. The third layer, adjacent to the alignment layer is a semi-infinite layer of liquid crystals. These types of structure are relevant to the understanding of photorefractive plasmonic liquid crystal cells.

We have studied the effect of the liquid crystal alignment, due to voltage, on the SPP effective index. The alignment of the liquid crystal is derived using matched asymptotic techniques. The resulting expression is then treated as a perturbation to the dielectric function of the cell. The final expression for the SPP effective index has been compared to numerical and experimental data and has been shown to describe the underlying physics to a high degree of accuracy.

Using Eqs. (22)–(26) the effects of the various experimentally controllable parameters can be estimated. The optimum voltage required to obtain the maximum sensitivity of the SPP is an important result. By differentiating Eq. (25) it is seen that the point of highest sensitivity is at $\gamma = 0.6228$, where γ is defined in Eq. (22) and is a function of both the optical wavelength and the low frequency dielectric constants of the liquid crystal. For a typical liquid crystal cell filled with E7, this corresponds to a maximum sensitivity at approximately 14.6 V.

This result is of importance in the optimization of hybrid photorefractive plasmonic liquid crystal structures. These systems rely on a DC voltage to create a periodic alignment in the liquid crystal structure. Because of the high impedance of the alignment layers it is often difficult to obtain a sufficiently large voltage drop across the liquid crystal layer reducing

the efficiency of these devices. By also applying a high frequency AC bias voltage to increase the sensitivity of the SPP it will be possible to produce a much greater device efficiency at low power.

The maximum possible variation in the SPP effective index due to voltage is given by κ_{nh}, determined by Eqs. (24b) and (23). The absolute value of this function monotonically decreases from its initial value to zero at high voltage. Therefore, the maximum possible shift in the SPP effective index is a function of the liquid crystal birefringence, the leading order dielectric constants, the PVK thickness, and the angle the liquid crystal makes with the SPP at the PVK boundary. In general these quantities are defined by the choice of materials, the thickness of the PVK layer, and the free space wavelength of the light.

The SPP sensitivity is maximized in terms of the twist angle for $\phi_{p0} = \pi/2$. This corresponds to the SPP propagating orthogonally to the director at zero volts and, hence, seeing only the ordinary refractive index. As the voltage is increased the director rotates to be perpendicular to the interface. At this point the SPP sees the maximum possible refractive index of the liquid crystal.

The presence of the optical guided modes in the system produces a significant design obstacle for plasmonic liquid crystal systems. For example, a photorefractive SPP system produced by the interaction of the SPP with the photoconductor could potentially cause unwanted diffraction of the SPP into the optical guided modes. By understanding and being able to control the position of the SPP and optical guided mode resonances it will be possible to eliminate these unwanted effects.

For example, consider the effect of the PVK layer thickness on the SPP. A thinner alignment layer allows the SPP to penetrate further into the liquid crystal. This will allow greater control of the SPP via external voltages. However, in the case of the photorefractive liquid crystal cells a thinner PVK layer may cause problems. First, it will decrease the minimum effective index of the SPP, which will push the SPP resonance closer to the optical guided modes. Second, the photoconductive layer is required to create the spatially modulated DC voltage, which produces the refractive index grating. Reducing the thickness of this layer will reduce this effect. The optimal balance of all these factors can be found by coupling Eqs. (22)–(26) to an accurate DC electrical model of the cell.

The results presented in this paper can be extended to include spatial modulations in the voltage, which aligns the liquid crystal. This analysis will be required to develop a thorough understanding of the mechanisms involved in photorefractive plasmon manipulation in liquid crystal cells. However, based on the simplified analysis presented here it is already possible to obtain a thorough understanding of the SPP response to the liquid crystal alignment and anisotropy. This analysis will lead to an increased efficiency of liquid crystal SPP systems and forms the basis for further development in this field.

REFERENCES

1. A. V. Zayats, I. I. Smolyaninov, and A. A. Maradudin, "Nano-optics of surface plasmon polaritons," Phys. Rep. **408**, 131–314 (2005).
2. R. H. Ritchie, "Plasma losses by fast electrons in thin films," Phys. Rev. **106**, 874–881 (1957).
3. I. R. Hooper and J. R. Sambles, "Differential ellipsometric surface plasmon resonance sensors with liquid crystal polarization modulators," Appl. Phys. Lett. **85**, 3017–3019 (2004).
4. X. Fan, I. M. White, S. I. Shopova, H. Zhu, J. D. Suter, and Y. Sun, "Sensitive optical biosensors for unlabeled targets: a review," Anal. Chim. Acta **620**, 8–26 (2008).
5. J. Homola, S. S. Yee, and G. Gauglitz, "Surface plasmon resonance sensors: review," Sensors Actuators B Chem **54**, 3–15 (1999).
6. K. Kneipp, H. Kneipp, I. Itzkan, R. R. Dasari, and M. S. Feld, Surface-enhanced Raman scattering and biophysics," J. Phys. Condens. Matter **14**, R597 (2002).
7. S. A. Maier, P. G. Kik, H. A. Atwater, S. Meltzer, E. Harel, B. E. Koel, and A. A. G. Requicha, "Local detection of electromagnetic energy transport below the diffraction limit in metal nanoparticle plasmon waveguides," Nat. Mater. **2**, 229–232 (2003).
8. M. Malmqvist, "Biospecific interaction analysis using biosensor technology," Nature **361**, 186–187 (1993).
9. W. L. Barnes, A. Dereux, and T. W. Ebbesen, "Surface plasmon subwavelength optics," Nature **424**, 824–830 (2003).
10. U. Bortolozzo and S. Residori, and J. P. Huignard, "Beam coupling in photorefractive liquid crystal light valves," J. Phys. D **41**, 224007 (2008).
11. G. Cook, A. V. Glushchenko, V. Reshetnyak, A. T. Griffith, M. A. Saleh, and D. R. Evans, "Nanoparticle doped organic-inorganic hybrid photorefractives," Opt. Express **16**, 4015–4022 (2008).
12. O. Buchnev, A. Dyadyusha, M. Kaczmarek, V. Reshetnyak, and Y. Reznikov, "Enhanced two-beam coupling in colloids of ferroelectric nanoparticles in liquid crystals," J. Opt. Soc. Am. B **24**, 1512–1516 (2007).
13. E. Kretschmann and H. Raether, "Radiative decay of non radiative surface plasmons excited by light," Zeitschrift Fuer Naturforschung, Teil A **23**, 2135–2136 (1968).
14. S. J. Elston and J. R. Sambles, "Surface plasmon-polaritons on an anisotropic substrate," J. Mod. Opt. **37**, 1895–1902 (1990).
15. K. R. Welford and J. R. Sambles, "Detection of surface director reorientation in a nematic liquid crystal," Appl. Phys. Lett. **50**, 871–873 (1987).
16. R. A. Innes and J. R. Sambles, "Optical nonlinearity in a nematic liquid crystal using surface plasmon-polaritons," Opt. Commun. **64**, 288–292 (1987).
17. R. A. Innes, S. P. Ashworth, and J. R. Sambles, "Large optical bistability in a nematic liquid crystal using surface plasmon-polaritons," Phys. Lett. A **135**, 357–362 (1989).
18. K. R. Welford, J. R. Sambles, and M. G. Clark, "Guided modes and surface plasmon-polaritons observed with a nematic liquid crystal using attenuated total reflection," Liq. Cryst. **2**, 91–105 (1987).
19. W. Dickson, G. A. Wurtz, P. R. Evans, R. J. Pollard, and A. V. Zayats, "Electronically controlled surface plasmon dispersion and optical transmission through metallic hole arrays using liquid crystal," Nano Lett. **8**, 281–286 (2008).
20. Y. Wang, "Voltage-induced color-selective absorption with surface plasmons," Appl. Phys. Lett. **67**, 2759–2761 (1995).
21. W. P. Chen and J. M. Chen, "Use of surface plasma waves for determination of the thickness and optical constants of thin metallic films," J. Opt. Soc. Am. **71**, 189–191 (1981).
22. E. Fontana, "Thickness optimization of metal films for the development of surface-plasmon-based sensors for nonabsorbing media," Appl. Opt. **45**, 7632–7642 (2006).
23. I. Pockrand, "Surface plasma oscillations at silver surfaces with thin transparent and absorbing coatings," Surf. Sci. **72**, 577–588 (1978).
24. W. P. Chen and J. M. Chen, "Surface plasma wave study of submonolayer Cs and Cs O covered Ag surfaces," Surf. Sci. **91**, 601–617 (1980).
25. M. Born and E. Wolf, *Principles of Optics, Electromagnetic Theory of Propagation Interference and Diffraction of Light*, 6th ed. (Cambridge University, 1980).
26. K. Okamoto, *Fundamentals of Optical Waveguides* (Academic Press, 2000).

27. R. H. Self, C. P. Please, and T. J. Sluckin, "Deformation of nematic liquid crystals in an electric field," Eur. J. Appl. Math. **13**, 1–23 (2002).
28. E. N. Glytsis and T. K. Gaylord, "Three-dimensional (vector) rigorous coupled-wave analysis of anisotropic grating diffraction," J. Opt. Soc. Am. A **7**, 1399–1420 (1990).
29. D. W. Berreman, "Optics in stratified and anisotropic media: 4×4-matrix formulation," J. Opt. Soc. Am. **62**, 502–510 (1972).
30. J. Li, C. H. Wen, S. Gauza, R. Lu, and S. T. Wu, "Refractive indices of liquid crystals for display applications," J. Display Technol. **1**, 51–61 (2005).
31. J. Li, S. T. Wu, S. Brugioni, R. Meucci, and S. Faetti, "Infrared refractive indices of liquid crystals," J. Appl. Phys. **97**, 073501 (2005).
32. E. P. Raynes, C. V. Brown, and J. F. Stromer, "Method for the measurement of the K_{22} nematic elastic constant," Appl. Phys. Lett. **82**, 13–15 (2003).

Photorefractive Control of Surface Plasmon Polaritons in a Hybrid Liquid Crystal Cell

Stephen B. Abbott,[1] Keith R. Daly,[2] Giampaolo D'Alessandro,[2] Malgosia Kaczmarek,[1] David C. Smith[1,*]

[1]*School of Physics and Astronomy, University of Southampton, Southampton, SO17 1BJ, UK*
[2]*School of Mathematics, University of Southampton, Southampton, SO17 1BJ, UK*
**Corresponding author: dcsmith@phys.soton.ac.uk*

Received Month X, XXXX; revised Month X, XXXX; accepted Month X, XXXX; posted Month X, XXXX (Doc. ID XXXXX); published Month X, XXXX

We present a photorefractive hybrid liquid crystal system which allows strong photorefractive effects on surface plasmon polaritons. We demonstrate its capability to couple energy between two 1.03eV SPP modes with an efficiency of 25.3±2.3%. We present the energy and grating pitch dependence of the diffraction and a model which can qualitatively explain them.

OCIS Codes: 190.5330, 160.3710, 240.6680

Plasmonics is an exciting technological field with many proven applications such as refractive index based chemical sensors [1], negative refraction [2], superlenses [3], and ultrasmall mode volume and wavelength plasmonic modes [4]. Plasmonic based applications that involve non-linear optical effects include surface enhanced Raman scattering [5] and white light continuum generation from low peak power laser sources [6]. Photorefractive and light-induced effects have also been explored in combination with plasmonic structures, such as for example photomodulation of the plasmonic resonance of gold nanoparticles [7], a photon turnstile which passes only one photon/plasmon at a time [8], ultracompact nanoantenna optical switches [9], photorefractive effects due to ultrafast excitation of aluminium films leading to coherent energy transfer [10] and surface plasmon polariton (SPP)-SPP interactions mediated by semiconductor quantum dots [11]. However, the demonstration of significant photorefractive coupling of energy between SPP modes and/or photorefractive gain for SPP modes has not yet been achieved.

Photorefractive materials generally have a trade-off between large photorefractive effects and fast response times. Liquid crystal (LC) based photorefractive systems, both dye doped and hybrid systems, demonstrate very strong photorefractive effects with photorefractive gain coefficients in excess of 2000cm^{-1} [12] although with relatively slow (>ms) response times. In hybrid photorefractive LC systems [13], a liquid crystal layer is combined with a photoconductive layer. The fraction of a potential applied to the cell which is across the LC layer depends on the conductivity of the photoconductive layer. Thus, the reorientation of LC's director, and effective refractive index, can be selectively controlled by light. In particular, if the cell is illuminated with a sinusoidal two-beam interference pattern this produces a periodic modulation of the LC director that is experienced by SPP as a refractive index grating which can diffract energy between modes (Fig 1a). In this paper we present a hybrid LC system which allows photorefractive control of SPPs propagating within the system. We demonstrate that an unoptimised example of such a system is capable of photorefractive coupling between two SPPs with efficiency of up to 25%.

The design of the new photorefractive SPP system is presented in Fig 1a. It consists of a high refractive index N-LaSF9 (Schott) glass substrate on to which is evaporated a <1nm Cr layer and a 40nm Au layer. A thin (~100nm) photoconducting poly-(N)-vinyl-carbazole (PVK) layer, doped with 10% wt. C_{60} is spin coated on top of the metal. This forms one side of a standard LC cell with a polyimide (PI) coated ITO glass substrate forming the other side using 12µm spacers. The cell is filled with E7 LC (Merck). Both the PVK and PI layers are rubbed to establish an initial, uniform planar alignment of the LC throughout the cell. In order to couple light in and out of SPP modes we use a hemispherical prism of N-LaSF9 glass (Fig 1b) with a radius of curvature of 12.5mm which has been modified by polishing the flat face so that the Au layer in the cell passes through the centre of curvature of the prism. The cells are attached to this prism with a thin layer of n=1.8900 index matching fluid (Cargille labs, Series H). The plasmons are excited using a 200µm fibre coupled to a white light source (Tungsten Halogen lamp, Ocean Optics) whose unpolarised output is collimated by one lens, passes through a rotatable broadband polarizer and is then focused, by a second lens, at the centre of curvature of the prism. A 0.5mm slit is placed after the polariser in some experiments in order to restrict the SPP excited to those with wavevectors in a single direction. The light reflected from or diffracted by the cell is detected using a fibre coupled (200µm) broadband spectrometer (HR4000, Ocean Optics). The collection fibre is mounted on two motorized rotation stages in such a manner that it can be rotated around the prism centre at a constant distance of 50mm to any angle, whilst always pointing at the prism centre. When determining the absorption due to the SPP, the ratio of the s- and p-polarised reflection spectra at the same angular position are used to remove the spectral

dependence of the light source and reduce the effects due to reflections at the prism interfaces and absorption from the index matching fluid. Diffraction efficiencies are determined by normalising the diffracted light intensity by the difference of the s and p reflection spectra at the peak of the SPP absorption for the zero order SPP. In order to induce SPP-SPP coupling, we use a refractive index grating in the LC layer generated by an interference pattern between two coherent, equal power, collimated 1mm diameter beams, with a variable separation angle. These beams are directed onto the sample via a flat face polished onto the prism parallel to the sample contacting face, Fig 1b.

Whilst SPP-SPP coupling can be observed using a DC potential applied across the ITO and Au layers in the cell, ionic drift with a timescale of minutes means that the devices operation is history dependent and samples tend to have a short lifetime. Therefore, we use a low frequency AC (0.5Hz) potential difference across the sample. Results obtained with AC biasing were reproducible and sample lifetimes in excess of six months were achieved. The frequency chosen gives the largest SPP-SPP effects; however, frequencies in the range of 0.1Hz to 5Hz all show SPP-SPP coupling. The AC waveform means that both the SPP dispersion and diffraction efficiency are dynamic and vary periodically. Therefore, we use a mechanical shutter between the two lenses in the illumination system whose opening for 0.05s is phase locked to the applied voltage to enable stroboscopic measurements. The measurements presented in this paper were all taken at the peak of the SPP-SPP coupling which coincided with the peak of the applied potential.

There are eight experimental parameters which control the strength of SPP-SPP coupling; the pitch (Λ) and direction of the light-defined grating (ϕ), the intensity modulation of the light grating (I_G) incident on the PVK, the SPP energy (E_{SPP}), the in-plane orientation of the LC director at the PVK and PI interfaces due to anchoring (θ), the magnitude of the slow AC potential applied to the cell $|V_{AC}|$ and the PVK and LC layer thicknesses (δ_{PVK} and δ_{LC}). In this paper we concentrate on two of the most essential ones, namely the grating pitch and SPP energy. The other parameters were fixed to I_G=5mWcm^{-2}, E_{SPP}=1.462eV, θ=0°, δ_{PVK}=95-120nm and $\delta_{LC}\approx$12μm.

Successful coupling of energy between SPP by a light grating is demonstrated in Fig 2. For this experiment SPP are excited with $1.66k_0 \leq k_x \leq 1.71k_0$ and $|k_y| \leq 0.05k_0$, where k_0 is the magnitude of the wavevector of the exciting light in air and the grating's wavevector is in the direction ϕ=93.2°. The outer two panels of Fig 2 present the light returning from the sample which is not due to specular reflection. This light is not spread broadly in k-space, as would be expected for scattering from sample irregularities, but is instead localised in three peaks. The difference in wavevector between the maximum of the largest of these peaks and the maximum intensity of the excited SPP is precisely the grating wavevector, i.e. this is light diffracted between one SPP and another. The other two peaks are -1 and +2 order resonant diffraction of energy from SPP modes with marginally off resonant wavevectors. A resonance in the SPP coupling is clearly observed with rotation of the grating wavevector (i.e. vs. ϕ).

The grating pitch dependence for a 1.462eV plasmon is presented in fig 3a. This figure shows the coupling strength increasing as pitch decreases from 12μm to a maximum value for a pitch of 4μm at which point the coupling decreases rapidly for smaller pitches, tending to zero as the pitch approaches zero. We observe this general dependence on pitch in all our experiments. The value of grating pitch which gives the maximum coupling is seen to vary, in the range 3-4μm, for different sample batches, although it does not depend on the PVK thickness within a batch. There is a small shift to lower pitches in this peak with increasing $|V_{AC}|$ and E_{SPP}. The E_{SPP} dependence of the diffraction efficiency with a 4μm grating is presented in fig 3b. The coupling efficiency clearly increases for decreasing E_{SPP} with a maximum of 25.3±2.2% for E_{SPP} =1.03eV.

These two main experimental results can both be understood by considering three things: (i) the spatial dependence of the light induced electric field grating in the LC, (ii) the fact that the SPP's electric field has a finite penetration distance within the PVK and LC layers, (iii) the surface layer in the LC next to the PVK interface, which due to anchoring and the form of the elastic energy of the LC, is not free to respond strongly to the light induced electric field. We present here a simplified model which allows us to understand the results and which is fully supported by a numerical model we have developed without the simplifying assumptions. If we approximate the PVK and LC layers as isotropic dielectrics, then the magnitude of the electric field in the LC by a light induced sinusoidal surface potential at the PVK-LC interface has the following form

$$|\boldsymbol{E_g}| \propto \boldsymbol{k_\Lambda} e^{-k_\Lambda z} \qquad (1)$$

With $k_\Lambda=2\pi/\Lambda$. The exponential term means that the grating inducing electric field is mostly confined to a layer of thickness Λ, whose thickness therefore decreases with pitch. Within this layer the magnitude of the electric field increases with decreasing pitch. Thus for large pitches where Λ is greater than the SPP penetration distance and the thickness of the surface LC layer, the grating inducing electric field and the diffraction efficiency increase with decreasing pitch. For very small pitches the grating inducing electric field is confined to the LC surface layer and the elastic energy of the LC means that LC response to field, and thus coupling efficiency, decreases with pitch. In the intermediate regime one would expect the peak seen in the data. Using the same length scales one would predict that if the SPP penetration depth is less than the pitch but greater than the LC surface layer one would expect that the coupling efficiency would increase with decreasing E_{SPP} due to increasing overlap between

the SPP and the LC grating. This is what is observed.

In conclusion, we have presented a new class of photorefractive SPP systems which demonstrates strong photorefractive control over SPP. They can be used to couple energy between SPP modes with an efficiency up to 25% which could be further improved by the use of different LCs and/or the addition of dopants to weaken the anchoring of the LC at the PVK surface. With further development of this device we aim to show full photorefractive gain for SPPs.

References

1. J. Homola, S. S. Yee, G. Gauglitz, Sensor Actuator B-Chem.,54 3 (1999).
2. H. J. Lezec, J.A. Dionne, H.A. Atwater, Science, 316 430 (2007).
3. D. O. S. Melville, R.J. Blaikie, Opt. Express, 13 2127 (2005).
4. H. T. Miyazaki, Y. Kurokawa, Phys. Rev. Lett., 96 (9) (2006).
5. G. A. Baker, D. S. Moore, Anal.Bioanal. Chem., 382 1751 (2005).
6. P. Muhlschlegel, H. J. Eisler, O. J. F. Martin, B. Hecht, D. W. Pohl, Science, 308 1607 (2005).
7. V. K. S. Hsiao, Y. B. Zheng, B. K. Juluri, T. J. Huang, Adv. Mater. 20 3528 (2008).
8. I. I. Smolyaninov, A. V. Zayats, A. Gungor, C. C. Davis, Phys. Rev. Lett., 88 (18) (2002).
9. M. Abb, P. Albella, J. Aizpurua, O. L. Muskens, Nano Lett., 11 2457 (2011).
10. K. F. MacDonald, Z. L. Samson, I. M. Stockman, N. I. Zheludev, Nat. Photon., 3 55 (2009)
11. D. Pacifici, H. J. Lezec, H. A. Atwater, Nat. Photon., 1 402 (2007).
12. S. Bartkiewicz, K. Matczyszyn, A. Miniewicz, F. Kajzar, Opt. Comm. 187 257 (2001).
13. M. Kaczmarek, A. Dyadyusha, S. Slussarenko, I.C.Khoo, J. Appl. Phys. 96 5 (2004).

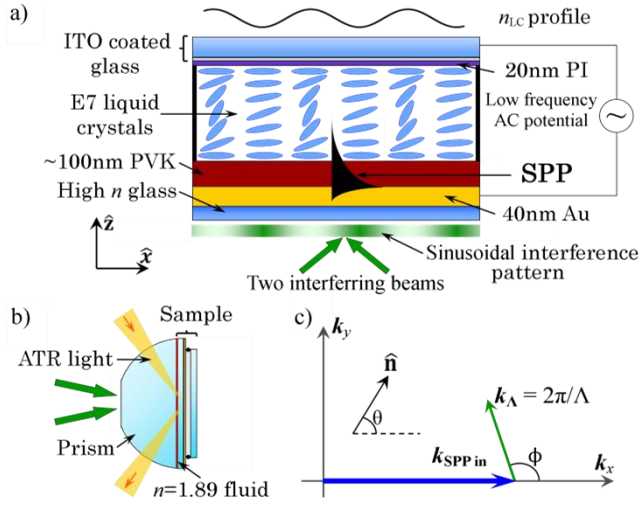

Figure 1: (Colour online) a) The design of the hybrid SPP photorefractive LC cell. b) SPP modes are excited in our cells by the Kretschmann method. c) **k**-space diagram of the SPP coupling system examined.

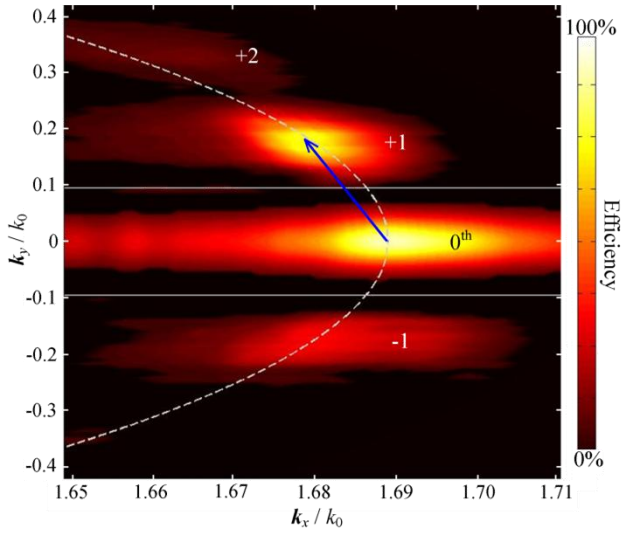

Figure 2: (Colour online) Diffraction of a 1.38eV SPP with a 5μm grating at an angle ϕ = 93.2°. Middle panel presents the excitation efficiency and the other two panels the diffraction efficiency (x10). The dashed line is the wavevector contour for a 1.38eV SPP and the arrow $\mathbf{k}_\Lambda$.

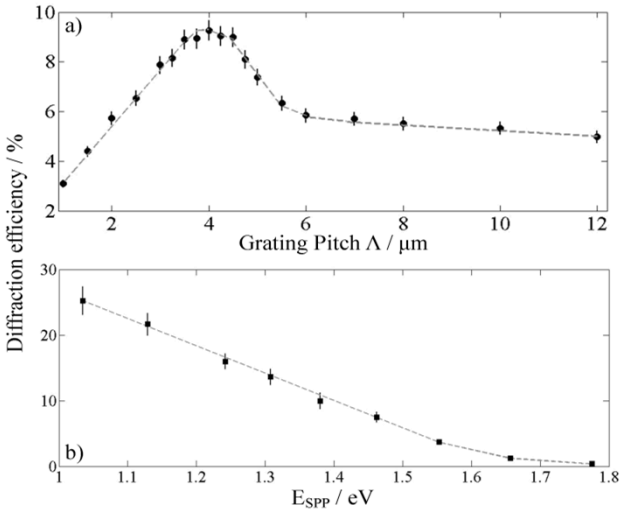

Figure 3: a) The pitch dependence of the SPP diffraction efficiency for a 1.462eV SPP. b) The diffraction efficiency dependence on E_{SPP} for a 4μm grating. The dashed lines are guides for the eye.